5-2023

First principles study of 2D polar heterostructures.

Safia Abdullah R Alharbi

Recommended Citation

Alharbi, Safia Abdullah R, "First principles study of 2D polar heterostructures." (2023). *Electronic Theses and Dissertations.* Paper 4112.
Retrieved from https://ir.library.louisville.edu/etd/4112

FIRST PRINCIPLES STUDY OF 2D POLAR HETEROSTRUCTURES

By

Safia Abdullah R Alharbi
B.S., Princess Nora bint Abdul Rahman University, 2002
M.S., King Saud University, 2013
M.S., University of Louisville, 2017

A Dissertation
Submitted to the Faculty of the
College of Arts and Sciences of the University of Louisville
in Partial Fulfillment of the Requirements
for the Degree of

Doctor of Philosophy
in Physics

Department of Physics and Astronomy
University of Louisville
Louisville, Kentucky

May 2023

FIRST PRINCIPLES STUDY OF 2D POLAR HETEROSTRUCTURES

By

Safia Abdullah R Alharbi

B.S., Princess Nora bint Abdul Rahman University, 2002

M.S., King Saud University, 2013

M.S., University of Louisville, 2017

A Dissertation approved on

April 19, 2023

by the following Dissertation Committee:

Dr. Ming Yu (Dissertation Director)

Dr. Chakram S. Jayanthi

Dr. Gamini Sumanasekera

Dr. Badri Narayanan

DEDICATION

This work is dedicated in memory of my role model, my father:
Mr. Abdullah R. Alharbi
The smartest, most amazing, and most successful man in the world. I never give up because he never did.
To the beautiful lady who sacrifices her whole life for her kids, my mother:
Mrs. Aljazi M. Alharbi
her prayers for me were what sustained me thus far.
To my beloved husband: Mr. Ahmad Alharbi
and my marvelous kids:
Hitham, Alanoud, Abdullah, and adorable baby Nawaf.
For glowing my life with joy and happiness
Special dedication to the primary example of what being a compassionate individual is like, my second father after my father, my big brother:
Professor. Saleh Alharbi
The most generous, kindest, human being on the planet.
To the most important person to me, who always has my back, my best friend, my big sister:
Mrs. Salihah Alharbi
I would be lost without her constant love and support.
To the precious family members who I shared grateful time with them here in the USA
My brother: Rakan, my niece: Budur, and my nephew: Bader
Finally, this dedication is extending to the rest of my brothers, sisters, nephews and nieces for their unconditional love and support.

ACKNOWLEDGMENTS

By the end of this journey, that was not an easy trip for any graduate student, especially for an international graduate student. I owe a profound debt to so many people; and without their inspiration and support, I would not have made it across the finish line. Therefore, I would like to pay them back by expressing my overwhelming gratitude to them.

First and foremost, all praise and thanks belong to Allah alone for giving me strength during this journey, who formed who I am in untold and unquantifiable ways.

I am deeply indebted to my supervisor professor Dr. Ming Yu, for her insightful guidance, support, patience, and belief in my ability to succeed. She is an extraordinary professor who always comes up with fruitful ideas, and I am honored to work with such a kind, caring, and great professor. She is not only an incredible advisor but also my best friend.

I am extremely grateful to professor Dr. Jayanthi for her support as a chair of the department and for her comments as a committee member. I am extremely grateful for having her in our CMT group and sharing knowledge and experience from such an intelligible professor.

I would like to express my deepest gratitude to professor Dr. Samman Kera for his support as Graduate Program Director. Also, for his participation in the committee and his insightful feedback

I am also grateful to Dr. Narayanan for accepting to be part of this journey, reviewing my work as a committee member, allowing me to be sitting in his useful class, and his insightful and valuable feedback.

Special thanks to the members of CMT group, Dr. Congyang Zhang, Mr. Sultan Alzahrani, Dr. Md Musa, Mrs. Tasnim Kasi, and Mr. Aswad Alhassan for sharing knowledge and experience.

I would like to extend my sincere thanks to my amazing friends, Dr. Alaa Alfailakawi, Dr. Shadi Alnaanah, Mrs. Hasna Alrfooh, and Mrs. Fatimah Algarni who were a fuel for my social life.

ABSTRACT

FIRST PRINCIPLES STUDY OF 2D POLAR HETEROSTRUCTURES

Safia Abdullah R Alharbi

April 19, 2023

Recently, two-dimensional (2D) heterostructures have attracted extensive attention in nanomaterials science. They have been successfully fabricated and applied to nanotechnology in many fields, such as nanoelectronics, solar cells, sensors, energy stores, quantum information, etc. The most common heterostructures are 2D-lateral heterostructure (LH) and 2D-vertical heterostructure (VH) where each of them exhibits unique features depending on the direction of assembly, i.e., along in-plane or out-of-plane direction.

Beyond the van der Waals-VH which possess of van der Waals (vdW) interaction, there are other types of heterostructures made of 2D polar materials that possess different types of chemical bonding nature, e.g., chemical bonds with less (e.g., SiC monolayer) or more (e.g., GeC and SiGe monolayers) charge transfer between atoms, forming covalent bonds with a certain ionicity. The goal of this work focused on shedding light on the physical aspects of 2D LH and VH, constructed by such polar materials (e.g., SiC, GeC, and SiGe monolayers). This work is a theoretical study by employing Density Functional Theory to unravel the unique physical properties of such heterostructures.

Because an artificial strain will be induced by the lattice mismatch in building heterostructures, the effect of strain on the electronic properties of SiC, GeC, and $SiGe$ monolayers was first investigated. It was found that these monolayers can tolerate strain up to 8%, and such strain can induce modifications on the physical properties. Interestingly, it was found that SiC and GeC monolayers undergo a direct-indirect band gap transition; while, $SiGe$ monolayer undergoes a metal-semimetal transition, which made them attractive candidates for building heterostructures.

Second, a systematic study on the aspect of 2D polar-LH of SiC/GeC, and $SiGe/GeC$ has been conducted. It was found that the synergistic effect of the lattice mismatch induced strain, the chemical bonding nature at the interface, and quantum confinement can lead to several interesting phenomena. For instance, their electronic properties can be modulated by tuning the domain size, the chemical bonding nature, and the designing of interface. Accordingly, a lateral spontaneous *p-n* junction triggered by the in-plane charge transfer was detected which implies the promising applications such as visible light photocatalyst.

Third, the roles of the stacking species arrangement and the interlayer interactions (including vdW and electrostatic forces) on stabilizing the structure and modulating electronic properties of 2D polar-VH of $SiGe/GeC$ were deeply studied. It was found that, in addition to the redistribution of the in-plane net-charge transfer, a net charge redistribution also occurs between layers and leads to a polarization in the interfacial region that induces a built-in electric field and helps to reduce the recombination of photogenerated electron-hole pairs.

TABLE OF CONTENTS

LIST OF TABLES

LIST OF FIGURES

CHAPTER I

1. INTRODUCTION

1.1. Introduction to 2D materials

The transition from an ordinary (macroscopic) scale to an atomic (microscopic) scale induces breakthroughs. In mechanics, for example, such a move led to the birth of the quantum mechanics field, which is the foundation of all modern physics. In materials science, it is the transition from three-dimensional (3D) materials to two-dimensional (2D), one-dimensional (1D), and zero-dimensional (0D) materials who plays a role in nanostructures. This section will introduce the 2D materials and their attractiveness to researchers.

The dimensionality makes qualitative changes to materials. Any material can be classified as 0D material (i.e., nanoparticle) when all dimensions are in the scale of nanometer (<100 nm) (e.g., quantum dot); 1D material (e.g., nanotube or nanowire) when one dimension is out of the scale of nanometer; 2D material (e.g., nanosheet) when two dimensions are out of the scale of nanometer; and 3D material when all dimensions are not confined to the nanoscale, such as bulk, multilayers, bundles of nanotubes or nanowires, and dispersions of nanoparticles. Figure 1-1 illustrates the dimensionality effect for carbon material as an example. Starting from 2D carbon sheet (graphene), we can build 0D carbon (fullerenes) by wrapped up graphene into a ball, 1D carbon nanotube by rolled graphene into nanotube, 3D carbons bulk (graphite) by stacking graphene; where 0D fullerenes, 1D carbon nanotube, 2D graphene, and 3D graphite manifest different properties. This example unintentionally appears the importance of 2D materials as a building rock of the different dimensional forms of a given material [1].

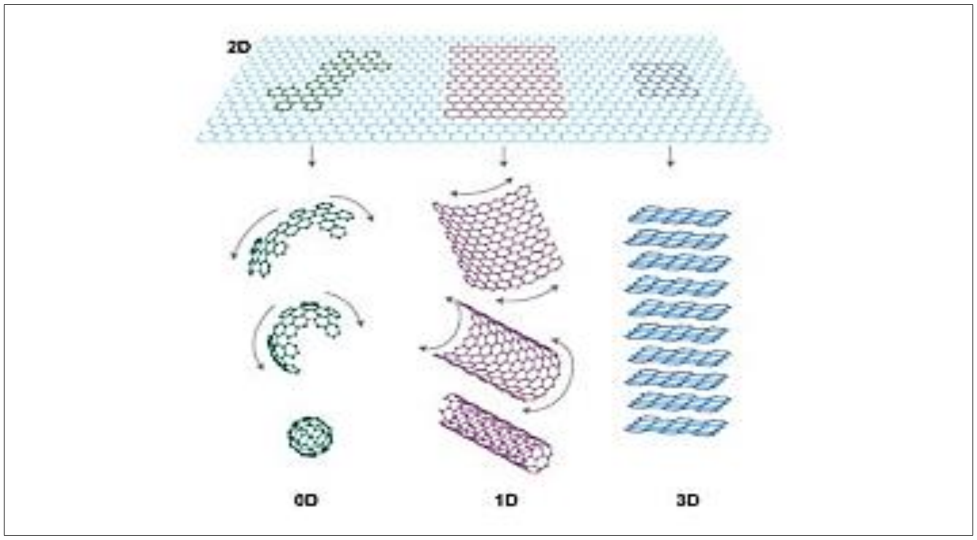

Figure 1-1: An illustration of graphene as a building rock of the different dimensional forms [1].

2D materials, by definition, are atomically thin crystalline solids having intralayer covalent bonding, interlayer vdW bonding, and a thickness of a single to few atomic thick layers (< 5 nm) [2]. However, the lateral size of 2D materials varies from nanometers up to micrometers. Hence, they are considered sheet-like structures [3, 4]. Nobody imagined using 2D materials in real-life applications or even their existence beyond the theoretical studies until 2004. In 2004, Andre Geim and Konstantin Novoselov, the holders of the 2010 Nobel Prize in Physics, isolated experimentally graphene (2D) from graphite (3D) [5, 6]. Graphene has extraordinary properties compared to 3D materials, therefore, not only what the material made of effects its properties but also its thickness.

2D materials have attracted extensive attention and become a rich topic for scientific and practical research. In scientific studies, the researchers have found novel fundamental physics, such as half-integer quantum Hall effect [7], Klein tunnelling [8], topological superconductivity [9, 10], and Boson Peak [11]. In practical studies, on the other hand, 2D materials possess interesting properties which make them favorable for real life applications, such as (i) the quantum size confinement [12] which enhances electronic properties for electronic devices; (ii) the large surface-to-volume ratio which grants them with ultrahigh specific surface area, such area is a desirable feature for surface-active applications [13]; (iii) flexible mechanical and tunable electronic, optical, and chemical properties, making them promising for electronic/optoelectronic applications [14, 15]; (iv) naturally passivated surface without any dangling bonds allow them to easy integration with photonic structures such as fibers and chips [16, 17]; (v) highly tunable band gap which divers from insulators to narrow gap semiconductors, topological insulators, semimetals, and metals which make them very suitable for electronic applications [16-20].

In the past decade, beyond graphene, there has been a competition to discover more 2D materials, and their data bases grow tremendously. For instance, theoretical prediction in the data base of 2DMatPedia includes more than 6,000 monolayer structures [21]. However, up to date, only about 2% of them have been experimentally synthesized. To name only a few, transition metal dichalcogenides (TMDs) [22], black phosphorus (BP) [23], and MXenes, and their van der Waals heterostructures (vdWs) [24]. Figure 1-2 shows classification of the current 2D materials available up to the date [25]. It is incumbent on interested researchers to follow up the ever-growing technological applications.

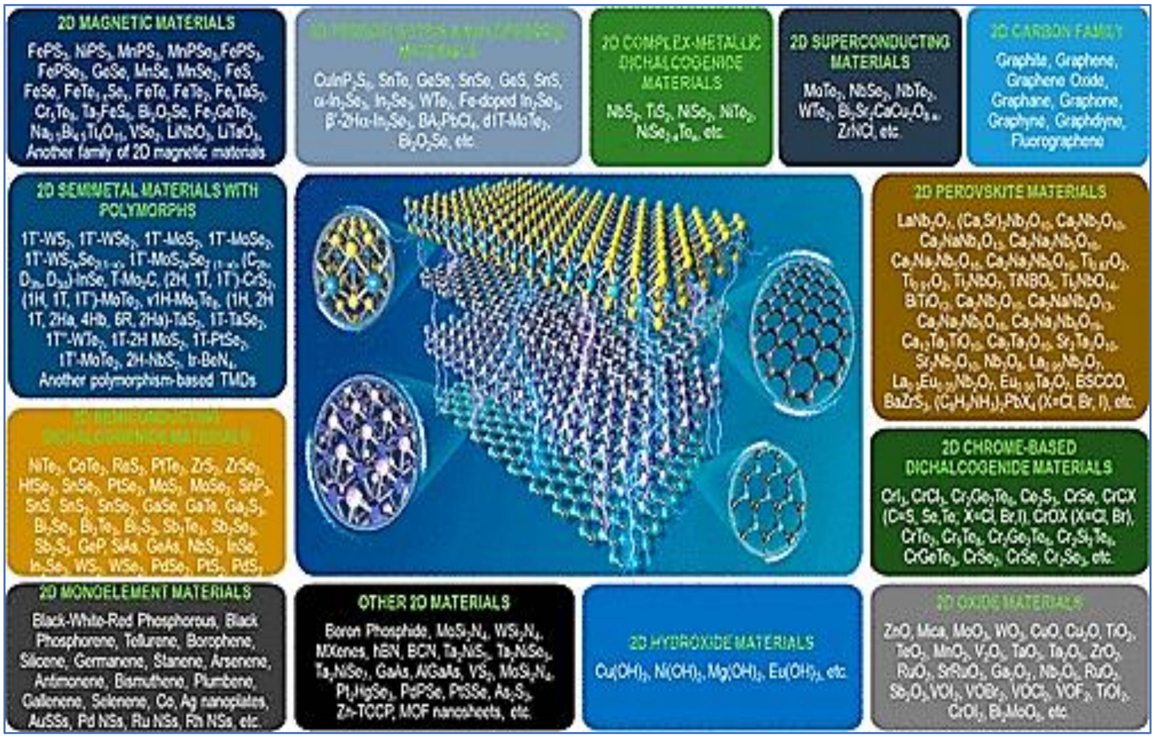

Figure 1-2: Classification of the current 2D materials available up to the date [25].

1.2. Introduction to 2D Heterostructures

1.2.1. Overview of heterostructures

Heterostructures (*i.e.*, heterojunctions) are the building blocks of the most advanced semiconductor devices being developed and produced. They have been found to be used in a variety of specialized applications where their unique characteristics are critical, such as semiconductor lasers, LED, heterojunction bipolar transistors (HBT) (see an example in Figure 1-3 (a)), and high electron mobility transistors (HEMT). It has played an important role in cutting-edge nanotechnology. The Nobel Prize in physics in 2000 was awarded for the developing semiconductor heterostructures used in high-speed- and opt-electronics [26].

Conventional heterojunction (i.e., three-dimensional (3D) heterostructures) is characterized by the interface that occurs between two layers or regions of dissimilar crystalline semiconductors, having different energy gaps. The carriers are confined by the heterojunction barriers. The nature of the heterojunction depends crucially on the alignment of the energy bands at the interface which is categorized by straddling gap (type I), staggered gap (type II), and broken gap (type III), respectively (see Figure 1-3 (b)). Several issues need to be considered in designing heterojunctions. It has been found that the interface in HBT is essentially atomically abrupt [31, 32]. The most obvious cause comes from the mismatch between the lattices of the participating semiconductors which produce defects in the form of dislocations in one or the other of the participating semiconductors. Such dislocations usually affect the electrical characteristics of the system by creating localized states which trap charge carriers. If the density of such interfacial traps is sufficiently large, they will dominate the electrical properties of the interface. This is what usually happens at poorly controlled interfaces such as the grain boundaries in polycrystalline materials.

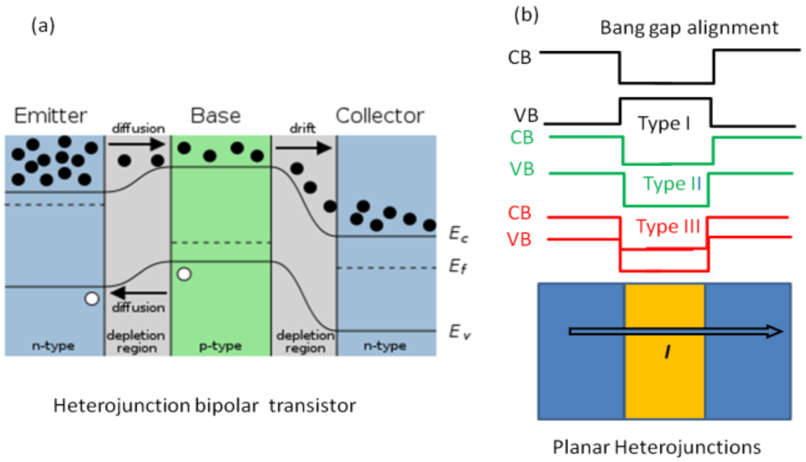

Heterojunction bipolar transistor

Planar Heterojunctions

Figure 1-3: Schematic illustrations of (a) a heterojunction bipolar transistor and (b) a planar heterojunction with three types of the band alignments (the arrow indicates the motion of the carriers).

Different from 3D heterostructures where different bulk slabs chemically bonded at the junctions, recently developed 2D heterostructures are assembled by layered materials either along the in-plane direction (called lateral heterostructures) or the out-of-plane direction (called vertical heterostructure). They commonly possess unique optical bandgap structures, extremely strong light–matter interactions, and large specific surface. 2D heterostructures can be classified as van der Waals heterostructures (vdWHs) (or non-polar heterostructures), polar heterostructures (where the electrostatic interlayer force also play the role), etc.[27].

The vdWHs have almost no change at the atomic scale, even with a large lattice mismatch in layered materials, because they are formed by weak vdW forces, which helps maintain the electronic structures of the participating materials. This unique property induces excellent physical properties in novel advanced heterojunctions based on lower dimension materials, giving rise to fascinating phenomena such as Hofstadter's butterfly spectrum according to the moiré patterns, strongly bound excitons, and spinvalley polarization. By combining the different properties of the building blocks, synthesized vdW structures may show integrated properties with respect to the segregated materials. In regard to the atomic thickness and excellent flexibility of 2D materials, vdWHs are applied to bandgap engineering to develop gate-tunable band structures. Devices based on vdWHs exhibit a big breakover current and fast responsivity, attributed to the ultrafast charge transfer in 2D materials, where electronic transport is strictly 2D and not scattered in the third dimension. More importantly, strong in-plane covalent bonding associated with the weak interaction between the layers of 2D materials can form numerous mismatched vdWHs based on the diversity of 2D materials including the layering of metals, semiconductors, insulators, and even superconductors.

Meanwhile, exploring new classes of 2D heterostructures beyond vdWHs is also highly desired for prospective applications in advanced nanotechnologies. 2D layered polar materials (usually with no 3D vdW counterparts) have strong electrostatic intra-layer bonding and less-strong (yet comparable to vdW) electrostatic interlayer bonding to hold the layers together. A distinguishing phenomenon, compared to 2D vdW heterostructure, is found in 2D vertical polar heterostructures. The equilibrium interlayer distance varies dramatically. Such change of the interlayer space is mainly correlated to the out-of-plane species ordering, which is much weaker in 2D vdW binary compound heterostructures. Therefore, the 2D polar vertical heterostructures, constructed by 2D polar materials, are expected to exhibit novel and unique features in the interfacial region. Manipulating such 2D layered polar structures using bottom-up approch (*i.e.*, starting from stable 2D monolayers of ionic compounds and buliding multilayer heterostructures) to construct 2D polar (lateral and vertical) heterostructures can open the door for the development of a new class of 2D heterostructures beyond currently available vdWHs for the next-generation of nanoelectronic, optoelectronic, and sensing devices.

1.2.2. Development of 2D heterostructures

The integration of 2D materials into a device will always involve interaction with other materials, which is critical to real-life applications. One type of such interaction is by building 2D heterostructures from 2D materials. 2D heterostructures are the building blocks of the most advanced devices with exotic electrical, optical, and thermal characteristics. A heterostructure is defined as a structure in which the chemical composition changes with position [28]. Thanks to the weak vdW interlayer interaction, the force that hold layered materials together allows us to exfoliate 2D materials and then create 2D homo-structures or heterostructures laterally or vertically, such as multilayer graphene (homo-structures) and graphene/ hexagonal-boron nitride (h-BN) (heterostructure).

Despite the fascinating properties of 2D materials, there are limitations in practice. Graphene, for example, possesses novel features desired for a wide range of technologies, such as superior strength, extremely high electrical conductivity, high mobility and flexibility, optical transparency, and large modulation band width [13, 29-31]. However, there are some limitations, such as weak optical absorption and zero band gap, that prevent the integration of graphene into optoelectronic applications [32, 33]. Integration of 2D materials to form 2D heterostructure is one of optimum ways to overcome some of these limitations due to its role in the emergence of synergistic effects and enhanced properties. In designing 2D heterostructure, we can combine different 2D structures to subject them into either intralayer interaction (laterally) at the interface or interlayer interaction (vertically) on the surface. Such interface interactions affect the structural and electronic properties of heterostructure which might lead to structural modulation and charge redistribution. In addition, these changes can be controlled due to the sensitivity of 2D heterostructure to lattice mismatch and relative orientation that appear as a plethora of pioneer opportunities to release limitations of 2D materials.

Moreover, miniaturization is a trend of innovative nanotechnology. The features of semiconductors and dielectrics do not serve miniaturization very well and are no longer compatible with electrical contacting in complex operation, such in robotics, artificial intelligence (AI), and ubiquitous electronics, mainly due to short channel effects, high leakage current, and high contact resistance [34, 35]. Therefore, 2D materials, in particular 2D heterostructures, are ideal candidates for nanotechnology, due to their size and novel features.

Besides, in practical prospect, 2D heterostructures span a full range of electronic, optoelectronic, and spintronic properties with controllable and tunable capability that can be combined to design promising electronic and optoelectronic devices with high performance, low power consumption, and other desirable properties (like transparency and flexibility) [25, 32-35]. With the efforts of many researchers, field-effect tunneling or transistors, LEDs, biosensors, light detectors, photovoltaics, energy storage devices, etc. have been reported. Figure 1-4 illustrates some of the recent 2D heterostructures applications.

The aim of 2D heterostructures is to control fascinating properties of 2D materials into ultimate materials that can face high demand of ever grown technology. Hence, they are considered as the best in the current field of 2D material science. Such research has been conducted by the driven of all the galore potentials of 2D heterostructures.

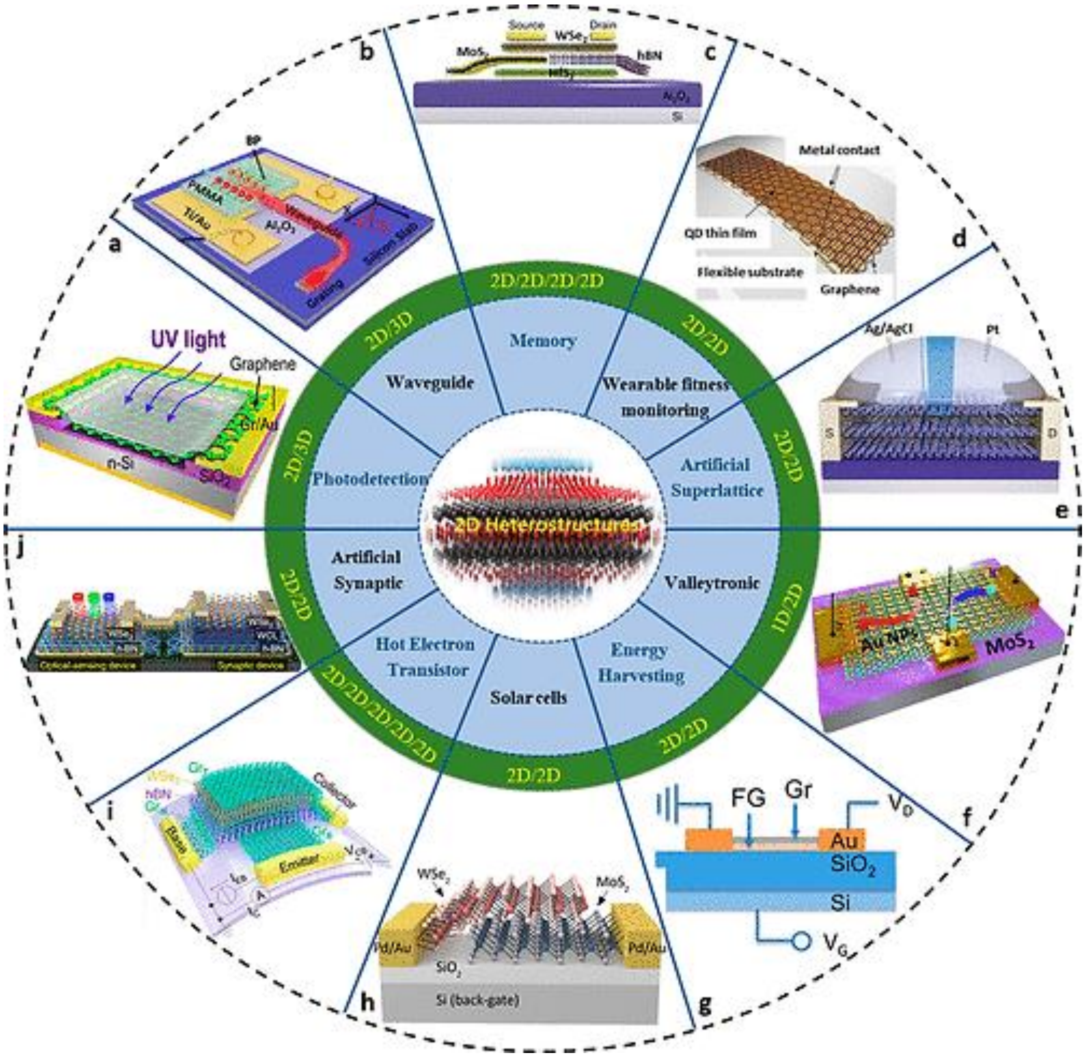

Figure 1-4: Illustration of recent 2D heterostructures applications.

1.3. Introduction to Group IV-based materials

In the periodic table, graphene belongs to Group IV. Namely, graphene is an allotrope of carbon, the first element in group IV with monolayer sheet form. Group IV has a special location in periodic table with nonmetals to the right of it and metals to the left of it. This section sheds light on Group IV-based materials and how they drew the researcher’s attention.

Group IV, which is also called group 14, tetrels, crystallogensis, or carbon group (or family), consists of the following elements: carbon (C), silicon (Si), germanium (Ge), tin (Sn), lead (Pb), and flerovium (Fl). Atoms of elements in this group have four valence electrons, two of them are in the s subshell, while the other two are in the p subshell. Only carbon has the $2s^2 2p^2$ outer configuration, which accounts for some of the differences between carbon and other elements in the family. When one moves down in group IV, the atomic radius, ionic radius, and element density increase, while electronegativity and ionization energy decrease. Carbon is nonmetal, silicon and germanium are metalloids, and tin and lead are metals. In other words, elements gain metallicity when one moves down group IV in the periodic table. On the compounds side, all elements of group IV tend to form covalent compounds except tin and lead which also form ionic compounds. Moreover, carbon and silicon are the fourth and eighth abundant elements in the universe by mass, respectively. Carbon is the basis for organic life, while silicon and germanium are very important elements for semiconductors, which grant group IV elements the importance in daily life and industry [36].

2D materials formed by group IV-based materials, also called graphene-like group IV materials or group IV X-enes (e.g., silicene, the 2D form of silicon [37, 38], germanene, the 2D form of germanium [37, 39, 40], and stanine, the 2D form of tin [41, 42]), attract scientists as graphene siblings in the carbon family. In principle, they share similar physicochemical and topological properties. In contrast, silicene [43], germanene [44], and stanene [45] are semimetals with gapless and hexagonal symmetry characters like graphene. However, they all have a buckled honeycomb structure due to the coexistence of sp^2 and sp^3 hybridization unlike graphene which has a flat structure due to sp^2 hybridization. Silicene, germanene, and stanine were recently synthesized by means of molecular beam epitaxy with require of a substrate: sliver, gold, and bismuth telluride (Bi2Te3), respectively.

Although the novel properties that Group IV X-enes possess, their zero-band gap nature limits their applications in nanoelectronics devices. To overcome this problem, the work in this dissertation has been intended to use the binary compounds made of group IV such as GeC, SiC, and $SiGe$ monolayers. The preliminary studies of such binary compounds show that in SiC or GeC, the band gap opens with indirect (SiC)/direct (GeC) nature. Furthermore, they are flat hexagonal lattice, forming sp^2 hybridization like graphene. However, $SiGe$, unlike graphene, is a buckled honeycomb lattice, forming sp^3 hybridization, and semimetal with zero-band gap. This opens a wide possibility to investigate the potential of using group IV elements-based binary compounds in nanoelectronics devices.

1.4. Overview of research project

Chapter 2 addresses the methodology of the study performed in this dissertation. It starts from the Density Functional Theory (DFT) with brief talking points about the Schrödinger equation of a system, Born–Oppenheimer approximation, Kohn-Sham (Schrödinger like) equations, and the exchange-correlation potential. Then, the computational details that have been used in this dissertation were introduced including structural and dynamic stability, and electronic properties.

Chapter 3 includes a report of the study of the strain effect on 2D binary compounds of Group IV element (SiC, GeC, and $SiGe$) with analysis of band structures under strain effect, charge transfer, and the electron localization function (ELF). The effects of strain, interface, and confinement on LH of 2D polar binary compounds (SiC/GeC and $GeC/SiGe$) together with analysis of band structure, band gap, and charge redistribution are discussed in Chapter 4.

In Chapter 5, a systematical study on VH of 2D polar binary compounds ($GeC/SiGe$) has been performed to show the synergistic effect of the interlayer interaction, the stacking arrangement, and the species ordering type on such type of VH. It addresses the feature of a commensurate structure and the relative energy and analyzes electronic properties, charge redistribution, and charge transfer.

Finally, Chapter 6 establishes a couple of ongoing works. The first one is about the study of potential energy surface (PES) in the Moiré patterns GeC bilayer. The second ongoing work conducts a comparison study of strain engineering in monolayer of group-IV binary compounds by using Quantum espresso code (QE) with the goal of applying

QE for further computational study on complex nanoscale materials with such open resource.

CHAPTER II

2. METHODOLOGY

2.1. Computational Materials Science (CMS)

Computational Materials Science (CMS)-based methods were employed in all projects of this dissertation. CMS provides researchers a modeling and simulation approach to design new materials and to understand and predict their behaviors. CMS-based methods vary based on range of length (nanometers - meters) and time (femtoseconds of atomic vibrations to decades) scales. In fact, all computational calculations included in this dissertation were within quantum and atomic multiscale that based on DFT. The DFT method used in this dissertation is implemented in Vienna ab initio simulation package (VASP)[46].

In contrast to computational methods, experimental methods are often expensive and time-consuming. CMS normally views what experiments cannot examine, which provides a deep understanding of a materials system. In addition, CMS might surpass experiments by predicting system behavior even under conditions that experiments cannot perform, such as extremely high/low temperature, or pressure. The experimental data, on the other hand, provides a validation test to check the accuracy of computational calculations. Accordingly, ongoing advance theoretical methods (such as DFT), hardware, and software (such as VASP code) are powerful tools in accelerating the developments in solid state physics and other related fields.

2.2. Density Functional Theory (DFT)

DFT is a well-established tool and the most successful approach for calculating the properties of materials at the atomic level. Walter Kohn (1923 − 2016) was dually awarded the 1998 Nobel Prize for his development of the DFT [26]. The results of DFT computations are frequently coupled with experimental results which indicate a verification of DFT validation. Furthermore, DFT came to prominence as an approach for solving Schrödinger equation for a system, a goal of most approaches in solid state physics and quantum chemistry.

2.2.1. Schrödinger equation for a system

In quantum mechanics, the time-dependent Schrödinger equation for a system is an equation of motion; it is analogue to Newton’s second law as an equation of motion in classical mechanics. When the potential energy of the system depends implicitly on the time, the time-dependent Schrödinger equation is then reduced to the time-independent Schrödinger equation (Equation 2-1):

$\hat{\mathrm{H}}\Psi(\{\mathbf{r}_\mathrm{i}, \{\mathbf{R}_\mathrm{I}\}) = \mathrm{E}\Psi(\{\mathbf{r}_\mathrm{i}\}, \{\mathbf{R}_\mathrm{I}\})$ Equation 2-1

Where $\hat{\mathrm{H}}$ is the Hamiltonian of the system, E is the energy, and $\Psi(\{\mathbf{r}_\mathrm{i}\}, \{\mathbf{R}_\mathrm{I}\})$ is the wave function.

$$\hat{\mathrm{H}} = -\frac{1}{2}\sum_{i=1}^{N}\nabla_i^2 - \frac{1}{2}\sum_{A=1}^{M}\frac{1}{M_A}\nabla_A^2 - \sum_{i=1}^{N}\sum_{A=1}^{M}\frac{Z_A}{|\mathbf{r}_i - \mathbf{R}_A|} + \sum_{i=1}^{N}\sum_{j>i}^{N}\frac{1}{|\mathbf{r}_i - \mathbf{r}_j|} + \sum_{A=1}^{M}\sum_{B>A}^{M}\frac{Z_A Z_B}{|\mathbf{R}_A - \mathbf{R}_B|} \quad \text{Equation 2-2}$$

The Hamiltonian of a system $\widehat{\mathrm{H}}$, as shown in Equation 2-2, contains three parts: the kinetic energy of the electrons and nuclei, $\widehat{\mathrm{T}}_e = -\frac{1}{2}\sum_{i=1}^{N} \nabla_i^2$ and $\widehat{\mathrm{T}}_n = -\frac{1}{2}\sum_{A=1}^{M} \frac{1}{M_A} \nabla_A^2$, respectively, the attractive electrostatic interaction between the nuclei and the electrons $\widehat{\mathrm{V}}_{ext} = -\sum_{i=1}^{N}\sum_{A=1}^{M} \frac{Z_A}{|\mathbf{r}_i - \mathbf{R}_A|}$, and repulsive potential due to the electron-electron and nucleus-nucleus interactions $\widehat{\mathrm{V}}_e = \sum_{i=1}^{N}\sum_{j>i}^{N} \frac{1}{|\mathbf{r}_i - \mathbf{r}_j|}$, and $\widehat{\mathrm{V}}_n = \sum_{A=1}^{M}\sum_{B>A}^{M} \frac{Z_A Z_B}{|\mathbf{R}_A - \mathbf{R}_B|}$, respectively. Here, A and B run over M nuclei while i and j denote N electrons in a system. These equations are in atomic units, in which the fundamental constants m, e, $\hbar$, etc. are all equal to 1, unit of energy is Hartree, and unit of length is Bohr. So, one can write $\widehat{\mathrm{H}}$ as Equation 2-3.

$$\widehat{\mathrm{H}} = \widehat{\mathrm{T}}_e + \widehat{\mathrm{T}}_n + \widehat{\mathrm{V}}_{ext} + \widehat{\mathrm{V}}_e + \widehat{\mathrm{V}}_n \text{ Equation 2-3}$$

Basically, solving Schrödinger equation means finding the wave function $\Psi(\{\mathbf{r}_\mathrm{i}\},\{\mathbf{R}_\mathrm{I}\},t)$. After knowing the wave function, one can, in principle, measures any desired observable A; hence, getting the property of a system. Equation 2-4 gives the average value of the operator A, for a normalized wave function. Accordingly, Schrödinger equation can be solved only for simple systems, e.g., Hydrogen atom; but for many-body system, approximations should be made, e.g., Born–Oppenheimer approximation.

$$\langle\widehat{\mathrm{A}}\rangle = \int \Psi^*(\mathbf{r})\widehat{\mathrm{A}}(\mathbf{r})\Psi(\mathbf{r})d\mathbf{r} \text{ Equation 2-4}$$

2.2.2. Born–Oppenheimer (BO) approximation.

In 1927, Max Born and J. Robert Oppenheimer proposed that the total wave function $\Psi(\mathbf{r},\mathbf{R})$ of a molecule can be separated into the wave functions of nuclei $\chi(\mathbf{R})$ and electrons $\psi(\mathbf{r})$ (Equation 2-5) due to the large difference relatively between masses and time scale for the nuclei and electrons in the system.

$\Psi(\mathbf{r},\mathbf{R}) = \psi(\mathbf{r})\chi(\mathbf{R})$ Equation 2-5

Based on that, BO approximation treated the coordinates of nuclei and electrons in a system as fixed and dynamic coordinates, respectively. Therefore, one can neglect the kinetic energy of nuclei and consider the nucleus-nucleus interaction as a constant. Then, the Hamiltonian of the system after BO approximation becomes:

$\widehat{\mathrm{H}} = \widehat{\mathrm{T}}_e + \widehat{\mathrm{V}}_{ext} + \widehat{\mathrm{V}}_e$ Equation 2-6

2.2.3. Hartree-Fock (HF) approximation

The electron-electron interaction $\widehat{\mathrm{V}}_e$, in Equation 2-6, is the most complicated term to be calculated. Therefore, to simplify the Hamiltonian $\widehat{\mathrm{H}}$, $\widehat{\mathrm{V}}_e$ must be approximated. In 1928, Hartree proposed his approximation, although Schrödinger equation was only published in 1926, that the total wave function consists of single particle functions for each electron after he supplanted $\widehat{\mathrm{V}}_e$ by a static potential. Consequently, the electronic wave function for a system with N electrons $\psi(\mathbf{r}_1,\mathbf{r}_2,\ldots\mathbf{r}_\mathrm{N})$ becomes a product of N single wave function:

$\psi(\mathbf{r}_1,\mathbf{r}_2,\ldots\mathbf{r}_\mathrm{N}) = \phi_1(\mathbf{r}_1)\,\phi_2(\mathbf{r}_2)\ldots\phi_N(\mathbf{r}_\mathrm{N})$ Equation 2-7

Despite that Hartree's approximation simplifies $\widehat{\mathrm{H}}$, $\psi(\mathbf{r}_1, \mathbf{r}_2, \dots \mathbf{r}_\mathrm{N})$ suffers from not being antisymmetric since it does not obey Pauli's exclusion principle. To solve this problem, a correction made by Fock in which he replaced $\psi(\mathbf{r}_1, \mathbf{r}_2, \dots \mathbf{r}_\mathrm{N})$ by staler determinant type wave function $\psi(\mathbf{r}_1, \mathbf{s}_1, \mathbf{r}_2, \mathbf{s}_2, \dots, \mathbf{r}_\mathrm{N}, \mathbf{s}_\mathrm{N})$:

$$\psi(\mathbf{r}_1, \mathbf{s}_1, \mathbf{r}_2, \mathbf{s}_2, \dots, \mathbf{r}_\mathrm{N}, \mathbf{s}_\mathrm{N}) = \frac{\mathbf{1}}{\sqrt{\boldsymbol{N}!}} det \begin{bmatrix} \phi_1(\mathbf{r}_1, \mathbf{s}_1) & \cdots & \phi_1(\mathbf{r}_\mathrm{N}, \mathbf{s}_\mathrm{N}) \\ \vdots & \ddots & \vdots \\ \phi_N(\mathbf{r}_1, \mathbf{s}_1) & \cdots & \phi_N(\mathbf{r}_\mathrm{N}, \mathbf{s}_\mathrm{N}) \end{bmatrix} \text{Equation 2-8}$$

HF approximation is very accurate and was the mainstay of electronic structure calculations, especially in quantum chemistry, for decades. However, it neglects the correlation energy, the energy associated with motion of the electrons being correlated; so that they stay apart from each other. Moreover, HF approximation is suitable for just small systems where the set of N single wave function can be solvable.

2.2.4. The Hohenberg- Kohn (HK) theorems

The cornerstone of DFT was made in 1964, after the two Hohenberg- Kohn (HK) theorems emerged. The first theorem states: "The ground-state energy from Schrödinger's equation is a unique functional of the electron density." [47] In other words, there is a direct dependence between the ground-state wave function and the electron density. The significance of this theorem is that it replaces 3N dimensional problem with 3-dimensional density of ground state electron.

The second theorem states: "The electron density that minimizes the energy of the overall functional is the true electron density corresponding to the full solution of the Schrödinger equation."[47] Taking an assumption that the functional is known, one needs to keep changing the electron density until the energy from the functional is minimized.

Despite the importance of HK theorems, which proved the existence of a functional of the electronic density ρ, it does not show what that functional is or how to find it.

2.2.5. Kohn-Sham (KS) or Schrödinger - like equations

In the early models to solve Schrödinger equation, such as Thomas -Fermi and Thomas-Fermi-Dirac model, most errors came from ignoring the discontinuities in the shell structure of the electrons that cause a significant impact on kinetic energy. Kohn and Sham overcame this issue by assuming that, for an N electron system, the electron density $\rho(\mathbf{r})$ equals to a sum of one-electron orbitals $\phi_i(\mathbf{r})$:

$\rho(\mathbf{r}) = \sum_{i=1}^{N} |\phi_i(\mathbf{r})|^2$ Equation 2-9

Then, the discontinuities in the shells become natural outcomes of the solutions [48]. Hence, KS model can reduce the Hamiltonian in Equation 2-6 to:

$\widehat{\mathrm{H}_{KS}} = \hat{\mathrm{T}}_e + \hat{\mathrm{V}}_{eff}$ Equation 2-10

Where $\hat{\mathrm{V}}_{eff}$ is the effective potential which is:

$\hat{\mathrm{V}}_{eff} = \hat{\mathrm{V}}_{ext} + \hat{\mathrm{V}}_{XC} + \int \frac{\rho(\acute{\mathbf{r}})}{|\mathbf{r}-\acute{\mathbf{r}}|} d\acute{\mathbf{r}}$ Equation 2-11

Here, $\hat{\mathrm{V}}_{XC} = \frac{\delta E_{xc}}{\delta\rho(\mathbf{r})}$ and E_{xc} is the exchange-correlation function of choice. Then, the time-independent Schrödinger equation for N electrons system is reduced to that for a single electron system by using the Hamiltonian in Equation 2-10:

$\widehat{\mathrm{H}_{KS}} \phi_i(\mathbf{r}) = \epsilon_i \phi_i(\mathbf{r})$ Equation 2-12

Which is similar to Schrödinger equation, but it includes the effective potential $\widehat{\mathrm{V}}_{eff}$ instead of the potential $\widehat{\mathrm{V}}$. For this reason, many authors call it the Schrödinger-like equation.

Up to date, the start point of most DFT calculations is by using the KS model, which implements an iterative method as shown in Figure 2-1. The iterative method starts with an initial guess of a set of wave functions ϕ_i^0; afterward, to calculate the electron density ρ_0 by following Equation 2-9. Then, by using this initial electron density ρ_0, one can form KS Hamiltonian (Equation 2-10); then, use it to solve KS equations (Equation 2-12). At this point, the solution contains a set of N orbital wave functions ϕ and 1-electron orbital energies ϵ, which can be used to calculate a new electron density ρ ,then $\widehat{\mathrm{V}}_{eff}$. Next, using this new $\widehat{\mathrm{V}}_{eff}$ to solve KS equations again; and the process continues in a loop until a self-consistent ρ is found, which means that the electron density ρ is converged [49].

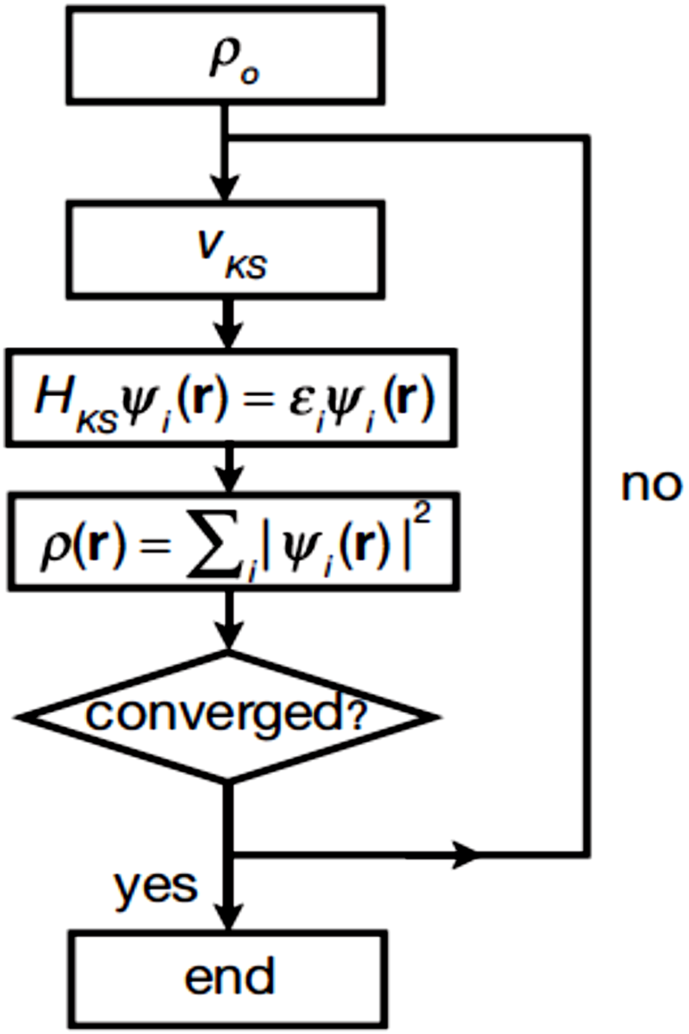

Figure 2-1: Schematic diagram of the iterative method in KS model [48].

2.2.6. The exchange-correlation potential

As has been noted in Equation 2-11, getting $\hat{V}_{eff}$ depends somehow on the choice of exchange-correlation potential $\hat{V}_{XC}$. The most popular choices of $\hat{V}_{XC}$ are the local density approximation (LDA) and generalized gradient approximation (GGA). In LDA, the exchange-correlation energy is just the adding of the exchange energy E_x, to the correlation energy E_c:

$E_{xc,LDA} = E_x + E_c$ Equation 2-13

Here, E_x and E_c are based on the uniform electron density. Therefore, LDA works well with systems of local charge density. On the other hand, GGA is still local-density approximation; but based on the gradient of the electron density:

$E_{xc,GGA} = \int \rho(\mathbf{r})\epsilon_{xc}(\rho, \boldsymbol{\nabla}\rho)d\mathbf{r}$ Equation 2-14

Where $\boldsymbol{\nabla}\rho(\boldsymbol{r})$ is the gradient of $\rho(\boldsymbol{r})$ [50, 51].

LDA and GGA give the structural properties of materials with reasonable accuracy. Typically, for lattice constant, LDA underestimates lattice constant by about 1-2%, while GGA slightly overestimates lattice constant by about 1-3%. For the cohesive energy, similarly, both LDA and GGA overestimate cohesive energies, though GGA yields results that are closer to the experiment than LDA. Indeed, there is no theory that explains the difference between the results of LDA and GGA. Furthermore, since DFT is based on theorems that employed ground state energy, it gives inaccurate results in calculating the excited states energy. Consequently, DFT yields to underestimate band gaps by a factor of 2 in most semiconductor materials. However, DFT does very well in determining the electron density, i.e., electron localization.

There are several flavors of GGA depending on the parameterization. The most popular GGA flavors are Perdew-Wang 91(PW91) and Perdew-Burke-Ernzerhof (PBE) [51]. The DFT outcomes vary with each GGA flavor, hence, it is necessary to state which type of GGA flavor has been used in any project. This dissertation has adopted GGA-PBE approximation in all projects included.

2.3. Stability analysis

When designing a new material, it is appropriate to check the stability of this new material before implementation of any property. This section scans some stabilities categories such as structural, dynamic, etc., along with stability analysis methods.

2.3.1. Structural stability analysis

It is important to get an optimal structure, i.e., structures with local energy minimum during the optimization process. Getting an optimal structure is one way to check structural stability. In the optimization process, one performs a relaxation calculation, in which a computer runs a code based on DFT (e.g., VASP code) to solve time-independent Schrödinger equation for a system (Equation 2-1) to get the total ground state energy E_{tot}:

$E_{tot} = \sum_i f_i \epsilon_i + E_{ion}$ Equation 2-15

Here, the First term, $f_i \epsilon_i$, is the band energy, where f_i is the Fermi occupation function; while the second term, E_{ion}, is the total ionic energy. Hence, the force on each atom, $\mathbf{F_i}$**,** can be obtained by applying Hellmann-Feynman theorem [52].

$\mathbf{F_i} = -\nabla_i E_{tot}$ Equation 2-16

Thereafter, a new set of coordinates of the system in this molecular dynamic (MD) step can be predicted based on calculating total ground state energy, forces, etc., which will be used in the next MD step. The MD calculation keeps continuously in an iteration way by using the Congregate-Gradient algorithm that implemented in VASP. This relaxation process ends and delivers a fully relaxed system when the defined energy and force criteria between adjacent MD steps have been reached, e.g., 10^{-4} eV for energy and 10^{-3} eV/Å for force.

There are two methods to optimize the lattice constants and interlayer distance to get an optimal structure: the manual and automatic method. These optimization methods depend on which principal degrees-of-freedom are allowed to change during the relaxation process. In the manual method, one uses ISIF = 2 tag in VASP code which allows changing the ionic positions only and run the relaxation calculation as mentioned above within a range of lattice constant values. Then, the energy minimum value should be taken since it is associated with the optimal structure and indicates the energetic stability of structure as illustrated in Figure 2-2.

In the automatic method, on the other hand, one releases all restrictions on degrees-of-freedom by using ISIF = 3 tag in the VASP code, in which ionic positions, cell volume, and cell shape are allowed to change simultaneously. Then, the optimal structure can be obtained as a result of the relaxation process. Note that the automatic method, in contrast to the manual method, is more expensive and time consuming.

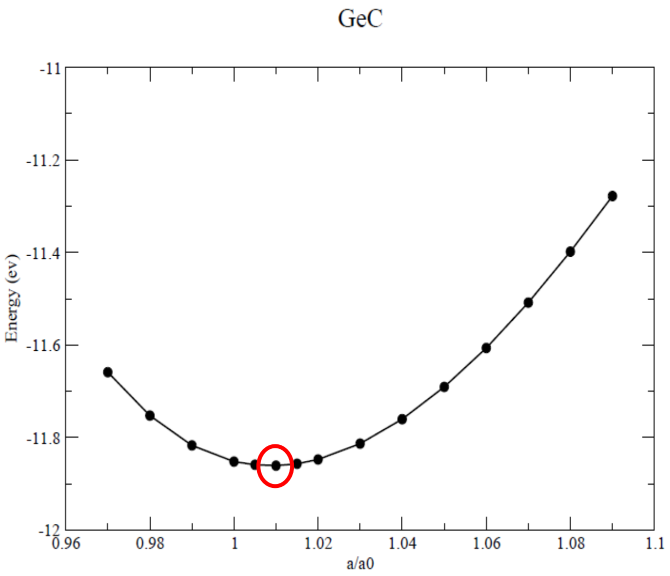

Figure 2-2: Plot of energy vs. lattice constant for GeC sheet in the manual optimization method, where the lattice constant a is scaled by the ratio of a/a_0 with $a_0 = 3.235$ Å, and a red circle represents the optimized lattice constant a^* =1.01x3.235Å $= 3.267$ Å associated with the minimum energy.

2.3.2. Dynamic stability analysis

The stabilized structure from the relaxation process discussed above needs further work to check its dynamic stability. To realize it, one needs to screen lattice vibration frequencies in particular, phonon dispersion spectrum, i.e., any imaginary value for lattice vibration frequencies means unstable structure.

2.3.2.1. Lattice vibration (Phonon Dispersion)

Lattice vibration, which is the oscillations of atoms in a solid about the equilibrium position, plays a significant role in understanding sound velocity, thermal, elastic, and optical properties of materials. In a crystal, any displacement for an atom from its equilibrium position will raise forces on all other atoms within the crystal. These forces will create phonons in terms of second quantization. Analysis of phonon frequencies is an important tool to determine the material physical properties such as thermal properties, mechanical properties, phase transition, and superconductivity [53, 54].

From computational aspect, one can obtain a phonon spectrum by using Phonopy code, a robust and easy-to-use open-source code, which implements first principles phonon calculations with a finite displacement method [55]. This approach is based on the harmonic approximation, in which the dynamical property of atoms is obtained by solving eigenvalue problem of dynamical matrix, $\mathbf{D}(\mathbf{q})$:

$$\mathbf{D}(\mathbf{q})\mathbf{e}_{\mathbf{q}j} = \omega_{\mathbf{q}j}^{2}\mathbf{e}_{\mathbf{q}j}\text{ , or } \sum_{\beta\acute{\kappa}} D_{\kappa\acute{\kappa}}^{\alpha\beta}(\mathbf{q})e_{\mathbf{q}j}^{\beta\acute{\kappa}} = \omega_{\mathbf{q}j}^{2}e_{\mathbf{q}j}^{\alpha\kappa} \quad \text{Equation 2-17}$$

With matrix element:

$$D_{\kappa\acute{\kappa}}^{\alpha\beta}(\mathbf{q}) = \sum_{l'} \frac{\Phi_{\alpha\beta}(0\kappa, l'\kappa')}{\sqrt{m_\kappa m_{\kappa'}}} e^{i\mathbf{q}.[\mathbf{r}(l'\kappa')-\mathbf{r}(0\kappa)]}$$ Equation 2-18

Where α, β are the Cartesian indices, m_κ is the mass of the atom κ, $\mathbf{q}$ is the wave vector, and j is the band index. $\omega_{\mathbf{q}j}$ and $\mathbf{e}_{\mathbf{q}j}$ are the phonon frequency and polarization vector of the phonon mode labeled by a set $\{\mathbf{q}, j\}$, respectively. $\Phi_{\alpha\beta}(l\kappa, l'\kappa')$ is an element of second - order force constants; and it obtained within the harmonic approximation in limit of small displacements at constant volume by:

$$\Phi_{\alpha\beta}(l\kappa, l'\kappa') = \frac{\partial^2\Phi}{\partial u_\alpha(l\kappa)\partial u_\beta(l'\kappa')} = -\frac{\partial F_\beta(l'\kappa')}{\partial u_\alpha(l\kappa)}$$ Equation 2-19

Where Φ is the crystal potential energy. As an example, the phonon band structure and phonon density of states (DOS) of pristine GeC sheet are shown in Figure 2-3.

The phonon DOS is defined as:

$$g(\omega) = \frac{1}{N}\sum_{\mathbf{q}j}\delta(\omega - \omega_{\mathbf{q}j})$$ Equation 2-20

where N is the number of unit cells in crystal.

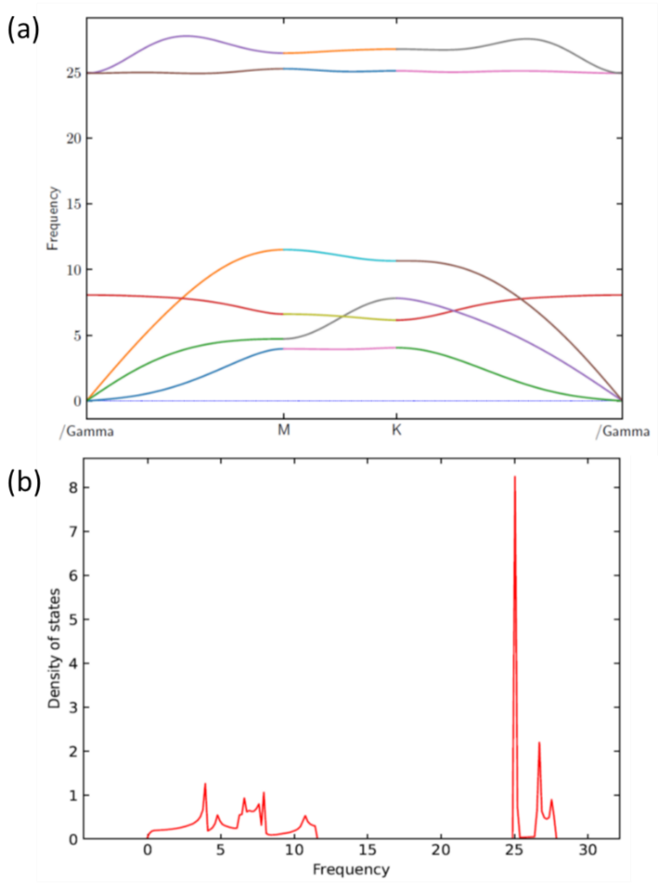

Figure 2-3: (a) Phonon band structure and (b) DOS of pristine GeC sheet.

At equilibrium, the structure is dynamically stable when the potential energy increases with any atomic displacement. Within the harmonic approximation, $\mathbf{D}(\mathbf{q})$, Equation 2-17, is a Hermitian matrix which must have real eigenvalues $\omega_{\mathbf{q}j}^2$. Therefore, when all phonons have real and positive frequencies that indicates a dynamic stability of the structure (such as pristine GeC sheet in Figure 2-3 (a)). Under virtual thermodynamic conditions, one might have an imaginary or negative frequency which indicates dynamical instability of the system, which means that the corrective atomic displacements of Equation 2-17 reduce the potential energy in the vicinity of the equilibrium atomic positions.

2.3.2.2.Thermal dynamics

It is important to know thermal properties of a system. The phonons' canonical distribution in statistical mechanics within the frame of harmonic approximation will help in determining several thermal properties, such as constant volume heat capacity C_V, Helmholtz free energy **F**, and entropy S. All what one needs to know is the phonon frequencies over Brillouin zone. Then, compute the energy E is straight forward by using the following relations:

$E = \sum_{\mathbf{q}j} \hbar\omega_{\mathbf{q}j} \left[\frac{1}{2} + \frac{1}{e^{\left(\frac{\hbar\omega_{\mathbf{q}j}}{k_B T}\right)}-1}\right]$ Equation 2-21

where T, k_B, and $\hbar$ are the temperature, the Boltzmann constant, and the reduced Planck constant, respectively. Once one has the energy E and phonon frequencies $\omega_{\mathbf{q}j}$, all thermal properties are straight forward by using the thermodynamic relations:

$C_V = \sum_{\mathbf{q}j} C_{\mathbf{q}j} = \sum_{\mathbf{q}j} k_B \left(\frac{\hbar\omega_{\mathbf{q}j}}{k_B T}\right)^2 \frac{\exp\left(\frac{\hbar\omega_{\mathbf{q}j}}{k_B T}\right)}{\left[\exp\left(\frac{\hbar\omega_{\mathbf{q}j}}{k_B T}\right)-1\right]^2}$ Equation 2-22,

$\mathbf{F} = \frac{1}{2}\sum_{\mathbf{q}j} \hbar\omega_{\mathbf{q}j} + k_B T \sum_{\mathbf{q}j} \ln\left[1 - \exp\left(\frac{-\hbar\omega_{\mathbf{q}j}}{k_B T}\right)\right.$ Equation 2-23,

$\mathrm{S} = \frac{1}{2T}\sum_{\mathbf{q}j} \hbar\omega_{\mathbf{q}j} \coth\left[\frac{\hbar\omega_{\mathbf{q}j}}{2k_B T}\right] - k_B \sum_{\mathbf{q}j} \ln\left[2\sinh\left[\frac{\hbar\omega_{\mathbf{q}j}}{2k_B T}\right]\right]$ Equation 2-24.

As an example, Figure 2 4 illustrates C_V (green curve), F (red curve), and S (blue curve) as a function of T of pristine for GeC sheet.

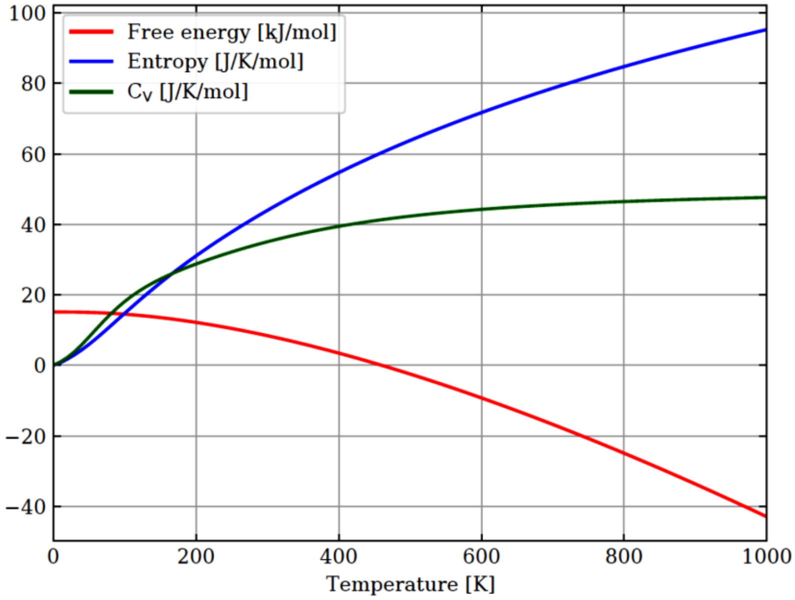

Figure 2-4: An illustration of the constant volume heat capacity C_V (green curve), Helmholtz free energy **F** (red curve), and entropy S (blue curve) as a function of temperature T of pristine for GeC sheet.

2.4. Electronic properties analysis

2.4.1. Band structure and Density of States (DOS)

In solid state physics, band structure refers to the way that energies of all the states change with k points. Because k is a 3D vector, it is common just to plot the energies along special high-symmetry directions. The energies along these lines represent either maximum or minimum energies for the bands across the whole Brillouin zone.

Because the lowest N states are occupied by electrons, at 0K there is an energy below which all states are occupied, and above which all states are empty; this is the Fermi energy (E_{Fermi}). Many band-structures are shifted so that the E_{Fermi} is at zero, but if not, the E_{Fermi} will usually be marked clearly.

In semiconductors and insulators there is a region of energy just above the Fermi energy which has no bands in it – this is called the band gap. The band structure is an effective way to visualize the wavevector-dependence of the energy states, the band gap, and the possible electronic transitions. However, the band structure is not a dependable guide here, since it only tells us about the bands along high symmetrical directions.

The actual transition probability depends on how many states are available in both the initial and final energies. Therefore, we need the full density of states across the whole Brillouin zone, not just the special directions. We must sample the Brillouin zone evenly, just as we do for the calculation of the ground state. Figure 2-5 shows the band structure and the DOS of GeC sheet, the first Brillouin zoon is inserted.

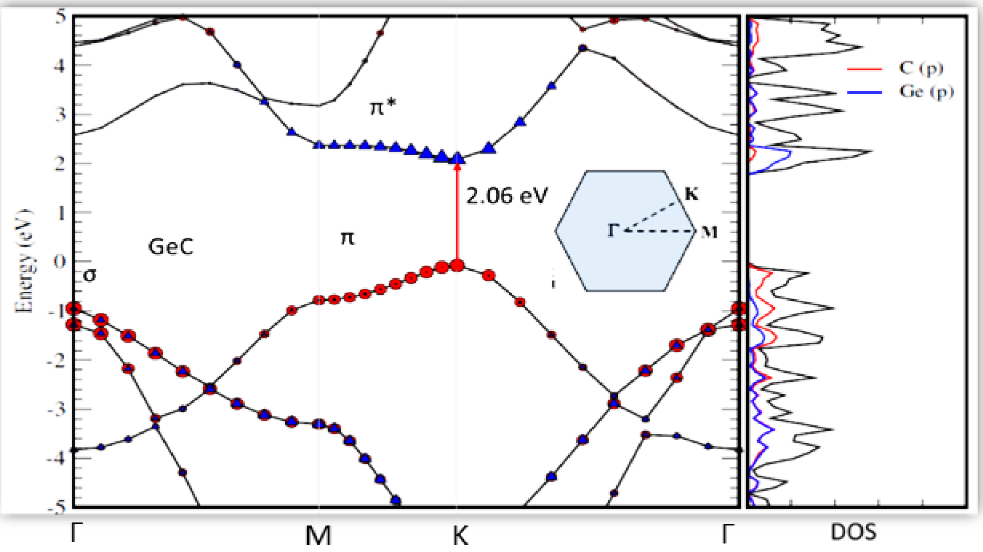

Figure 2-5:The band structure (left panel) and the DOS (right panel) of GeC sheet, the first Brillouin zoon is inserted. The Fermi level is set to be zero. The red and blue color (curves and balls/triangles) denote the contributions from C and Ge atoms, respectively.

2.4.2. Charge distribution (with Bader analysis)

The materials properties are often described by analyzing charges distribution on atoms or molecules. The electronic properties, for example, can be understood by analyzing the electronic charge distribution. In theoretical calculations, this is not an easy task since electronic charge density is continuous in quantum mechanical theory-based calculation which makes distinguishing electrons within atoms or molecules very difficult. Therefore, there are several schemes, based on electronic orbitals or charge density, which have been proposed.

This dissertation adopts the charge density scheme that is based on Bader idea [56] and employed Bader decomposition of charge density algorithm proposed by G. Henkelman et al. [57], referred as Bader scheme or analysis. The theory behind Bader scheme is that space is divided into atomic regions (referred as Bader regions). Each dividing surface is at a minimum in the charge density, i.e., the gradient of the charge density is zero along the surface normal. Each Bader region often contains one nucleus. Then, the estimated total charge on an atom can be obtained by integrating the electronic density within the Bader region. Finding the critical points of the charge density where $\nabla\rho = 0$, followed by the construction of the zero-flux surfaces which intersect these points and then integration of the electronic density within each region, is expensive computationally and makes the complexity of the algorithms. In Bader decomposition of charge density algorithm, therefore, only steepest descent trajectories confined to the grid points are used to identify the Bader regions which make the algorithms robust and fast, because in this case the computational effort scales linearly with the number of grid points.

Once one performs Bader analysis and gets charge distribution, many electronic properties can be inferred after that.

Table 2-1 shows Bader charges for carbon C and germanium Ge in the GeC sheet, where one can infer that there is a charge (~1.3623e) transfer from Ge atom to C atom when they combine to form a binary compound GeC monolayer.

Table 2-1:The electronegativity, Bader charge, and charge transfer for carbon C and germanium Ge in GeC monolayer.

Atom	C	Ge
Electronegativity	2.55	2.01
Bader charge (e)	5.362	2.6376
Charge transfer (e)	1.3623	-1.3623

2.4.3. Charge redistribution (with differential of charge density analysis)

In material designing, it is essential to understand how the charges redistribute among the system constituents. Differential of charge density analysis (DCD) is a useful method that helps tracking charge density in the combined system. DCD analysis applies the following relation:

$$\nabla\rho_{AB} = \rho_{AB} - \rho_A - \rho_B \text{ Equation 2-25}$$

where ρ_{AB} is the charge density of combined system, ρ_A,and ρ_B are the charge density of subsystem A and B, respectively. To illustrate the method, Figure 2-6 provides an example of the DCD for the SiC/GeC LH combined by GeC and SiC sheets. Namely, ρ_{SiC} (ρ_{GeC}) was evaluated by removing GeC (SiC) domain from the relaxed combined system and calculating the density of states without further relaxation. Thus, the DCD tracks the charge transfer between layers to visualize the interaction scenario made inside the system and determines its strength. As a result, one can infer that the charge transfer occurs along the interface in SiC/GeC LH (guided between the green dashed lines in Figure 2-6) where the electron accumulation and depletion are represented by the yellow and blue contours, , respectively (with the isosurface of $4.0\ x10^{-4}\ e/\text{Å}^3$).

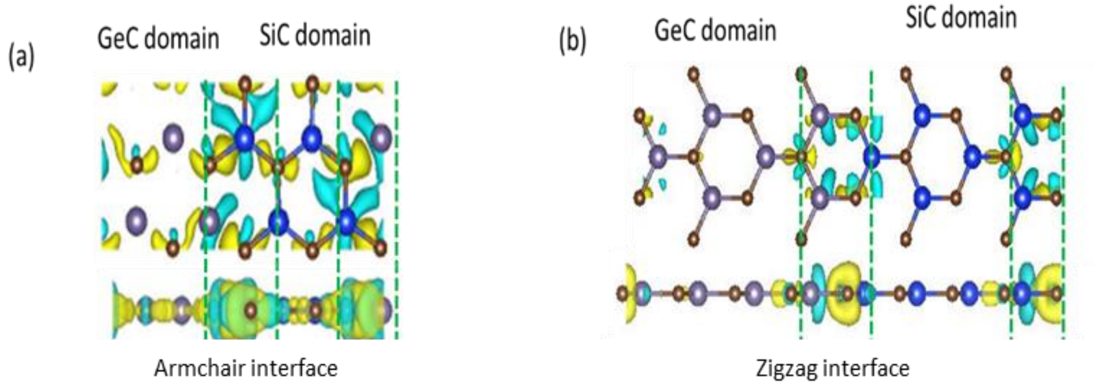

Figure 2-6: (a) and (b) show the top (upper) and side (bottom) views of DCD of $1x4$ SiC/GeC hybrid LH with Armchair (a) and Zigzag (b) interfaces. The electron accumulation and depletion are represented by the yellow and blue contours, respectively (with the isosurface of $4.0\ x10^{-4}\ e/\text{Å}^3$). The C, Si, Ge atoms are noted by brown, blue, and grey spheres, respectively.

2.4.4. Work function (band alignment)

Work function is an important property for phenomena related to applications where electron transfer between two different materials in contact (e.g., LED, solar cell, battery, etc.) or from a material into vacuum (electron emission) (e.g., collider, photodetector, electron lithography), etc. as shown in Figure 2-7 [58]. All the projects involved in this dissertation lay in these two categories which need imperative inspection of work function. Additionally, work function as a surface property governs many surface related phenomena, such as the ideal Schottky barrier height (SBH) [59], the potential of oxidation in fuel cells [60], and the dissociation of molecules on catalytic metals [61, 62].

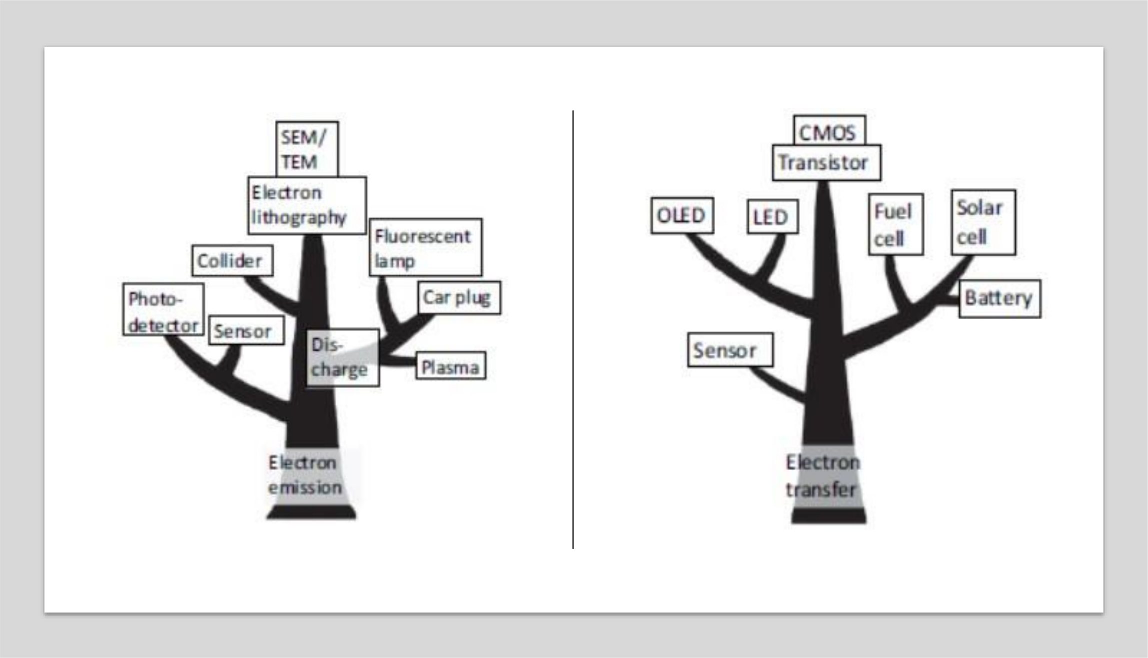

Figure 2-7: Some applications related to electron emission (left), and electron transfer (right) phenomena.

By definition, work function Φ, in general, is equal to the energy difference between the E_{Fermi} and the electrostatic potential in vacuum level (E_{vacuum}) at the surface of the material at zero temperature [58]:

$\Phi = E_{vacuum} - E_{Fermi}$ Equation 2-26

The definition of work function is sensitive to the type of solid. More precisely, for a metal, the work function is the minimum energy required to extract one electron. For a semiconductor or insulator, however, the minimum energy required to extract one electron is the ionization energy (IE) not the work function. To evaluate Φ, one needs to determine E_{Fermi} and E_{vacuum}. The E_{Fermi} is computed directly in DFT theory for metals, but this is not the case for semiconductor. In materials with band gap, experimentalists usually define E_{Fermi} as the middle of the band gap. However, by standard DFT calculations, the band gap is usually under-estimated; therefore, E_{Fermi} is typically calculated from the highest occupied eigenvalue in DFT calculations. E_{vacuum}, on the other hand, can be calculated from the averaged electrostatic potential.

Work function can also be utilized to determine many crucial factors such as band alignment. In practice, it is important to study the band alignment since all applications require contact between materials starting from a switch (as a simple application) to a solar cell (as a complicated one). In a metal– n-type semiconductor interface, for example, the E_F of the metal aligns with that of the semiconductor in order to realize thermodynamic equilibrium in the electronic system. Here, the band is bending at the interface due to electron redistribution or the interface potential where the energy of band bending ΔE equals to the difference in the work function between the metal ϕ_m and semiconductor ϕ_s. Consequently, the SBH, which is the activation energy needed to excite an electron in the E_F of the metal to the minimum conduction band of the semiconductor E_C , is defined as $\mathrm{SBH} = \phi_m - \mathrm{EA}$, where EA is the electron affinity of the semiconductor (see Figure 2-8) [58]. Therefore, for a metal–semiconductor interface in a switch, a larger metal work function is preferred, whereas a low metal work function is preferred in solar cell.

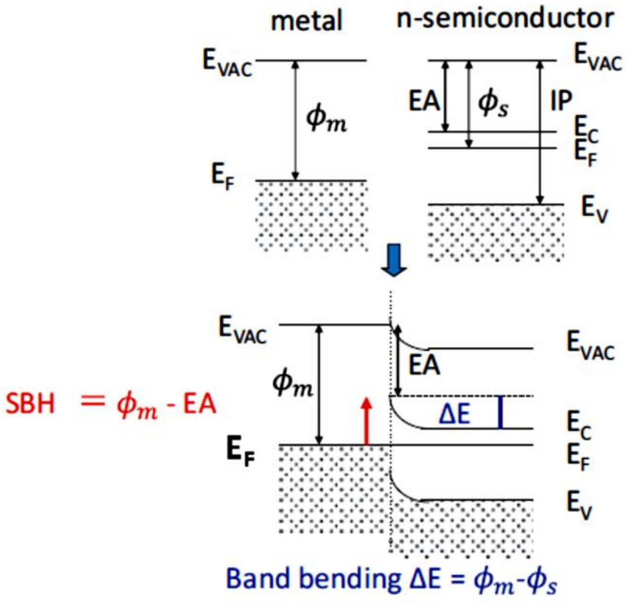

Figure 2-8: Plot of the band alignment in a system with metal– n-type semiconductor interface[58].

CHAPTER III

3. STRAIN EFFECT ON 2D BINARY COMPOUNDS OF GROUP IV ELEMENTS: SiC, GeC, AND $SiGe$

3.1. Introduction

In real-life applications, there is a strain that comes from substrate, interface, thermal vibration, etc. This strain has a regarded influence on the structural and electronic material properties which must be examined. Furthermore, a strain engineering is a beneficial strategy that can be applied to materials over a wide range to tune their structural and physical properties, e.g., electronic band structures, charge transition, bond length, angle, strength, and positions of atoms [63-69].

2D materials, in general, can endure a various value of strain exceeding the elastic deformation limit (i.e., strain ≤ 1 %). Besides, those atomic thin materials exhibit flexibility and sensitivity to the applied strain which drives, currently, a strong interest in studying and understanding how their electronic properties can be modulated by applying a strain. Graphene, as an example, shows remarkable properties, and further, modified electronic properties after the strain is applied. Graphene has been reported to create polarized carrier puddles and induce pseudomagnetic fields after the strain has been applied [70-72]. However, the lack of band gap limits graphene from the use in electronic devices.

Beyond graphene, there is a group of binary compounds sheets made of group IV elements such as GeC, SiC, and $SiGe$. Those binary compound sheets possess interesting electronic properties, such as a direct (indirect) band gap in GeC (SiC), respectively (totally differ from graphene which is gapless). Hence, strain engineering in such binary compounds may provide a fertile library to further explore effects and phenomena.

Triggered by all the above, this project has been conducted to study the strain effect on stability and electronic properties of GeC, SiC, and $SiGe$ binary compounds.

3.2. Computational methods

This project has been carried out by means of first principles calculations within DFT [73, 74], which was implemented in VASP [46]. The core-valance interaction is described by the projector augmented wave (PAW) algorithm [75]. The GGA approach [76] with PBE functional [51] is utilized to describe the exchange-correlation interactions. To avoid the interaction caused by the periodic boundary condition, a vacuum region has been set as 15 Å between two successive slabs. The Monk horst -Pack scheme [77] for the k-point mesh centered at gamma point was applied to sample the reciprocal space for geometric optimization and electronic properties calculations. A cutoff energy of 400 eV was applied for all calculations for SiC and GeC, while for $SiGe$ calculations the cutoff energy was set to be 245 eV. Conjugate gradient algorithm [78] was used in the whole relaxation processes and all systems are relaxed until the force on each atom is less than 10^{-3} eV/Å, and the energy convergent reached to the criteria of 10^{-5}eV. All systems, e.g., SiC, GeC, and $SiGe$, are constructed as a monolayer with $1x1$

unit cell. The primitive lattice vectors in units of the lattice constant (a) are (1,0,0), (−1/2, √3/2, 0), and (0, 0, c/a) for a hexagonal lattice.

The dynamic stability of the three monolayers is studied by performing the phonon band structure calculations within the density-functional perturbation theory (DFPT) [79] implemented in phonopy code [79]. The Bader analysis scheme [57] was employed to analyze charge redistribution and charge transfer between atoms.

3.3. Structural properties (optimization and stability)

Figure 3-1 shows fully relaxed structures of SiC, GeC, and $SiGe$ monolayer. Clearly, SiC (GeC) monolayer forms a flat hexagonal lattice with optimized lattice constant/bond length of 3.089 Å (3.267 Å)/1.7834 Å (1.886 Å), respectively, which agree with other DFT calculations [80-86] and experiment measurements [87-89]. These results are, further, close to lattice constant (2.458 Å) and bond length (1.42 Å) of graphene which give an explanation to the flatness structure of SiC and GeC monolayers. Namely, the shorter bond length between Si (Ge) and C atom in SiC (GeC) sheet reinforce sp^2 hybridization that leads to form a planar sheet.

On the other hand, $SiGe$ monolayer is a 2D buckled honeycomb structure with optimized lattice constant and bond length of 3.95 Å and 2.357 Å, respectively; and the buckling height (which is the distance between the top (Si) and bottom (Ge) atoms) is 0.59086 Å. These findings match closely with the reported ones [90, 91].

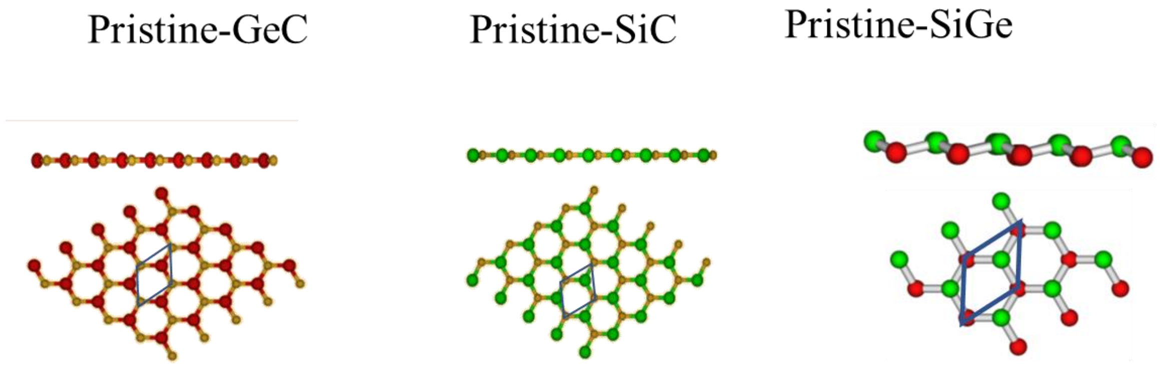

Figure 3-1:Atomic visualization of the top (bottom) and side (top) views of the lattice structures of SiC, GeC, and $SiGe$ monolayers. The red, green, and brown balls represent Si, Ge, and C atoms, respectively. The blue rhombic represents the $1x1$ unit cell.

The bond length in $SiGe$ is much longer compared with that of graphene which prevents $SiGe$ from forming strong bonds, thus leading to deviations from the sp^2 hybridization. Therefore, $SiGe$ adopt buckled hexagonal honeycomb structures with two triangular sublattice-stacks. To stabilize it in a hexagonal arrangement, the buckling between Si and Ge atoms brings them closer together to enable a stronger overlap of their bonding of p_z orbitals, resulting in a mixed sp^2– sp^3 hybridization since the buckling height is related to the bond angle between the framework atoms and the hybridization of the atomic orbitals.

From the stability perspective, among the three monolayers, SiC is energetically the most stable, followed by GeC, and $SiGe$ is the least stable. Additionally, from the dynamical stability standpoint, these three monolayers, SiC, GeC, and $SiGe$, are dynamically stable as sheet structures (i.e., no imaginary phonon frequencies are observed within the first Brillouin zone). The phonon band structures for the three monolayers are shown in Figure 3-2

Table 3-1: The optimized Lattice constant, bond length, buckling, bond angle, and cohesive energy per atom for each system.

system	Optimized Lattice constant	Bond length	Buckling	Bond angle	Cohesive Energy/atom
SiC	3.08Å	1.783 Å	0 Å	120^0	$-6.8650532\ eV$
GeC	3.267 Å	1.886 Å	0 Å	120^0	$-5.7701598\ eV$
$SiGe$	3.951 Å	2.357 Å	0.591 Å	113.94^0	$-4.19655335\ eV$

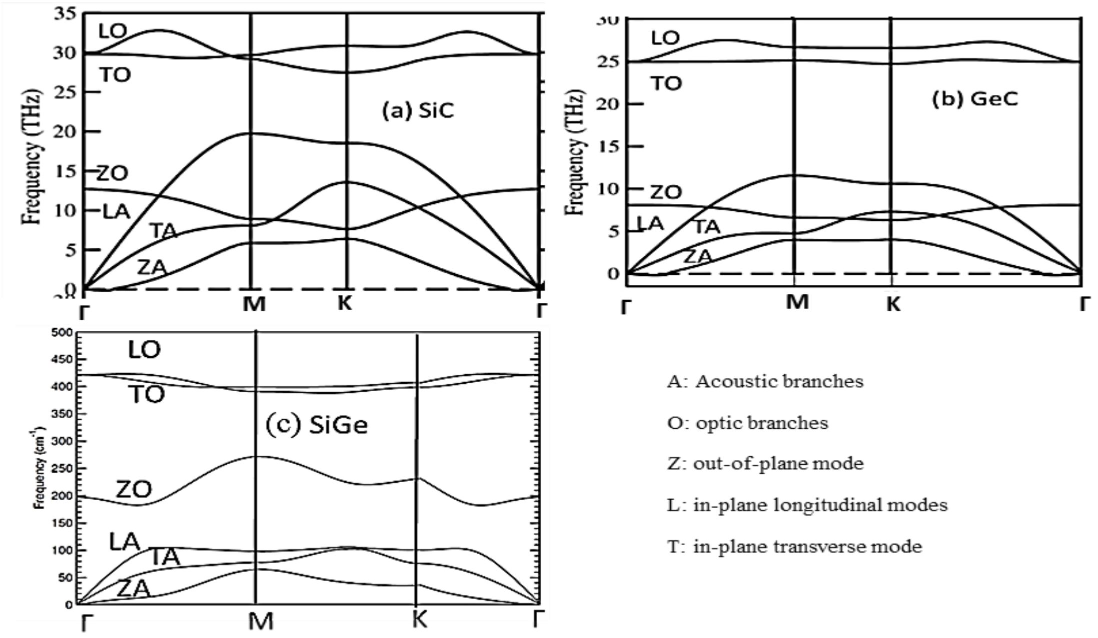

Figure 3-2: The phonon band structure of (a) SiC, (b) GeC, and (c) $SiGe$ monolayer over the entire Brillouin zone. The labels of LA, TA, and ZA (LO, TO, and ZO) denote longitudinal, transverse, and out-of-plane acoustic (optic) branches, respectively.

3.4. Electronic properties

3.4.1. Charge transfer and electron localization function (ELF)

By using Bader scheme [56, 57], the charge distribution around each atom of SiC, GeC, and $SiGe$ monolayers has been analyzed. Based on that, Figure 3-3 visualizes the total charge density of the three monolayers (yellow contour) on a top and side views for each monolayer. The blue arrows (Figure 3-3) represent the direction of charge transfer and red numbers represent the quantity of charge between atoms in a binary compound. It turns out that SiC, among the three monolayers, has the largest amount of charge transfer (2.095e) from Si atom to C atom, followed by GeC with 1.362e charge transfer from Ge atom to C atom, and the last is $SiGe$ with just 0.0618e charge transfer from Si atom to Ge atom. This apparent behavior indicates that $Si-C$ bonds are more ionic-like covalent bonding, while $Ge-C$ bonds are less ionic-like covalent boding. Furthermore, the trend of charge transfer can be explained by the electronegativity where the large charge transfer is related to the large electronegativity difference between atoms, note that the electronegativity for the three atoms is 2.55, 2.01, and 1.9 for C, Ge, and Si, respectively. The amount of the charge transfer between two atoms can also inferred from the bond length where the longer bond length between atoms, the less charge transfer between atoms will be, see 3rd column of Table 3-1

(a) SiC monolayer (isosurface of 0.053 e/Å^3)

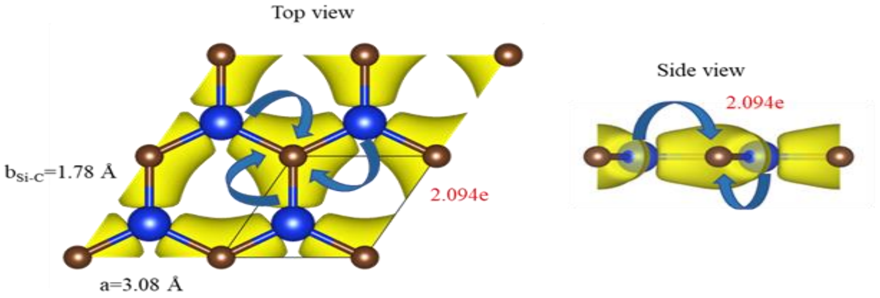

(b) GeC monolayer (isosurface of 0.053 e/Å^3)

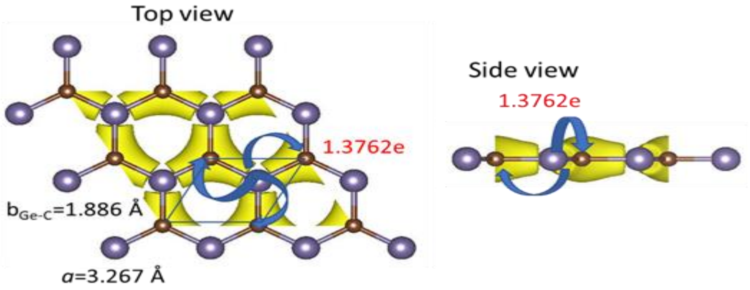

(c) SiGe monolayer (isosurface of 0.053 e/Å^3)

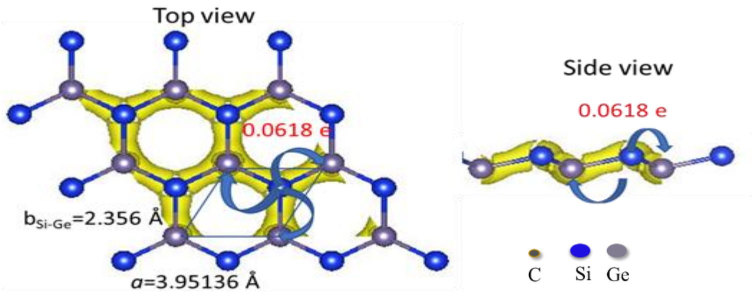

Figure 3-3: Top (left) and side (right) views of optimized SiC, GeC, and $SiGe$ monolayers. Optimized lattice constants (a) and bond lengths (b) are indicated by numbers. The total charge density contour was depicted (yellow) and the Bader charge transfer is indicated by the blue arrows and red numbers. The C, Si, Ge atoms are noted by brown, blue, and grey spheres, respectively.

In Addition, the electronegativity difference effect appears on the localization of the electron, where SiC monolayer shows more localized behavior, $SiGe$ monolayer shows more delocalized behavior, and GeC monolayer behaves in between (see Figure 3-4 where the yellow contour represents electron localization function ELF with isosurface value of 0.63 e/Å^3).

Top view Side view

(a) SiC monolayer (isosurface of 0.63 e/Å^3)

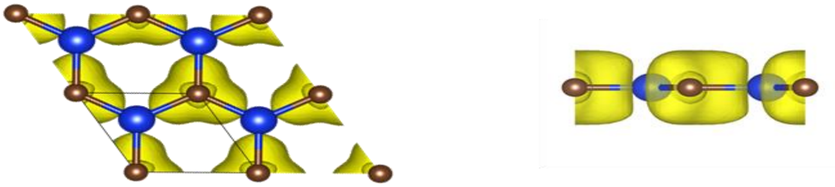

(b) GeC monolayer (isosurface of 0.63 e/Å^3)

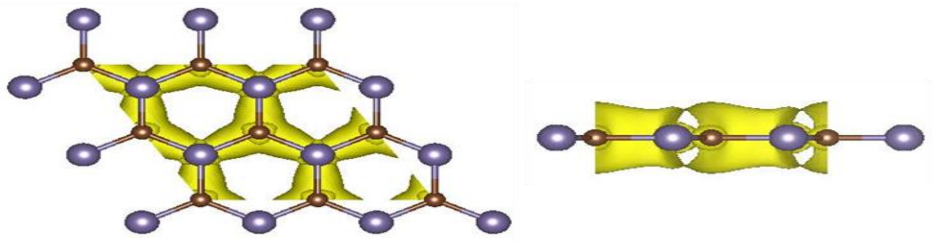

(c) SiGe monolayer (isosurface of 0.63 e/Å^3)

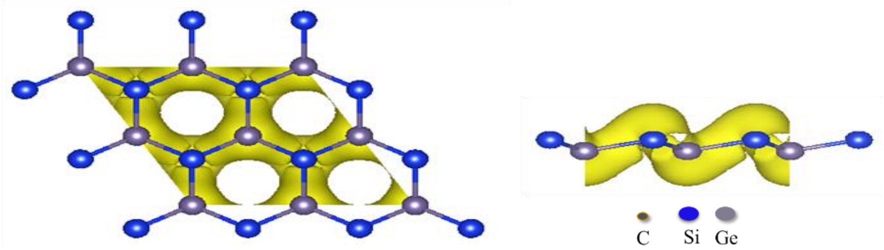

Figure 3-4: Top (left) and side (right) views of optimized (a) SiC, (b) GeC, and (c) $SiGe$ monolayers with ELF depicted in yellow contour. The C, Si, Ge atoms are noted by brown, blue, and grey spheres, respectively.

3.4.2. DOS and band structure

Due to the success of band theory for describing many electronic properties of solids, DOS and band structure calculations have been conducted during the simulation after each system was fully optimized. The results are presented in Figure 3-5 (i.e., the DOS (right panels) and band structure (left panels), respectively). The red arrows in the band structures indicate directions from the tops of the maximum valence bands to the bottoms of the conduction bands, where E_{Fermi} shifted to zero energy. Apparently, the band structures demonstrate semiconductor behaviors in SiC and GeC monolayers with indirect band gap of 2.55 eV (3.41 eV in HSE06 [92]) between M and K points for SiC monolayer (Figure 3-5 (a)) and direct band gap of 2.06 eV (2.84 eV in HSE06 [92]) at K point for GeC monolayer (Figure 3-5 (b)), respectively. $SiGe$ monolayer, on the other hand, has a tiny band gap of 0.0743 eV, like graphene, which classify it as semimetal as shown in Figure 3-5 (c). In contrast to the sheet structure, theoretical calculation of bulk SiC and GeC show the indirect band gaps of 1.6 eV and 2.5 eV (GGA with Gaussian orbitals) [93]. The $SiGe$ bulk, on the other hand, possess a band gap around 0.95 eV [94]. Furthermore, it was found that C atoms make major contribution on the top valence bands, and Si (Ge) atoms make major contributions to the bottom of conduction bands in SiC and GeC monolayers, while Ge atoms make the major contributions on both valence and conduction bands in $SiGe$ monolayer.

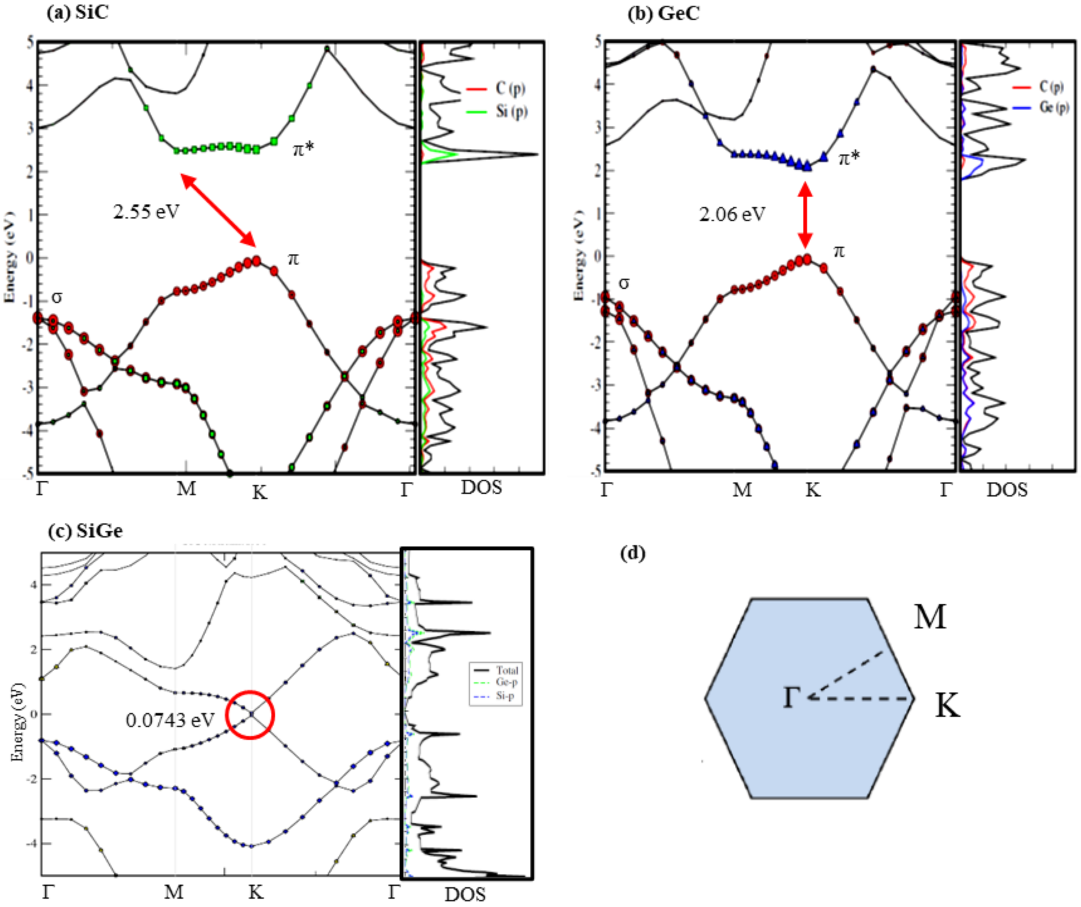

Figure 3-5: Band structures (right panel) and DOS (left panel) of (a) SiC, (b) GeC, and (c) $SiGe$. The red dots (curves) represent the contribution from C, the green squares (curves) for Si, and the blue triangles (curves) from Ge, respectively. The Fermi level is set to be zero. (d) the first Brillouin zoon.

3.5. The strain effect on structural and electronic properties

A comparative strain dependent study on SiC, GeC, and $SiGe$ monolayers has been conducted. Structurally, these three monolayers tolerate a wide range of tensile or compressive biaxial strain. In fact, it was found that SiC, GeC, and $SiGe$ monolayers incur a biaxial strain range from -4% to 8%, -4% to 4%, and -12% to 4%, respectively. Moreover, no structure distortion has been noted in these monolayers, and SiC and GeC

keep flat, but the buckling in $SiGe$ increases/decreases with compressive/tensile strain. Figure 3-6 shows a plot of energy verses the biaxial strain (δ) , $\delta = {}^{a}/_{a_0}$, where a_0 is the optimized lattice constant of the three monolayers, and the inserts are the top and side views of each unstrained monolayer structure.

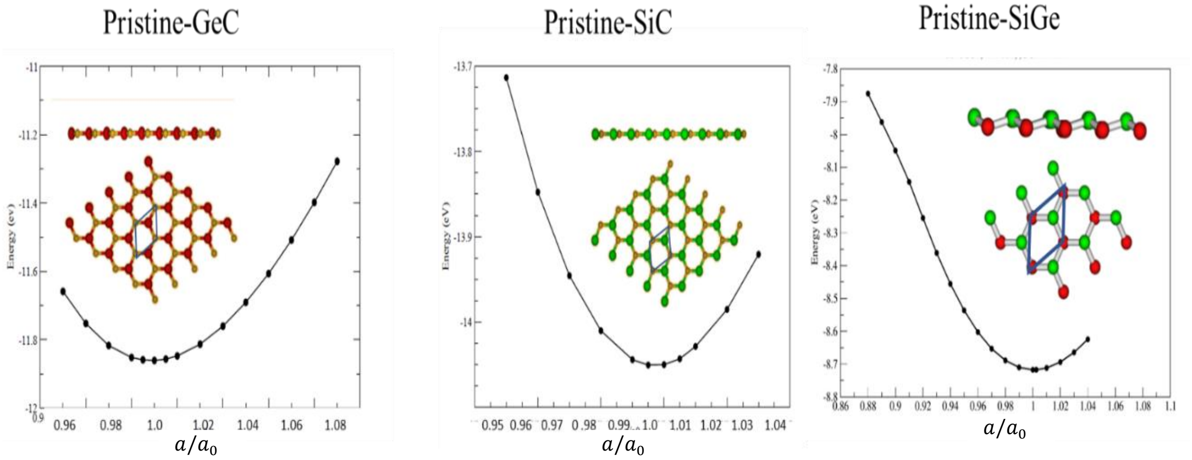

Figure 3-6: Plot of energy verses biaxial strain (δ) , $\delta = {}^{a}/_{a_0}$, where a_0 is the optimized lattice constant of SiC, GeC, and $SiGe$ monolayers, respectively.

For the electronic aspects, both SiC and GeC sheets retain the semiconductor nature under the biaxial strain. Interestingly, the study has found that $SiGe$ sheet undergoes a metal-semimetal transition with compressive biaxial strain.; while SiC and GeC sheets undergo a direct-indirect band gap transition. Specifically, the direct band gap in GeC transfers to an indirect band gap with expansion; however, the indirect band gap of SiC transfers to a direct band gap. Also, the band gap deceases with increasing the biaxial strain, indicating the ability of tuning the nature of band gap by controlling the strain, see Figure 3-7 and Appendix A for detail information.

(a) Pristine SiC under strain

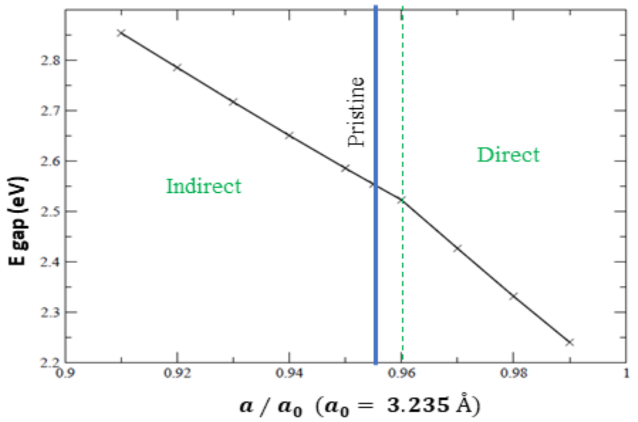

(b) Pristine GeC under strain

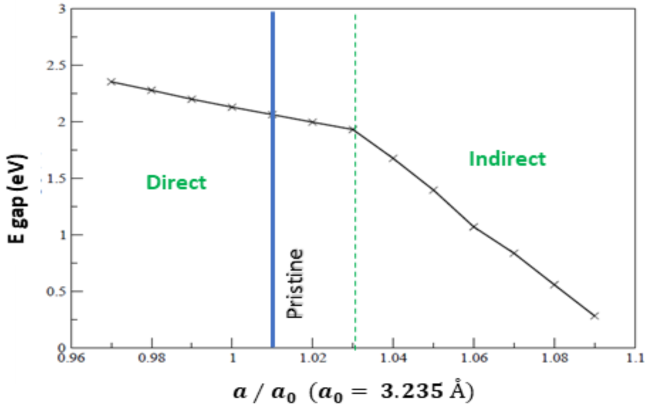

(c) Pristine SiGe under strain

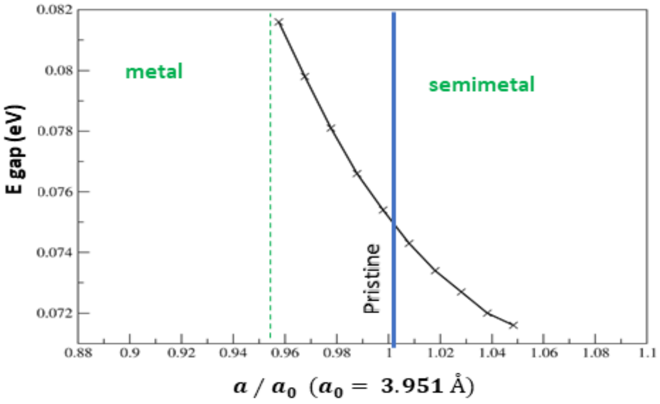

Figure 3-7: Plot of energy gap verses biaxial strain of SiC, GeC, and $SiGe$ monolayers. The blue and green-dashed lines denote the positions of corresponding unstrained pristine monolayer and the band gap transition, respectively.

For further analysis, the effect of uniaxial strain on the electronic properties, which might happen in constructing heterostructures, was examined through the band structures analysis under the uniaxial strain along Y and X axes (e.g., SiC sheet stretched by 2.94% and GeC sheet compressed by 2.66%). It was found that the nature of the band gap keeps indirect along X axis but changes to direct along Y axis in SiC sheet, and the band gap decreases with increasing the strain, indicating anisotropic electronic property for SiC monolayer. Nevertheless, the nature of the band gap of GeC keeps direct under the strain along both axes and the band gap increase with decreasing the strain, as shown in Figure 3-8. The results prompt researchers to consider uniaxial strain and study anisotropic electronic property on such monolayers in future work.

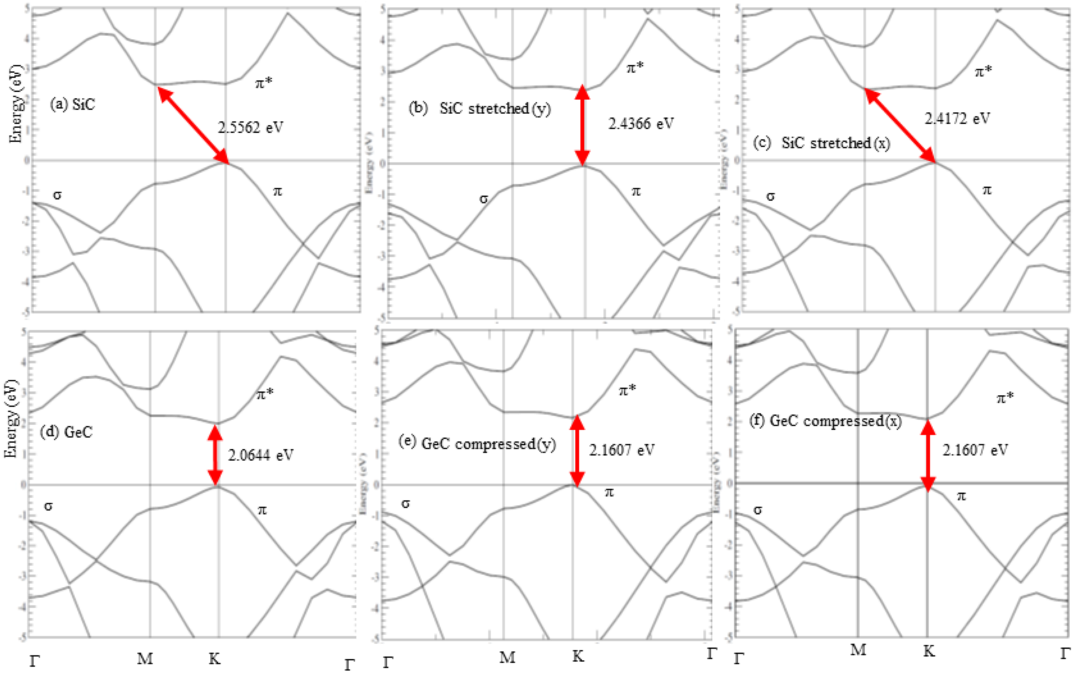

Figure 3-8: Plot of band gap verses uniaxial strain of monolayers SiC (upper panels), and GeC (bottom panels). The red arrows denote the direct/indirect band gaps.

3.6. Conclusion

Trigged by the sensitivity and toleration of 2D materials to the applied strain, this study has been conducted to theoretically investigate the role played by the strain engineering on 2D binary compounds of group IV elements: SiC, GeC, and $SiGe$ monolayers. The biaxial tensile and compressive strain can be applied up to 4% which is beyond the elastic deformation limit (i.e., strain ≤ 1 %). As a result, it was found that the three monolayers tolerate large amounts of strain (up to 8%, like most 2D materials) which tend to be a characteristic of 2D materials. Besides, electronic modification appears in those monolayers, especially in the band gap. Namely, SiC and GeC undergo a direct-indirect band gap transition, while $SiGe$ undergo metal-semimetal transition. Those findings confirm that the strain is a good tuning parameter for 2D materials properties to use in electronics applications.

CHAPTER IV

4. LATERAL HETEROSTRUCTURE OF 2D POLAR BINARY COMPOUNDS: (SiC/GeC AND SiGe/GeC)

4.1. Introduction

Currently, most advanced electronic, optoelectronic, and photovoltaic applications count on heterostructures (i.e., heterojunctions) as a built-up component, e.g., field effect transistors (FETs) [95-97], p-n diodes [90, 91, 98-107], and photodetectors [108-110]. In contrast to 3D heterostructures, 2D heterostructures have a great interest due to the atomic thickness, flexibility, and ability of 2D materials to be integrated into heterostructures. Besides 2D materials novel physical and chemical properties due to the electron and phonon confinement effect, integrating them into heterostructures opens a new way of modifying those intriguing properties and emerges new physics to be explored.

Further, 3D heterostructures construct by chemically bonding different bulk slabs at junctions, whereas the most common 2D heterostructures constructed by compose the constituent sheets along either in-plane direction (referred as LH) [100-110] or by out-of-plane direction (referred as VH) heterostructures [24, 96, 98, 99, 103, 104, 110-116]. A sharp 1D interface in LH, which has been built by stitching seamlessly two semi-infinite layers within the same atomic plane, plays a key role that may lead to unique optical and electrical transport properties.

Moreover, among many assemblies of heterostructures, semiconductor–semiconductor, and metal–semiconductor heterostructures have shown potential for electronic applications. Namely, semiconductor–semiconductor heterostructures show good performance in electronic and optoelectronic applications (e.g., FETs [107, 117], photodetectors [109, 110], and light emitting diodes [LEDs][24, 111]). On the other hand, metal–semiconductor heterostructures show the ability of the sensing gases [118, 119], organics [120], and DNA [121], in addition to use them in electronic and optoelectronic devices, energy storage, and electrocatalysis.

Based upon and trigged by the electronic properties that obtained in Chapter 3, e.g., the polar SiC and GeC monolayer show a semiconductor band gap nature, while the polar $SiGe$ monolayer appears metal band gap nature, the project in this chapter has been conducted to unravel the physical properties of semiconductor–semiconductor and metal–semiconductor LH built by SiC/GeC-LH and SiGe/GeC-LH, respectively.

4.2. Effects under study (Interface – Strain – Confinement)

For LH heterostructures, the chemical bonding nature at the interface, the lattice mismatch induced strain, and the domain size induced confinement will play the key roles in stabilizing the heterostructures and electronic properties.

In this project, the 2D SiC/GeC-LH and 2D SiGe/GeC-LH have been designed by stitching the edges of constituents in the same atomic plane along either armchair (AC) or zigzag (ZZ) directions, forming 1D thin interface, which are denoted by AC-SiX/GeC-

LH and ZZ-SiX/GeC-LH (where X=C,Ge), respectively (see Figure 4-1). These two diverse types of the interface, i.e., AC and ZZ for each LH (e.g., 2D SiC/GeC-LH and 2D SiGe/GeC-LH), enable us to study the interface effect on such LH. For instance, each C atom bonds with Si or Ge atom alternatively at the interface in AC-SiC/GeC-LH (Figure 4-1 (a)); while C atom bonds just with Ge (Si) atom at the interface in ZZ-SiC/GeC-LH (Figure 4-1 (b)). Furthermore, there are different configurations in the chemical bonding for a given type of interface. For instance, the chemical bonds at the interface of the AC/ZZ-SiGe/GeC-LH are formed either by Si-C and Ge-Ge (see Figure 4-2 (a)-(b)) or by alternative elements between Si, C, and Ge (see Figure 4-2 (c)-(d)). These different chemical bonds affect the properties of the structure which have been investigated and addressed in this chapter.

Moreover, as found in Chapter 3, the lattice constants of the three constituents of LH (i.e., SiC, GeC, and SiGe monolayers) are 3.089 Å, 3.267 Å, and 3.951 Å, respectively. Such difference in lattice constants leads to a lattice mismatch when they form 2D SiC/GeC-LH (~ 6%) and 2D SiGe/GeC-LH (~17%), respectively. These small (in 2D SiC/GeC-LH) and relatively large (in 2D SiGe/GeC-LH) lattice mismatches induce artificial strain which may cause stress or defect at the interface. Varying lattice mismatches between 2D SiC/GeC-LH and 2D SiGe/GeC-LH assists to examine the impact of the level of induced strain on the physical properties of structures under study.

2D materials exhibit many unique physical and chemical properties, and most of them are related to the electron and phonon confinement effect. Therefore, studying the effect of domain sizes in LH could help us to inspect the confinement effect on electronic properties. Thus, this chapter will focus on unraveling the synergistic effect of mismatch induced strain, the microstructure of interface, and the confinement effect represented by the width of domains on the features of constructed 2D SiC/GeC-LH and 2D SiGe/GeC-LH.

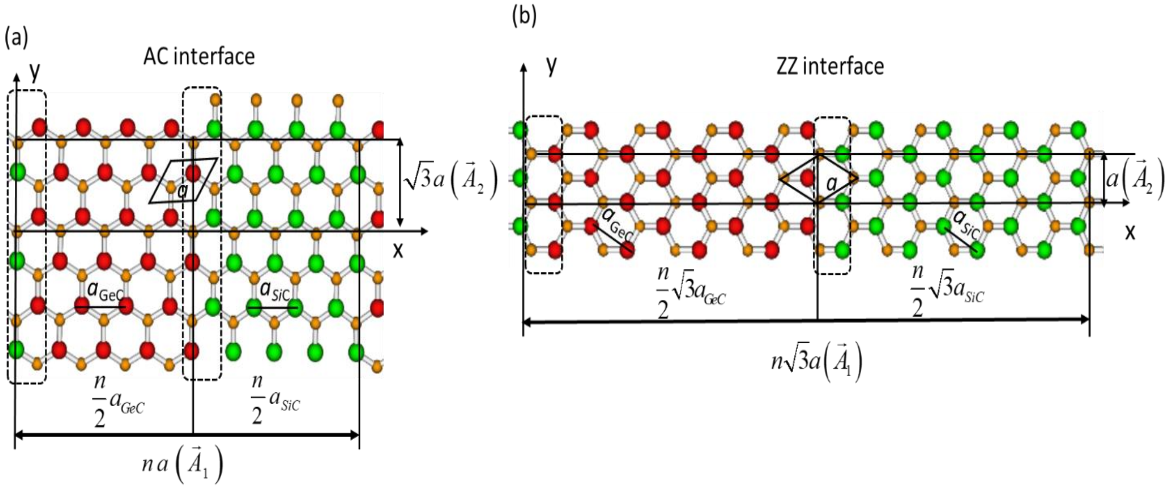

Figure 4-1: Schematic visualization of the top views of the 2D polar (a) AC-SiC/GeC-LH and (b) ZZ-SiC/GeC-LH with the interface indicated by the black-dashed boxes. The lattice vectors of the supercell are $\vec{A}_1 = (na, 0{,}0)$ and $\vec{A}_2 = (0, \sqrt{3}a, 0)$ for AC heterostructures, and $\vec{A}_1 = (n\sqrt{3}a, 0{,}0)$ and $\vec{A}_2 = (0, a, 0)$ for ZZ heterostructures, where a denotes the average lattice constant of the combined systems. The domain sizes of GeC and SiC are scaled by $\frac{n}{2}a_{GeC}$ and $\frac{n}{2}a_{SiC}$ for AC heterostructures, and $\frac{n}{2}\sqrt{3}a_{GeC}$ and $\frac{n}{2}\sqrt{3}a_{SiC}$ for ZZ heterostructures, where a_{GeC} and a_{SiC} are the average lattice constants in the corresponding domains of combined systems. The yellow, red, and green spheres represent C, Ge, Si atoms, respectively.

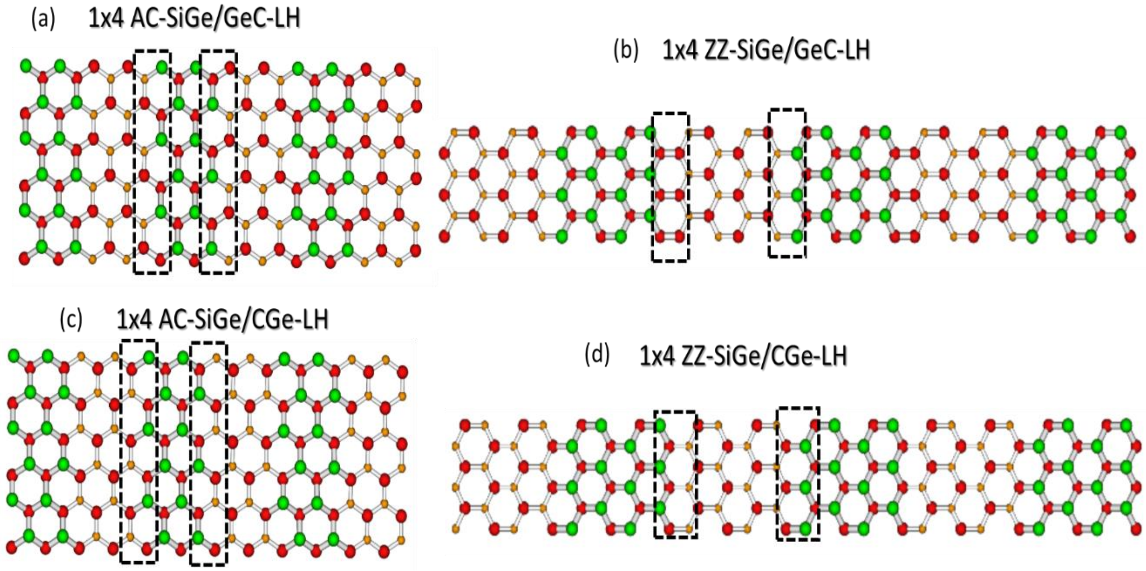

Figure 4-2: Schematic visualization of the top views of the 2D polar (a) 1x4 AC-SiGe/GeC-LH and (b) 1x4 ZZ-SiGe/GeC-LH with Ge-Ge and Si-C bonds at the interfaces, (c) 1x4 AC-SiGe/CGe-LH and (d) 1x4 ZZ-SiGe/CGe-LH with C-Ge and Si-Ge bonds at the interfaces, respectively. The interfaces are indicated by the black-dashed boxes. The yellow, red, and green spheres represent C, Ge, Si atoms, respectively.

4.3. Construction of SiC/GeC-LH and SiGe/GeC-LH

The AC-SiC/GeC-LH and ZZ-SiC/GeC-LH with alternative elements bonding at the interface were constructed (as visualized in Figure 4-1). The chemical bonding nature (see the black-dashed boxes in Figure 4-1(a)) shows an alternative alignment of Si-C and Ge-C bonds for AC-SiC/GeC-LH. While, either the Si-C or Ge-C bonds align at two edges of domains along the ZZ-SiC/GeC-LH (see the black-dashed boxes in Figure 4-1(b)). Other configurations of chemical bonding at AC and ZZ interfaces, i.e., with C-C (~ 1.40 Å) and Si-Ge (~ 2.35 Å) bonds are out of the study consideration since such significant difference in bond length between C-C and Si-Ge bonds will lead to a large structural distortion at the interface region of the LH. Obviously, this type of LH is energetically unfavorable.

On the other hand, we considered two configurations in SiGe/GeC-LH. The first configuration of AC-SiGe/GeC-LH and ZZ-SiGe/GeC-LH was constructed, as visualized in Figure 4-2 (a)-(b). The chemical bonding nature (see the black-dashed boxes in Figure 4-2 (a)) shows an alternative alignment of Si-C and Ge-Ge bonds along the interface of AC-SiGe/GeC-LH. While, either the Si-C or Ge-Ge bonds align at two edges of domains along the interface of ZZ-SiGe/GeC-LH (see the black-dashed boxes in Figure 4-2(b)). However, contrast to such rather large difference in bond length between Si-C (~ 1.78 Å) and Ge-Ge (~ 2.42 Å), the other configuration at the AC and ZZ interfaces of 2D SiGe/GeC-LH, referred as AC or ZZ-SiGe/CGe-LH, has been considered where the chemical bonding is formed by alternatively alignment of Si-Ge (~2.356 Å) and Ge-C (~1.886 Å) bonds in the AC- SiGe/CGe-LH (Figure 4-2 (c)) and by either the Si-Ge or Ge-C bonds alignments at two edges of domains along the ZZ- SiGe/CGe-LH (Figure 4-2 (d)).

The corresponding lattice vectors are given by $\vec{A}_1 = (na, 0,0)$,$\vec{A}_2 = (0, \sqrt{3}a, 0)$ for AC-LH, and $\vec{A}_1 = (n\sqrt{3}a, 0,0)$, $\vec{A}_2 = (0, a, 0)$ for ZZ-LH, where a denotes the average lattice constant of the combined system, and n characterizes the width of a LH, in terms of a. The width of each domain, therefore, is given by $\frac{n}{2}a_{domain}$ for AC -LH, and $\frac{n}{2}\sqrt{3}a_{domain}$for ZZ -LH, where a_{domain} is the average lattice constant of individual domain (see Figure 4-1). For SiC/GeC-LH, four different domain sizes (i.e., n = 4, 8, 16, 32, referred as 4x1, 8x1, 16x1, and 32x1) were considered to study the confinement effect on the electronic properties. It is noticed that due to the small lattice mismatch (~0.178 Å) between SiC and GeC domains, the combined LH are commensurate with negligible strain.

For SiGe/GeC-LH, however, only domain size with n = 4 was considered in the present work, since the strong strain induced by the large lattice mismatch (17%) and the mixture of sp^2 and sp^3 chemical bonding at the interface that cause strong structural distortion for large domain sizes (i.e., n = 8, 16, 32). Consequently, the study moved to considering commensurate structure of SiGe/GeC-LH to reduce the distortion caused by large mismatch lattice constant (17%). In commensurate SiGe/GeC-LH (Figure 4-3), the width of each domain is given by na_{domain} for AC -LH and $n\sqrt{3}a_{domain}$ for ZZ -LH, and the periodicity of each domain along the interface is given by $m(m')\sqrt{3}a_{domain}$ for AC -LH and $m(m')a_{domain}$ for ZZ -LH, where a_{domain} is the average lattice constant of individual domain (*e.g.*, $n = 4, m = 5$ for $SiGe$ domain and $n = 4, m' = 6$ for GeC domain, as shown in Figure 4-3).

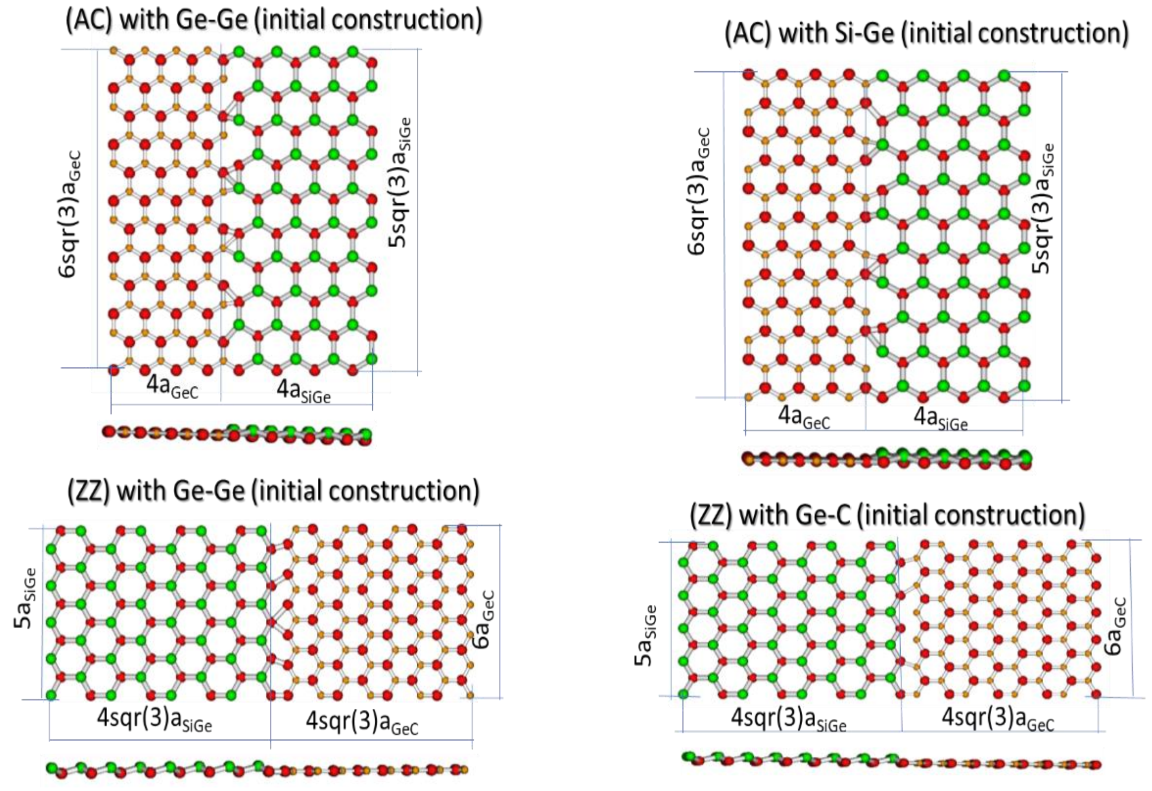

Figure 4-3: Schematic illustrations of the top and side views of the commensurate 2D polar 5x4 SiGe/6x4 GeC-LH with Ge-Ge/Ge-C bonding at the AC and ZZ interfaces (left panels) and Si-C/Ge-C bonding nature at AC/ZZ interfaces (right panels), respectively. The yellow, red, and green spheres represent C, Ge, Si atoms, respectively.

4.4. Computational methods

All calculations involved in this project were computed under DFT framework [73, 74] and PAW algorithm [75] as implemented in VASP [46]. The PBE [51] with GGA approach [76] was used to describe the exchange-correlation interactions, and the plane-wave basis was expanded up to a cutoff energy of 400 eV. A vacuum region of 15 Å perpendicular to the LH was introduced to avoid the interaction caused by the periodic boundary condition. Brillouin zones were sampled by a series of k-point grids in the framework of the Monk-horst scheme [77]. Conjugate gradient algorithm [78] was used in the whole relaxation processes and the in-plane atomic coordinates were fully relaxed until the forces on atoms were less than 10^{-3} eV/Å. The formation energy (defined as $E_f = E_{total} - E_{SiX} - E_{GeC}$, where E_{total}, E_{SiX}, and E_{GeC} are the total energy of the combined system and the energies of corresponding SiX and GeC domains, respectively, $X = C, Ge$), electronic band structures, local density of states (LDOS), and partial charge of valence band maximum (VBM) and conduction band minimum (CBM) of these 2D polar LH within the supercell model were calculated using the PBE functional. Note that in 2D polar LH, the in-plane long-range vdW interaction is much weaker than the electrostatic interaction forming chemical bonds and is out of our consideration in current calculations.

The dynamic stability of the systems was examined through the phonon dispersion calculations based on Parlinski-Li-Kawazoe method [78] (implemented in the phonopy code) and the Raman shift evaluations within the double harmonic approximation from the lattice vibrational frequencies [122]. The Bader analysis scheme [57, 123-125] was employed to analyze charge redistribution and charge transfer between domains of the combined system, and the electronic properties at the interface region were analyzed from the differential electron charge density (DCD), defined as $\Delta\rho = \rho_{total} - \rho_{SiX} - \rho_{GeC}$ (where ρ_{total} is the total electron charge density of the LH, ρ_{SiX} and ρ_{GeC} are the electron charge densities associated with the SiX and GeC domains in the combined system, respectively, $X = C, Ge$), to track the net charge transfer between domains and provide the detail information about the interaction between domains at the interface region.

4.5. 2D SiC/GeC-LH (structural properties)

Structurally, Figure 4-4 depicts the fully relaxed structure of AC and ZZ of SiC/GeC-LH with supercell domains ranging from 4x1 to 32x1. Clearly, SiC/GeC-LH shows flat honeycomb lattices with no buckling distortion at the interface region due mainly to the small lattice mismatch between SiC and GeC monolayers. The thermodynamic stability was further studied by heating the 8x1 AC heterostructures, as an example, to certain temperature levels (see Figure 4-5). No bond breaking and local structural distortion were found even at 1000 K, implying that the optimized 2D polar LH could sustain under the environment of high temperatures. Furthermore, the formation energy (E_f) of the optimized SiC/GeC-LH, shown in 2nd column of Table 4-1, attains negative value and decays monotonically as increasing the width of LH, clearly demonstrating that the assembly of SiC and GeC monolayers in such a planar heterostructure is an exothermic process and thermodynamically stable.

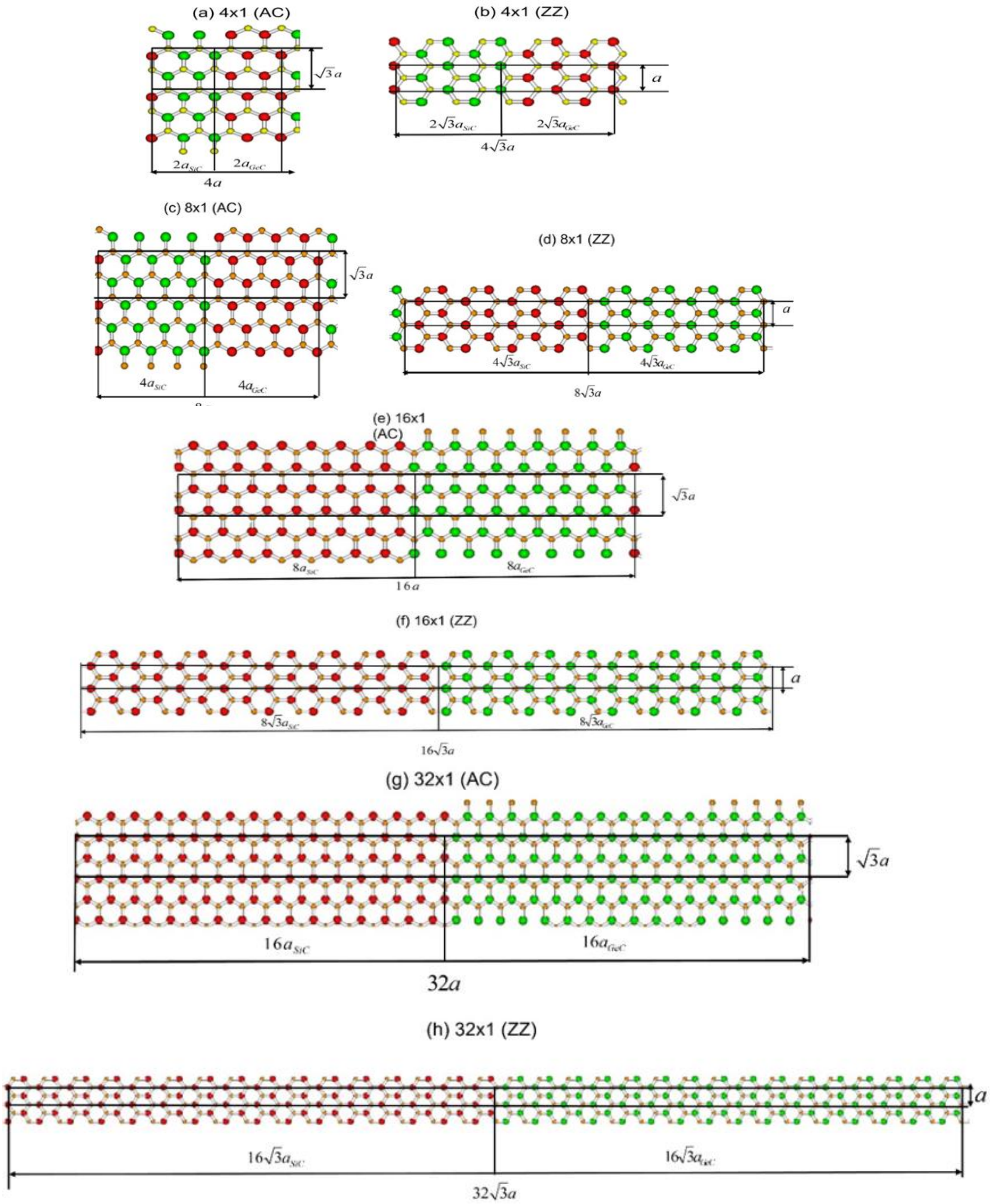

Figure 4-4: Schematic illustration of the top views of optimized 2D SiC/GeC-LH with AC and ZZ interfaces. The lattice vectors of the supercell are $\vec{A}_1 = (na, 0,0)$ and $\vec{A}_2 = (0, \sqrt{3}a, 0)$ for AC and, $\vec{A}_1 = (n\sqrt{3}a, 0,0)$ and $\vec{A}_2 = (0, a, 0)$ for ZZ, where a denotes the average lattice constant of the combined systems. The domain sizes of GeC and SiC are scaled by $\frac{n}{2}a_{GeC}$ and $\frac{n}{2}a_{SiC}$ for AC, and $\frac{n}{2}\sqrt{3}a_{GeC}$ and $\frac{n}{2}\sqrt{3}a_{SiC}$ for ZZ, where a_{GeC} and a_{SiC} are the average lattice constants in the corresponding domains of combined systems. The size of domain is indicated in terms of nx1, where n = 4 ((a) & (b)), 8((c) & (d)), 16 ((e) & (f)), and 32 ((g) & (h)). The yellow, red, and green spheres represent C, Ge, Si atoms, respectively.

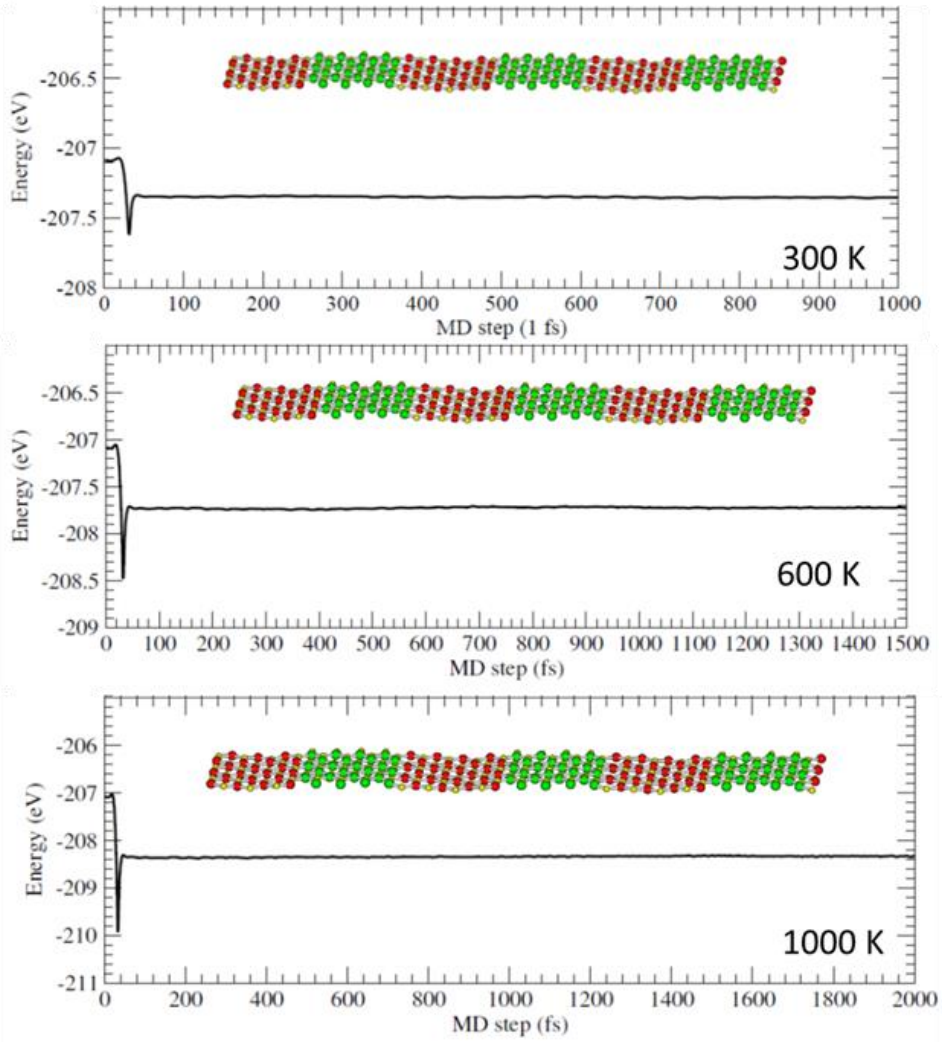

Figure 4-5: Total energy of 8x1 SiC/GeC LH with the AC interface as a function of MD steps under 300 K, 600 K, and 1000 K, respectively. The insets illustrate the structures under each temperature. The yellow, red, and green dots represent C, Ge, Si atoms, respectively.

Table 4-1: The formation energy (E_f) per atom of optimized 2D polar SiC/GeC-LH, associated average lattice constants (a) and corresponding averaged lattice constants in GeC (a_{GeC}) and the SiC (a_{SiC}) domains, together with the uniaxial strain along x/y directions in GeC and SiC domains.

System	$\boldsymbol{E_f}$ (meV/atom)	$\boldsymbol{a}$ (Å)	$\boldsymbol{a_{GeC}}$(Å)	$\boldsymbol{a_{SiC}}$ (Å)	$\boldsymbol{Uniaxial\ strain}_{\boldsymbol{GeC}}$ $\boldsymbol{x/y}$ (%)	$\boldsymbol{Uniaxial\ strain}_{\boldsymbol{SiC}}$ $\boldsymbol{x/y}$ (%)
4x1 (AC)	-1045	3.1801	3.261	3.099	-0.184/-2.659	0.324/2.949
4x1 (ZZ)	-592	3.1797	3.265	3.095	-0.061/-2.672	0.194/2.936
8x1 (AC)	-545	3.1798	3.276	3.084	0.275/-2.669	-0.162/2.939
8x1 (ZZ)	-299	3.1800	3.293	3.067	0.796/-2.663	-0.712/2.946
16x1 (AC)	-273	3.1797	3.290	3.069	0.704/-2.672	-0.647/2.946
16x1 (ZZ)	-150	3.1800	3.291	3.077	0.735/-2.662	-0.388/2.946
32x1 (AC)	-134	3.1800	3.289	3.070	0.673/-2.663	-0.615/2.946
32x1 (ZZ)	-31	3.1799	3.290	3.069	0.704/-2.666	-0.647/2.943

4.5.1. Lattice mismatch induced strain.

Optimized lattice constants for the combined 2D polar SiC/GeC-LH are listed in Table 4-1. The interesting finding from the structural relaxation is that the optimized average lattice constant (a) for the combined system is ~3.180 Å (within a tiny fluctuation of 0.0003 Å), almost independent of the width of domain (e.g., 4x1, 8x1, 16x1, and 32x1) and the type of interface (e.g., AC or ZZ) (see the 3rd column in Table 4-1). The corresponding average domain lattice constants (i.e., a_{SiC} and a_{GeC} as shown in Figure 4-1), on the other hand, are close to the lattice constants of their pristine sheets (i.e., 3.089 Å for the pristine SiC sheet and 3.267 Å for the pristine GeC sheet, see the 4th and 5th columns in Table 4-1), indicating that the strain induced by the lattice mismatch does not spread uniformly in each domain but only distributes along the interface direction, leading to a uniaxial strain. Estimated the uniaxial strain perpendicular to the interface (i.e., along x direction shown in Figure 4-1) is very weak (from -0.184% to 0.796%). But the uniaxial strain along the interface direction (i.e., along y direction shown in Figure 4-1) leads to ~2.94% of expansion at the SiC domain and ~2.67% of compression at the GeC domain, respectively, which is also independent of the domain size (see the 6th and 7th columns in Table 4-1). Consequently, designing semiconductor-semiconductor LH with small lattice mismatch such as SiC/GeC-LH makes each domain retain intrinsic its structural properties and induce local strain along the interface.

4.5.2. Strain and interface effects on lattice vibration frequency

The dynamic stability of the optimized 2D polar SiC/GeC-LH was examined from their phonon dispersion, Raman spectrum, and the frequency of lattice vibration, respectively. No imaginary frequency was found in the combined 2D SiC/GeC systems, indicating that they are dynamically stable. The phonon dispersion of 4x1 AC LH (Figure 4-6 (a)), as an example, shows a wide band in the low frequency region (< 400 cm-1), a few bands located in the range of 450-620 cm^{-1}, and a narrow band located at high frequency (~850-1050 cm^{-1}). At the high frequency range, the intensity and distribution of Raman shift of 8x1 LH (Figure 4-6 (b)), on the other hand, show broaden peaks with the AC interface and pronounced peaks with the ZZ interface, respectively. This scenario is also found from the densities of vibration frequency (Figure 4-7). It is found that the peaks located around 880 cm^{-1} characterize a tiny blue shift of the in-plane (LO/TO) modes of the pristine GeC (~ 867 cm^{-1}) due to the uniaxial compression along the interface, almost independent of the size of GeC domain and the type of interface (indicated by the blue arrows on Figure 4-6). The peaks located around 920 cm^{-1} characterize a big red shift of the in-plane (LO/TO) modes of the pristine SiC (~ 995 cm^{-1}) due to the uniaxial expansion along the interface (indicated by the red arrows on Figure 4-6). The peaks associated with the out-of-plane modes (ZO) of the pristine SiC (~ 425 cm^{-1}) and GeC (~ 259 cm^{-1}) sheets are flattened and merged to the low frequency modes when they are stitched together (see the black- and red-dashed lines indicated in Figure 4-7). Furthermore, by comparing the vibrational frequencies of 8x1 LH with pristine SiC and GeC sheets (Figure 4-8), we found that the additional vibrational frequencies located in the range of 460-650 cm^{-1} mainly come from the Si-C bond vibrations at the SiC domain. Clearly, these frequencies are sensitive to the size of the domain and the type of the interface (see Figure 4-7).

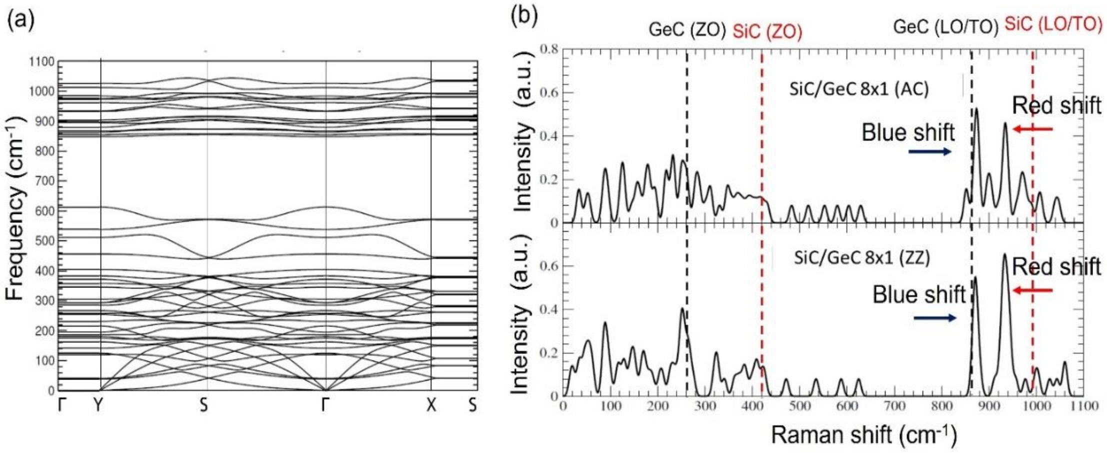

Figure 4-6: (a) Band structure of the phonon dispersion of the optimized 2D 4x1 SiC/GeC LH with the AC interface. (b) Calculate Raman shift of optimized 2D 8x1 SiC/GeC LH with AC (upper panel) and ZZ (bottom panel) interfaces, respectively. A Gaussian broadening ($5\ cm^{-1}$) was used in plotting Raman spectrum. The dashed lines guide the peak positions of LO, TO, and ZO vibration modes for the pristine SiC (red) and GeC (black) sheets, respectively.

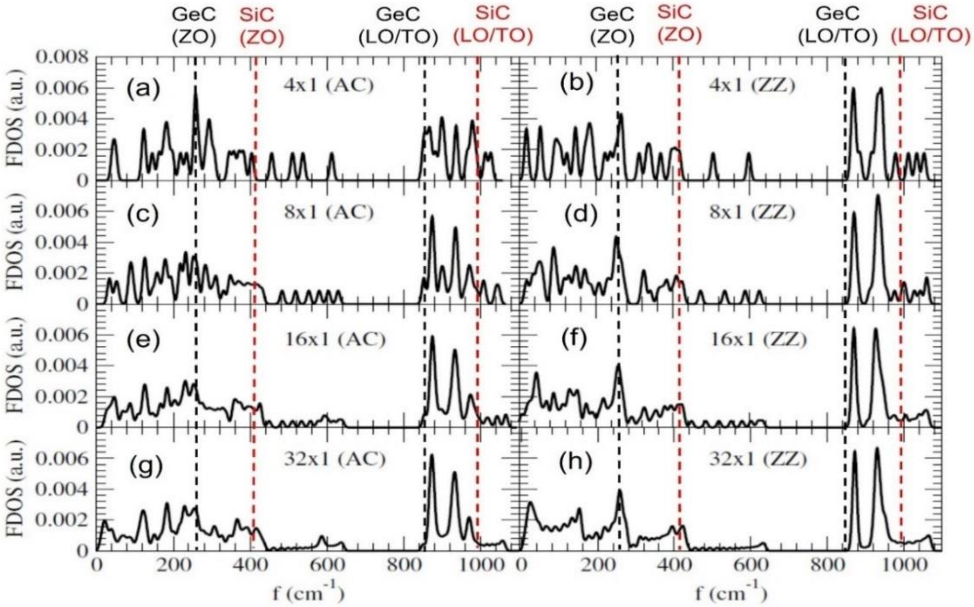

Figure 4-7: (a) Calculate vibrational frequency densities of states (FDOS) of optimized 2D polar SiC/GeC LH with AC (left panels) and ZZ (right panels) interfaces, respectively. The width of the LH is characterized by n = 4 ((a) & (b)), 8((c) & (d)), 16 ((e) & (f)), and 32 ((g) & (h)). A Gaussian broadening (5 cm^{-1}) was used in plotting FDOS. The dashed lines guide the peak positions of LO, TO, and ZO vibration modes of the pristine SiC (red) and GeC (black) sheets, respectively.

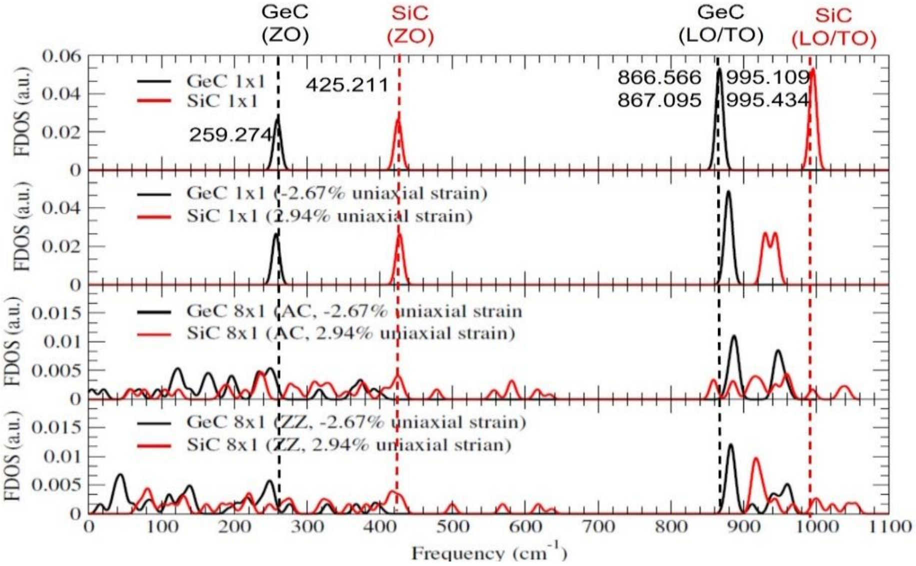

Figure 4-8: The vibrational frequency densities of states of the pristine SiC monolayer with/without 2.94 % expansion (red) and the pristine GeC monolayer with/without 2.67 % compression (black) with 1x1 (top two panels) and 8x1 (bottom two panels) unit cells, respectively. The black and red dashed lines indicate the vibrational frequencies of LO, TO, and ZO modes associated by the corresponding values.

4.6. 2D SiC/GeC-LH (electronic properties)

When the SiC and GeC sheets combine to form an LH, a 2.94% uniaxial expansion occurs in the SiC domain along the interface direction AC or ZZ, and a 2.67% uniaxial compression occurs in the GeC domain along the interface direction AC or ZZ. This artificial strain along with the other changes, i.e., sharp interface which allows charge transfer between constituent domains and confine charge carriers within various finite domains, impact LH properties, in particular electronic properties that will address in detail in the next section.

4.6.1. Strain, interface, and confinement effect on band structure

The calculated band structures of the 2D SiC/GeC-LH with different types of the interfaces (i.e., AC and ZZ) and the various width of domains (e.g., 4x1, 8x1, 16x1, 32x1) at DFT-PBE level are shown in Figure 4-9. From there, it was found that 2D semiconductor- semiconductor SiC/GeC-LH is again a semiconductor regardless of the type of interface or the width of each constituent domain. Namely, 2D AC-SiC/GeC-LH exhibits indirect band gap, while 2D ZZ-SiC/GeC-LH shows a direct band gap, independent of the domain width. To better understand the band nature of 2D SiC/GeC-LH, we compared the results of the indirect band gap nature from 2.94% uniaxial expansion along AC direction of pristine SiC, and the direct band gap nature from 2.67% uniaxial compression along AC or ZZ direction of pristine GeC (see Chapter 3, Figure 3-9). Consequently, 2D AC-SiC/GeC-LH retains the band gap behavior of AC orientated uniaxial expansion of pristine SiC while 2D ZZ-SiC/GeC-LH retains the band gap behavior of ZZ orientated uniaxial strain of the pristine GeC and SiC.

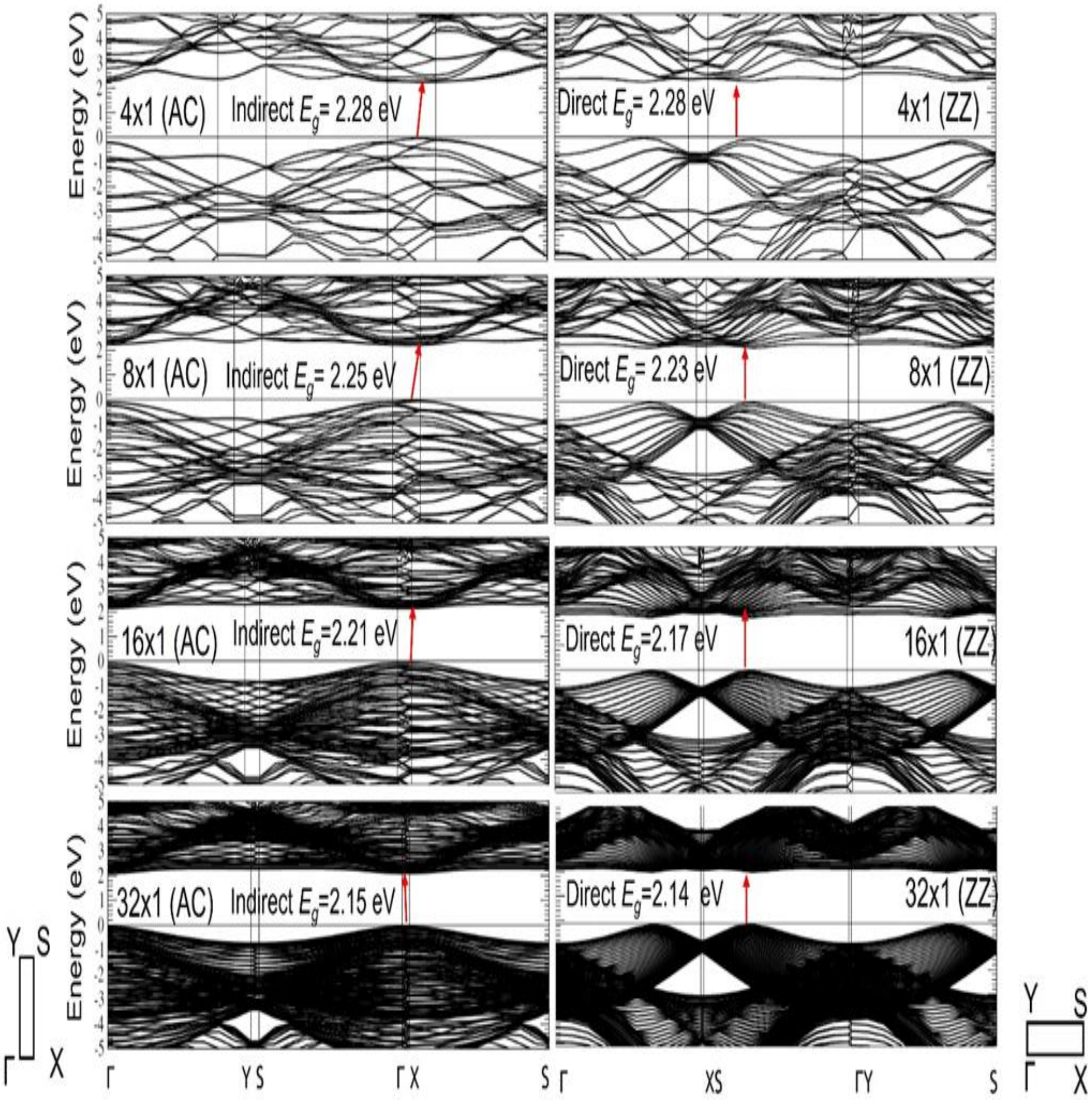

Figure 4-9: Band structures of 2D polar SiC/GeC LH with AC (left panels) and ZZ (right panels) interfaces, respectively. The width of domain is indicated in terms of *n*x1, where *n* = 4, 8, 16, and 32. The Brillouin zone with special k points are illustrated at the bottom left (right) corner for AC (ZZ) interface, respectively. The band gaps are represented by the numbers, the direct/indirect band gap natures are denoted by red arrows, and the Fermi level is shifted to the zero.

Furthermore, the band gap monotonically decreases as increasing the width (L) of LH (Figure 4-10) and obeys the reciprocal law of $2.06 + \frac{1.0}{L^{0.5}}$, demonstrating a quantum confinement effect. It is also found that under a given width of the domain, the band gap of ZZ-LH is slightly larger than that with the AC-LH (Figure 4-10). Thus, the band gap can be modulated by adjusting the size of the domain and fine-tuned by adjusting the type of the interface, demonstrating their promising applications in band gap engineering. In addition, the proposed 2D SiC/GeC-LH possess a tunable band gap in the range of 2.14-2.28 eV, exhibiting significantly improved visible-light absorption capability (as compared with the single pristine SiC or GeC monolayer). It should be noted that DFT-PBE calculations for the band structures usually underestimate the fundamental gap, as compared with the experimental result. Method, such as the Heyd–Scuseria–Ernzerh of screened Coulomb hybrid functional (referred as HSE06) [126] could be applied to improve the band gap. Such calculations are expensive for large systems, such as the 2D SiC/GeC-LH studied here, and the calculations at DFT-PBE level can still report the basic physics.

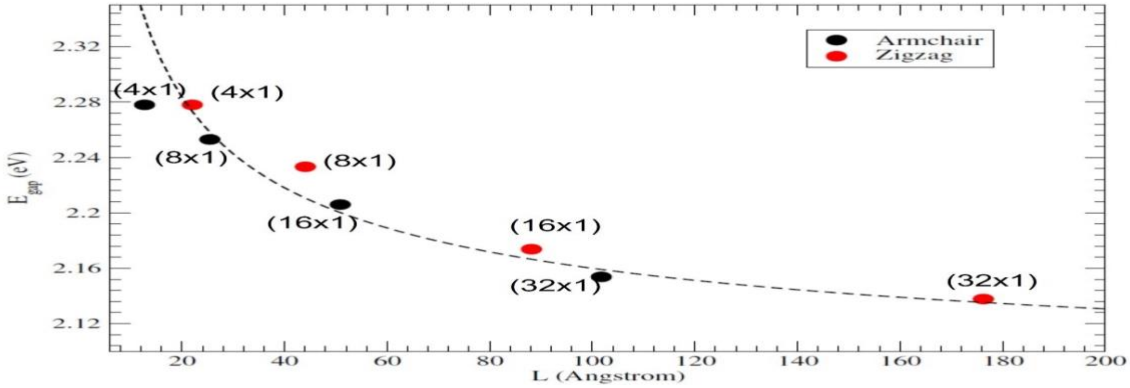

Figure 4-10: Calculated band gaps of the 2D polar SiC/GeC LH with the AC (black dots) and ZZ (red dots) interfaces, respectively, as a function of the width (L) of the lateral heterostructures. The black-dashed curve is the fitting function following the formula of $2.06 + \frac{1.0}{L^{0.5}}$.

The band partition analysis (the left panels of Figure 4-11 (a), and Figure 4-12 (a); Figure 4-13 (a), and Figure 4-14 (a); Figure 4-15 (a), and Figure 4-16 (a); Figure 4-17 (a), and Figure 4-18 (a) for 4x1, 8x1 16x1, and 32x1 LH, respectively) clearly shows that the VBM band mainly originates from the contribution of C-2p orbitals (red dots), and the CBM band mainly dominated by the Ge-4p orbitales (blue triangles). This nature is further confirmed from the DOS (the right panel of Figure 4-11 (a), and Figure 4-12 (a); Figure 4-13 (a), and Figure 4-14 (a); Figure 4-15 (a), and Figure 4-16 (a); Figure 4-17 (a), and Figure 4-18 (a) for 4x1, 8x1 16x1, and 32x1 LH, respectively). The band decomposed charge density of the 2D SiC/GeC-LH shows that both VBM and CBM bands possess the π (pz)-orbital behavior perpendicular to the heterostructure surface (see yellow contours in (b) and (c) of Figure 4-11, and Figure 4-12; Figure 4-13 , and Figure 4-14 ; Figure 4-15 , and Figure 4-16 ; Figure 4-17 , and Figure 4-18 for 4x1, 8x1 16x1, and 32x1 LH, respectively). However, the shapes of VBM and CBM bands strongly depend on the interface and the width of domain. Furthermore, the charge density at VBM band is mainly contributed from C-2p orbitals in the GeC domain and partially contributed from C-2p orbitals in the SiC domain, while the charge density at CBM band is mostly contributed from Ge-4p orbitals in the GeC domain, consistent with the band partition analysis. When the width of the domain increases, the Ge-4p orbitals become dominate in the LH (see Figure 4-11 to Figure 4-18). Such scenario implies that when electrons at the SiC domain are excited to the respective empty bands, they prefer to move to the CBM band at the GeC domain.

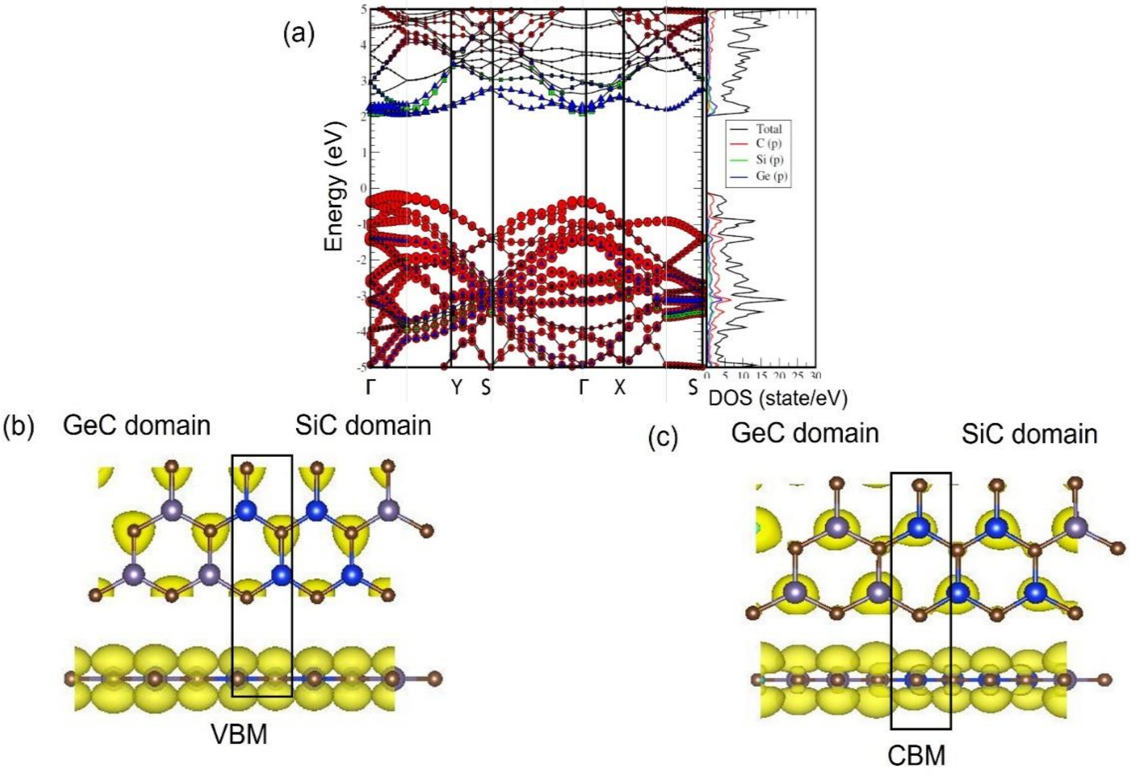

Figure 4-11: (a) Calculated partial band structures (left panel) and DOSs (right panel) of 4x1 2DSiC/GeC-LH with the AC interface (black box). The band/DOS partition from C-2p orbitals is represented by red circles/curve, Si-3p orbitals, by green squares/curve, and Ge-4p orbitals, by blue triangles/curve, respectively. The sizes of these circles/squares/triangles reflect the weight of each species contribution in the bands. (b) and (c) show the top (upper) and side (bottom) views of corresponding band decomposed charge density (yellow contours) at VBM (b) and CBM (c) bands with the isosurface value of 0.002 e/Å^3. The C, Si, Ge atoms are noted by brown, blue, and grey spheres, respectively.

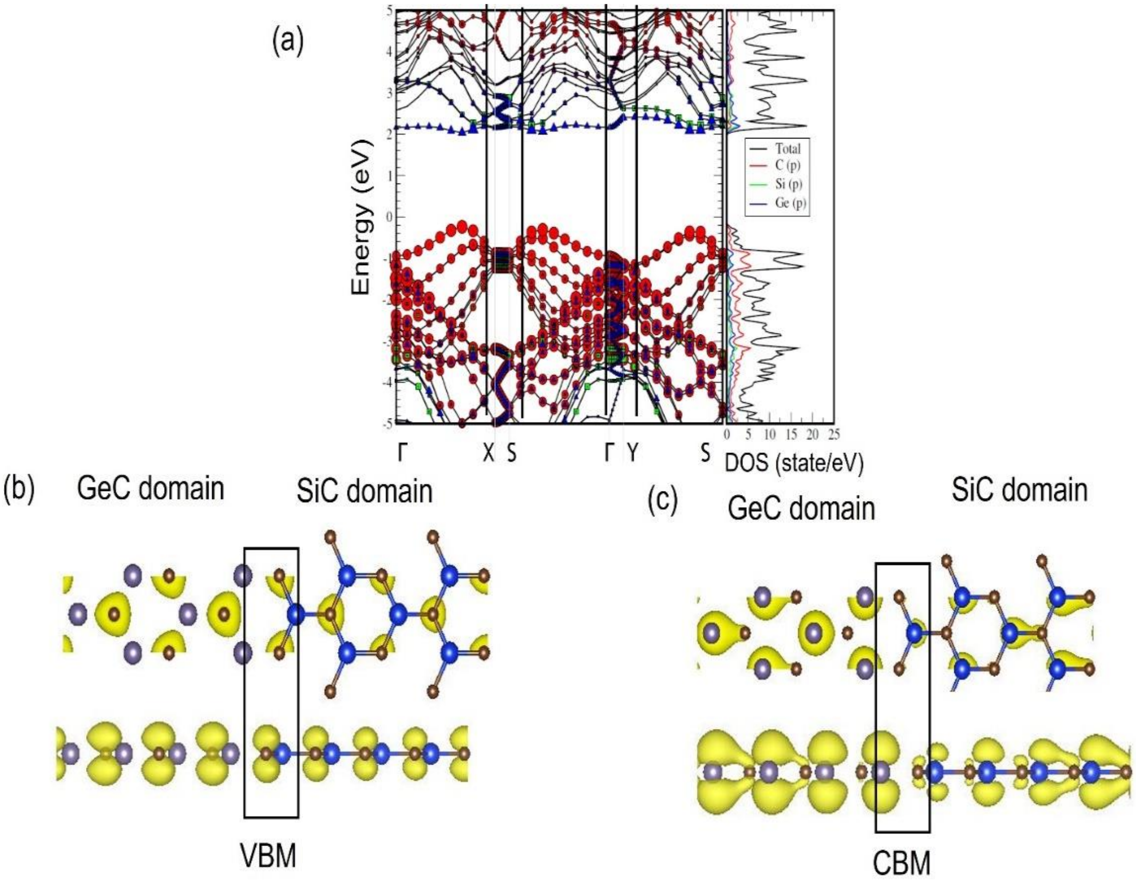

Figure 4-12: (a) Calculated partial band structures (left panel) and DOSs (right panel) of 4x1 2DSiC/GeC-LH with the ZZ interface (black box). The band/DOS partition from C-2p orbitals is represented by red circles/curve, Si-3p orbitals, by green squares/curve, and Ge-4p orbitals, by blue triangles/curve, respectively. The sizes of these circles/squares/triangles reflect the weight of each species contribution in the bands. (b) and (c) show the top (upper) and side (bottom) views of corresponding band decomposed charge density (yellow contours) at VBM (b) and CBM (c) bands with the isosurface value of 0.002 e/Å^3. The C, Si, Ge atoms are noted by brown, blue, and grey spheres, respectively.

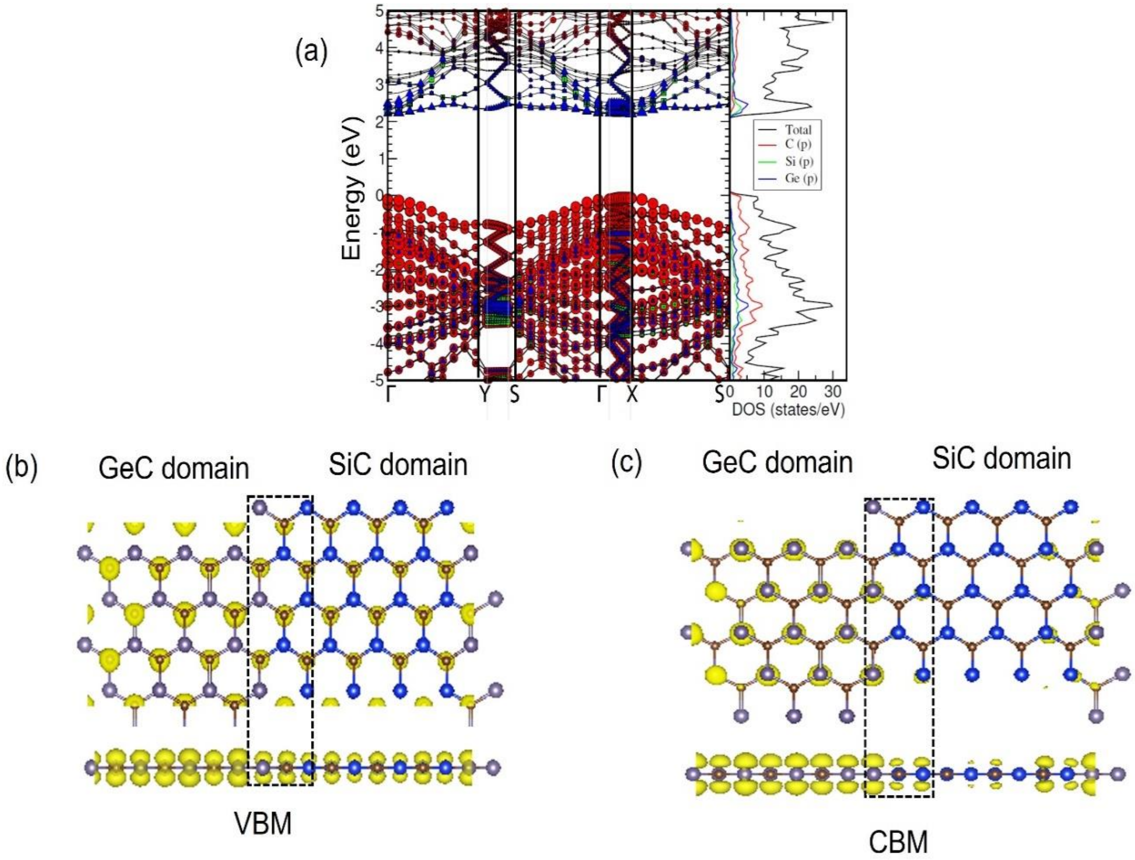

Figure 4-13: (a) Calculated partial band structures (left panel) and DOSs (right panel) of 8x1 2DSiC/GeC-LH with the AC interface (black box). The band/DOS partition from C-2p orbitals is represented by red circles/curve, Si-3p orbitals, by green squares/curve, and Ge-4p orbitals, by blue triangles/curve, respectively. The sizes of these circles/squares/triangles reflect the weight of each species contribution in the bands. (b) and (c) show the top (upper) and side (bottom) views of corresponding band decomposed charge density (yellow contours) at VBM (b) and CBM (c) bands with the isosurface value of 0.002 e/Å^3. The C, Si, Ge atoms are noted by brown, blue, and grey spheres, respectively.

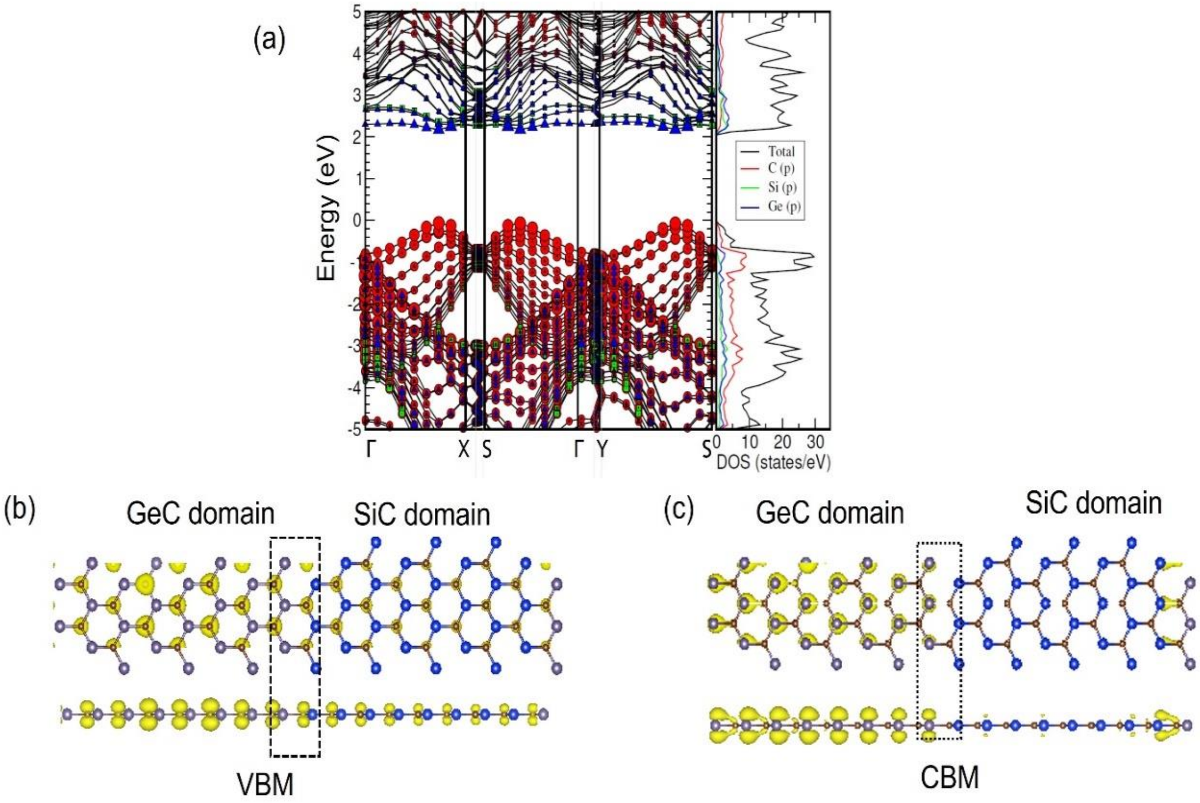

Figure 4-14: (a) Calculated partial band structures (left panel) and DOSs (right panel) of 8x1 2DSiC/GeC-LH with the ZZ interface (black box). The band/DOS partition from C-2*p* orbitals is represented by red circles/curve, Si-3*p* orbitals, by green squares/curve, and Ge-4*p* orbitals, by blue triangles/curve, respectively. The sizes of these circles/squares/triangles reflect the weight of each species contribution in the bands. (b) and (c) show the top (upper) and side (bottom) views of corresponding band decomposed charge density (yellow contours) at VBM (b) and CBM (c) bands with the isosurface value of 0.002 e/Å^3. The C, Si, Ge atoms are noted by brown, blue, and grey spheres, respectively.

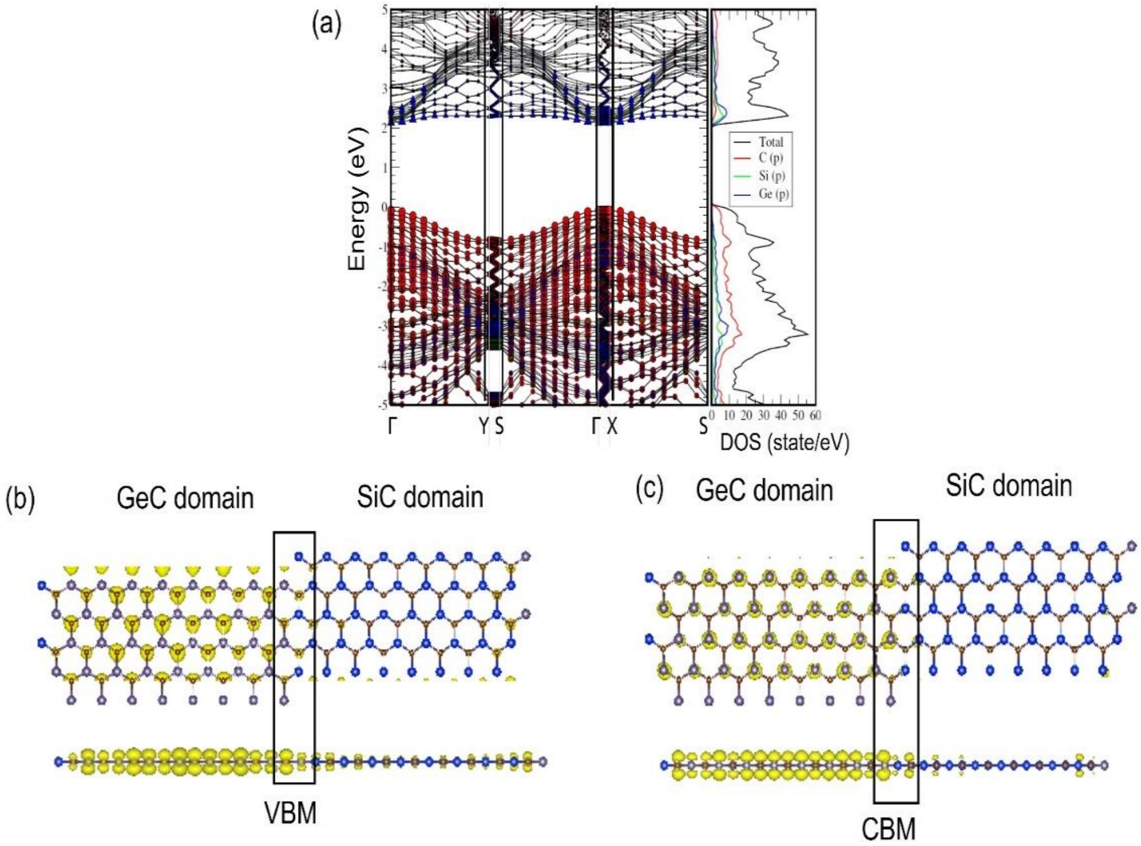

Figure 4-15: (a) Calculated partial band structures (left panel) and DOSs (right panel) of 16x1 2DSiC/GeC-LH with the AC interface (black box). The band/DOS partition from C-2p orbitals is represented by red circles/curve, Si-3p orbitals, by green squares/curve, and Ge-4p orbitals, by blue triangles/curve, respectively. The sizes of these circles/squares/triangles reflect the weight of each species contribution in the bands. (b) and (c) show the top (upper) and side (bottom) views of corresponding band decomposed charge density (yellow contours) at VBM (b) and CBM (c) bands with the isosurface value of 0.002 e/Å^3. The C, Si, Ge atoms are noted by brown, blue, and grey spheres, respectively.

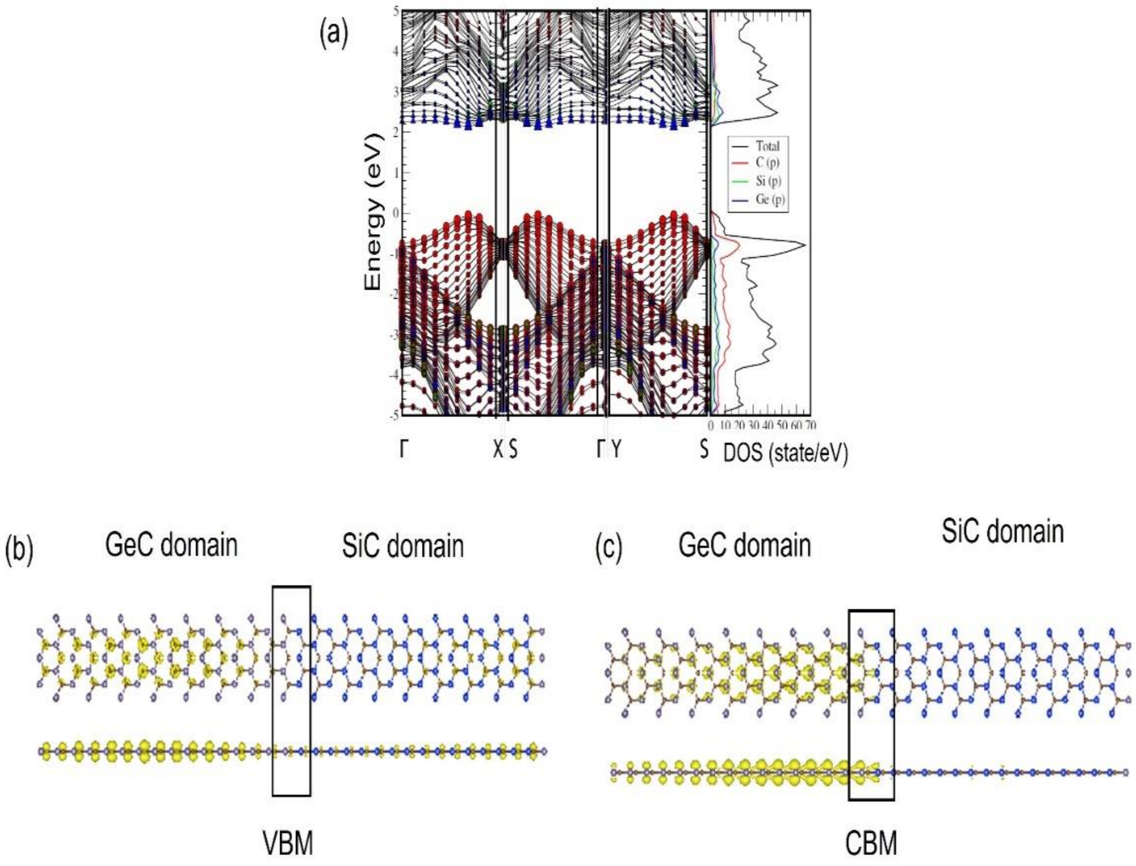

Figure 4-16: (a) Calculated partial band structures (left panel) and DOSs (right panel) of 16x1 2DSiC/GeC-LH with the AC interface (black box). The band/DOS partition from C-2p orbitals is represented by red circles/curve, Si-3p orbitals, by green squares/curve, and Ge-4p orbitals, by blue triangles/curve, respectively. The sizes of these circles/squares/triangles reflect the weight of each species contribution in the bands. (b) and (c) show the top (upper) and side (bottom) views of corresponding band decomposed charge density (yellow contours) at VBM (b) and CBM (c) bands with the isosurface value of 0.002 e/Å^3. The C, Si, Ge atoms are noted by brown, blue, and grey spheres, respectively.

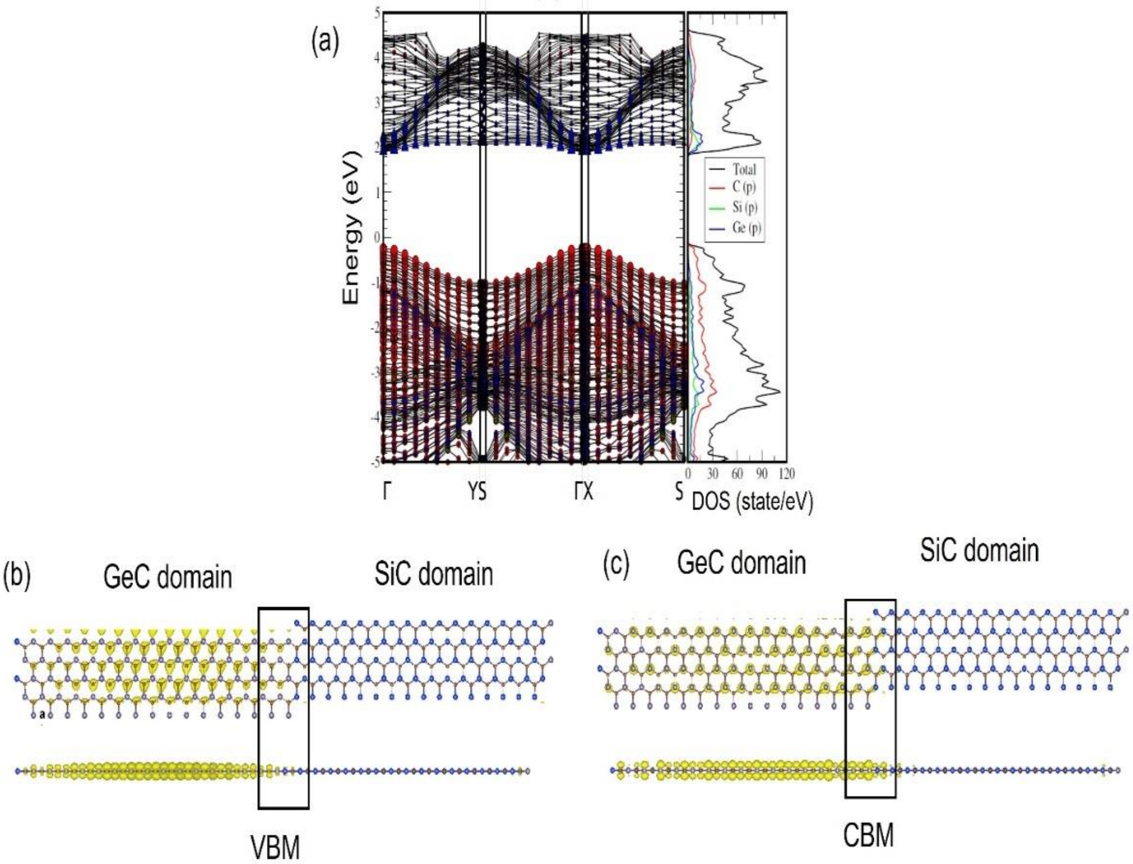

Figure 4-17: (a) Calculated partial band structures (left panel) and DOSs (right panel) of 32x1 2DSiC/GeC-LH with the AC interface (black box). The band/DOS partition from C-2p orbitals is represented by red circles/curve, Si-3p orbitals, by green squares/curve, and Ge-4p orbitals, by blue triangles/curve, respectively. The sizes of these circles/squares/triangles reflect the weight of each species contribution in the bands. (b) and (c) show the top (upper) and side (bottom) views of corresponding band decomposed charge density (yellow contours) at VBM (b) and CBM (c) bands with the isosurface value of 0.002 e/Å^3. The C, Si, Ge atoms are noted by brown, blue, and grey spheres, respectively.

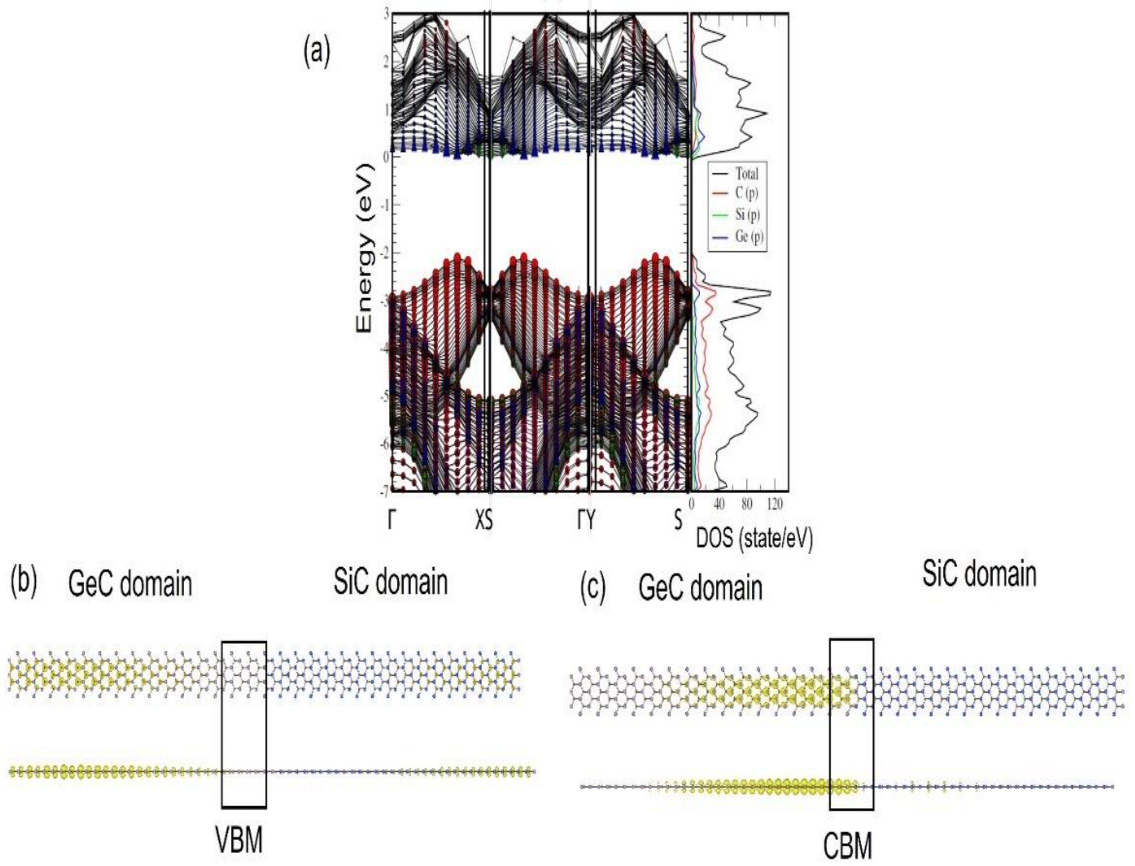

Figure 4-18: (a) Calculated partial band structures (left panel) and DOSs (right panel) of 32x1 2DSiC/GeC-LH with the AC interface (black box). The band/DOS partition from C-2p orbitals is represented by red circles/curve, Si-3p orbitals, by green squares/curve, and Ge-4p orbitals, by blue triangles/curve, respectively. The sizes of these circles/squares/triangles reflect the weight of each species contribution in the bands. (b) and (c) show the top (upper) and side (bottom) views of corresponding band decomposed charge density (yellow contours) at VBM (b) and CBM (c) bands with the isosurface value of 0.002 e/Å^3. The C, Si, Ge atoms are noted by brown, blue, and grey spheres, respectively.

4.6.2. Strain, interface, and confinement effect on charge redistribution

To further understand the charge transfer between two domains in an LH, a quantitative charge transfer was obtained from the Bader charge analysis (listed in Table 4-2). It was found that there is a charge transfer of 2.094 e between Si and C in the pristine SiC sheet and a charge transfer of 1.3623 e between Ge and C in the pristine GeC sheet. The different amount of the charge transfers in the SiC and GeC sheets is mainly due to their different electronegativities. Such charge transfers hold when two polar sheets are stitched to form an LH. Interesting finding from the charge transfer analysis is that the charge transfers are sensitive to the interface and the size of domain. More electrons transfer from Si (Ge) to C atoms in the combined systems with the ZZ interface than those with the AC interface, and the larger the domain size, the more electrons loss at Si (Ge) atoms (see columns 3rd and 5th in Table 4-2). Even more interesting finding is that there is a net charge transfer from the SiC domain to the GeC domain (see the 6th and 7th columns in Table 4-2). The amount of net charge transfer between two domains increases as the increase of the domain size. Especially, more electrons loss at Si atoms at the SiC domain and transfer to C atoms at the GeC domain when the size is over 16x1 (see the 2nd and 5th columns in Table 4-2), indicating that the GeC domain gains more net electrons as increasing the width of the LH. Such net charge redistribution between two domains, originated from the in-plane charge transfer, leads to a lateral spontaneous *p*-*n* junctions, characterizing the unique property of 2D SiC/GeC-LH (as indicated in Figure 4-19).

Table 4-2: Bader charge analysis (in the unit of e/atom) of the charge transfer between Si, Ge, and C atoms in the pristine SiC and GeC monolayers and the 2D SiC/GeC-LH with different interface and width of domain. There are two types of C atoms: one is at the SiC domain (denoted by $C\ (SiC)$), and the other is at the GeC domain (denoted by $C\ (GeC)$. The net charge per atom in GeC and SiC domains are listed in the 6th and 7th columns, respectively.

Systems	$C\ (GeC)$ (e/atom)	Ge (e/atom)	$C\ (SiC)$ (e/atom)	Si (e/atom)	GeC (e/atom)	SiC (e/atom)
GeC	-1.362	1.362	-	-	0	-
SiC	-	-	-2.094	2.094	-	0
1x4 (AC)	-1.657	1.498	-2.166	2.325	-0.0795	0.0795
1x4 (ZZ)	-1.898	1.775	-3.094	3.217	-0.0615	0.0615
1x8 (AC)	-1.578	1.501	-2.309	2.386	-0.0385	0.0385
1x8 (ZZ)	-1.798	1.744	-3.261	3.316	-0.0272	0.0272
1x16 (AC)	-2.451	1.385	-1.447	2.512	-0.5326	0.5326
1x16 (ZZ)	-3.254	1.784	-1.812	3.282	-0.7351	0.7351
1x32 (AC)	-2.816	1.451	-1.484	2.850	-0.6828	0.6828
1x32 (ZZ)	-3.313	1.790	-1.804	3.327	-0.7615	0.7615

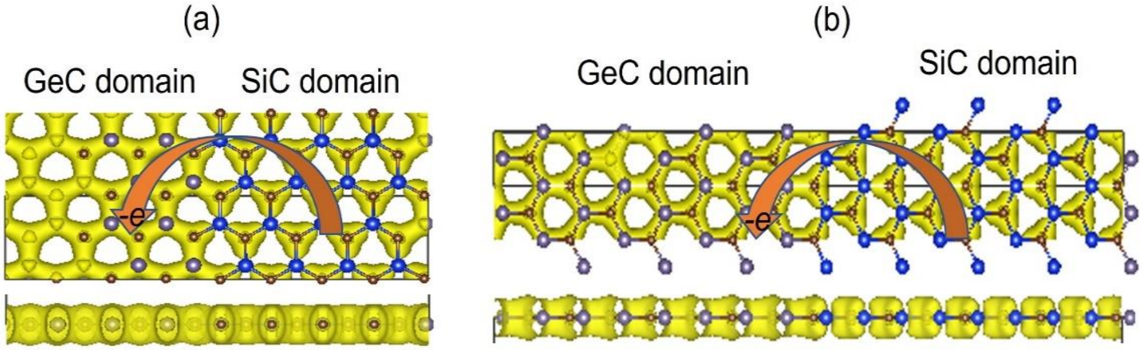

Figure 4-19: The top (upper) and side (bottom) views of the electron localization functions (yellow contours with the isosurface value of 5.8x10^{-1} e/Å^3) of 2D 8x1 SiC/GeC polar LH with AC (a) and ZZ (b) interfaces, indicating the covalent boding nature with CT in the GeC domain and the covalent bonding nature with more CT in the SiC domain, respectively. The net charge transfer from the SiC domain to the GeC domain is illustrated by the brown arrows. The C, Si, Ge atoms are noted by brown, blue, and grey spheres, respectively.

The DCD induced by the net charge redistribution between two polar material domains (illustrated in Figure 4-20 - Figure 4-23 (a) and (b) for 4x1, 8x1,16x1, and 32x1 heterostructures) characterize the interfacial hybridization of the 2D SiC/GeC-LH. The net electron accumulation and depletion are shown by the yellow and blue contours. Clearly, the net electron redistribution in the interface region, induced by the coupling between SiC and GeC domains, is sensitive to the type of interface and the size of the domain and reflects the degree of the hybridization of orbitals between adjacent domains. As shown in Figure 4-20 - Figure 4-23, the net charge redistribution solely locates at the interfacial region, with the net electrons depleting around the Si and Ge atoms and accumulating around C atoms. For the AC interface ((a) in Figure 4-20 - Figure 4-23), most net electrons deplete around Si atoms at the side of SiC domain and accumulate around the C atoms at the side of the GeC domain. For the ZZ interface ((b) Figure 4-20 -

Figure 4-23), more net electrons deplete around Si (Ge) atoms and accumulate around corresponding C atoms at the edges of the domains with Si-C (Ge-C) bonds, but still with the net depletion mainly distributed in the SiC domain, consistent with the Bader results (see the 6th and 7th columns in Table 4-2). Such net charge transfer from the SiC domain to the GeC domain, therefore, forms in-plane dipoles along the interface.

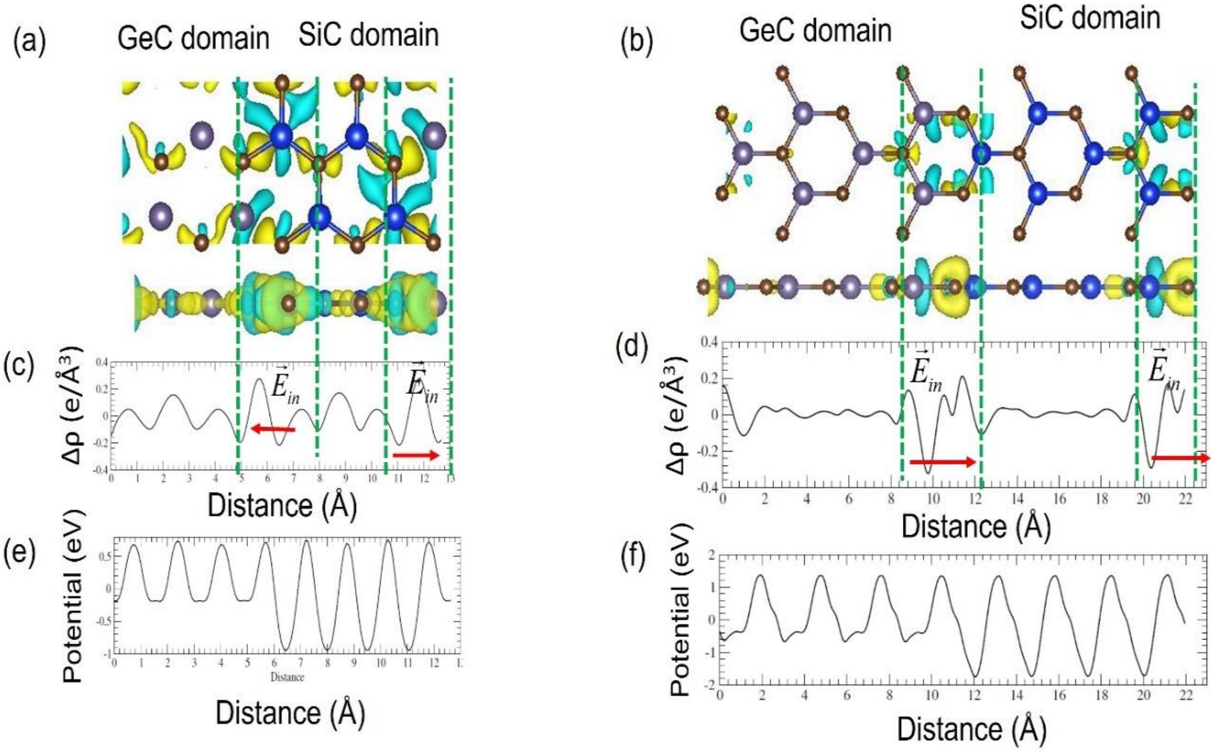

Figure 4-20: (a) and (b) show the top (upper) and side (bottom) views of differential charge densities (DCD) of 4x1 SiC/GeC LH with AC (a) and ZZ (b) interfaces. The electron accumulation and depletion are represented by the yellow and blue contours (with the isosurface of 4.0 x10^{-4}e/Å^3). The C, Si, Ge atoms are noted by brown, blue, and grey spheres, respectively. (c) and (d) show the plane-averaged DCD ($\Delta\rho$) along the surface of the 4x1 SiC/GeC lateral heterostructures with AC (c) and ZZ (d) interfaces, respectively. The interface region is highlighted by green-dashed lines and the build-in electric field is indicated by the red arrows. (e) and (f) show the plane-averaged electrostatic potential along the surface of the 4x1 SiC/GeC lateral heterostructures with AC (e) and ZZ (f) interfaces, respectively.

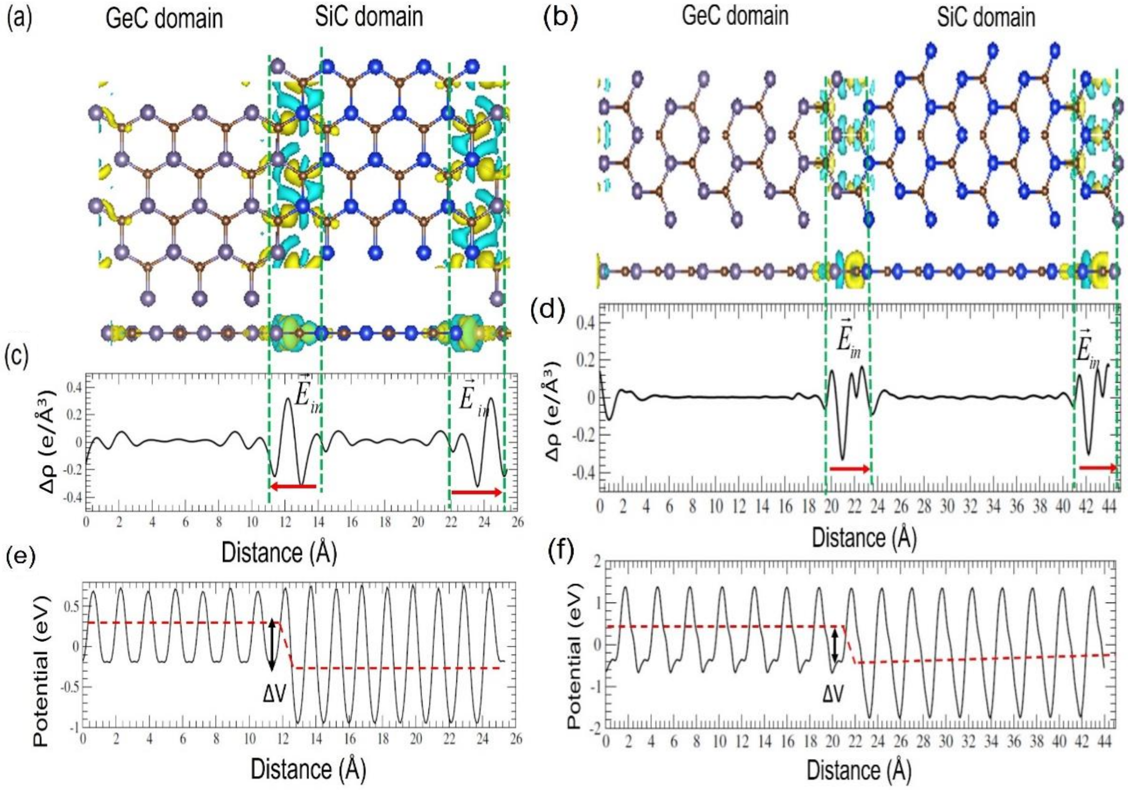

Figure 4-21: (a) and (b) show the top (upper) and side (bottom) views of differential charge densities (DCD) of 8x1 SiC/GeC lateral heterostructures with AC (a) and ZZ (b) interfaces. The electron accumulation and depletion are represented by the yellow and blue contours (with the isosurface of 4.0 x10^{-4} e/Å^3). The C, Si, Ge atoms are noted by brown, blue, and grey dots, respectively. (c) and (d) show the plane-averaged DCD ($\Delta\rho$) along the surface of the 8x1 SiC/GeC lateral heterostructures with AC (c) and ZZ (d) interfaces, respectively. The interface region is highlighted by green-dashed lines and the build-in electric field is indicated by the red arrows. (e) and (f) show the plane-averaged electrostatic potential along the surface of the 8x1 SiC/GeC lateral heterostructures with AC (e) and ZZ (f) interfaces, respectively.

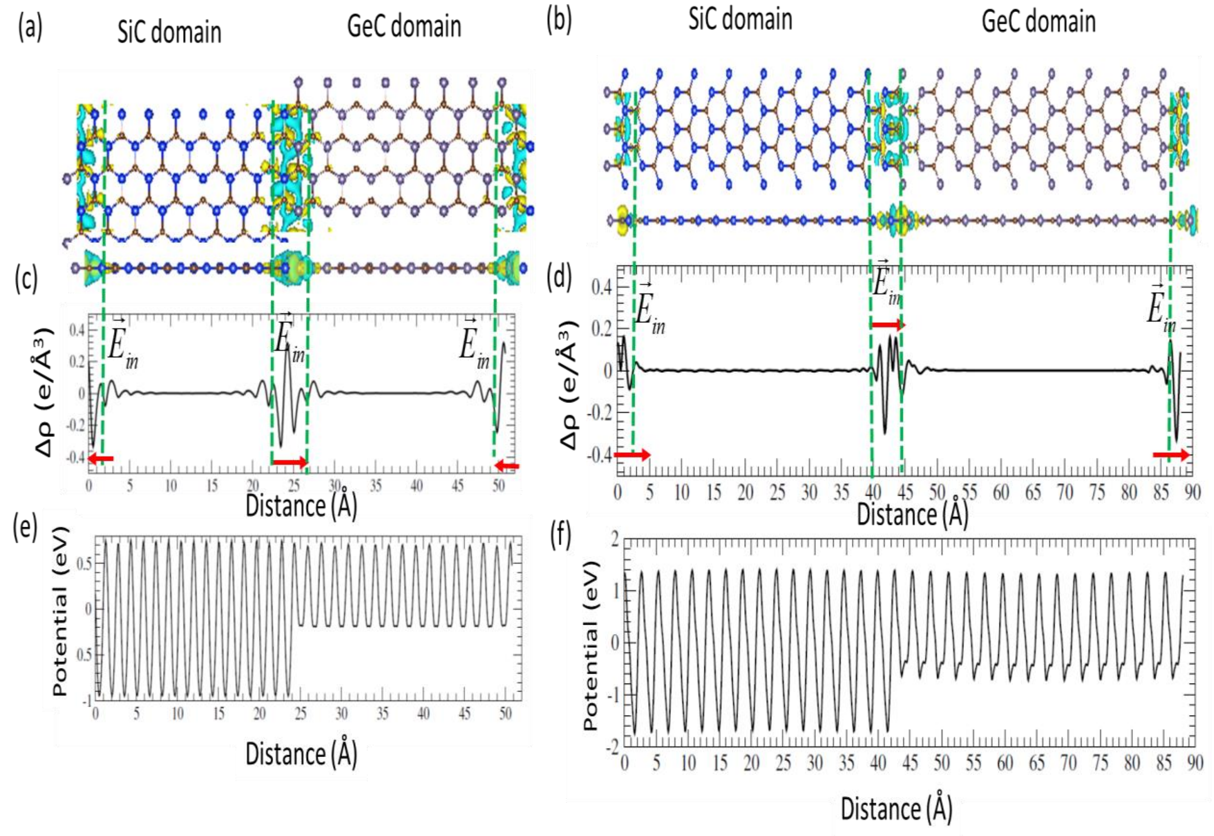

Figure 4-22: (a) and (b) show the top (upper) and side (bottom) views of differential charge densities (DCD) of 16x1 SiC/GeC lateral heterostructures with AC (a) and ZZ (b) interfaces. The electron accumulation and depletion are represented by the yellow and blue contours (with the isosurface of 2.0 x10^{-4}e/$Å^3$). The C, Si, Ge atoms are noted by brown, blue, and grey spheres, respectively. (c) and (d) show the plane-averaged DCD ($\Delta\rho$) along the surface of the 16x1 SiC/GeC lateral heterostructures with AC (c) and ZZ (d) interfaces, respectively. The interface region is highlighted by green-dashed lines and the build-in electric field is indicated by the red arrows. (e) and (f) show the plane-averaged electrostatic potential along the surface of the 16x1 SiC/GeC lateral heterostructures with AC (e) and ZZ (f) interfaces, respectively.

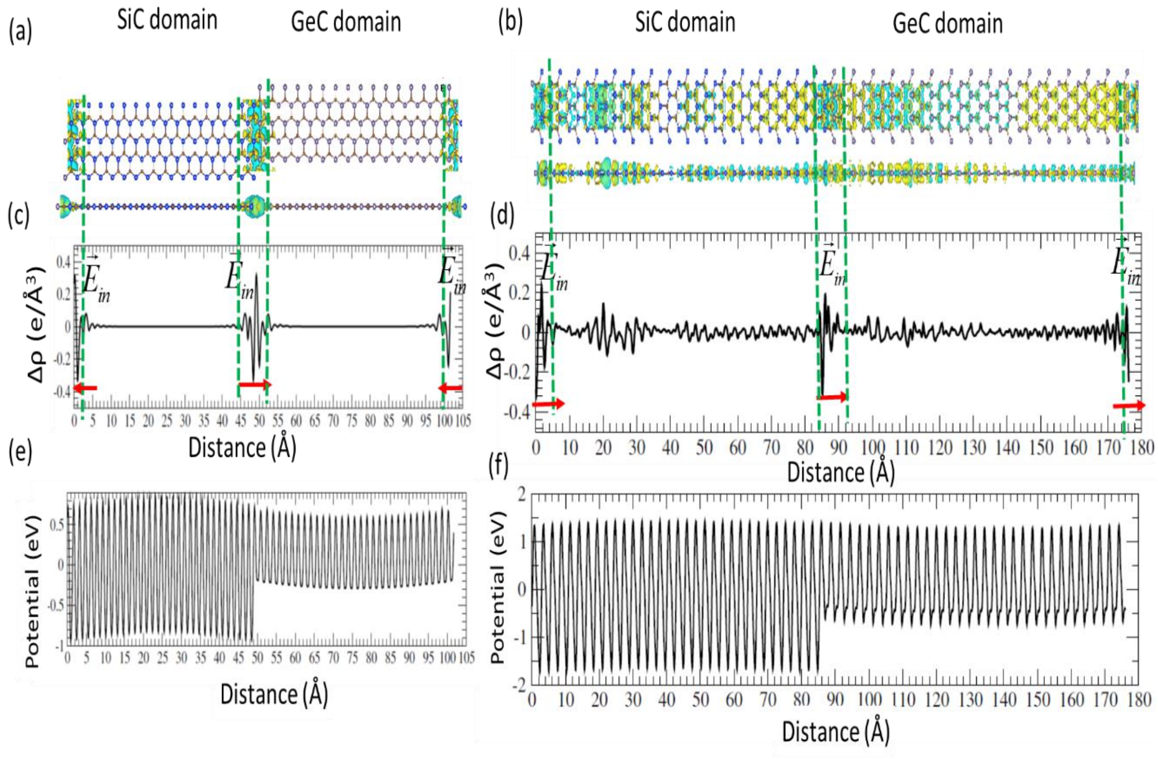

Figure 4-23: (a) and (b) show the top (upper) and side (bottom) views of differential charge densities (DCD) of 32x1 SiC/GeC lateral heterostructures with AC (a) and ZZ (b) interfaces. The electron accumulation and depletion are represented by the yellow and blue contours (with the isosurface of 2.0 x10^{-4} e/Å^3). The C, Si, Ge atoms are noted by brown, blue, and grey spheres, respectively. (c) and (d) show the plane-averaged DCD ($\Delta\rho$) along the surface of the 32x1 SiC/GeC lateral heterostructures with AC (c) and ZZ (d) interfaces, respectively. The interface region is highlighted by green-dashed lines and the build-in electric field is indicated by the red arrows. (e) and (f) show the plane-averaged electrostatic potential along the surface of the 32x1 SiC/GeC lateral heterostructures with AC (e) and ZZ (f) interfaces, respectively.

Furthermore, the plane-averaged differential charge density ($\Delta\rho$) along the surface of LH (perpendicular to the interface, see (c) for the AC interface in Figure 4-20 - Figure 4-23, and (d) for the ZZ interface in Figure 4-20 - Figure 4-23) shows a pronounced polarization. For the AC heterostructures, the electron depletion is mainly in the interfacial region at the side of the SiC domain, and the electron accumulation at the side of the GeC domain ((c) in Figure 4-20 - Figure 4-23). For the ZZ heterostructures, on the other hand, the electron depletion is mainly in the interfacial region at the left sides of the SiC and GeC domains, and the electron accumulation at the right side of the SiC and GeC domains ((d) in Figure 4-20 - Figure 4-23) . This redistribution of net charge density leads to a net charge flow with a quantitative charge transfer of ~ 0.3 $|e|$ between the adjacent domains, about two order in magnitude larger than that found in the SiC/GeC VH [92]. Such amount of charge transfer between the SiC and the GeC domains can be linked with the atomic electronegativity values of domains and lead to a built-in electric field (E_{in}) in the interfacial region (indicated by the red arrow between the green-dashed lines), analogue to the SiC/GeC bilayer [92]. Interesting finding from the DCD analysis is that the orientation of the built-in electric field strongly depends on the bonding nature at the interface. Since the bonding nature at the AC interface shows an alternative alignment of Si-C and Ge-C bonds (Fig. 4-1 1 (a)), and the most net electron deplete (accumulate) at the edge of the SiC (GeC) domain, the built-in electric fields at two edges of the domains point to the GeC domain (see (c) in Figure 4-20 - Figure 4-23). While, since bonding nature at the ZZ interface shows the Si-C bonds aligned at one edge and the Ge-C bonds aligned at the other edge (Figure 4-1(b)), the built-in electric fields at two edges of the domains point to the same direction (see (d) in Figure 4-20 - Figure 4-23). The type of induced built-in electric field in the AC heterostructures will play a role in hindering the recombination of photo-generated electron-hole pairs, demonstrating another advance feature of the 2D lateral polar heterostructures and paving a pathway for functional design of photoelectronic nanodevices. The built-in electric field in ZZ heterostructures, on the other hand, will behave differently. Since this type of induced built-in electric field at the edges of the domains will align on the same direction and will accelerate the transfer of photo-excited electrons in both SiC and GeC domains to the same direction, forming an in-plane charge flow in the whole lateral heterostructure.

The electrostatic potential profile along the surface of hybrid SiC/GeC lateral polar heterostructures, obtained by solving the Poisson equation[127], is depicted in Figure 4-20 - Figure 4-23 (e) and (f) for 4x1, 8x1,16x1, and 32x1 heterostructures, respectively. The potentials oscillate around atoms with different average values at SiC and GeC domains (indicated by the red-dashed lines). The potential at the SiC domain is deeper than that at the GeC domain, leading to a relative potential drop (ΔV) between the SiC and GeC domains for all patterns (~0.9 eV for AC interface and ~1.5 eV for ZZ interface), which is a rather weak comparable to SiC/GeC VH [92] and other 2D hetero-bilayers [100, 128-133]. Such potential drop supports the existence of a built-in electrostatic field across the interfacial region which may affect carrier dynamics and will certainly enhance electron-hole separation for AC heterostructures. Therefore, by hybridizing monolayers of SiC and GeC, a *p–n* junction with a potential drop of ~0.9-1.5 eV can be formed between the two domains, and different fascinating features can be developed.

4.6.3. Work function and band alignment

The work function of the structures ϕ, a significant parameter to control the field-emission properties of 2D optoelectronic devices, is listed in the 2nd column of Table 4-3 and shown in Figure 4-24. The small work function offset between strained SiC and GeC domains (~0.04-0.06 eV) might not easily block electrons flow from SiC domain to GeC domain when two sheets are stitched. The work function of the SiC/GeC-LH, on the other hand, depends on the interface and the domain size ranging from 3.7709 eV to 3.8161 eV. The shifts of VBM and CBM bands with respect to the vacuum level are depicted in Figure 4-24 and listed in Table 4-3. The VBM and CBM band of the pristine SiC sheet moves down by ~ 0.014-0.023 eV and ~ 0.133-0.167 eV, respectively, when the sheet is uniaxially stretched by 2.94%. The CBM of the pristine GeC monolayer lifts by ~0.081 eV and the VBM moves down by ~ 0.015 eV under the compressive strain of 2.67%. Therefore, the band offset is slightly reduced under the strain which will further modulate the band gap when the two sheets are coupled.

The coupled system, however, has its conduction/valence bands moved down/up with respective to the levels of individual SiC or GeC monolayers, demonstrating a modulated band gap (wider than that of pristine GeC sheet but narrow than that of the pristine SiC sheet) under the synergistic effect of the interface, the uniaxial strain, and the size of the domains (as illustrated on Figure 4-24 and Table 4-3). Such variation in the band gap reflects the strong effects of the bonding nature at the interface and the quantum confinement, providing a fascinating method to engineer the band gap and design new-generation nano-electronic devices. As discussed in section 4.6.1., for the SiC/GeC-LH with the AC interface, the direct band gap of the compressed GeC sheet is preserved at the GeC domain, and the indirect band gap nature of expanded SiC sheet along AC direction is preserved in SiC domain. While, in the system with the ZZ interface, the direct band gap nature of compressed (expanded) GeC (SiC) sheet is preserved in both domains (see Figure 4-9 and Figure 3-8). Comparing the positions of VBM and CBM bands levels (Figure 4-11 - Figure 4-18, and Figure 4-24), it was found that the band alignment of SiC/GeC-LH is analogous to a straddling gap (type-I) which are useful for applications in LED and laser *etc*. Furthermore, the AC heterostructures with the help of the built-in electric field at the interfaces could separate photo-excited electrons and holes which are useful for the application of photovoltaic devices. The band gap of the SiC/GeC-LH is still larger than the minimum of 1.230 eV required for the photocatalysis reactions, showing its potential appealing application for visible light photocatalyst and water splitting to achieve clean and renewable energy [89, 134].

Table 4-3: The work function and VBM (CBM) band levels (with respect to the vacuum) of pristine SiC and GeC monolayers with/without strain and the SiC/GeC-LH with different interface and size of domain.

Systems	**WF (ϕ) (eV)**	**E_{VBM} (eV)**	**E_{CBM} (eV)**
GeC (pristine)	3.8205	-4.8526	-2.7883
GeC (uniaxial compression)	3.7877	-4.8680	-2.7074
SiC (pristine)	3.7519	-5.0300	-2.4739
SiC (uniaxial expansion along ZZ)	3.8252	-5.0435	-2.6069
SiC (uniaxial expansion along AC)	3.8441	-5.0527	-2.6356
GeC/SiC 1x4 (AC)	3.7923	-4.9313	-2.6532
GeC/SiC 1x4 (ZZ)	3.7913	-4.9304	-2.6522
GeC/SiC 1x8 (AC)	3.7928	-4.9192	-2.6663
GeC/SiC 1x8 (ZZ)	3.7838	-4.9004	-2.6671
GeC/SiC 1x16 (AC)	3.7844	-4.8857	-2.6831
GeC/SiC 1x16 (ZZ)	3.8161	-4.903	-2.7292
GeC/SiC 1x32 (AC)	3.7709	-4.8438	-2.698
GeC/SiC 1x32 (ZZ)	3.7798	-4.8487	-2.7109

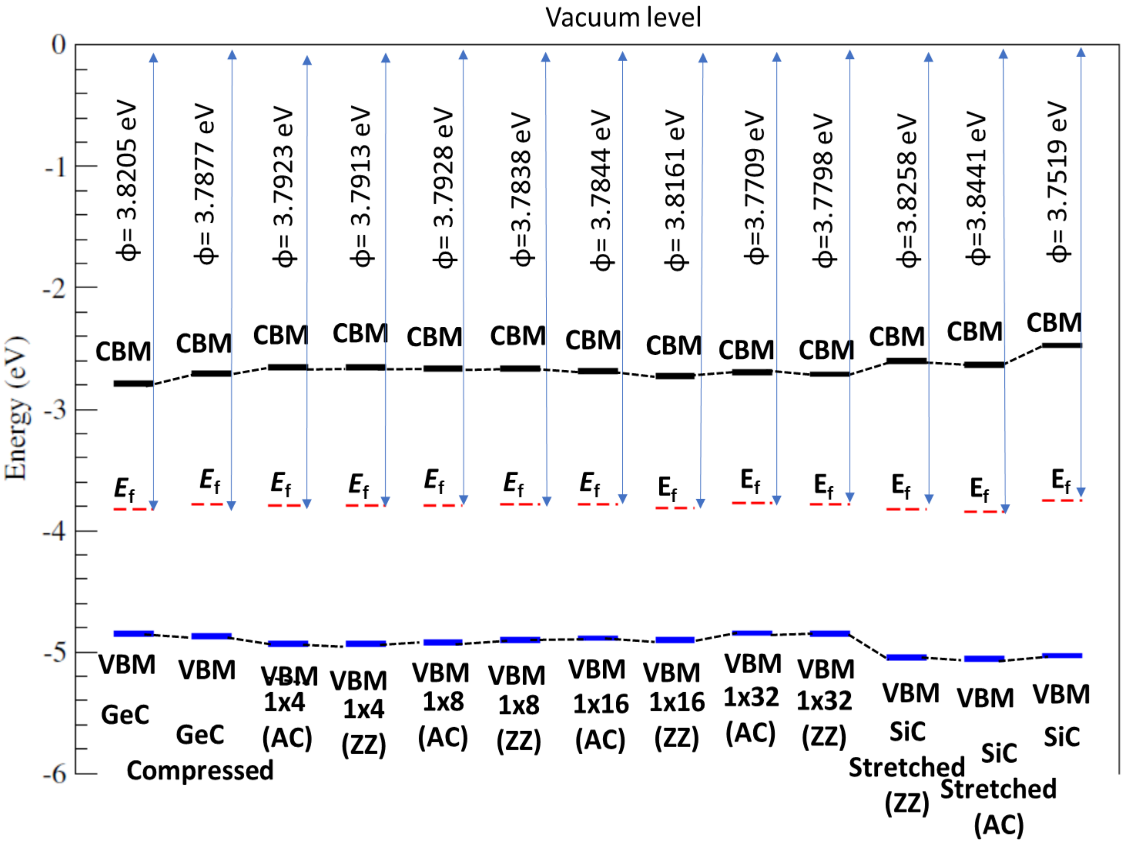

Figure 4-24: Schematic illustration of the band alignment of the 2D SiC/GeC-LH with different interface and domain size, together with the pristine SiC and GeC (with/without strain) monolayers related to the vacuum level. Absolute energy levels of VBM and CBM for those structures are denoted by the blue and black lines, respectively. The corresponding Fermi levels are denoted by red dashed lines. Blue and black dashed lines connecting these steps indicate the energy shift when the material is reshaped (in the case of pristine SiC and GeC monolayers) or re-arranged (in the case of the SiC/GeC hybrid LH).

4.7. 2D SiGe/GeC-LH (structural properties)

Since there exists over 17% large lattice mismatch in SiGe/GeC-LH and the competition of chemical bonding at the interface, the stability of such LH is a critical issue. To have a comprehensive understanding the structural stability, we have carried out a systematic study on the relaxation process, including (i) releasing the degrees of freedom only for atoms (e.g., ISIF=2 in the VASP code), (ii) releasing the degrees of freedom on the atoms and the volume (e.g., ISIF=4 in the VASP code), and releasing all the degrees of freedom on the atoms, the lattice vectors, and the volume (e.g., ISIF=3 in the VASP code), etc. Figure 4-25 (a) and (b) show the total energy/atom under various relaxation processes as a function of the lattice constant a along the interface for 1x4 AC-SiGe/GeC-LH (a) and 1x4 ZZ-SiGe/GeC-LH (b), with two different chemical bonding at each interface (see Figure 4-2 for the classification of the chemical bonding at the interface). It can be seen from the results that for 1x4 AC-SiGe/GeC-LH with Si-C/Ge-Ge bonding at the interface, the system under various relaxation processes is finally stabilized to a structure with the lattice constant a ~ 3.51 Å along the interface and the energy of -5.03 eV/atom (red squres on the red dashed line on Figure 4-25 (a)). The 1x4 AC-SiGe/CGe-LH with Ge-C/Si-Ge bonding at the interface, on the other hand, is stablized with a ~3.49 Å along the interface with the total energy/atom lower than that with Si-C/Ge-Ge bonding (green and blue triangles at green dashed line on Figure 4-25 (a)). Oppositely, the energy of the 1x4 ZZ-SiGe/GeC-LH with Si-C/Ge-Ge bonding at the interface gradualy decreases with decreasing the lattice constant (see Figure 4-25 (b)), and then sharply drops to the stage where the layered structure is totally distored (e.g., see the structures of 1x4 ZZ SiGe/GeC-LH at ~3.19 Å and 3.2 Å along the interface in Figure 4-25 (b) and Figure 4-26, respectvily). Similar results were also found for SiGe/GeC-LH with larger domains (e.g., n = 8, 16), indicating that $SiGe$ and GeC sheets are difficult to stich seemlessly and form 2D-LH, except 1x4 AC-SiGe/GeC-LH due to the even distrubution of chemical bonds at the interfaces on both sides of domains.

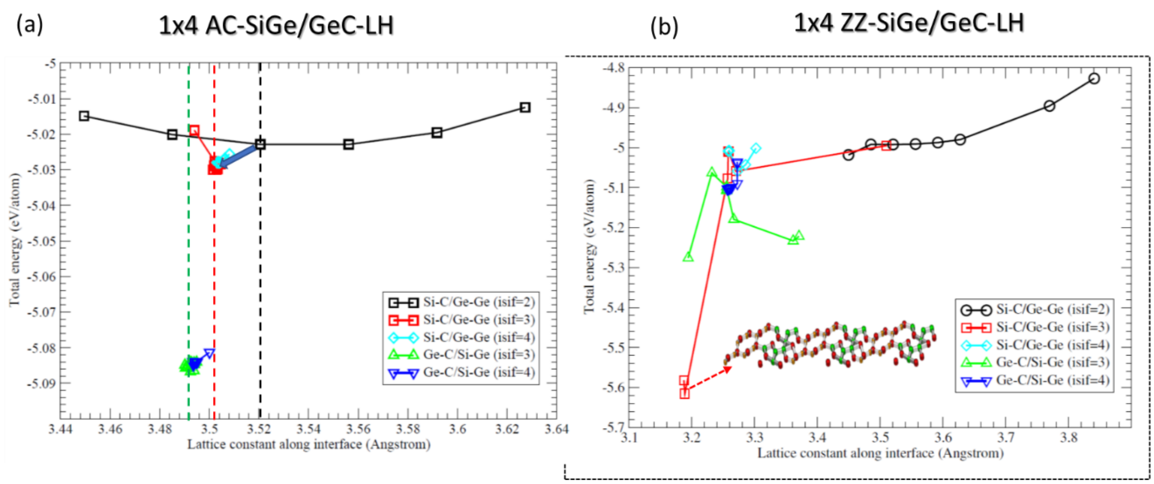

Figure 4-25: The total energy per atom versus the lattice constant along the interface for 1x4 AC-SiGe/GeC-LH (a) and 1x4 ZZ-SiGe/GeC-LH (b) (with two different types of chemical bonding at the interfaces) under various relaxation processes. The dashed black, red, and green lines denote the minimum energy under different relaxation processes for 1x4 AC-SiGe/GeC-LH. The insert on (b) shows the side view of the relaxed structure at that position.

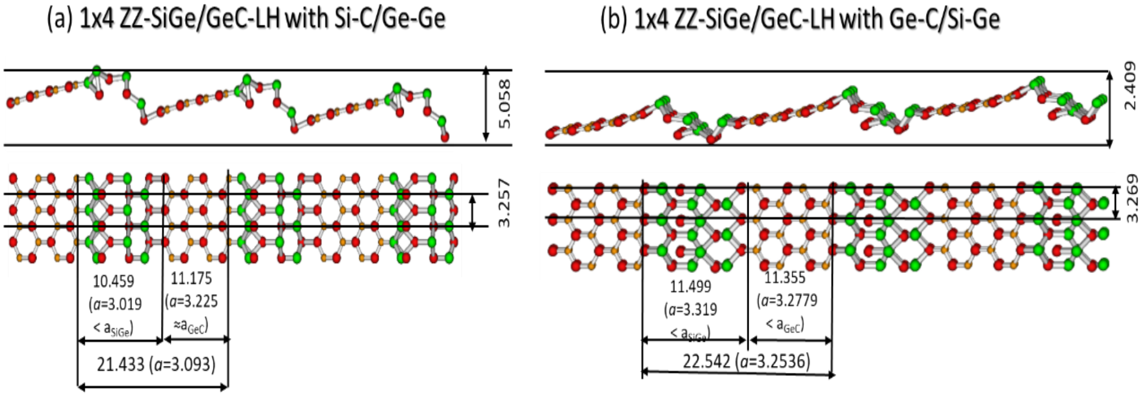

Figure 4-26: Schematic illustration of relaxed structures of 1x4 ZZ-SiGe/GeC-LH with SiC/Ge-Ge bonding (a) and Ge-C/Si-Ge bonding (b). The buckling and lattice constants along the interface and horizontal directions are indicated by numbers in Angstrom. The yellow, red, and green spheres represent C, Ge, Si atoms, respectively.

Figure 4-27 illustrates the optimized structures of AC-SiGe/GeC-LH with Si-C/Ge-Ge bonding (a) and Ge-C/Si-Ge bonding (b), respectively. Due to the large lattice mismatch induced strain, the systems are stabilized to a corrugation form where the GeC domain keeps flat, and the $SiGe$ domain maintains buckled structures, respectively. Similarly as found in 2D SiC/GeC-LH, the lattice constants along the horizontal direction in each domain almost keep the same values as in their pristine sheets, but the lattice constants along the interface are ~ 7% expansion in the GeC domain and ~11% compression in the $SiGe$ domain, demonstrating that the strain induced by the large lattice mismatch is distributed along the interface, reflecting the uniaxial strain feature in 1x4 AC-SiGe/GeC-LH.

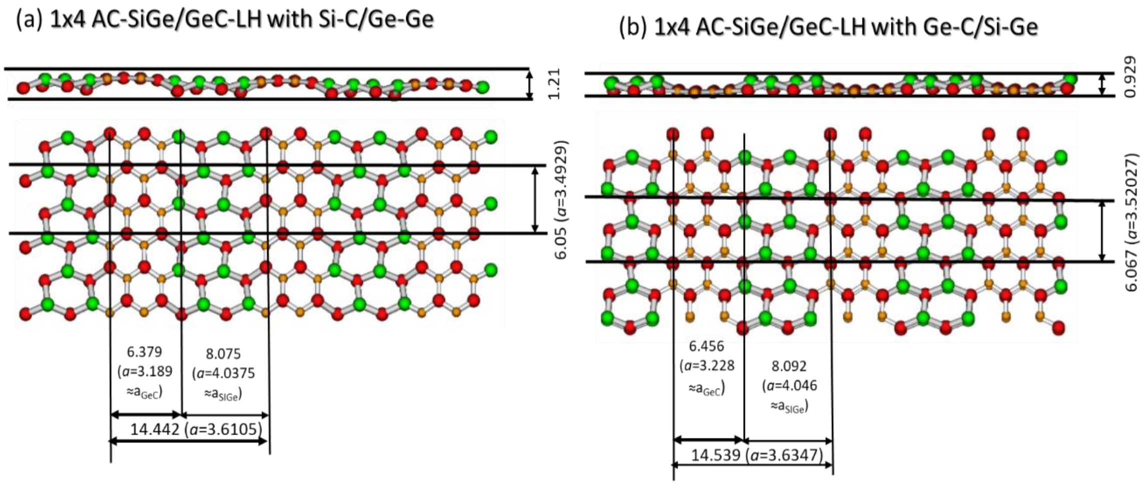

Figure 4-27 The side and top views of optimized structures of 1x4 AC-SiGe/GeC-LH with Si-C/Ge-Ge bonding (a) and Ge-C/Si-Ge bonding (b), respectively. The buckling and lattice constants along the interface and horizontal directions are indicated by numbers in Angstrom. The yellow, red, and green spheres represent C, Ge, Si atoms, respectively.

4.8. 1x4 AC-SiGe/GeC-LH (electronic properties)

In 1x4 AC-SiGe/GeC-LH, we stitched $SiGe$ sheet (metal) to GeC sheet (semiconductor) to form 2D metal-semiconductor LH and released the artificial strain due to the large lattice mismatch between the constituent strips $SiGe$ and GeC. With this designed structure, along with the artificial strain, we analyzed the charge transfer in the domains of metal ($SiGe$) and semiconductor (GeC) through a thin 1D boundary. This contact behavior is a critical key for the metal–semiconductor junctions, which affect the electronic properties that was unraveled in this section.

4.8.1. DOS and Band structures

Figure 4-27 despites the calculated band structures of 1x4 AC -SiGe/GeC-LH with Si-C/Ge-Ge bonding (a) and 1x4 AC -SiGe/CGe-LH with Ge-C/Si-Ge bonding (b) at DFT-PBE level. From there, we found that 1x4 AC-2D SiGe/GeC-LH in both types of bonding possess semiconductor nature with a direct band gap of 0.65 eV for Si-C/Ge-Ge bonding and 0.71 eV for Ge-C/Si-Ge bonding, respectively. It is well known that DFT-PBE calculations for the band structures usually underestimate the fundamental band gaps, as compared with the experimental results. Therefore, this small band gap opening obtained at DFT-PBE level is expected to be improved by applying band correction methods, such as the Heyd–Scuseria–Ernzerh of screened Coulomb hybrid functional [126] (referred as HSE06). Such calculations are computationally expensive for large systems, such as the 2D SiGe/GeC-LH studied here.

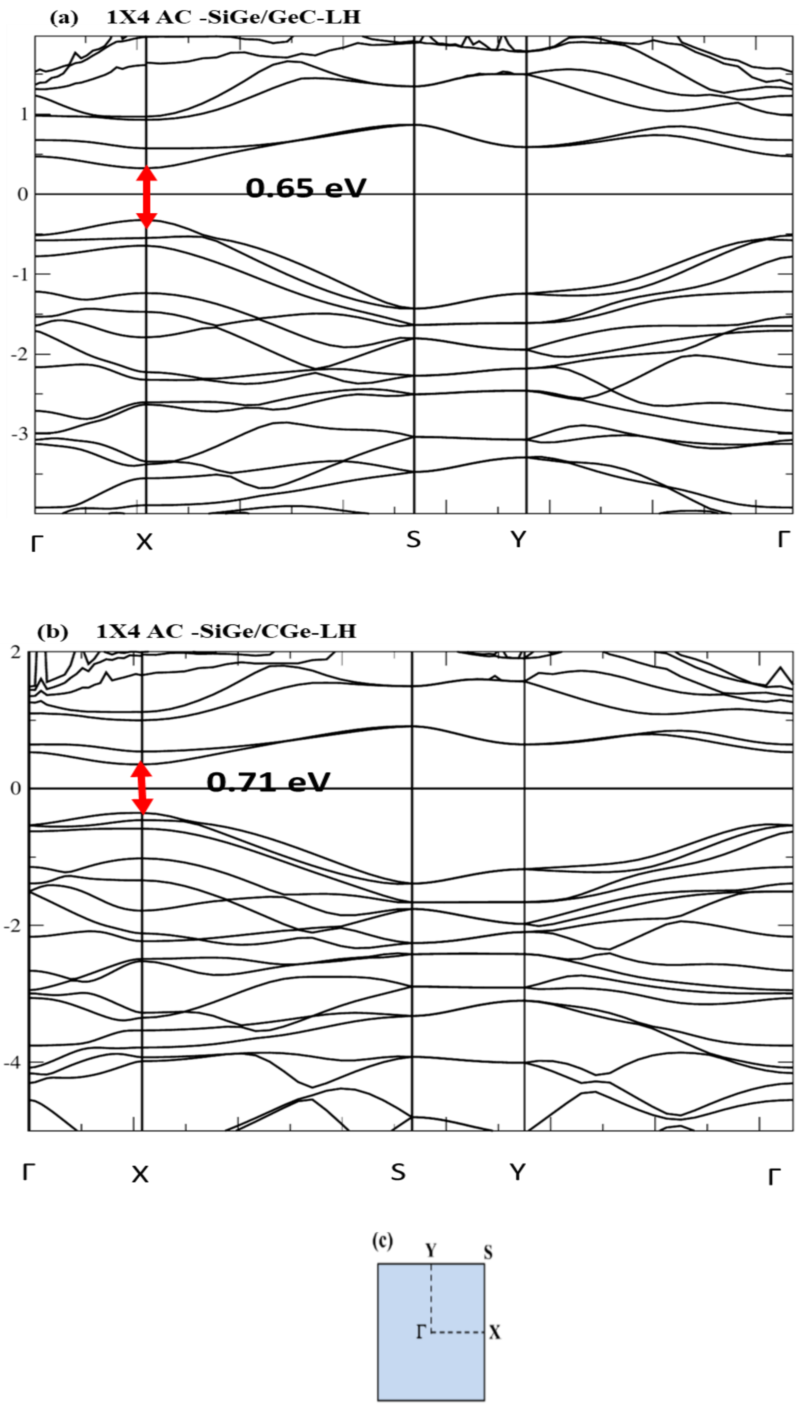
(a) 1X4 AC -SiGe/GeC-LH

(b) 1X4 AC -SiGe/CGe-LH

(c)

Figure 4-28: The band structures of 1x4 AC-SiGe/GeC-LH with Si-C/Ge-Ge bonding (a) and 1x4 AC-SiGe/CGe-LH with Ge-C/Si-Ge bonding (b). The Brillion zone is inserted (c) The red arrows denote the position of the direct band gap, and the Fermi level is set at zero.

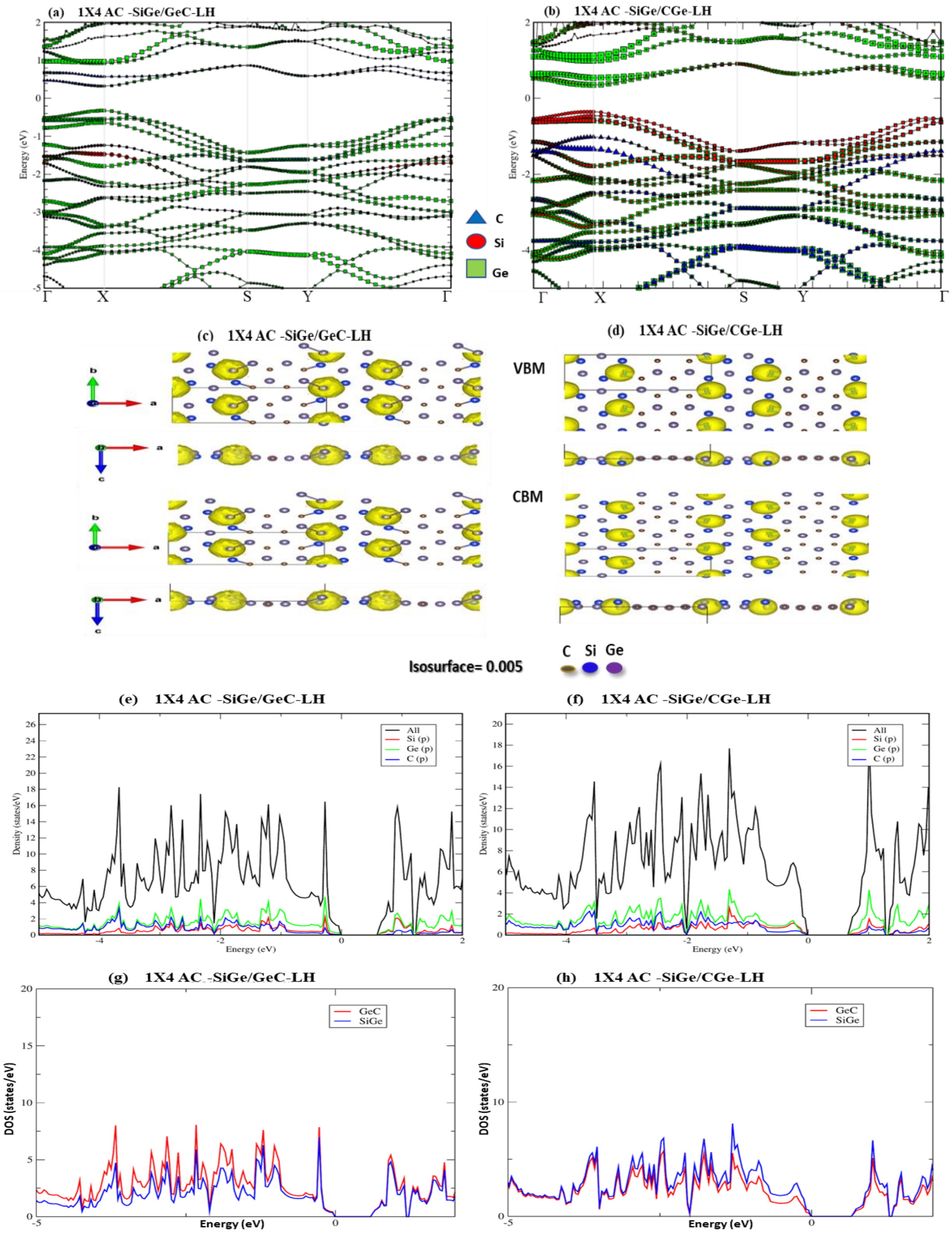

Figure 4-29: Calculated projected band structures of 1x4 AC-SiGe/GeC-LH with Si-C/Ge-Ge bonding (a) and 1x4 AC-SiGe/CGe-LH with Ge-C/Si-Ge bonding (b). (c) and (d): the corresponding top (upper) and side (bottom) views of VBM and CBM. (e)-(h): the corresponding total DOS, projected density of states (PDOS), and the local density of states (LDOS) of 1x4 2D-SiGe/GeC-LH with Si-C/Ge-Ge ((e) and ((g)) and 1x4 AC-SiGe/CGe-LH with Ge-C/Si-Ge ((f) and (h)), respectively.

Figure 4-29 shows the projected band structures; the top and side views of VBM and CBM, the projected density of states (PDOS), and the local density of states (LDOS) of 1x4 AC-SiGe/GeC-LH. From these results, we can infer that the direct band gaps in the semiconductor AC-SiGe/CGe-LH with both types of bonding at the interface are not located at Γ but at X point, similar as in the case of pristine $SiGe$; and the corresponding values are slightly depending on the bonding nature at the interface. Moreover, based on the projected band structures and the orbital isosurface analysis of VBM / CBM, we found that the most contribution of VBM / CBM is from Ge-4p orbitals (green squares/curve) and Si-3p orbitals (red circles/curve). Thus, such band gap is located in the $SiGe$ domain near the interface. This nature is further confirmed from DOS and LDOS, demonstrating that a band gap can be opened in the $SiGe$ domain when stitching it to GeC domain.

4.8.2. Charge density and Differential of charge density (DCD)

We conduct Bader charge analysis to better understand atomic charge density and charge transfer between domains of 1x4 AC-SiGe/GeC-LH, where the quantitative results are listed in Table 4-4. It was found that there is a charge transfer of 0.0618 e between Si and Ge in the pristine $SiGe$ sheet and a charge transfer of 1.362 e between Ge and C in the pristine GeC sheet. The different amount of the charge transfers in the $SiGe$ and GeC sheets is mainly due to their different electronegativities (see the inserted table in Figure 4-30). Such charge transfers still hold on the GeC domain and on $SiGe$ domain of 1x4 AC-SiGe/GeC-LH with Si-C/Ge-Ge bonding. However, the scenario is different on $SiGe$ domain of 1x4 AC-SiGe/CGe-LH with Ge-C/Si-Ge bonding, where both Ge and Si lost charge of 0.1 -0.2 e. Interesting finding from the charge transfer analysis is that although the behavior of charge transfer of the $SiGe$ domain is different from the pristine $SiGe$, over all, there is still a net charge transfer from the $SiGe$ domain to the GeC domain in all kinds of bonding at 1x4 AC-SiGe/GeC-LH (see Figure 4-30), which is similar to the behave of the net charge transfer of 2D SiC/GeC-LH.

Table 4-4: Bader charge analysis (in the unit of e/atom) of the charge transfer between Si, Ge, and C atoms in the pristine $SiGe$ and GeC monolayers and the 2D SiGe/GeC-LH with different chemical bonding. There are two types of Ge atoms: one is at the $SiGe$ domain (denoted by $Ge\,(SiGe)$), and the other is at the GeC domain (denoted by $Ge\ (GeC)$). The net charge per atom in GeC and $SiGe$ domains are listed in the 6th and 7th columns, respectively.

Systems	Ge (GeC) (*e*/atom)	C (*e*/atom)	Ge (SiGe) (*e*/atom)	Si (*e*/atom)	GeC (*e*/atom)	SiGe (*e*/atom)
GeC	1.362	-1.362	-	-	0	-
SiGe	-	-	-0.0618	0.0618	-	0
SiGe/CGe (AC)	0.323	-0.41905	-0.65014	0.7462	-0.096	0.096
SiGe/GeC (AC)	0.9855	-1.29986	0.2444	0.07	-0.3144	0.3144

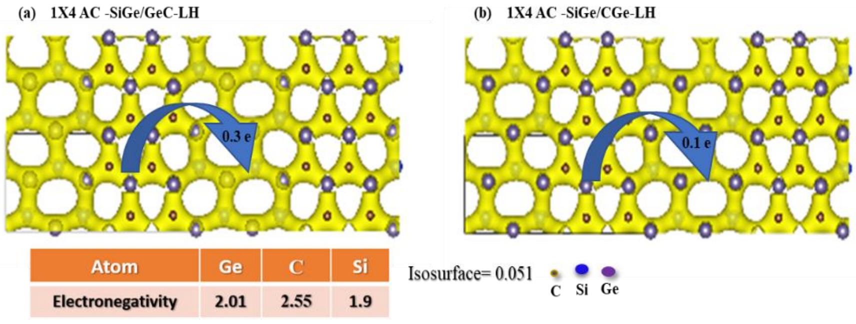

Atom	Ge	C	Si
Electronegativity	2.01	2.55	1.9

Figure 4-30: The charge density contours of 1x4 AC-SiGe/GeC-LH with Si-C/Ge-Ge bonding (a) and 1x4 AC-SiGe/CGe-LH with Ge-C/Si-Ge bonding (b), respectively. The blue arrows denote the net charge transfer from the $SiGe$ domain to the GeC domain.

The DCD (i.e., the net charge redistribution between 2D material domains) illustrated in Figure 4-31 characterize the interfacial hybridization of the 2D 1x4 AC-SiGe/GeC-LH. The net electron accumulation and depletion are shown by the yellow and blue contours, respectively. Clearly, most net electron redistribution is located at the interface region, induced by the coupling between $SiGe$ and GeC domains, and is sensitive to the type of interface and the boding nature, reflecting the degree of the hybridization of orbitals between adjacent domains. Furthermore, as shown in Figure 4-31, the net charge redistribution solely locates at the interfacial region and GeC domain for the AC interface, with the net electrons depleting around the Si and Ge atoms and accumulating around C atoms. Such net charge transfer from the $SiGe$ domain to the GeC domain, therefore, forms in-plane dipoles along the interface.

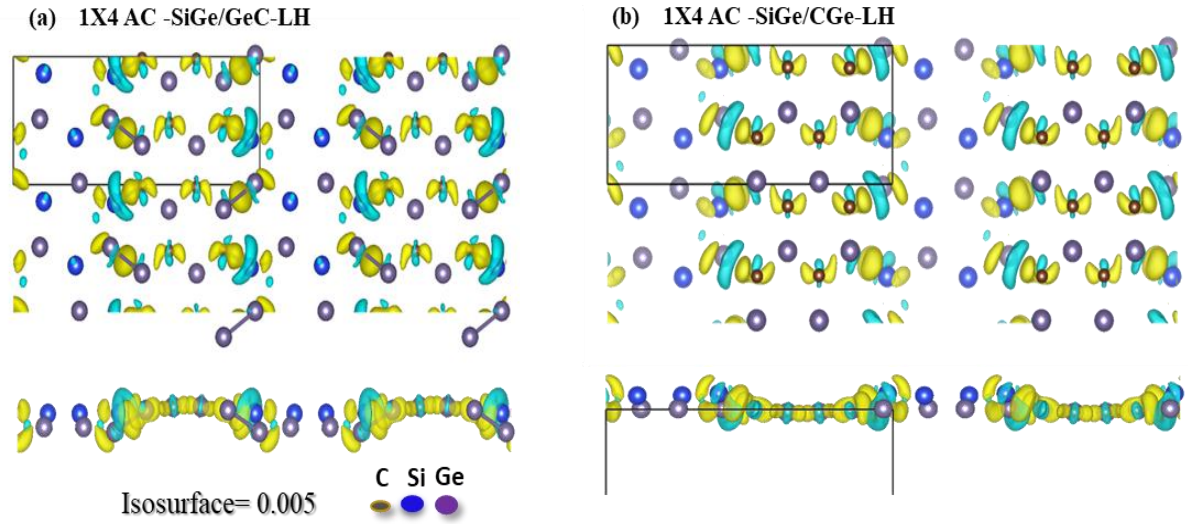

Figure 4-31: The DCD of 1x4 AC-SiGe/GeC-LH with Si-C/Ge-Ge bonding (a) and 1x4 AC-SiGe/CGe-LH with Ge-C/Si-Ge bonding (b) with the isosurface value of 0.005 e/Å^3. The electron accumulation (depletion) is denoted by the yellow (blue). The black boxes denote the supercell.

4.9. Commensurate 2D 5x4 SiGe/6x4 GeC-LH

The results of deformed 2D SiGe/GeC-LH for 1x4 ZZ SiGe/GeC-LH and others with larger domains due to large mismatch trigged us to consider 2D SiGe/GeC -LH with commensurate domains to reduce the large lattice mismatch between 2D pristine $SiGe$ and GeC (i.e., ~0.7 Å). To achieve such commensurate lattice and reduce the strain, we considered supercells with the sizes of 5x4 and 6x4 for $SiGe$ and GeC domains, respectively. In such case, the lattice mismatch is much reduced to ~0.1548 Å which is close to the small lattice mismatch in 2D SiC/GeC-LH (see section 4.5.1).

Structurally, we designed four types of commensurate 2D 5x4 SiGe/6x4 GeC-LH with different interface and bonding nature. Namely, the commensurate AC and ZZ SiGe/GeC-LH with Ge-Ge bonding at the interfaces (left panels on Figure 4-32) and the commensurate AC and ZZ SiGe/CGe-LH with Si-Ge or Ge-C bonding at the interfaces (see right panels on Figure 4-32). It is noted that even though the lattice mismatch is reduced significantly, the significant difference in the bond lengths between Si, C, and Ge will produce lots of dangling bonds at the interfaces in the commensurate structures. Such dangling bonds are fatal in stabilizing the commensurate structures. As shown in Figure 4-32, after performing a full relaxation (without any restriction on degrees of freedoms for atoms, lattice vectors, and volume, i.e., set the tag ISIF=3 in VASP code), most commensurate structures crashed and were finally stabilized to a bulk-like-structure with strong interlayer interaction, except the commensurate LH with Ge-Ge bonding at the ZZ interface, which still keeps 2D layered structure (see the left-bottom panel on Figure 4-32). These results point out that the dangling bonds at the interfaces of the commensurate LH structures indeed generate local defects and lead to such LH unstable.

The commensurate LH with Ge-Ge bonding at the ZZ interface, on the other hand, could produce pentagons and minimize the dangling bonds in stabilizing the system.

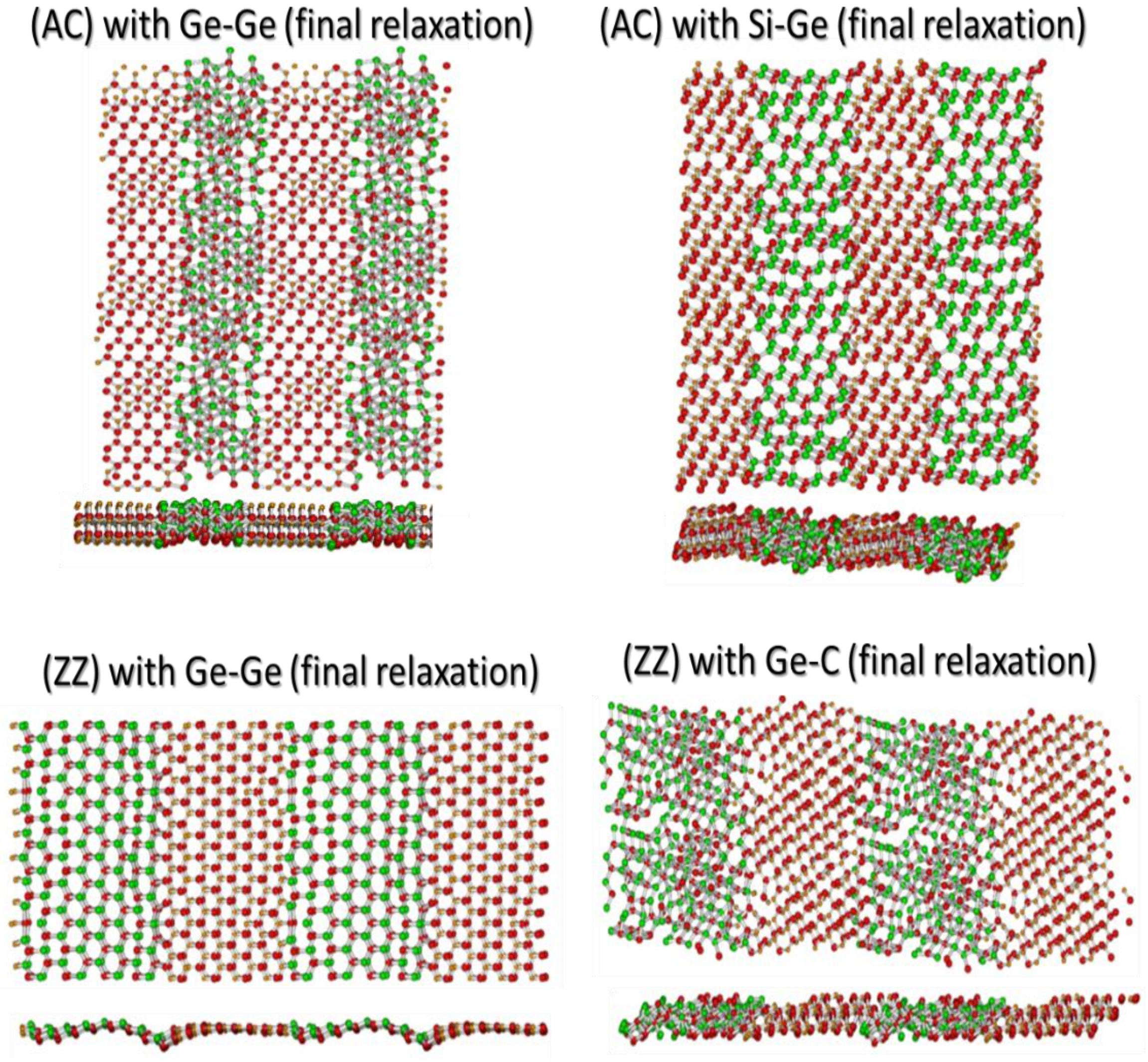

Figure 4-32: The top and side views of relaxed structures of commensurate 5x4 SiGe/6x4 GeC-LH with Ge-Ge bonding at the AC and ZZ interfaces (left panels) and SiC/GeC bonding nature at AC/ZZ interfaces (right panels), respectively. The yellow, red, and green dots represent C, Ge, Si atoms, respectively.

4.10. Conclusion

The fundamental aspects of 2D SiC/GeC-LH and 2D SiGe/GeC-LH have been systematically studied at the first-principles level. The characteristics of such 2D polar LH are correlated to the lattice mismatch induced strain, the chemical bonding nature at the interface, the size of domain induced quantum confinement, and the electronegativity induced in-plane charge transfer in each domain. The synergistic effect of these factors leads to several interesting phenomena, charactering the unique properties of the 2D SiC/GeC~~,~~ and 2D SiGe/GeC polar LHs.

First, the fully relaxed 2D SiC/GeC polar LHs are stabilized in the flat format, and the small lattice mismatch induced strain in two domains is distributed along the interface direction. While the large lattice mismatch in 2D SiGe/GeC-LH leads unstable structures, except those with the smallest domain (e.g., 1x4 SiGe/GeC-LH). It was found that induced strain mainly spread along the interface, resulting uniaxial strain. Thus, each constituent domain in 2D polar LHs almost keeps its pristine structure inside the domains and with extension/compression mainly directed along the interface.

Second, the designed 2D polar LHs can adjust the nature of the band structures and each type of interface can persevere a certain nature of the band structure of one of the constituent domains. Namely, an indirect band gap nature was found in AC-SiC/GeC-LH which is a characteristic of SiC, a direct band gap nature was found in ZZ-SiC/GeC-LH which is a characteristic of GeC, a semiconductor nature with direct band gap was found in 1x4 AC- SiGe/GeC-LH which is a characteristic of GeC . Furthermore, the band gap can be modulated by tuning the domain size, the chemical bonding nature at the interface, and type structure of designed interface.

Third, a net charge transfer was found from the SiC or $SiGe$ domain to the GeC domain in 2D SiC/GeC polar LHs or 2D SiGe/GeC polar LHs, respectively. Triggered by the in-plane charge transfer, such net charge transfer leads to a lateral spontaneous p-n junction, characterizing the unique property of 2D polar LHs.

Fourth, the net charge redistribution was found solely locating at the interfacial region with the net electrons depleting around the Si and Ge atoms and accumulating around C atoms, forming in-plane dipoles along the interface. The plane-averaged charge density difference ($\Delta\rho$) along the surface of LH shows a net charge flow with a quantitative charge transfer of ~ 0.3 |e| between the adjacent domains. Such amount of charge transfer will lead to a built-in electric field in the interfacial region and will play a role in hindering the recombination of photo-generated electron-hole pairs. These unique features imply the promising application of the 2D polar LH, beyond the vdW heterostructures, for visible light photocatalyst, photovoltaics, and water splitting to achieve clean and renewable energy.

CHAPTER V

5. VERTICAL HETEROSTRUCTURE OF 2D POLAR BINARY COMPOUNDS: (SiGe/GeC)

5.1. Introduction

Recently, layer-by-layer staking of 2D materials to form vertical heterostructure governed by weak interaction in between the adjacent layers have attracted scientists in nanomaterials science. These 2D heterostructures appear appealing performance in electronic and optoelectronic applications besides their novel phenomena, such as ultrafast charge transfer in MoS_2/WS_2 heterostructures [135] and self-similar Hofstadter butterfly states in graphene/h-BN heterostructures [136]. Moreover, wide range of 2D crystals and their heterostructures have been successfully fabricated, e.g., transition metal dichalcogenides (TMDs), the hexagonal boron nitride (h-BN), metal chalcogenides, phosphorene, MXenes, layered oxides, etc. [111, 137-142]. They have been extensively applied to vital applications such as nanoelectronics, excitonic solar cells, digital data storage, optoelectronics, spintronics and opto-spintronics, ferroelectronics, energy storage, sensor, electrocatalysis, heat transfer, brain-inspired computing, etc. [90, 91, 97, 98, 109, 113, 143-145].

The aforementioned 2D materials and their heterostructures have been classified into 2D-vdW material and 2D-vdW heterostructures (vdW-H) due to their possession of vdW interaction. An interesting finding is that the physical and electronic properties of vdW-H are sensitive and differ radically with any changing of the number of stacking layers, stacking pattern, strain level, applied electric field, etc. [112, 146-148].

Different from 2D-vdW materials, there are other types of 2D materials that have no layered vdW bulk counterparts and possess a chemical bonding nature similar to their bulk counterparts, such as the SiC, GeC, and $SiGe$ monolayers. In fact, the SiC monolayer is considered as more ionic-like covalent bonding [84] while GeC monolayer as less ionic-like covalent bonding [149, 150]. Therefore, they are classified as 2D polar materials. Motivated by the effect of the electrostatic force triggered by such in-plane charge transfer, this project aims to design a VH build by 2D polar monolayers. In fact, this work intended to investigate the role that plays by such electrostatic interaction, compared to the vdW interaction, in stabilizing such hybrid heterostructures and influencing their electronic properties.

To unravel such interesting phenomena, this project has been conducted as a comprehensive theoretical study on such 2D polar heterostructures, focusing on the commensurate SiGe/GeC hybrid bilayer to study the stability and electronic properties governed by the stacking configuration and the out-of-plane interaction on these heterostructures.

5.2. Vertical Heterostructure (VH) verses Lateral Heterostructure (LH)

The most two popular classes of heterostructure are VH and LH, depending on the direction of the construction. The LH is formed when the constituent sheets stitch along in-plane direction [9-19]; while the VH is made of a combined constituent sheets along out-of-plane direction. Accordingly, there are essential differences between VH and LH.

First, the interface effect originates mainly from the week inter-layer chemical bonding, i.e., vdW or weak electrostatic interaction, in 2D-VH, while it comes from the strong intra-layer chemical bonding, i.e., ionic or covalent bonds within the plane, in 2D-LH. Therefore, this variation in dominated chemical bonding at the interface is strongly reflected on the variation in chemical and physical properties of the two types of 2D-H.

Second, the interface in 2D-VH is a 2D infinite surface, but a 1D thin line is in 2D-LH. Then, different dimensionality and size of the interface play a key role in determine the distinct characteristics for each type of HS.

Third, the lattice mismatch, which is the main source of the strain induced effect, can be tunable by changing the way of assembly, for it can be maximized and spread on the surface to introduce a strain all over the surface in the 2D-VH, or it can be minimized around the interface to introduce a local strain in 2D-LH, which can be accounted for different properties between 2D-VH and 2D-LH.

Forth, the construction nature enhances the electrons' confinement into different layers of 2D-VH, but, in contrast to 2D-VH, it enhances the efficiency of the carriers' mobility in 2D-LH.

Finally, 2D-VH is easier to fabricate, whereas fabricate 2D-LH is difficult and has limitations. Table 5-1 summarizes the main differences between 2D-VH and 2D-LH.

Table 5-1: The main differences between 2D-VH and 2D-LH

2D-VH	2D-LH
Interface effect comes from the weak inter-layer bonding	Interface effect comes from the strong intra-layer bonding
Interface effect is on the surface (2D infinite surface)	Interface effect is at the boundary (1D thin line)
Enhances confinements of electrons in different constituents	Enhance the efficiency of carriers' mobility
Lattice mismatch effect is spread on each surface	Lattice mismatch effect induced local strains depend on different domains on the plane
Easy to fabricate	The fabrication has limitations

5.3. Effects under study (Interlayer interaction –Species stacking pattern)

It is well known that vdW interaction plays a leading role between adjacent layers in 2D vertical heterostructures. However, the electrostatic force in 2D polar materials, such as $SiGe$ or GeC monolayer, has a significant impact by triggering the in-plane charge transfer between elements. Its influence may be extended to the interlayer in 2D-VH built by such 2D polar materials. Trigged by this interesting premise, this work aimed to study and understand the role plays by both the interlayer weak interaction (i.e., the vdW) and electrostatic interlayer-bonding, in stabilizing such hybrid heterostructures and influencing their electronic properties (e.g., SiGe/GeC hybrid VH).

Equally important, the quantity and direction of in-plane charge transfer depend on the interaction between elements, so it important to investigate the arrangement of the charged atoms in adjacent layers when designing 2D polar VH. Namely, the system under study will be utilized to a commensurate structure with different species stacking pattern depending on the arrangement of the charged atoms. For instance, in constructing SiGe/GeC-VH, there are four types of species arrangements. They are classified into two groups, referred as the C-group (i.e., patterns I and II) and the Ge-group (i.e., patterns III and IV), respectively. In pattern I/II (i.e., in C-group), C atom in GeC sheet has been stacked on the top of Ge/Si atom in $SiGe$ sheet, respectively, while in pattern III/IV (i.e., in Ge-group), Ge atom in GeC sheet has been stacked on the top of Ge/Si atom in $SiGe$ sheet, respectively. The chemical interlayer-bonding varies between different atoms, i.e., C, Ge, and Si, in different pattern, and it may inspire the physical properties of the system, which was investigated and addressed in this work.

5.4. Commensurate supercell

In material science, designing an ideal VH is not an easy task since it requires a joint supercell that composed from two different constituent of unit cells. Experimentally, the growth of the joint supercell will be gained, after a chemical bonding competitive with strain induced by lattice mismatch, when the system reaches out the energy minimization. Besides, the weak interaction between layers makes the system tends to minimize the strain within the layer and allows incommensurately growth. In contrast, the ideal joint supercell in theoretical computations requires commensurate unit cells, i.e., the unit cell that has small number of atoms and weak strain. Therefore, producing joint supercell manually is not an easy task if the two-unit cells are different geometrically, for example, the case of producing SiGe/GeC VH in this project.

According to the results in Chapter 3, GeC and $SiGe$, the two constituents of SiGe/GeC VH, have different lattice constants (3.267 Å and 3.951 Å, respectively). Hence, this relatively large lattice mismatch (17%) induces large artificial strain in constructed SiGe/GeC VH which may cause stress or defect at the interface. As we found in Chapter 4, such large artificial strain led to unstable structures when forming SiGe/GeC-LH. Thus, we need to construct commensurate SiGe/GeC-VH to reduce this type of large strain. For such purpose, we adopted the method that implemented in the Cell Match code produced by Predrag Lazic [151]. For a given pattern, the Cell Match code searches within a given combinatorial space (e.g., 1%) and sorts the results by the strain imposed on one crystal (e.g., GeC monolayer), while no strain on the other crystal (e.g., $SiGe$ monolayer). Constructed bilayers are listed starting from the smallest strain where the first option should be taken as the commensurate joint supercell (see Table 5-2). As the result, the commensurate joint supercell for all four species stacking patterns of SiGe/GeC-VH are built by a 6x6 supercell of GeC monolayer with 0.8% compression

Table 5-2: The various commensurate supercells of SiGe/GeC heterostructures (denoted by index) with different strain. The red rectangular denote the chosen supercell.

```
Index   strain        atoms      surf_ratio      indices1       indices2
-----------------------------------------------------------------------------------
|   1 |    0.00373831 |   122 |   36  25 |  -6   0  -5   0 |   0  -6   0  -5   |
|   2 |    0.01219265 |   100 |   30  20 |  -6   0  -5   0 |  -6   5  -5   4   |
|   3 |    0.07721725 |    40 |   11   9 |  -6   5  -5   4 |  -5   6  -4   5   |
|   4 |    0.12800262 |    22 |    6   5 |  -6   6  -5   5 |  -6   5  -5   4   |
-----------------------------------------------------------------------------------
```

and a 5x5 supercell of $SiGe$ monolayer that contains 122 atoms in total with negligible strain of ~0.0038. Figure 5-1 represents all four constructed patterns of SiGe/GeC-VH.

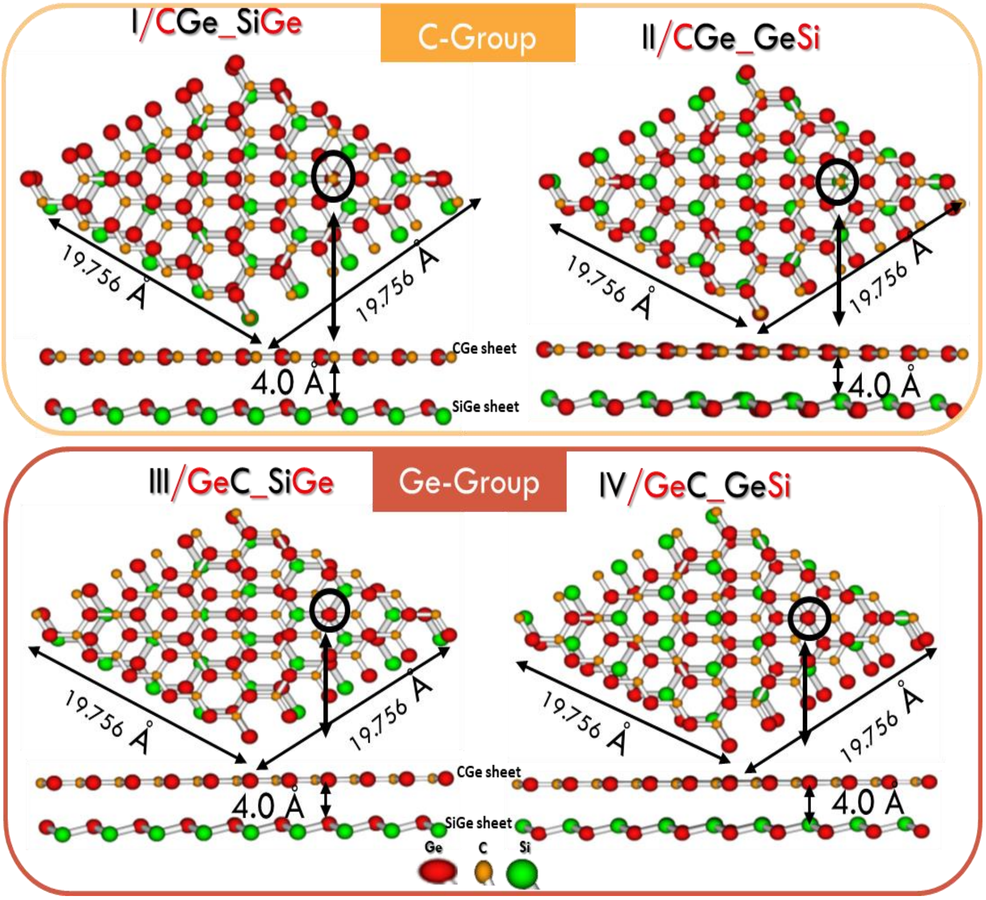

Figure 5-1: Schematic illustrations of the top and side views of the commensurate joint supercell for all the four species stacking patterns of C-group (top panels) and Ge-group (bottom panels) of SiGe/GeC-VH. The red, green, and brown ball represent Ge, Si, and C atom, respectively. The black arrows in the side views indicate the positions of species on the top/bottom layers. The initial lattice constants and interlayer distances of the supercell are denoted by the numbers.

5.5. Computational methods

This project was performed within the framework of DFT [73, 74] implemented in VASP code [46]. Through DFT, the core-valance interaction, the exchange-correlation functional, and the van der Waals interactions were described by the projector augmented wave (PAW) algorithm [75], the Perdew–Burke–Ernzerhof (PBE) [51] within generalized gradient approximation (GGA) approach [76], and the zero damping DFT-D3 method proposed by Grimme et al [152-154], respectively.

To maintain the 2D frame during the simulations, a vacuum region is set of 25 Å to avoid the interaction caused by periodic boundary condition. Moreover, the reciprocal space was sampled by gamma centered 9X9X2 k-point mesh based on Monk horst scheme [77]. A cutoff energy of 500 eV was applied for all calculations. To reach the full relaxation, the conjugate gradient algorithm [78] was used with no restriction on the volume, cell shape, and atomic positions. The energy and force convergent criteria were set as 10^{-5} eV and 10^{-3} eV $Å^{-1}$, respectively.

To study the dynamic stability, the vibration frequencies at gamma point were calculated by solving the force constants or Hessian matrix [155]. The binding energy (E_b) was calculated to analysis the role of the electrostatic interlayer interaction verses vdW interlayer interaction in stabilizing the commensurate SiGe/GeC VH, defined as $E_b = E_{total} - E_{SiGe} - E_{GeC}$, where E_{total}, E_{SiGe}, and E_{GeC} are the energies of the combined SiGe/GeC bilayer, the $SiGe$ monolayer, and the GeC monolayer, respectively. To analyze the contributions from the vdW and electrostatic interlayer interactions, the energy difference E_{diff} ($E_{diff} = E_{vdW} - E_{no\ vdW}$), in terms of the energies with (E_{vdW}) and without ($E_{no\ vdW}$) vdW correction, and the difference of interlayer separation ($d_{diff} = d_{vdW} - d_{no\ vdW}$), in terms of the interlayer distances with (d_{vdW}) and without ($d_{no\ vdW}$) vdW correction, were introduced.

Bader analysis scheme [56, 57] was performed to study the charge redistribution of the combined system which is an intuitive way of separating the charge related to each atom to enable us to track the charge transfer between atoms.

The differential electron charge density (DCD), defined as $\Delta\rho = \rho_{total} - \rho_{SiGe} - \rho_{GeC}$, where ρ_{total} is the total electron charge density of the combined system, ρ_{SiGe} and ρ_{GeC} are the electron charge densities associated with the $SiGe$ and GeC monolayers in the combined system, respectively, was applied to compute the charge redistribution which gives evaluation to the electronic properties at the interface region. Namely, ρ_{SiGe} (ρ_{GeC}) was evaluated by removing GeC ($SiGe$) layer from the relaxed combined system and calculating the density of states without further relaxation. Thus, the DCD tracks the charge transfer to get an idea of what is interacting with what in the system and how strongly they interact.

5.6. Structural properties of commensurate SiGe/GeC-VH

5.6.1. Structural optimization

Figure 5-2 visualizes the four species stacking patterns of the optimized structure of SiGe/GeC-VH after the full relaxation has been reached. As expected for commensurate structure, both monolayers exhibit small artificial strain, i.e., GeC ($SiGe$) monolayer compressed by 0.02-0.03% (0.8%) in C-group, and by 0.1% (0.9%) in Ge-group, respectively. The optimized lattice constant for SiGe/GeC-VH is 19.577 Å and 19.598 Å for the system with and without vdW-correction (see the 2nd column in Table 5-3). Consequently, the difference in the lattice constant between patterns (with and without vdW-correction) is exceedingly small (within ~ 0.02 Å) which indicates that the species stacking pattern and interlayer interaction have weak effect on the lattice constant in such commensurate system.

On the other hand, the equilibrium interlayer distance differs for all species stacking patterns of SiGe/GeC-VH (the difference is within ∼ 0.1 - 0.7 Å), and the difference of interlayer distance between with and without vdW-correction (d_{diff}) is within ∼ 0.03 - 0.2 Å, (see the 5th and 8th column in Table 5-3). Also, the Ge-group shows smaller interlayer distance than that in the C-group, due to the factor that Ge atoms tend to form sp^3 hybridization, whereas C atoms tend to form sp^2hybridization. These results are signature of the interlayer distance dependance on the species stacking pattern and interlayer interaction.

From the standpoint of energy, the energetics of the SiGe/GeC-VH has been analyzed in terms of the binding energy and are listed in 6th column in Table 5-3 . It was found that the binding energy of SiGe/GeC-VH is between -43 and -51 meV/atom, which is almost as twice as that of the vdW-VHs (e.g., −27.08 meV/atom in bilayer graphene [72] and −20.75 meV/atom in graphene/h-BN [73]) and comparable to other heterostructures stacked by a vdW material with a 2D polar material (e.g., ~-41.55 meV/atom in SiC/GeC [92], ∼−48 meV/atom in AlAs/germanene [74], and ∼−48.9/54.5meV/atom in MoS_2 /$SiC(GeC)$ [47]). This interesting finding implies that the existence of the electrostatic interlayer interaction in hybrid 2D polar heterostructures, together with the vdW interaction, play the key roles on stabilizing the combined 2D polar bilayers. Moreover, based on the binding energy, Ge-group patterns are more stable than C-group. In particular, the IV pattern is the most energetic favorable among the four patterns. Interesting, the electrostatic interlayer interaction between Ge-Ge pair in pattern

III is also strong, since such interaction comes from the different nature of in-plane charge transfer: i.e., Ge atoms gain electrons from Si atoms on SiGe layer, but Ge atoms lost electrons to C atoms on GeC layer.

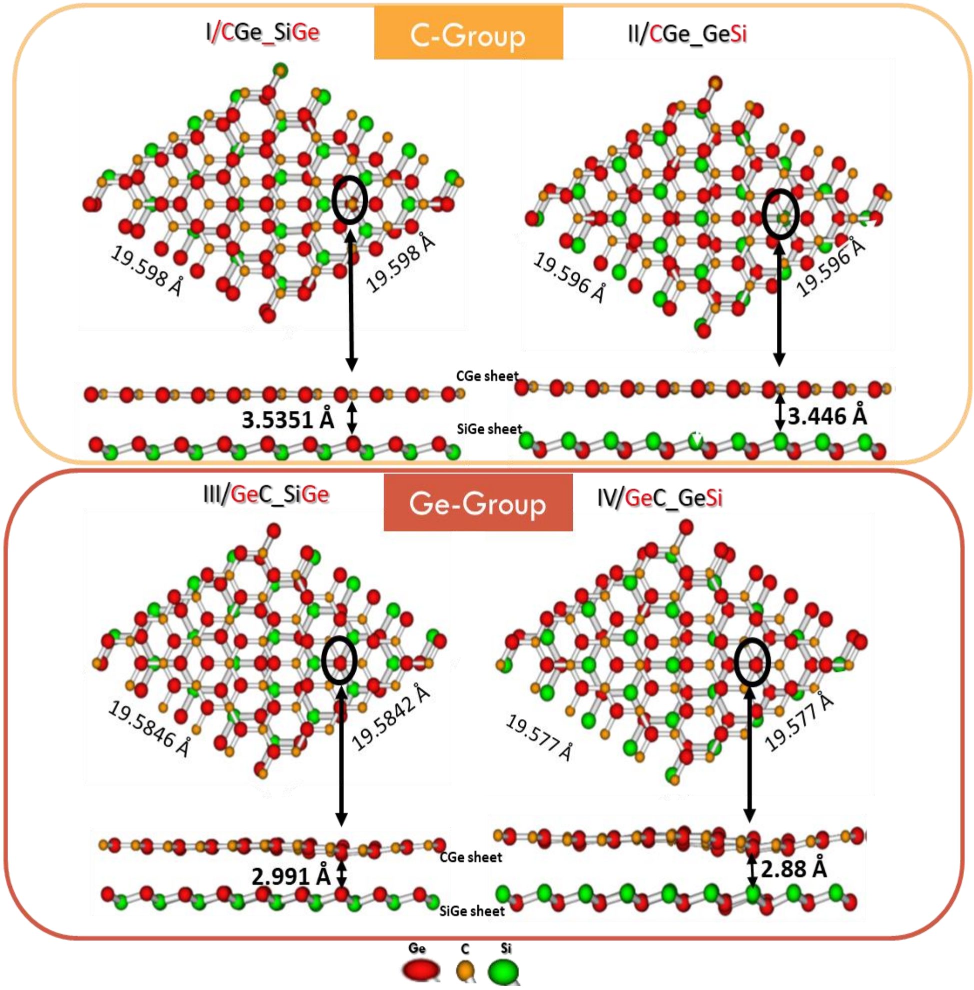

Figure 5-2: Schematic illustrations of the top and side view of species stacking patterns of C-group (top panels) and Ge-group (bottom panels) for the optimized structure of SiGe/GeC-VH. The red, green, and brown ball represent Ge, Si, and C atom, respectively. The optimized lattice constants and interlayer distances are denoted by the numbers.

Table 5-3 The optimized lattice constant (a), strain percentage per monolayer, optimized interlayer distance (d), binding energy (E_b) per atom, the energy difference (E_{diff}) per atom, and the interlayer distance difference (d_{diff}) of the composed SiGe/GeC bilayer with different pattern of species stacking.

Pattern	a	Strain	Strain	d	E_b	E_{diff}	d_{diff}
	(Å)	GeC	SiGe	(Å)	(meV/atom)	(meV/atom)	(Å)
I/CGe_SiGe	19.598	-0.02%	0.80%	3.535	-42.98361	-37.6459	0.17
II/CGe_GeSi	19.596	-0.03%	0.80%	3.446	-44.3061	-38.2159	0.23
III/GeC_SiGe	19.585	-0.09%	0.90%	2.991	-45.888	-39.7228	0.03
IV/GeC_GeSi	19.577	-0.10%	-0.90%	2.88	-50.82975	-40.37037	0.04

5.6.2. Dynamic stability

The phonon dispersion relation has been studied to examine the dynamic stability of the optimized SiGe/GeC-VH. Based on the previous results in Chapter 3, the calculated phonon spectrum over the entire Brillouin zone for $SiGe$ and GeC monolayers show six branches, i.e., three acoustic (LA, TA, ZA) branches and three optic (LO, TO, ZO) branches (see Figure 5-3). The phonon dispersions in these monolayers show a linear behavior for the in-plane LA and TA branches around the Γ point, while a quadratic dispersion was found for the out-of-plane ZA mode, consistent with previous results [83, 86]. When the two monolayers combined vertically to form SiGe/GeC-VH, the phonon spectra at the Γ point have positive frequencies for all patterns, which confirming the dynamic stability of these heterostructures.

Furthermore, the density of lattice vibration frequency (FDOS) of the optimized SiGe/GeC-VH has been analyzed (the top panel in Figure 5-3) along with partial FDOS projected on the top GeC and the bottom $SiGe$ layers (i.e., the middle red curves and the bottom blue curves panel in Figure 5-3, respectively). The interesting finding is that the higher phonon frequencies (above 800 cm^{-1}) of all patterns of SiGe/GeC-VH come from GeC monolayer contribution, while the lower phonon frequencies (around 400 cm^{-1}) of all of them come from $SiGe$ monolayer contribution. Finally, the fluctuation of the peak positions of FDOS for all patterns of SiGe/GeC-VH are quite small, indicating that the phonon modes are not sensitive to the species stacking pattern. These finding are a consequence of the small compressive strain on $SiGe$ and GeC monolayers and the symmetry breaking induced by interlayer coupling.

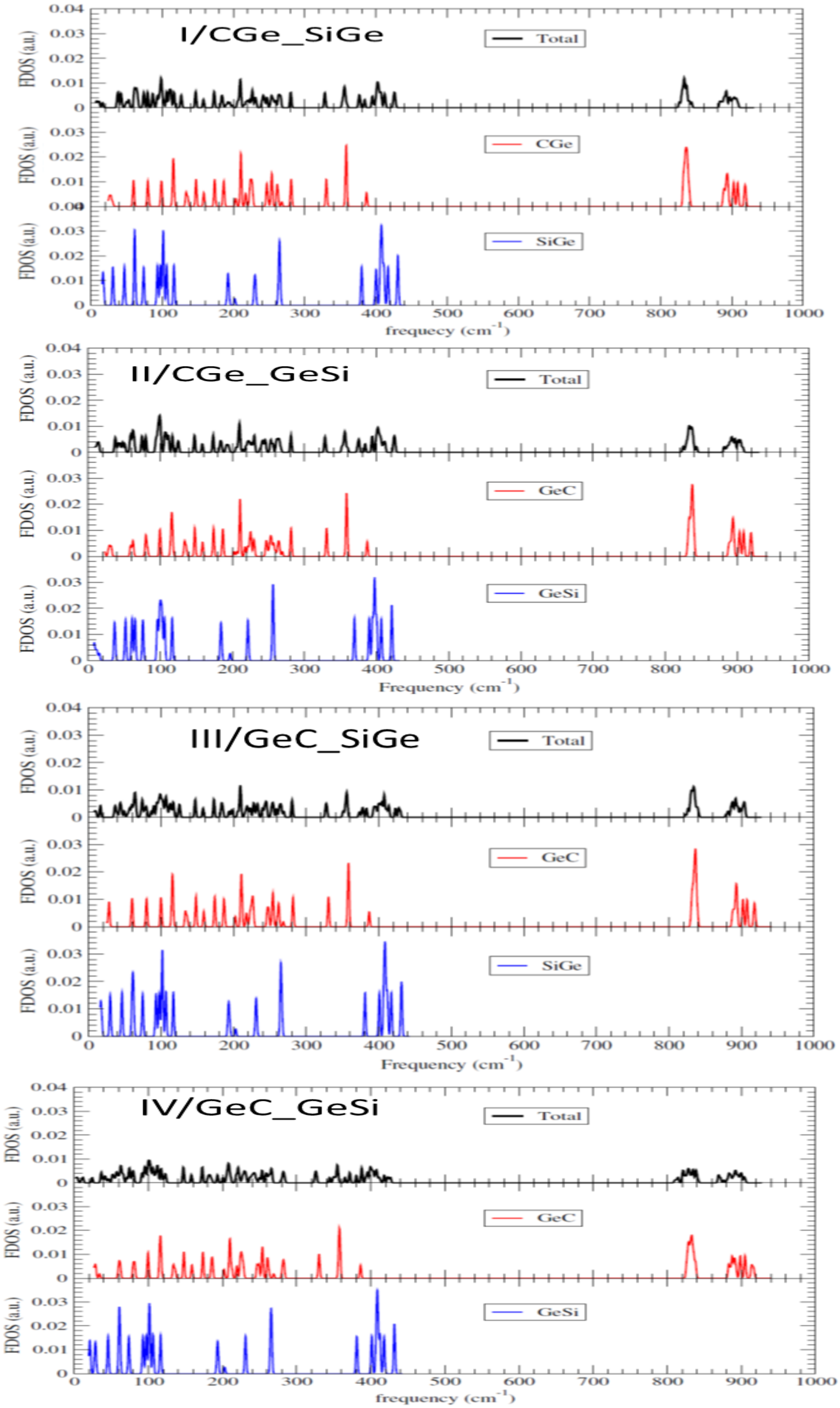

Figure 5-3: The total FDOS of SiGe/GeC-VH (black curves in the upper panels) and the partial FDOS projected on the top GeC layer (red curves in the middle panels) and the bottom $SiGe$ layer (blue curves the bottom panel), respectively.

5.6.3. Interlayer interaction (Electrostatic – VdW)

As shown in section 3.4.1 in Chapter 3, there is an in-plane charge transfer between Si and Ge atoms in 2D $SiGe$ monolayer, and between Ge and C atoms in 2D GeC monolayer due to the electronegativity difference between these atoms, which leads to the classification of $SiGe$ and GeC monolayers as polar materials. In fact, the charge redistribution due to the charge transfer causes an accumulation of a net positive charge around Si (Ge) atoms and a net negative charge around Ge (C) atoms in $SiGe$ (GeC) monolayer. Therefore, when such 2D polar materials are stacked to form VH, the charge redistribution will not only produce a strong in-plane electrostatic bonding, but also a moderate electrostatic interlayer bonding between atoms in adjacent layers. Thus, both the electrostatic interlayer interaction along with the vdW interaction will play the key role in stabilizing the interlayer distance of the SiGe/GeC-VH.

To clearly understand how these two types of interlayer forces interact with atoms on two adjacent layers, we calculated the binding energy of the SiGe/GeC-VH with distinct species stacking patterns which can be traced back to analyze the contributions of electrostatic and vdW interlayer interactions. The results are shown in Figure 5-4 . The black (red) curves represent the binding energy as a function of equilibrium interlayer distance of the combined systems without (with) the vdW correction, respectively. It was found that, without the vdW correction, the minimum of the binding energy in the Ge-group is slightly deeper (~ -9.0 - -17.5 meV/atom), and the interlayer distance is short ($\sim$3.0 Å), in contrast to the slightly shallow binding energy in the C-group (~ -6.2 - -7.3 meV/atom; $\sim$3.7 Å). Obviously, the role of the electrostatic interlayer forces in stabilizing the stacked two layers is not negligible, especially in Ge-group. Apparently, the strength of the electrostatic interlayer force strongly depends on the arrangement of net positive and negative charges between adjacent layers. The binding energy of the combined system is further deepened by ~ 37.6 – 40.4 meV/atom after considering the vdW interlayer interactions. Comparing the binding energy with/without vdW interactions (i.e., $E\_{}_{\mathrm{diff}}$ in 7th column of Table 5-3) and the difference in the equilibrium interlayer distance (i.e., $d\_{}_{\mathrm{diff}}$ in 8th column of Table 5-3 and guided by the dashed lines in Figure 5-4), it is found that the electrostatic interlayer force, trigged by the vertical species stacking induced by the in-plane charge transfer, plays a significant role in forming the interlayer bonding and acts as a driving force to stabilize the system, while the vdW interactions play an important role in stabilizing the systems by making the system attains a lower binding energy.

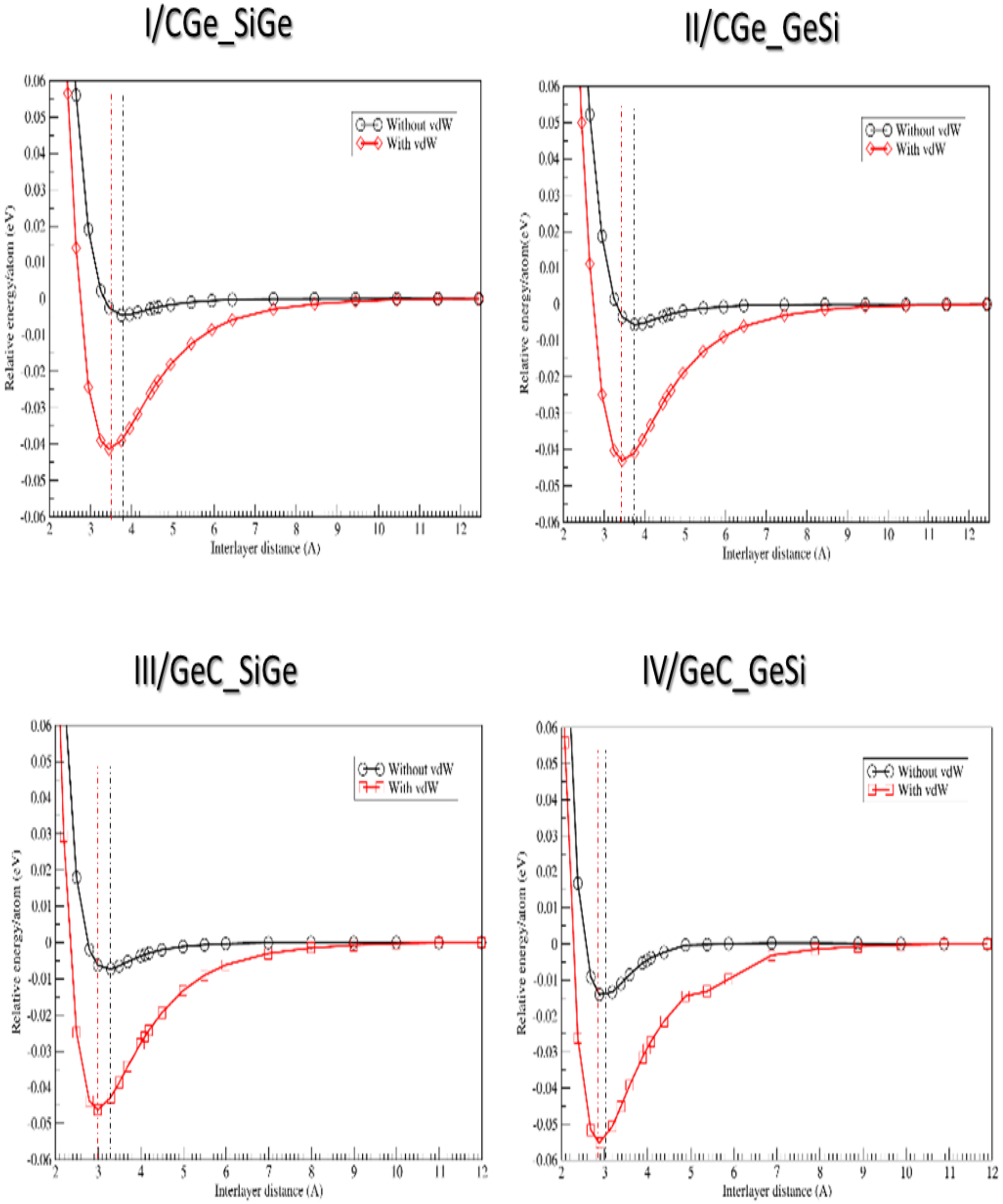

Figure 5-4: The binding energy (E_b) as a function of the interlayer distance for the combined SiGe/GeC-VH with (the red curves)/without vdW (the black curves) correction in I/CGe_SiGe pattern, II/CGe_GeSi pattern, III/GeC_SiGe pattern, and IV/GeC_GeSi pattern. The dashed lines denote the difference (d_{diff}) of interlayer distance with (red dashed line)/without vdW (black dashed line) correction.

5.7. Electronic properties of commensurate SiGe/GeC-VH

5.7.1. Band structure and DOS

To investigate the electronic properties of commensurate SiGe/GeC-VH, the band structure and projected band orbitals were calculated and plotted in Figure 5-5. It was found that all the four patterns of SiGe/GeC-VH are semimetals with tiny direct band gap at K point (also listed in Table 5-4), where the C-group has slightly larger band gap than that of the Ge-group. These results are also reflected on DOS and partial-DOS (Figure 5-6) which emphasize that more contributions on the band structure come from $SiGe$ monolayer than GeC monolayer.

Also, the analysis of the projected-DOS corresponding to each atom displays that Ge atoms in $SiGe$ have the biggest contribution near the top of valence band and the bottom of the conduction band, followed by Si atoms, and then C atoms, while Ge atoms from GeC have the smallest contribution. This trend is also confirmed by the projected band structure on each atom (see Figure 5-7) which confirms the strong impact of $SiGe$ monolayer on the electronic properties of the combined system.

In addition, the projected band orbitals associated with each atom show that the main contribution comes from p_z orbital for all atoms, which indicates the strong out of plane hybridization (Figure 5-8). In fact, the p_z of C and Ge atoms in GeC layer appear in VB and CB, respectively, but p_z of Si and Ge in $SiGe$ layer appear in both VB and CB, which means that SiGe/GeC-VH keeps the same band structure pictures as those in pristine GeC and $SiGe$ monolayers (see Chapter 3).

Interestingly, the appearance of p_x and p_y orbitals in the CB were pronounced for all atoms, especially for Si and Ge atoms of $SiGe$ layer where the contributions of p_x and p_y are very close to CBM (Figure 5-8). This is also confirmed the impact of in-plane hybridization in SiGe/GeC-VH. Also, the orbitals are significantly delocalized over both layers (as shown from the overlap of the colored balls and the corresponding orbital distributions (Figure 5-8)), which implies the strong in-plane and interlayer hybridization.

Moreover, the band gap originates mainly from the $SiGe$ monolayer at K point. Namely, the VBM and CBM are located at Si and Ge (in $SiGe$ layer). This implies that SiGe/GeC-VH possesses type -I band alignment, i.e., the VBM and CBM are from same monolayer, which is useful for designing light emitting diode and laser [156, 157].

These results demonstrate that calculated band structures of the four species ordering patterns of SiGe/GeC-VH maintain the basic electronic natures of the individual band structures of the pristine $SiGe$ and GeC monolayers (Figure 3-5) besides the existence of the strong correlation of the in-plane and out-of-plane hybridization.

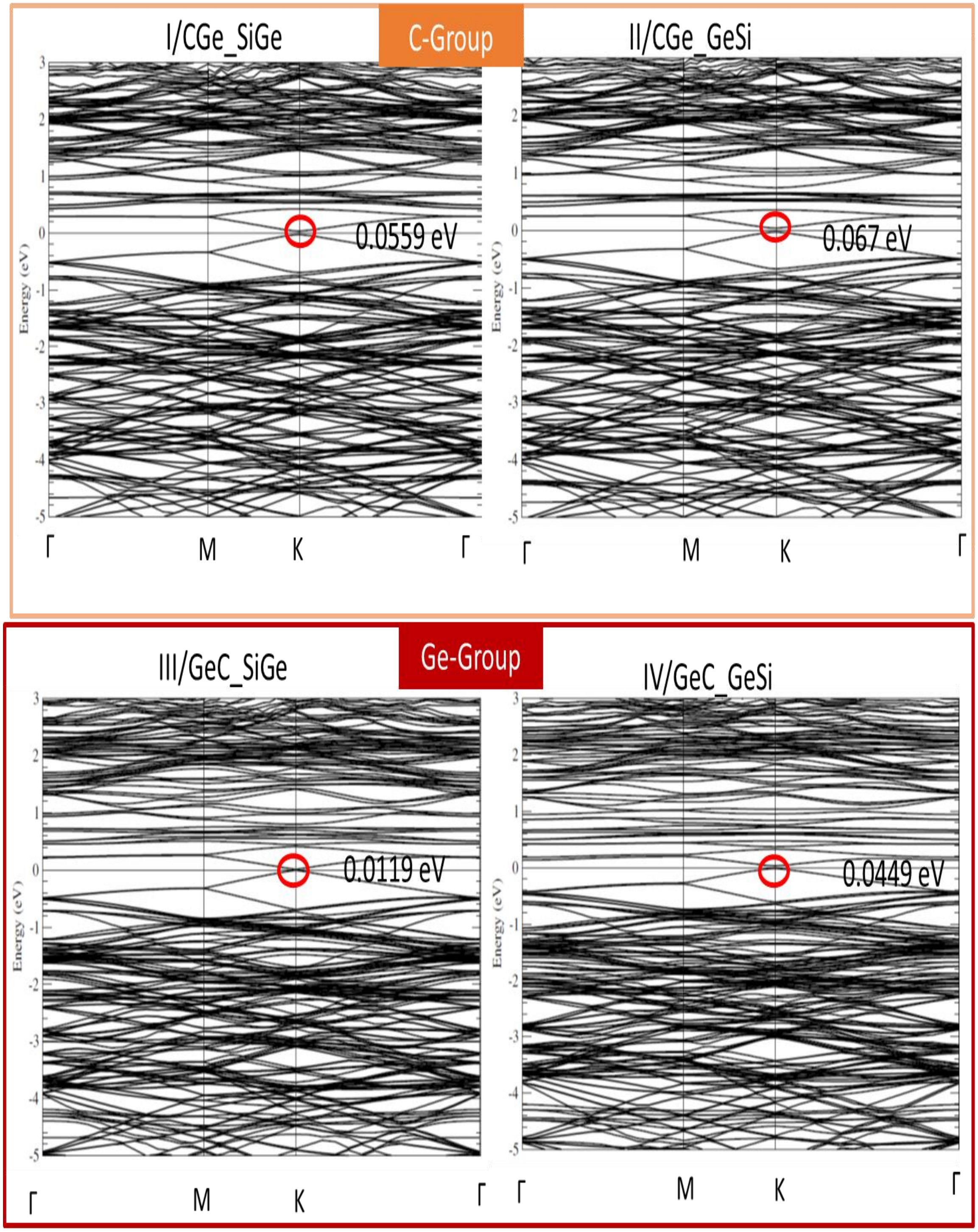

Figure 5-5: Band structures of 2D SiGe/GeC-VH. The numbers represent the band gaps, and the red circles denote the semimetal band gap natures. The Fermi level is set to be zero.

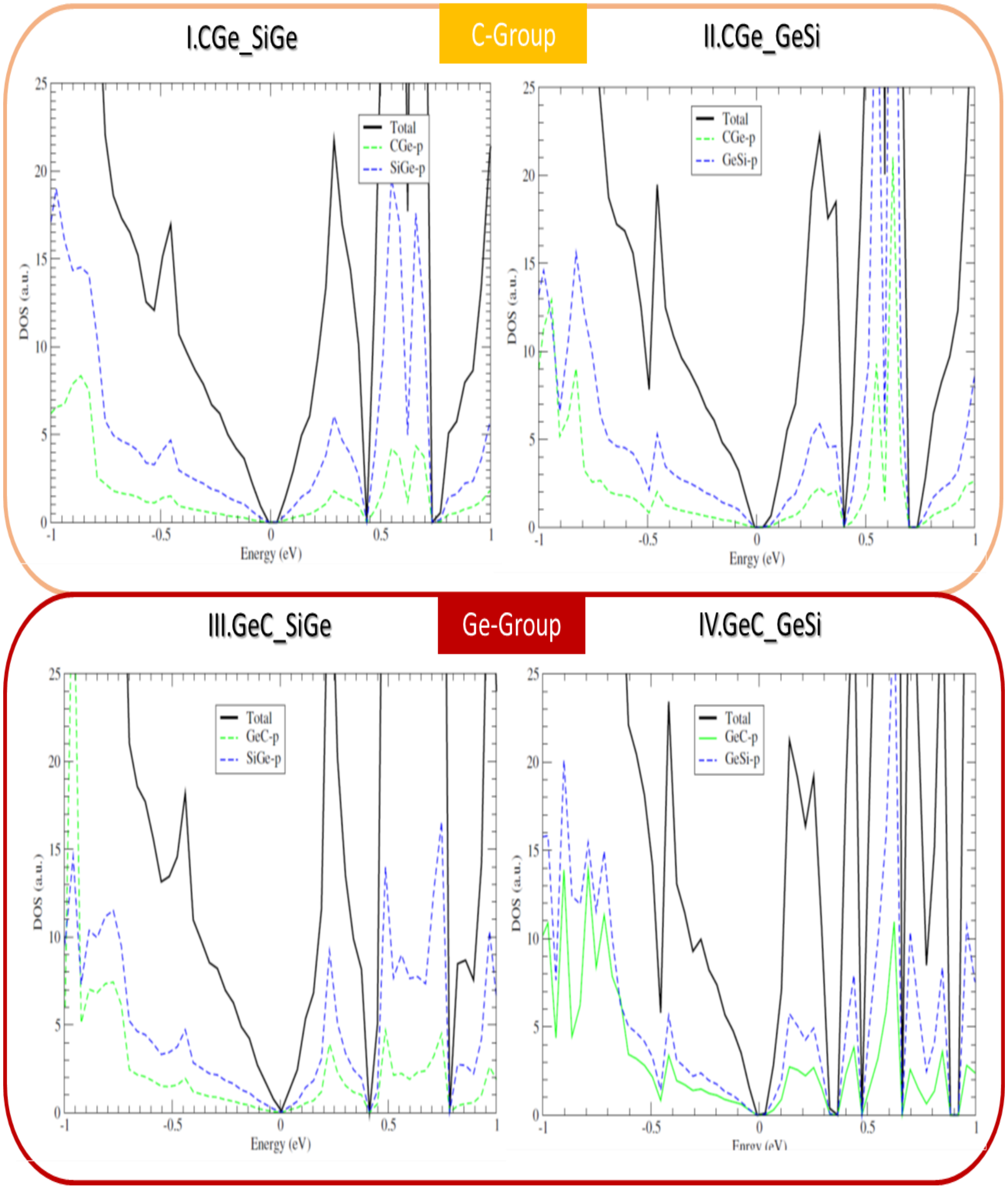

Figure 5-6: Total DOS (black curves) and partial DOS (dashed green curves donated GeC sheet and dashed dashed blue curves donated $SiGe$ sheet) of 2D SiGe/GeC-VH in C-group (top panels) and Ge-group (bottom panels). The Fermi level is set to be zero.

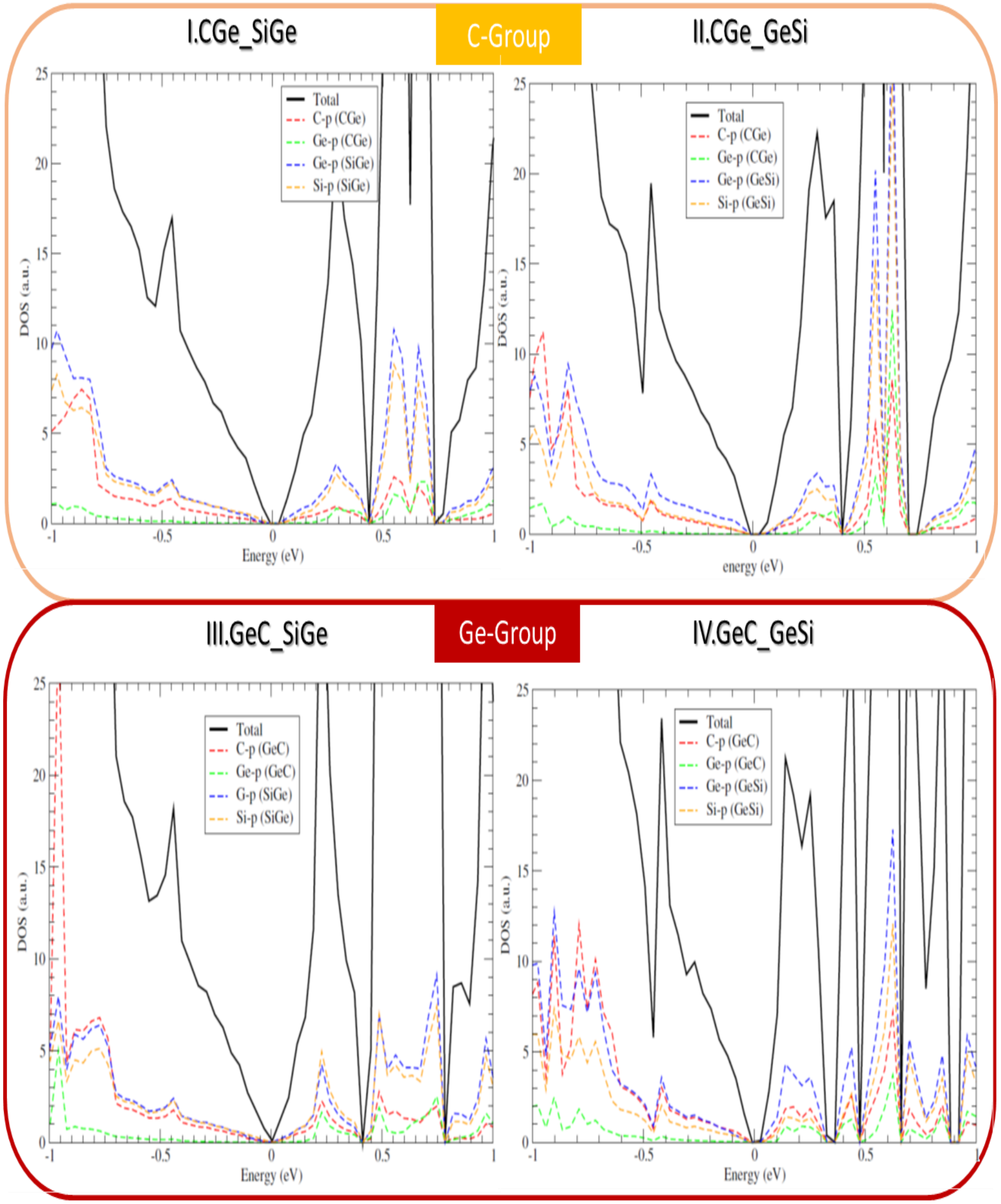

Figure 5-7: Total DOS (black curves) and *p*-orbital projected DOS (dashed colored curves donated C atom (red), Si atom (orange), Ge atom in GeC sheet (green), and Ge atom in $SiGe$ sheet (blue)) of 2D SiGe/GeC-VH in C-group (top panels) and Ge-group (bottom panels), respectively. The Fermi level is set to be zero.

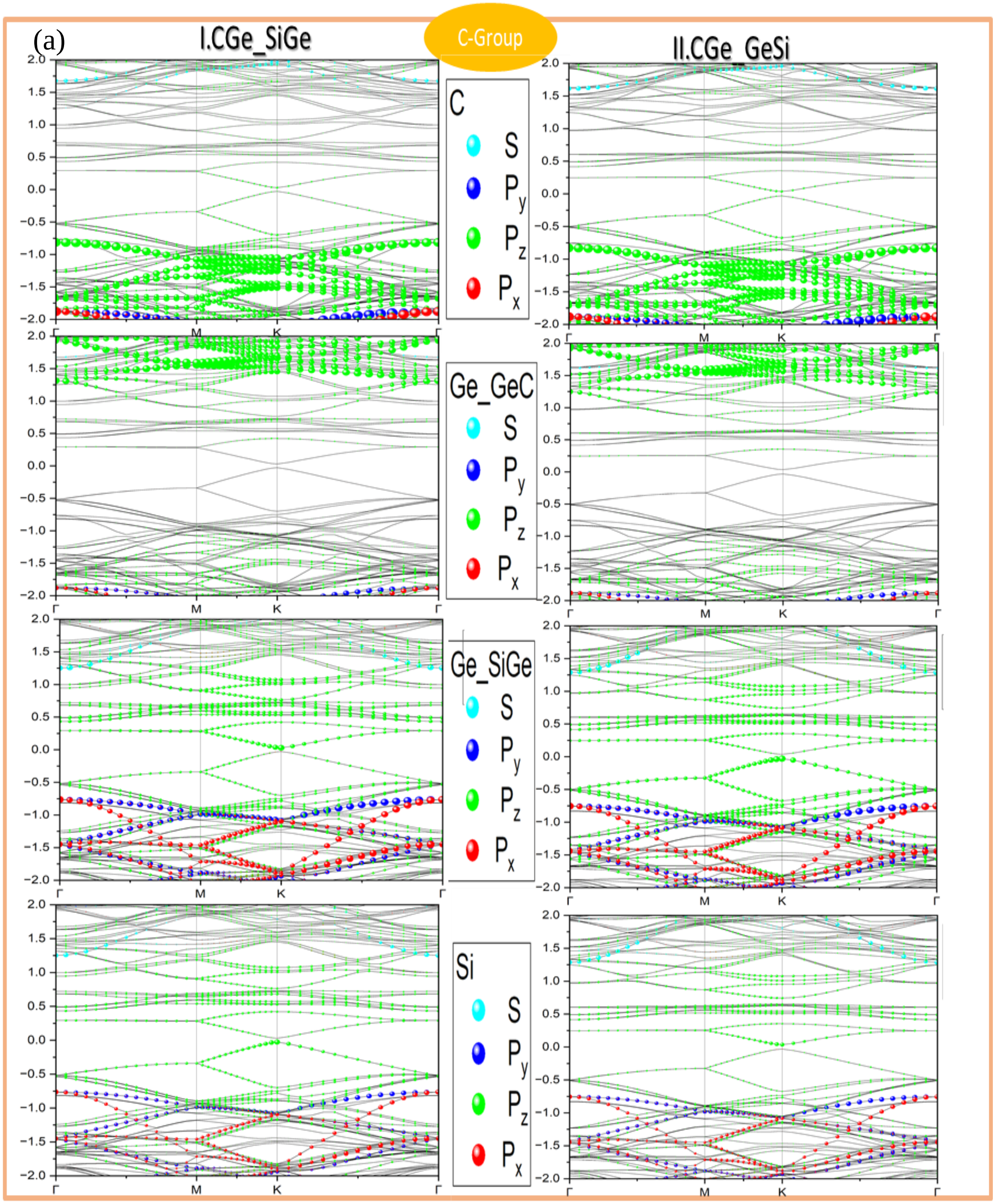
(a)
I.CGe_SiGe
C-Group
II.CGe_GeSi
C
S
P_y
P_z
P_x
Ge_GeC
Ge_SiGe
Si
Γ
M
K
2.0
1.5
1.0
0.5
0.0
−0.5
−1.0
−1.5
−2.0

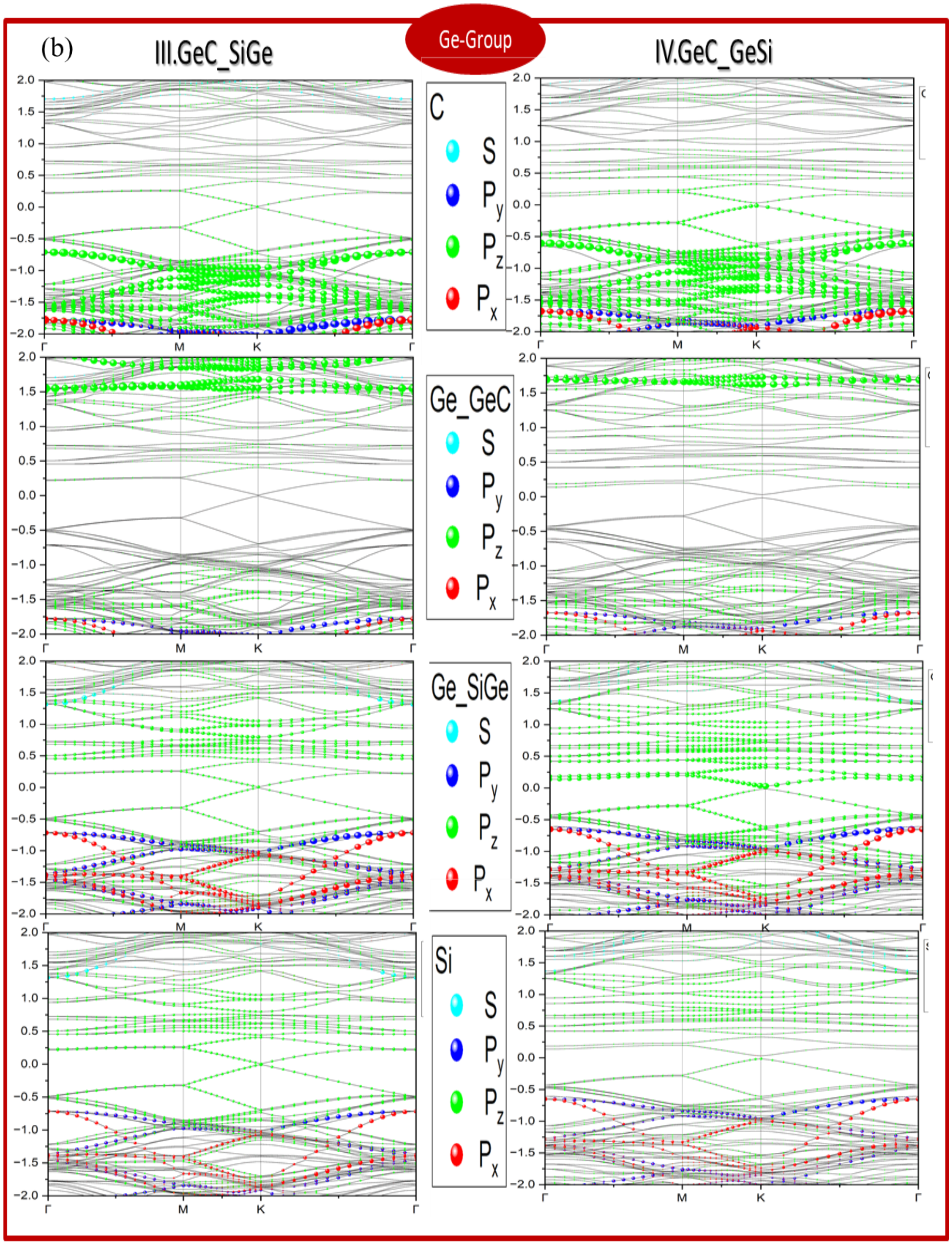

Figure 5-8: Orbital projected on band structures of each atom of 2D SiGe/GeC-VH in (a) C-group and (b) Ge-group with $s, p_x, p_y, and\ p_z$ orbitals represented by turquoise, blue, green, and red spheres, respectively. The Fermi level is set to be zero.

Table 5-4 : **Band gap (2nd column) and Bader charge analysis (in the unit of e/atom) of the charge transfer between $\boldsymbol{Si}$, $\boldsymbol{Ge}$, and $\boldsymbol{C}$ atoms in the pristine $\boldsymbol{SiGe}$ and $\boldsymbol{GeC}$ monolayers and the 2D SiGe/GeC-VH. There are two types of $\boldsymbol{Ge}$ atoms: one is at the SiGe layer (denoted by $\boldsymbol{Ge}$ ($\boldsymbol{SiGe}$)), and the other is at the $\boldsymbol{GeC}$ domain (denoted by $\boldsymbol{Ge}$ ($\boldsymbol{GeC}$). The net charge per atom in $\boldsymbol{SiGe}$ and $\boldsymbol{GeC}$ layer is listed in the 7th and 8th columns, respectively.**

System	Band gap (eV)	Ge(SiGe) (e/atom)	Si(e/atom)	Ge(GeC) (e/atom)	C (e/atom)	SiGe (e/cell)	GeC (e/cell)
I/CGe_SiGe with C-Ge	0.0599 (K-K)	0.141996	-0.138488	-1.1498	1.1474	0.088	-0.088
II/CGe_GeSi with C-Si	0.067 (K-K)	0.274200	-0.264200	-1.1857	1.1787	0.250	-0.252
III/GeC_SiGe with Ge-Ge	0.0119 (K-K)	0.229380	-0.231190	-1.1978	1.199	-0.045	0.045
IV/GeC_GeSi with Ge-Si	0.0449 (K-K)	0.123600	-0.132670	-1.1628	1.169	-0.227	0.225
Pristine SiGe monolayer	0.0743 (K-K)	0.061850	-0.061850	-	-		
Pristine GeC monolayer	2.0644 (K-K)	-	-	-1.3762	1.3762		

5.7.2. Charge transfer and Interlayer hybridization

Since GeC and $SiGe$ monolayers possess an in-plane charge transfer, a quantitative charge transfer analysis has been conducted to SiGe/GeC-VH by applying

Bader charge analysis (listed in Table 5-4 and Appendix B). In pristine GeC ($SiGe$) monolayer, there is a charge transfer of 1.38 e/atom (0.06 e/atom) from Ge to C atom (Si to Ge atom), (see Chapter 3). When $SiGe$ and GeC monolayers have been coupled to form SiGe/GeC-VH, due to the strain induced change in the bond length, Ge (Si) atom gained (lost) more charges than what Ge (Si) atom gained (lost) in pristine $SiGe$, while C (Ge) atom gained (lost) less charges than what C (Ge) atom gained (lost) in pristine GeC (Table 5-4).

For deep examination, however, the net charge difference ($Charge_{diff}$), defined as $Charge_{diff} = Charge_{VH}$– $Charge_{pristine}$, in terms of the net charge transfer of an atom in SiGe/GeC-VH ($Charge_{VH}$) and in pristine monolayer ($Charge_{pristine}$), were analyzed and has shown different trend, especially for GeC, i.e., C atom lost charges, but Ge atom gained charges in GeC layer (see Figure 5-9). The calculated $Charge_{diff}$ has been depicted in Figure 5-9: where green and red atoms represent gaining and losing charges, respectively. From Figure 5-9, it is found that the net charge difference due to the redistribution of the net charge transfer, when SiGe and GeC layers are stacked to form a SiGe/GeC-VH, shows an asymmetric behavior, due to the large lattice mismatch between the constituents’ layers that forms asymmetric stacking, e.g., AA, AB, etc., and species ordering throughout the cell.

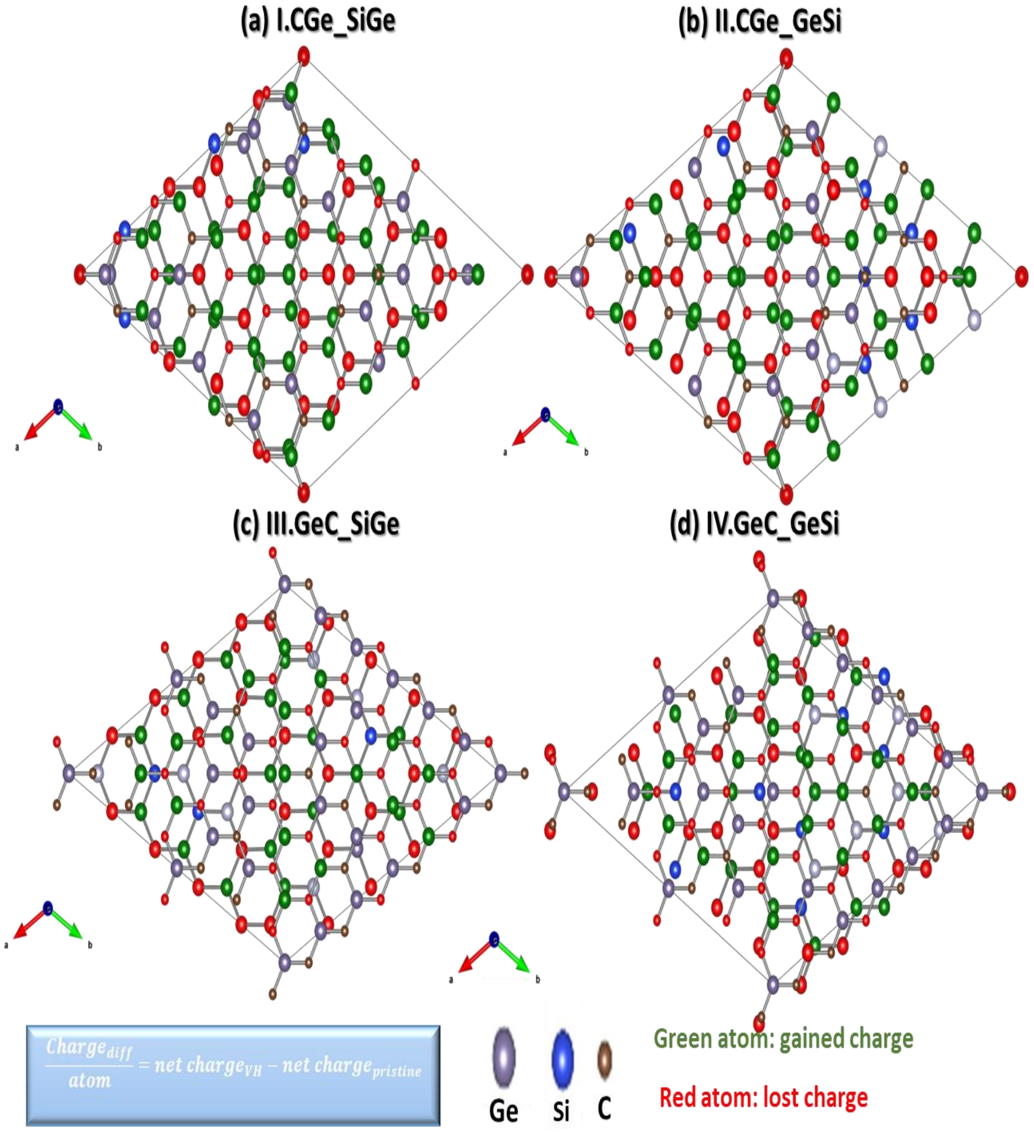

Figure 5-9: The net charge difference ($Charge_{diff}$) of SiGe/GeC-VH for patterns (a) I , (b) II, (c) III, and (d) IV by using the formula in the bule rectangular. Green and red spheres represent gaining and losing charges, while C, Si, Ge atoms are noted by brown, blue, and grey spheres, respectively.

Overall, there is also a net charge transfer between adjacent layers where the charge flow direction is from GeC to $SiGe$ layer in the C group, while it is from $SiGe$ to GeC layer in the Ge-group. This net charge transfer is slightly small (~0.05 - 0.09 e/cell) in I and III pattern, while it is significant (~0.25 - 0.23 e/cell) in II and IV pattern (Table 5-4). The net charge transfer is different quantitatively due equally to differences in elements electronegativity and the strong interlayer hybridization trigged by electrostatic interaction and interlayer distance between charged atoms in different layers. Namely, the large electronegativity differences between Si at the top of the buckled $SiGe$ sheet and C or Ge at flat GeC sheet counts for the significant charge transfer in II and IV pattern. However, the small electronegativity differences between Ge at the top of the buckled $SiGe$ sheet and C or Ge at the flat GeC sheet is the main reason that pattern I or III has small charge transfer.

To better understanding the charge redistribution behavior, the DCD has been calculated and illustrated in Figure 5-10 with the isosurface of 2.4×10^{-4} (e A^{-3}). The yellow and blue contours represent the net electron accumulation and depletion, respectively. Clearly, there is in-plane orbital hybridization on each layer coming mainly from the strain induced effect, and it counts for the in-plane charge transfer. Interestingly, the charge redistribution in the interlayer region due to strong out of plane orbital hybridization is pronounced and it counts for the interfacial charge transfer.

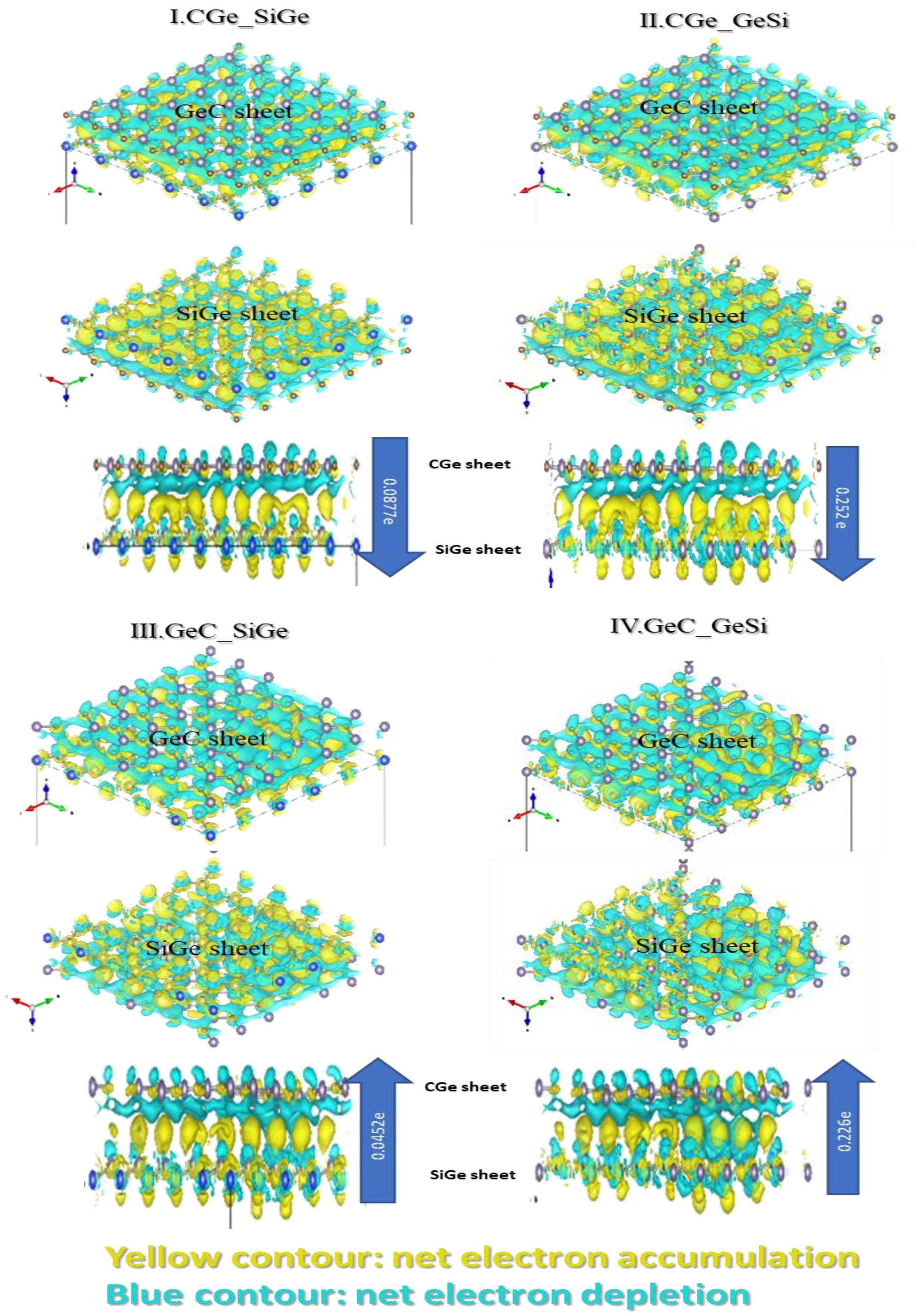

Figure 5-10: The top views with rotation of 45^0 around z axis of GeC sheet (upper) and $SiGe$ sheet (middle); and side views (bottom) of DCD of 2D SiGe/GeC-VH for patterns I , II, III, and IV. The electron accumulation and depletion are represented by the yellow and blue contours (with the isosurface of 2.4×10^{-4} (e A^{-3}).). The C, Si, Ge atoms are noted by brown, blue, and grey balls, respectively.

Furthermore, the plane-averaged electron density difference ($\Delta\rho_z$) in Figure 5-11(a) shows that a dipole in the interfacial region is produced which indicates that GeC ($SiGe$) donates electrons to $SiGe$ (GeC) monolayers, realizing a n-type doping in GeC ($SiGe$) and a p-type doping in $SiGe$ (GeC) layer in C-group (Ge-group). This pronounced polarization could lead to a built-in electric field (E_{in}) (indicated by the blue arrow) in the interfacial region (between the green dashed lines).

Moreover, the electrostatic potential across the interface of the junctions is presented in Figure 5-11 (b) which obtained by solving the Poisson equation [127]. The potential around the bottom $SiGe$ layer is slightly deeper than that around the top GeC layer due mainly to the in-plane charge redistribution and partially to the interfacial charge redistribution. Clearly, as can be seen from the Table 5-4, the charge redistribution in the $SiGe$ layer is ~3 or 4 times more than that in the pristine $SiGe$ (due to ~0.8-0.9% compression induced a shortening in bond length), while it is about 15% less in GeC layer as compared to pristine GeC (due to ~0.02-0.1% compression). Because of such small potential difference (~0.36-0.9 eV) at the two layers, it is easier to switch the interlayer charge transfer from $SiGe$ (GeC) to GeC ($SiGe$). This is quite different from the SiC/GeC bilayer, where the interlayer charge transfer always from the GeC layer to the SiC (~ 7.1 eV deeper potential)[92].

To sum up, the commensurate SiGe/GeC-VH exhibits in-plane and out of plane charged redistributions due to the strong hybridization vertically and horizontally, which is trigged by the electrostatic interaction between charged atoms besides the electronegativity differences. This change in charges flow could lead to a polarized built-in electric field (E_{in}) which may affect carrier dynamics and will certainly enhance electron-hole separation.

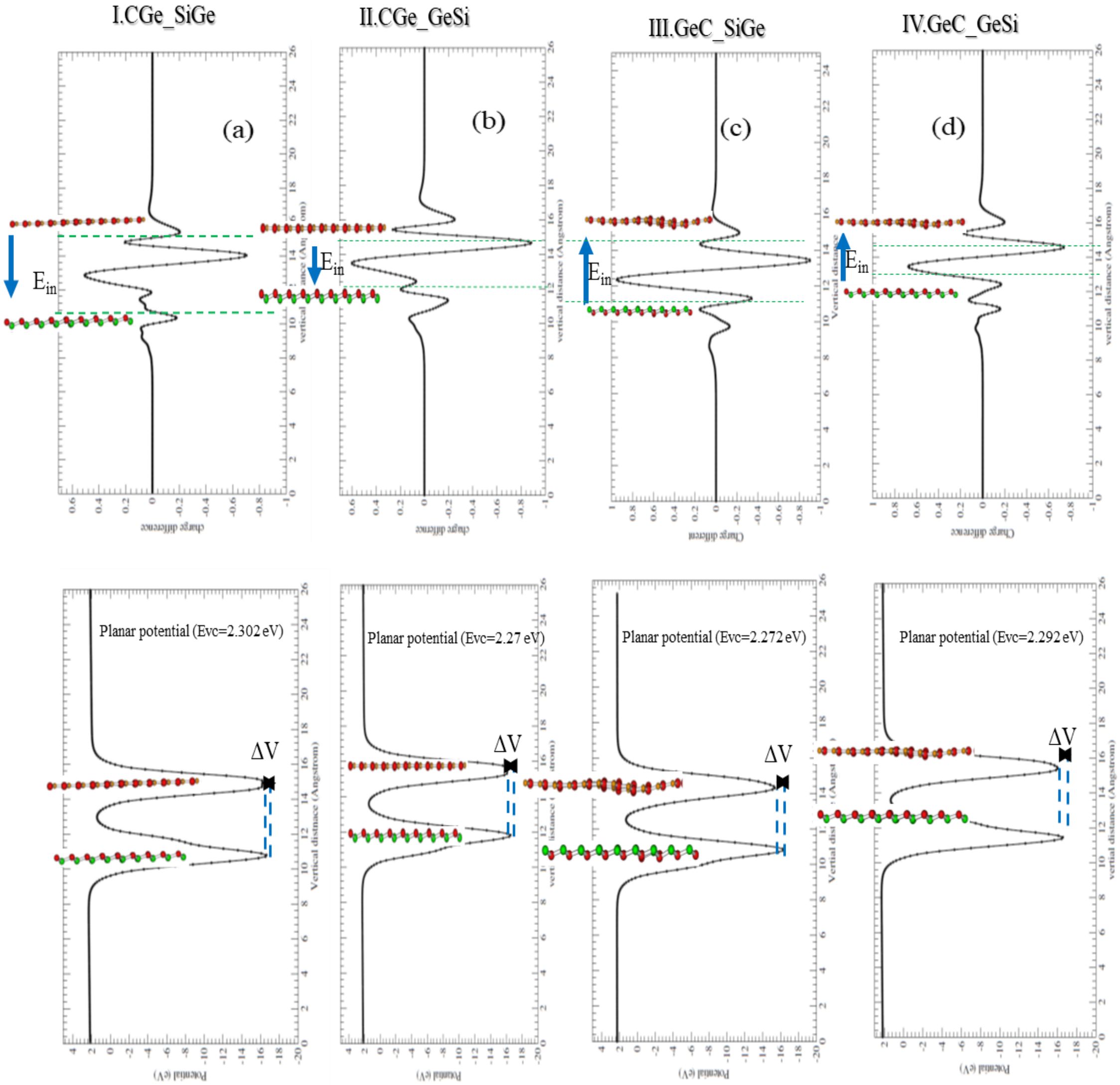

Figure 5-11: The plane-averaged DCD ($\Delta\rho$) of the 2D SiGe/GeC-VH for patterns (a) I, (b) II, (c) III, and (d) IV. The interface region is highlighted by green-dashed lines and the build-in electric field is indicated by the blue arrows. The plane-averaged electrostatic potential of 2D SiGe/GeC-VH for patterns (e) I, (f) II, (g) III, and (h) IV. The blue-dashed lines represent the average potentials, and ΔV is the potential difference between $SiGe$ and GeC sheets.

5.8. Conclusion

This chapter addressed a comprehensive theoretical study within DFT frame on the role of the stacking species arrangement and interlayer interaction on the stability and electronic properties of 2D polar vertical heterostructures built by commensurate SiGe/GeC bilayer with four species stacking patterns (classified as the C-group and the Ge-group). It has been found that the commensurate SiGe/GeC-VH with negligible strain is energetically and dynamically stable, with the Ge-group being the most energetically favorable than the C-group.

This stability is mainly trigged by interfacial interaction, i.e., the electrostatic interlayer bonding, the vdW interaction, as well as the sp^2/sp^3 hybridization nature. The larger binding energy (comparable with other vdW-Hs), its dependence (as well as the interlayer distance) on the species stacking pattern and interlayer interaction, and the independence of the lattice constant are the prove of the effective influence of interfacial interaction in stabilizing SiGe/GeC-VH system.

A net charge redistribution occurs in both the in-plane and the out-of-plane directions, when the 2D polar materials are combined vertically forming a polar heterostructure, indicates a strong intra and inter hybridization. This verified hybridization causes a charge transfer on each layer and in the interfacial region. The charge transfer is significant (~0.25 - 0.23 e/cell) in II and IV pattern due to large electronegativity differences between Si at the top of the buckled $SiGe$ sheet and C or Ge at flat GeC sheet. Whereas it is slightly small (~0.05 - 0.09 e/cell) in I and III pattern due to small electronegativity differences between Ge at the top of the buckled $SiGe$ sheet and C or Ge at the flat GeC sheet.

Such charge transfer strongly depends on the ordering of the out-of-plane species and could lead to a polarization in the interfacial region with the electron depletion (accumulation) close to the GeC layer and the electron accumulation (depletion) close to the $SiGe$ layer in C-group (Ge-group). This interface dipole could induce a built-in electric field in opposite direction, depending on the species stacking group, which could help reduce the recombination of photogenerated electron-hole pairs.

In the electronic properties prospective, the commensurate SiGe/GeC-VH is semimetal with tiny direct band gap at K point, which reflects a strong influence of the semimetal $SiGe$ monolayer on the electronic properties of the coupled layers over the semiconductor GeC monolayer. Moreover, the VBM and CBM originate from the $SiGe$ monolayer to form type-I band alignment which is promise for solar cell, light emitting diode and laser application.

CHAPTER VI

6. ONGOING WORK

6.1. Study of Potential Energy Surface (PES) in Moiré Patterns of GeC Bilayer

Moiré pattern is a gorgeous pattern that results in slightly mis-stacking structures [158]. Recently, there is an increasing interest in studying Moiré pattern in 2D materials due to its ability to tune the physical properties. In fact, a spontaneous gap opening [159], Hofstadter's butterfly [136], interlayer Moiré excitons [160], unconventional superconductivity, and correlated insulators [10, 161] are remarkable properties that entrusted with the rotation angle in layered 2D materials.

However, the mobility of a layer onto another, which is one way to achieve Moiré pattern, could produce an unfavorable phenomenon or disappear a favorable one. Super lubricity in layered graphene, for instance, can be completely vanished with rotate one layer for a certain angle [162-164]. Another example is the commensurate layered MoS_2, which is energetically more favorable for layered materials, could lead to a very large friction that cause more dissipated energy [165, 166]. Therefore, it is essential to study the potential energy surface (PES) corrugation for any system. PES is a function of the relative position of two sheets in terms of the interlayer interaction. Then, the importance of PES corrugation is centered on determines the intrinsic resistance that origin from the frictional force and causing energy dissipation.

Furthermore, GeC is a binary compound made of group IV and possess attractive properties such as a graphene like structure and a tunable direct band gap by applying strain engineering. Also, it was confirmed by CVD method [167] and laser ablation [168, 169]. Therefore, this proposal intends to investigate the PES of GeC bilayer by modulating a bilayer GeC with sliding of the top layer with respect to the bottom layer starting from AA stacking through a N x N grid as shown in Figure 6-1. Hence, one can determine the global and local minimum energy which are the energetically more favorable and next energetically favorable, respectively, as well as the potential energy barrier.

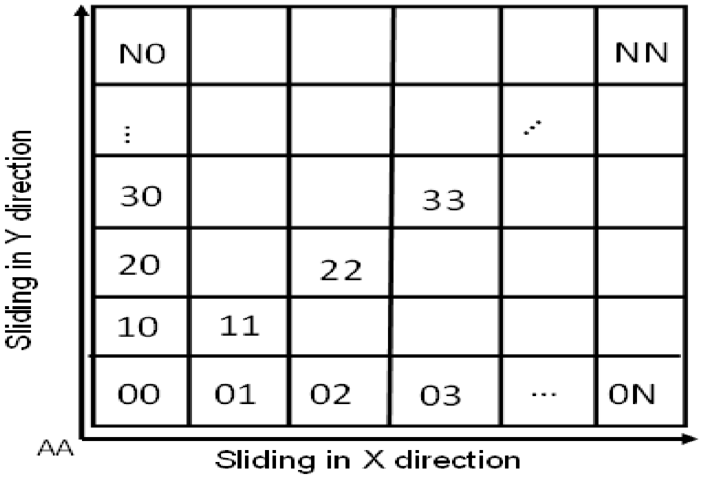

Figure 6-1: Schematic illustration for N x N grid for PES

The significance of PES is that it helps to determine the path of transition from the local minimum energy to global minimum energy during the sliding with the advantage of avoiding large energy barrier that can result in high friction. As an illustration, Figure 6-2 shows two examples of PES of graphene and MoS_2 bilayers [159, 170].

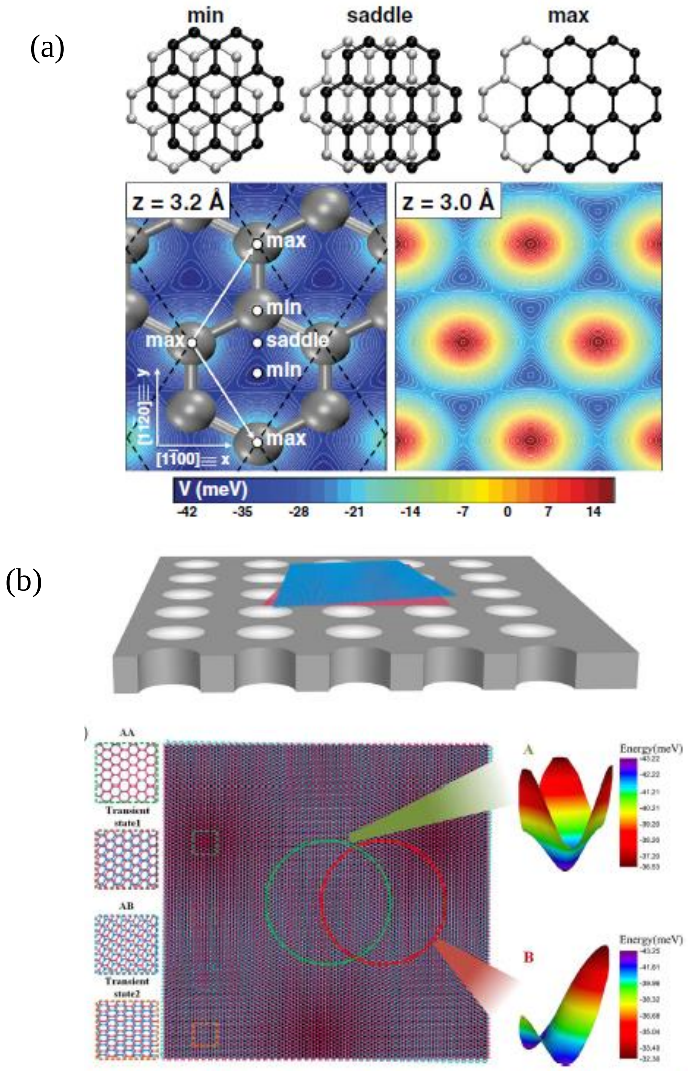

Figure 6-2:An illustration of PES in (a) graphene [159] and (b) MoS^2[170].

Bilayer GeC homo-structure has a characteristic of being a polar material, unlike vdW bilayer graphene homo-structure, due to intrinsic charge transfer between the elements. Since PES mainly describes the interlayer interaction, the existence of electrostatic interaction besides vdW in bilayer GeC homo-structure gives a fertile land to explore more physics in such system.

In brief, motivating by the correlated Moiré patterns with ultralow friction in 2D vdW layers, this theoretical project has been proposed to systematically explore the energy landscape that represented by PES of Moiré patterns formed by bilayer GeC homo-structure to unveil the physics that influences friction.

6.2. Comparison Study of Strain Engineering in Monolayer of Group-IV Binary Compounds by using Quantum Espresso (QE) package.

Chapter 3 addressed the effect of strain engineering on 2D binary compounds of group IV elements: SiC, GeC, and $SiGe$ monolayers. These monolayers show promising stability and electronic properties. A dynamic stability, tunable band gap, tolerating strain, and intrinsic charge transfer make them bright candidates for many nanoelectronics applications. The results that have been obtained in chapter 3 were the fundamental factors for the following work in heterostructures (see Chapters IV and V). Since these outcomes have been obtained by implementing DFT method through VASP code, it would be wise to run the calculations again by using a different DFT code, like Quantum espresso QE, to confirm the results.

QE works in the scope of first-principles calculations within the frame of DFT, pseudopotentials, and plane waves, similar as implemented in VASP. But it is an open-source distribution of computer codes, i.e., it opens freely to external contributions for electronic-structure calculations and materials modeling at the nanoscale, taking the advantage of world-wide collaboration that implemented cutting edge computational materials science methods relatively quickly. Besides, it is known for its performance on a wide range of hardware architectures, from laptops to massively parallel computers, as well as for the breadth of its applications [171, 172].

This work adopted DFT implementation through QE distribution to study the strain engineering and its influence on the electronic properties of SiC, GeC, and $SiGe$ monolayers. Figure 6-3 shows the optimized structures for the three monolayers, and Table 6-1 appears the structural optimization parameters of the three monolayers, lattice constant, bond length, etc. For instance, the optimized lattice constant is 3.1 Å, 3.24 Å , and 3.94 Å for SiC, GeC, and $SiGe$, respectively, which consistent with the values obtained from VASP code shown in Chapter 3 and the previously reported values [89, 173, 174] (Table 6-1). In contrast, QE results for the structural optimization are quite similar to VASP results which indicates the reality of the calculation.

To sum up, this work has been proposed to confirm the effect of strain on the electronic properties including the band gap transition and charge transfer of group-IV binary compounds SiC, GeC, and $SiGe$ by taking the advantage of QE codes. It is expected for this work to provide a solid understanding of the electronic behavior of the group-IV binary compounds.

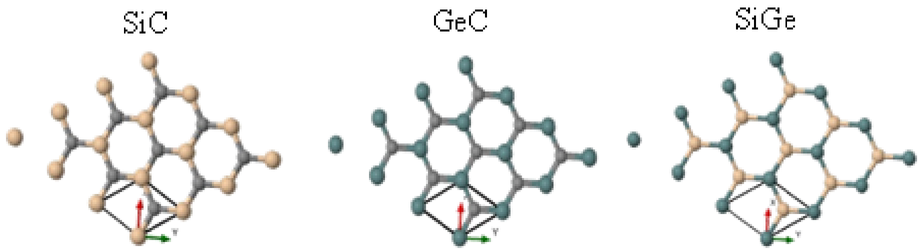

Figure 6-3:The optimized structures of SiC, GeC, and $SiGe$ monolayer.

Table 6-1:The comparison of the structural optimization parameters of SiC, GeC, and $SiGe$ monolayers

System	Optimized Lattice constant	Bond length	Buckling	Bond angle
	QE (VASP) Å	QE (VASP) Å	QE (VASP) Å	QE (VASP)
SiC	3.1 (3.089)	1.79 (1.783)	0 (0)	120^0 (120^0)
GeC	3.24 (3.267)	1.87 (1.886)	0 (0)	120^0 (120^0)
$SiGe$	3.94 (3.951)	2.34 (2.3570)	0.591 (0.59)	114.2^0 (113.94^0)

REFERENCES

1. Das, S., et al., *Synthesis and characterization of graphene.* Carbon Nanomaterials for Advanced Energy Systems: Advances in Materials Synthesis and Device Applications, 2015: p. 85-131.
2. Shinde, P.V. and M.K. Singh, *Synthesis, characterization, and properties of graphene analogs of 2D material*, in *Fundamentals and Sensing Applications of 2D Materials*. 2019, Elsevier. p. 91-143.
3. Tan, C., et al., *Recent advances in ultrathin two-dimensional nanomaterials.* Chemical reviews, 2017. **117**(9): p. 6225-6331.
4. Zafeiratos, S., *2D Nanomaterials for Energy Applications: Graphene and Beyond*. 2019: Elsevier.
5. Gerstner, E., *Nobel prize 2010: Andre geim & konstantin novoselov.* Nature Physics, 2010. **6**(11): p. 836-836.
6. NobelPrize.org. *The Nobel Prize in Physics 2010*. Nobel Prize Outreach AB 2023 [cited 2023 7 Mar 2023]; Available from: https://www.nobelprize.org/prizes/physics/2010/summary/.
7. Zhang, Y., et al., *Experimental observation of the quantum Hall effect and Berry's phase in graphene.* nature, 2005. **438**(7065): p. 201-204.
8. Katsnelson, M., K. Novoselov, and A. Geim, *Chiral tunnelling and the Klein paradox in graphene.* Nature physics, 2006. **2**(9): p. 620-625.
9. Wang, J., Y. Xu, and S.-C. Zhang, *Two-dimensional time-reversal-invariant topological superconductivity in a doped quantum spin-Hall insulator.* Physical Review B, 2014. **90**(5): p. 054503.
10. Cao, Y., et al., *Unconventional superconductivity in magic-angle graphene superlattices.* Nature, 2018. **556**(7699): p. 43-50.
11. Tømterud, M., et al., *Observation of the Boson Peak in a 2D Material.* arXiv preprint arXiv:2205.02486, 2022.
12. Zhang, H., *ACS Nano 2015, 9, 9451.* Crossref, Medline, CAS, 2019.
13. Geim, A.K. and K.S. Novoselov, *The rise of graphene.* Nature materials, 2007. **6**(3): p. 183-191.
14. Geethalakshmi, K., T.Y. Ng, and R. Crespo-Otero, *Tunable optical properties of OH-functionalised graphene quantum dots.* Journal of Materials Chemistry C, 2016. **4**(36): p. 8429-8438.
15. Duerloo, K.-A.N., Y. Li, and E.J. Reed, *Structural phase transitions in two-dimensional Mo-and W-dichalcogenide monolayers.* Nature communications, 2014. **5**(1): p. 4214.
16. Yao, B., et al., *Broadband gate-tunable terahertz plasmons in graphene heterostructures.* Nature Photonics, 2018. **12**(1): p. 22-28.

17. Yao, B., et al., *Gate-tunable frequency combs in graphene–nitride microresonators.* Nature, 2018. **558**(7710): p. 410-414.
18. Tan, T., et al., *2D material optoelectronics for information functional device applications: status and challenges.* Advanced Science, 2020. **7**(11): p. 2000058.
19. Bao, Q., et al., *Atomic-layer graphene as a saturable absorber for ultrafast pulsed lasers.* Advanced Functional Materials, 2009. **19**(19): p. 3077-3083.
20. Xia, F., et al., *Two-dimensional material nanophotonics.* Nature Photonics, 2014. **8**(12): p. 899-907.
21. Zhou, J., et al., *2DMatPedia, an open computational database of two-dimensional materials from top-down and bottom-up approaches.* Scientific data, 2019. **6**(1): p. 86.
22. Mak, K.F., et al., *Atomically thin MoS 2: a new direct-gap semiconductor.* Physical review letters, 2010. **105**(13): p. 136805.
23. Li, L., et al., *Black phosphorus field-effect transistors.* Nature nanotechnology, 2014. **9**(5): p. 372-377.
24. Geim, A.K. and I.V. Grigorieva, *Van der Waals heterostructures.* Nature, 2013. **499**(7459): p. 419-425.
25. Pham, P.V., et al., *2D heterostructures for ubiquitous electronics and optoelectronics: principles, opportunities, and challenges.* Chemical Reviews, 2022. **122**(6): p. 6514-6613.
26. NobelPrize.org. *The Nobel Prize in Physics 2000*. Nobel Prize Outreach AB 2023 [cited 2023 13 Mar 2023]; Available from: https://www.nobelprize.org/prizes/physics/2000/summary/.
27. Liu, T., et al., *Interfacial engineering in two-dimensional heterojunction photocatalysts.* International Journal of Hydrogen Energy, 2023.
28. Frensley, W.R., *Heterostructure and quantum well physics*, in *VLSI Electronics Microstructure Science*. 1994, Elsevier. p. 1-24.
29. Geim, A.K., *Graphene: status and prospects.* science, 2009. **324**(5934): p. 1530-1534.
30. Neto, A.C., et al., *The electronic properties of graphene.* Reviews of modern physics, 2009. **81**(1): p. 109.
31. Lee, C., et al., *Measurement of the elastic properties and intrinsic strength of monolayer graphene.* science, 2008. **321**(5887): p. 385-388.
32. Cao, R., et al., *Mid-infrared optoelectronic devices based on two-dimensional materials beyond graphene: status and trends.* Nanomaterials, 2022. **12**(13): p. 2260.
33. Bonaccorso, F., et al., *Graphene photonics and optoelectronics.* Nature photonics, 2010. **4**(9): p. 611-622.
34. Keyes, R.W., *Fundamental limits of silicon technology.* Proceedings of the IEEE, 2001. **89**(3): p. 227-239.
35. Jena, D., K. Banerjee, and G.H. Xing, *Intimate contacts.* Nature materials, 2014. **13**(12): p. 1076-1078.
36. Novoselov, K.S., et al., *2D materials and van der Waals heterostructures.* Science, 2016. **353**(6298): p. aac9439.
37. Cahangirov, S., M. Topsakal, and E. Aktürk, *S ahin H and Ciraci S 2009.* Phys. Rev. Lett. **102**: p. 236804.

38. Feng, B., et al., *Evidence of silicene in honeycomb structures of silicon on Ag (111).* Nano letters, 2012. **12**(7): p. 3507-3511.
39. Dávila, M., et al., *Elemental group IV two-dimensional materials beyond graphene*, in *Semiconductors and Semimetals*. 2016, Elsevier. p. 149-188.
40. Zhang, L., et al., *Structural and electronic properties of germanene on MoS 2.* Physical review letters, 2016. **116**(25): p. 256804.
41. Zhu, F.-f.C.W.-j., X.Y.G.C.-l. Guan, and D.-d.L.C.-h. Qian, *D. Zhang S.-C. Jia J.-f.* Nat. Mater, 2015. **14**: p. 1020-1025.
42. Tang, P., et al., *Stable two-dimensional dumbbell stanene: A quantum spin Hall insulator.* Physical Review B, 2014. **90**(12): p. 121408.
43. Kara, A., et al., *A review on silicene—new candidate for electronics.* Surface science reports, 2012. **67**(1): p. 1-18.
44. Acun, A., et al., *Germanene: the germanium analogue of graphene.* Journal of physics: Condensed matter, 2015. **27**(44): p. 443002.
45. Lyu, J.K., et al., *Stanene: a promising material for new electronic and spintronic applications.* Annalen der Physik, 2019. **531**(10): p. 1900017.
46. Kresse, G. and J. Furthmüller, *Efficient iterative schemes for ab initio total-energy calculations using a plane-wave basis set.* Physical review B, 1996. **54**(16): p. 11169.
47. Sham, L.J. and W. Kohn, *One-particle properties of an inhomogeneous interacting electron gas.* Physical Review, 1966. **145**(2): p. 561.
48. LeSar, R., *Introduction to computational materials science: fundamentals to applications*. 2013: Cambridge University Press.
49. Nogueira, F., A. Castro, and M.A. Marques, *A tutorial on density functional theory.* A primer in density functional theory, 2003: p. 218-256.
50. Lee, C., W. Yang, and R.G. Parr, *Development of the Colle-Salvetti correlation-energy formula into a functional of the electron density.* Physical review B, 1988. **37**(2): p. 785.
51. Perdew, J.P., K. Burke, and M. Ernzerhof, *Generalized gradient approximation made simple.* Physical review letters, 1996. **77**(18): p. 3865.
52. Feynman, R.P., *Forces in Molecules.* Physical Review, 1939. **56**(4): p. 340-343.
53. Dove, M., *Introduction to the theory of lattice dynamics.* École thématique de la Société Française de la Neutronique, 2011. **12**: p. 123-159.
54. Dove, M.T., *Introduction to lattice dynamics*. 1993: Cambridge university press.
55. Togo, A. and I. Tanaka, *First principles phonon calculations in materials science.* Scripta Materialia, 2015. **108**: p. 1-5.
56. Bader, R., *Atoms in molecules: a quantum theory: Oxford Univ.* Press.: Oxford, 1990.
57. Henkelman, G., A. Arnaldsson, and H. Jónsson, *A fast and robust algorithm for Bader decomposition of charge density.* Computational Materials Science, 2006. **36**(3): p. 354-360.
58. Yoshitake, M., *Work Function and Band Alignment of Electrode Materials.* Springer, 2021. **437**: p. 7-34.
59. Çankaya, G. and N. Ucar, *Schottky barrier height dependence on the metal work function for p-type Si Schottky diodes.* Zeitschrift für Naturforschung A, 2004. **59**(11): p. 795-798.

60. Ishihara, A., et al., *Tantalum (oxy) nitrides prepared using reactive sputtering for new nonplatinum cathodes of polymer electrolyte fuel cell.* Electrochimica Acta, 2008. **53**(16): p. 5442-5450.
61. Lang, N., S. Holloway, and J. Nørskov, *Electrostatic adsorbate-adsorbate interactions: The poisoning and promotion of the molecular adsorption reaction.* Surface Science, 1985. **150**(1): p. 24-38.
62. Brown, J., A. Luntz, and P.A. Schultz, *Long-range poisoning of D2 dissociative chemisorption on Pt (111) by coadsorbed K.* The Journal of chemical physics, 1991. **95**(5): p. 3767-3774.
63. Mohta, N. and S.E. Thompson, *Mobility enhancement.* IEEE circuits and devices magazine, 2005. **21**(5): p. 18-23.
64. Fischetti, M.V., et al., *Six-band k· p calculation of the hole mobility in silicon inversion layers: Dependence on surface orientation, strain, and silicon thickness.* Journal of Applied Physics, 2003. **94**(2): p. 1079-1095.
65. Janjan, B., V. Ahmadi, and M. Heidari. *Electrically driven CMOS CompatibleVO 2-based silicon modulator*. in *2017 Iranian Conference on Electrical Engineering (ICEE)*. 2017. IEEE.
66. Guinea, F., M.I. Katsnelson, and A. Geim, *Energy gaps and a zero-field quantum Hall effect in graphene by strain engineering.* Nature Physics, 2010. **6**(1): p. 30-33.
67. Smith, A.M. and S. Nie, *Semiconductor nanocrystals: structure, properties, and band gap engineering.* Accounts of chemical research, 2010. **43**(2): p. 190-200.
68. Yablonovitch, E. and E. Kane, *Band structure engineering of semiconductor lasers for optical communications.* Journal of lightwave technology, 1988. **6**(8): p. 1292-1299.
69. Chidambaram, P., et al., *Fundamentals of silicon material properties for successful exploitation of strain engineering in modern CMOS manufacturing.* IEEE Transactions on Electron Devices, 2006. **53**(5): p. 944-964.
70. Deng, S. and V. Berry, *Wrinkled, rippled and crumpled graphene: an overview of formation mechanism, electronic properties, and applications.* Materials Today, 2016. **19**(4): p. 197-212.
71. Molle, A., et al., *Buckled two-dimensional Xene sheets.* Nature materials, 2017. **16**(2): p. 163-169.
72. Levy, N., et al., *Strain-induced pseudo–magnetic fields greater than 300 tesla in graphene nanobubbles.* Science, 2010. **329**(5991): p. 544-547.
73. Kohn, W. and L.J. Sham, *Self-consistent equations including exchange and correlation effects.* Physical review, 1965. **140**(4A): p. A1133.
74. Hohenberg, P. and W. Kohn, *Inhomogeneous electron gas.* Physical review, 1964. **136**(3B): p. B864.
75. Blöchl, P.E., *Projector augmented-wave method.* Physical review B, 1994. **50**(24): p. 17953.
76. Perdew, J.P., et al., *Erratum: Atoms, molecules, solids, and surfaces: Applications of the generalized gradient approximation for exchange and correlation.* Physical Review B, 1993. **48**(7): p. 4978.
77. Monkhorst, H.J. and J.D. Pack, *Special points for Brillouin-zone integrations.* Physical review B, 1976. **13**(12): p. 5188.

78. Gonze, X., *First-principles responses of solids to atomic displacements and homogeneous electric fields: Implementation of a conjugate-gradient algorithm.* Physical Review B, 1997. **55**(16): p. 10337.
79. Baroni, S., et al., *Phonons and related crystal properties from density-functional perturbation theory.* Reviews of Modern Physics, 2001. **73**(2): p. 515-562.
80. Vu, T.V., et al., *Electronic, optical and photocatalytic properties of fully hydrogenated GeC monolayer.* Physica E: Low-dimensional Systems and Nanostructures, 2020. **117**: p. 113857.
81. Hoat, D., et al., *Transition from indirect to direct band gap in SiC monolayer by chemical functionalization: A first principles study.* Superlattices and Microstructures, 2020. **137**: p. 106320.
82. Luo, M. and Y. Xu, *Tunable band-gap of the GeC monolayer by strain and electric field: A first-principles study.* Optik, 2019. **195**: p. 163147.
83. Hsueh, H., G. Guo, and S.G. Louie, *Excitonic effects in the optical properties of a SiC sheet and nanotubes.* Physical Review B, 2011. **84**(8): p. 085404.
84. Shi, Z., et al., *Predicting two-dimensional silicon carbide monolayers.* ACS nano, 2015. **9**(10): p. 9802-9809.
85. Lü, T.-Y., et al., *Tuning the indirect–direct band gap transition of SiC, GeC and SnC monolayer in a graphene-like honeycomb structure by strain engineering: a quasiparticle GW study.* Journal of Materials Chemistry, 2012. **22**(19): p. 10062-10068.
86. Xu, Z., et al., *Tunable electronic and optical behaviors of two-dimensional germanium carbide.* Applied Surface Science, 2016. **367**: p. 19-25.
87. Lin, S., et al., *Quasi-two-dimensional SiC and SiC2: interaction of silicon and carbon at atomic thin lattice plane.* The Journal of Physical Chemistry C, 2015. **119**(34): p. 19772-19779.
88. Lin, S., *Light-emitting two-dimensional ultrathin silicon carbide.* The Journal of Physical Chemistry C, 2012. **116**(6): p. 3951-3955.
89. Gao, X., et al., *A water splitting photocatalysis: blue phosphorus/g-GeC van der Waals heterostructure.* Applied Physics Letters, 2019. **114**(9): p. 093902.
90. Li, N. and J. Fan, *Computational insights into modulating the performance of MXene based electrode materials for rechargeable batteries.* Nanotechnology, 2021. **32**(25): p. 252001.
91. Yao, Y., et al., *Recent progress on emergent two-dimensional magnets and heterostructures.* Nanotechnology, 2021. **32**(47): p. 472001.
92. Tasnim, K.J., et al., *Insight into the stacking and the species-ordering dependences of interlayer bonding in SiC/GeC polar heterostructures.* Nanotechnology, 2022. **33**(15).
93. Pandey, R., et al., *A theoretical study of stability, electronic, and optical properties of GeC and SnC.* Journal of Applied Physics, 2000. **88**(11): p. 6462-6466.
94. Wang, X., et al., *Band alignments in sidewall strained Si/strained SiGe heterostructures.* Solid-State Electronics, 2002. **46**(12): p. 2021-2025.
95. Ajayan, P., P. Kim, and K. Banerjee, *van der Waals materials.* Phys. Today, 2016. **69**(9): p. 38.

96. Xia, W., et al., *Recent progress in van der Waals heterojunctions.* Nanoscale, 2017. **9**(13): p. 4324-4365.
97. Ju, L., et al., *Two-dimensional Janus van der Waals heterojunctions: A review of recent research progresses.* Frontiers of Physics, 2021. **16**: p. 1-16.
98. Zhang, Y.-n., et al., *2D van der Waals materials for ultrafast pulsed fiber lasers: Review and prospect.* Nanotechnology, 2021. **33**(8): p. 082003.
99. Seo, S., et al., *Recent progress in artificial synapses based on two-dimensional van der Waals materials for brain-inspired computing.* ACS Applied Electronic Materials, 2020. **2**(2): p. 371-388.
100. Zhang, J., et al., *Structural and electronic properties of interfaces in graphene and hexagonal boron nitride lateral heterostructures.* Chemistry of Materials, 2016. **28**(14): p. 5022-5028.
101. Liu, B., et al., *High-performance WSe2 field-effect transistors via controlled formation of in-plane heterojunctions.* Acs Nano, 2016. **10**(5): p. 5153-5160.
102. Cheng, K., et al., *2D lateral heterostructures of group-III monochalcogenide: Potential photovoltaic applications.* Applied Physics Letters, 2018. **112**(14): p. 143902.
103. Gong, Y., et al., *Vertical and in-plane heterostructures from WS 2/MoS 2 monolayers.* Nature materials, 2014. **13**(12): p. 1135-1142.
104. Aras, M., C.e. Kılıç, and S. Ciraci, *Lateral and vertical heterostructures of transition metal dichalcogenides.* The Journal of Physical Chemistry C, 2018. **122**(3): p. 1547-1555.
105. Huang, C., et al., *Lateral heterojunctions within monolayer MoSe 2–WSe 2 semiconductors.* Nature materials, 2014. **13**(12): p. 1096-1101.
106. Wang, J., et al., *Recent advances in 2D lateral heterostructures.* Nano-Micro Letters, 2019. **11**: p. 1-31.
107. Li, Y. and F. Ma, *Size and strain tunable band alignment of black–blue phosphorene lateral heterostructures.* Physical Chemistry Chemical Physics, 2017. **19**(19): p. 12466-12472.
108. Duan, X., et al., *Lateral epitaxial growth of two-dimensional layered semiconductor heterojunctions.* Nature nanotechnology, 2014. **9**(12): p. 1024-1030.
109. Ahammed, S., et al., *Lateral and flexural thermal transport in stanene/2D-SiC van der Waals heterostructure.* Nanotechnology, 2020. **31**(50): p. 505702.
110. Lotsch, B.V., *Vertical 2D heterostructures.* Annual Review of Materials Research, 2015. **45**: p. 85-109.
111. Georgiou, T., et al., *Vertical field-effect transistor based on graphene–WS2 heterostructures for flexible and transparent electronics.* Nature nanotechnology, 2013. **8**(2): p. 100-103.
112. Chhowalla, M., et al., *The chemistry of two-dimensional layered transition metal dichalcogenide nanosheets.* Nature chemistry, 2013. **5**(4): p. 263-275.
113. Zheng, W., et al., *Emerging van der Waals junctions based on TMDs materials for advanced gas sensors.* Coordination Chemistry Reviews, 2021. **447**: p. 214151.

114. Yang, S., et al., *Monolithic interface contact engineering to boost optoelectronic performances of 2D semiconductor photovoltaic heterojunctions.* Nano letters, 2020. **20**(4): p. 2443-2451.
115. Meng, F., et al., *Photodetectors Based on MoS 2/MAPbBr 3 van der Waals Heterojunction.* IEEE Electron Device Letters, 2022. **43**(3): p. 414-417.
116. Yang, S., et al., *2D Cu9S5/PtS2/WSe2 double heterojunction bipolar transistor with high current gain.* Advanced Materials, 2021. **33**(52): p. 2106537.
117. Rao, Y.C., S. Yu, and X.M. Duan, *Electrical and optical behaviors of SiC(GeC)/MoS(2) heterostructures: a first principles study*. Phys Chem Chem Phys, 2017. **19**(26): p. 17250-17255.
118. Cho, B., et al., *Chemical sensing of 2D graphene/MoS2 heterostructure device.* ACS applied materials & interfaces, 2015. **7**(30): p. 16775-16780.
119. Zhang, S., et al., *Rational design of nanoporous MoS2/VS2 heteroarchitecture for ultrahigh performance ammonia sensors.* Small, 2020. **16**(12): p. 1901718.
120. Chen, W.Y., et al., *Nanohybrids of a MXene and transition metal dichalcogenide for selective detection of volatile organic compounds.* Nature communications, 2020. **11**(1): p. 1302.
121. Loan, P.T.K., et al., *Graphene/MoS2 heterostructures for ultrasensitive detection of DNA hybridisation.* Advanced materials, 2014. **26**(28): p. 4838-4844.
122. Porezag, D. and M.R. Pederson, *Infrared intensities and Raman-scattering activities within density-functional theory*. Physical Review B, 1996. **54**(11): p. 7830.
123. Bader, R.F., *A quantum theory of molecular structure and its applications.* Chemical Reviews, 1991. **91**(5): p. 893-928.
124. Tang, W., E. Sanville, and G. Henkelman, *A grid-based Bader analysis algorithm without lattice bias.* Journal of Physics: Condensed Matter, 2009. **21**(8): p. 084204.
125. Yu, M. and D.R. Trinkle, *Accurate and efficient algorithm for Bader charge integration.* The Journal of chemical physics, 2011. **134**(6): p. 064111.
126. Heyd, J. and G.E. Scuseria, *Efficient hybrid density functional calculations in solids: Assessment of the Heyd–Scuseria–Ernzerhof screened Coulomb hybrid functional.* The Journal of chemical physics, 2004. **121**(3): p. 1187-1192.
127. Butt, H.-J., K. Graf, and M. Kappl, *Physics and chemistry of interfaces*. 2023: John Wiley & Sons.
128. Sun, M., et al., *Electronic properties of blue phosphorene/graphene and blue phosphorene/graphene-like gallium nitride heterostructures.* Physical Chemistry Chemical Physics, 2017. **19**(26): p. 17324-17330.
129. Cai, Y., G. Zhang, and Y.-W. Zhang, *Electronic properties of phosphorene/graphene and phosphorene/hexagonal boron nitride heterostructures.* The Journal of Physical Chemistry C, 2015. **119**(24): p. 13929-13936.
130. Xiong, W., et al., *Band engineering of the MoS2/stanene heterostructure: strain and electrostatic gating.* Nanotechnology, 2017. **28**(19): p. 195702.
131. Xu, L., et al., *Two-dimensional MoS2-graphene-based multilayer van der Waals heterostructures: enhanced charge transfer and optical absorption, and electric-*

field tunable Dirac point and band gap. Chemistry of Materials, 2017. **29**(13): p. 5504-5512.

132. Tang, K., et al., *Electronic properties of van der Waals heterostructure of black phosphorus and MoS2.* The Journal of Physical Chemistry C, 2018. **122**(12): p. 7027-7032.
133. Wang, Z., et al., *Combined strategies in structure-based virtual screening.* Physical Chemistry Chemical Physics, 2020. **22**(6): p. 3149-3159.
134. Wang, Z., et al., *2D van der Waals heterostructures of graphitic BCN as direct Z-scheme photocatalysts for overall water splitting: the role of polar π-conjugated moieties.* Physical Chemistry Chemical Physics, 2020. **22**(41): p. 23735-23742.
135. Hong, X., et al., *Ultrafast charge transfer in atomically thin MoS2/WS2 heterostructures.* Nature nanotechnology, 2014. **9**(9): p. 682-686.
136. Dean, C.R., et al., *Hofstadter's butterfly and the fractal quantum Hall effect in moiré superlattices.* Nature, 2013. **497**(7451): p. 598-602.
137. Yuan, J., et al., *Wafer-scale fabrication of two-dimensional PtS2/PtSe2 heterojunctions for efficient and broad band photodetection.* ACS applied materials & interfaces, 2018. **10**(47): p. 40614-40622.
138. Jin, W., et al., *Tuning the electronic structure of monolayer graphene/Mo S 2 van der Waals heterostructures via interlayer twist.* Physical Review B, 2015. **92**(20): p. 201409.
139. Wang, Z., Q. Chen, and J. Wang, *Electronic structure of twisted bilayers of graphene/MoS2 and MoS2/MoS2.* The Journal of Physical Chemistry C, 2015. **119**(9): p. 4752-4758.
140. Yankowitz, M., et al., *van der Waals heterostructures combining graphene and hexagonal boron nitride.* Nature Reviews Physics, 2019. **1**(2): p. 112-125.
141. Ponomarenko, L., et al., *Tunable metal–insulator transition in double-layer graphene heterostructures.* Nature Physics, 2011. **7**(12): p. 958-961.
142. Britnell, L., et al., *Field-effect tunneling transistor based on vertical graphene heterostructures.* Science, 2012. **335**(6071): p. 947-950.
143. Islam, M.R., et al., *Superior tunable photocatalytic properties for water splitting in two dimensional GeC/SiC van der Waals heterobilayers.* Scientific reports, 2021. **11**(1): p. 17739.
144. Zhou, J., et al., *Multi-stimuli-responsive synapse based on vertical van der Waals heterostructures.* ACS Applied Materials & Interfaces, 2022. **14**(31): p. 35917-35926.
145. Mohanta, M.K., A. Kishore, and A. De Sarkar, *Two-dimensional ultrathin van der Waals heterostructures of indium selenide and boron monophosphide for superfast nanoelectronics, excitonic solar cells, and digital data storage devices.* Nanotechnology, 2020. **31**(49): p. 495208.
146. Manzeli, S., et al., *2D transition metal dichalcogenides.* Nature Reviews Materials, 2017. **2**(8): p. 1-15.
147. Ramasubramaniam, A., D. Naveh, and E. Towe, *Tunable band gaps in bilayer transition-metal dichalcogenides.* Physical Review B, 2011. **84**(20): p. 205325.
148. Zhou, C., et al., *Carrier type control of WSe2 field-effect transistors by thickness modulation and MoO3 layer doping.* Advanced functional materials, 2016. **26**(23): p. 4223-4230.

149. Drissi, L., F. Ramadan, and N.B.-J. Kanga, *Optoelectronic properties in 2D GeC and SiC hybrids: DFT and many body effect calculations.* Materials Research Express, 2018. **5**(1): p. 015061.
150. Chagarov, E., et al., *Density-functional theory molecular dynamics simulations and experimental characterization of a-Al2O3/SiGe interfaces.* ACS applied materials & interfaces, 2015. **7**(47): p. 26275-26283.
151. Lazić, P., *CellMatch: Combining two unit cells into a common supercell with minimal strain.* Computer Physics Communications, 2015. **197**: p. 324-334.
152. Grimme, S., *Semiempirical GGA-type density functional constructed with a long-range dispersion correction.* Journal of computational chemistry, 2006. **27**(15): p. 1787-1799.
153. Grimme, S., S. Ehrlich, and L. Goerigk, *Effect of the damping function in dispersion corrected density functional theory.* Journal of computational chemistry, 2011. **32**(7): p. 1456-1465.
154. Grimme, S., et al., *A consistent and accurate ab initio parametrization of density functional dispersion correction (DFT-D) for the 94 elements H-Pu.* The Journal of chemical physics, 2010. **132**(15): p. 154104.
155. Sasson, A., F. Viloria, and F. Aboytes, *Optimal load flow solution using the Hessian matrix.* IEEE Transactions on Power Apparatus and Systems, 1973(1): p. 31-41.
156. Tangi, M., et al., *Type-I band alignment at MoS2/In0. 15Al0. 85N lattice matched heterojunction and realization of MoS2 quantum well.* Applied Physics Letters, 2017. **111**(9): p. 092104.
157. Bellus, M.Z., et al., *Type-I van der Waals heterostructure formed by MoS 2 and ReS 2 monolayers.* Nanoscale Horizons, 2017. **2**(1): p. 31-36.
158. Oster, G., M. Wasserman, and C. Zwerling, *Theoretical interpretation of moiré patterns.* Josa, 1964. **54**(2): p. 169-175.
159. Reguzzoni, M., et al., *Potential energy surface for graphene on graphene: Ab initio derivation, analytical description, and microscopic interpretation.* Physical Review B, 2012. **86**(24): p. 245434.
160. Lin, M.-L., et al., *Moiré phonons in twisted bilayer MoS2.* Acs Nano, 2018. **12**(8): p. 8770-8780.
161. Cao, Y., et al., *Pauli-limit violation and re-entrant superconductivity in moiré graphene.* Nature, 2021. **595**(7868): p. 526-531.
162. Shibuta, Y. and J.A. Elliott, *Interaction between two graphene sheets with a turbostratic orientational relationship.* Chemical Physics Letters, 2011. **512**(4-6): p. 146-150.
163. Tartaglino, U., V.N. Samoilov, and B.N. Persson, *Role of surface roughness in superlubricity.* Journal of Physics: Condensed Matter, 2006. **18**(17): p. 4143.
164. Popov, A.M., et al., *Barriers to motion and rotation of graphene layers based on measurements of shear mode frequencies.* Chemical Physics Letters, 2012. **536**: p. 82-86.
165. Martin, J.-M., *Superlubricity of molybdenum disulfide,* in *Superlubricity*. 2007, Elsevier. p. 207-225.

166. Onodera, T., et al., *A computational chemistry study on friction of h-MoS2. Part II. Friction anisotropy.* The Journal of Physical Chemistry B, 2010. **114**(48): p. 15832-15838.
167. Wu, X., et al., *The deposition and optical properties of Ge1− xCx thin film and infrared multilayer antireflection coatings.* Thin Solid Films, 2008. **516**(10): p. 3189-3195.
168. Yuan, H. and R.S. Williams, *Synthesis by laser ablation and characterization of pure germanium-carbon alloy thin films.* Chemistry of materials, 1993. **5**(4): p. 479-485.
169. Din, H., et al., *Rashba spin splitting and photocatalytic properties of GeC− M SSe (M= Mo, W) van der Waals heterostructures.* Physical Review B, 2019. **100**(16): p. 165425.
170. Liu, R., et al., *Moiré tuning of the dynamic behavior of a twisted bilayer van der Waals material resonator.* Journal of Applied Mechanics, 2022. **89**(12): p. 121001.
171. Giannozzi, P. and C. Cavazzoni, *Large-scale computing with Quantum ESPRESSO.* Il nuovo cimento C, 2009. **32**(2): p. 49-52.
172. *QUANTUM ESPRESSO.* 2023 [cited 2023 03/23]; Available from: https://www.quantum-espresso.org/.
173. Ji, Y., et al., *Monolayer graphitic germanium carbide (g-GeC): the promising cathode catalyst for fuel cell and lithium–oxygen battery applications.* Journal of Materials Chemistry A, 2018. **6**(5): p. 2212-2218.
174. Giannozzi, P., et al., *QUANTUM ESPRESSO: a modular and open-source software project for quantum simulations of materials.* Journal of physics: Condensed matter, 2009. **21**(39): p. 395502.

APPENDIX

Appendix A: Band structures of SiC, GeC, and $SiGe$ pristine sheets under various strains

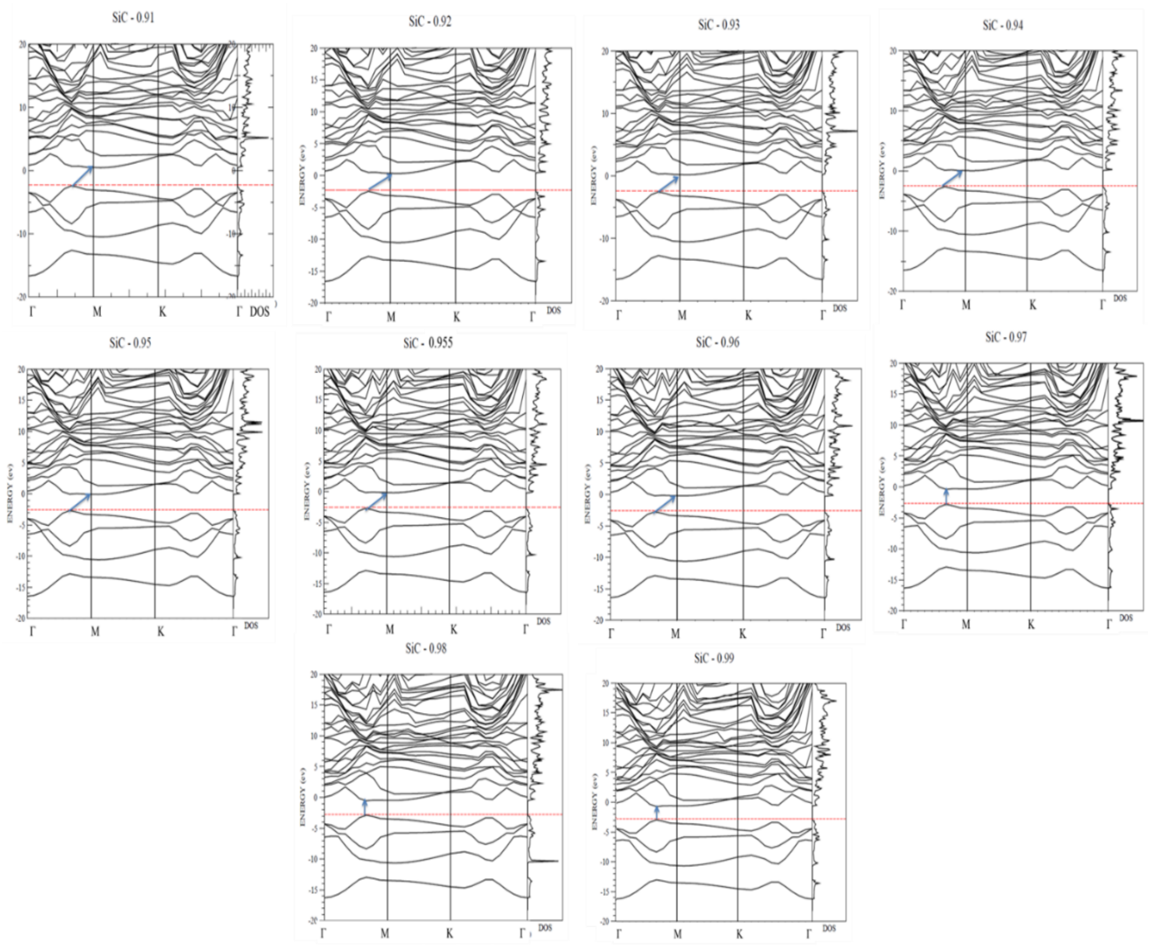

.

Figure A-1: The band structures of SiC pristine sheet under various strains. The index on each top of the band structure denotes the ratio of lattice constant a to the reference value of a_0 ($a_0 = 3.235$ Å). The blue arrows indicate the direct/indirect band gaps and red-dashed lines are fermi levels, respectively.

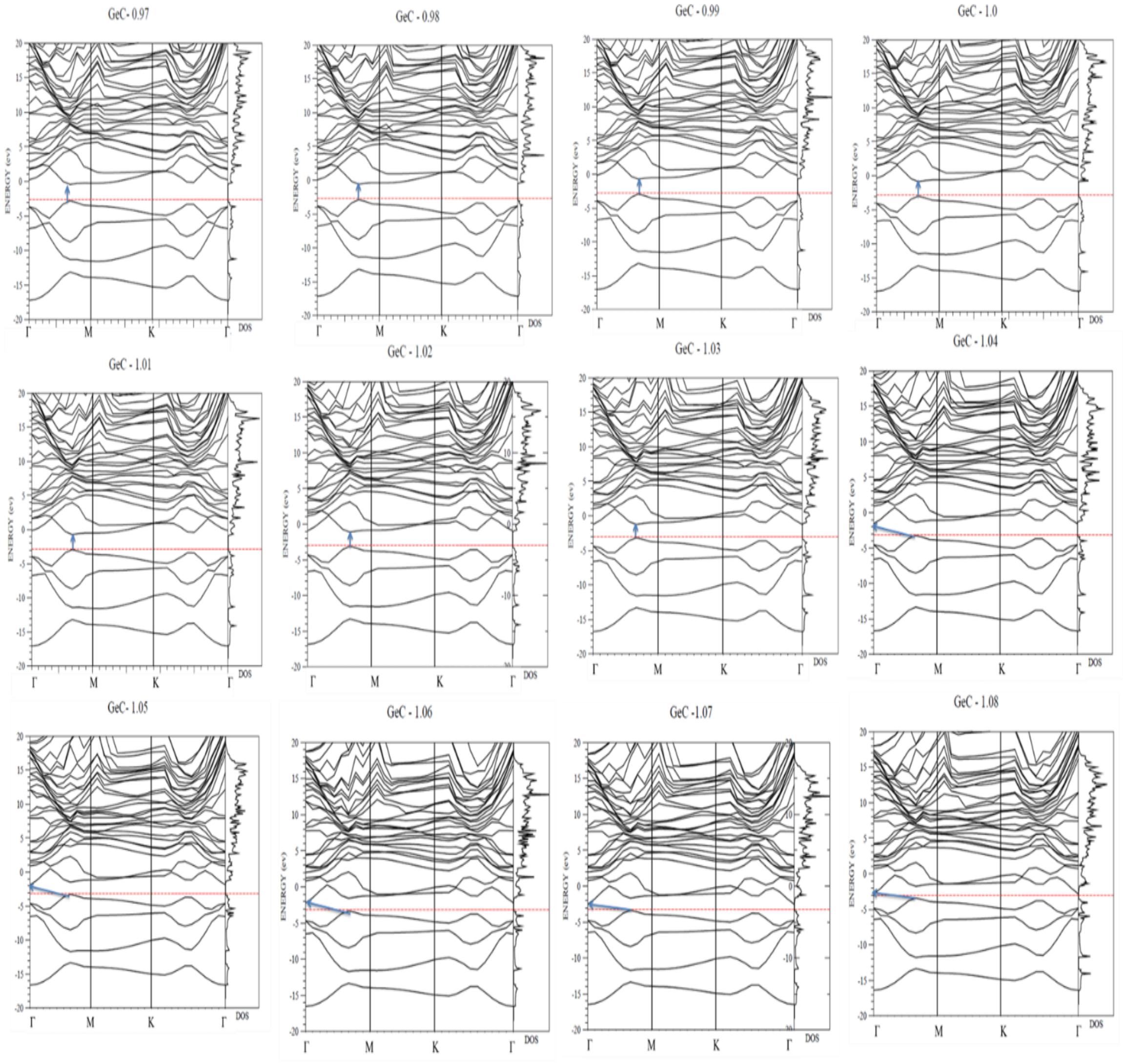

Figure A-2:The band structures of GeC pristine sheet under various strains. The index on each top of the band structure denotes the ratio of lattice constant a to the reference value of a_0 ($a_0 = 3.235$ Å). The blue arrows indicate the direct/indirect band gaps and red-dashed lines are fermi levels, respectively.

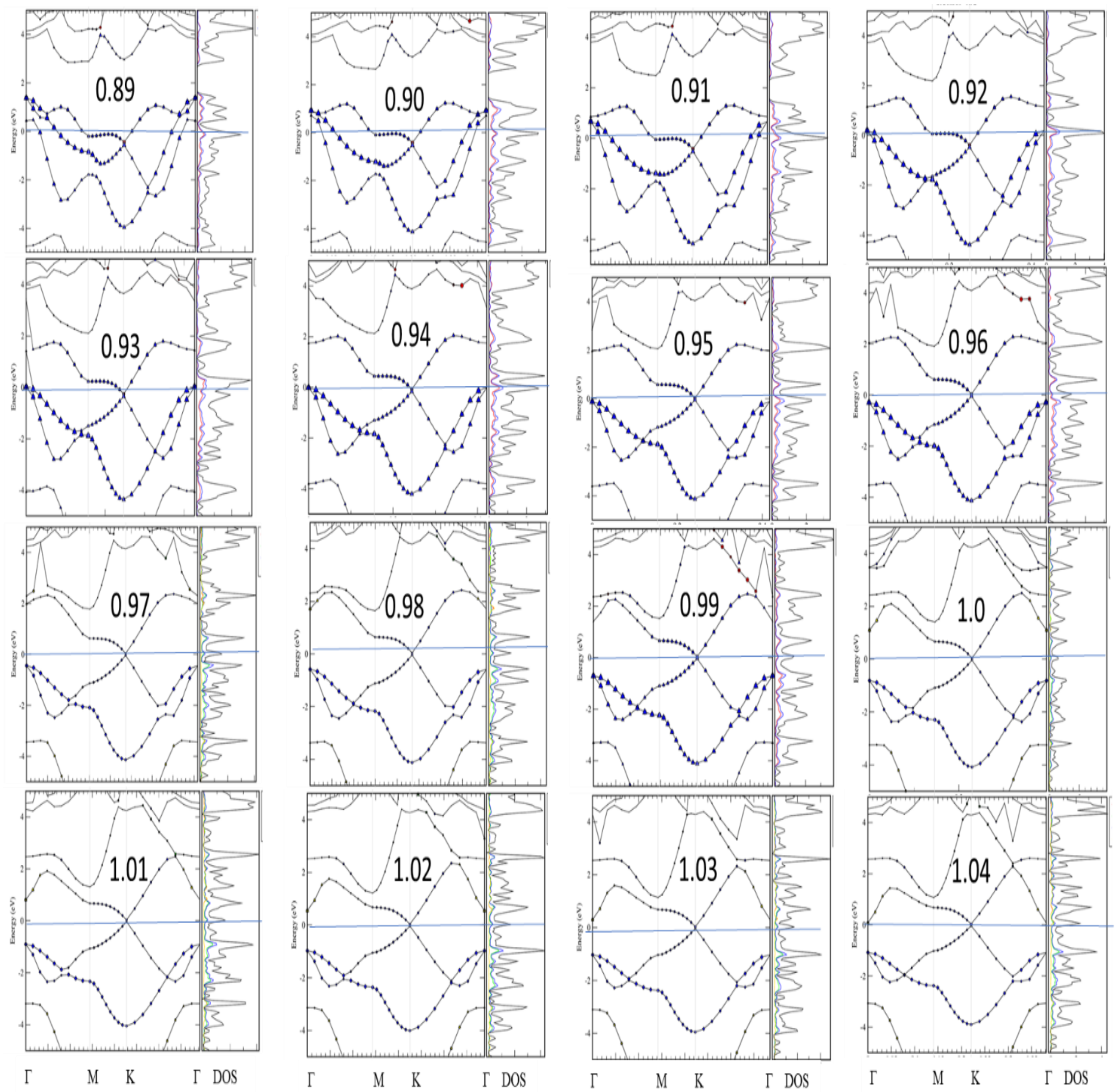

Figure A-3: The band structures of $SiGe$ pristine sheet under various strains. The number on each of the band structure denotes the ratio of lattice constant a to the reference value of a_0 ($a_0 = 3.951$ Å). The blue lines are fermi levels.

Appendix B: The net charge distribution analysis of SiGe/GeC-VH with four patterns.

Table B-1: The charge distribution analyses of SiGe/GeC-VH (I-CGe_SiGe pattern) for the top GeC layer (left panel), the bottom SiGe layer (right bottom panel), and the summary of the charge analysis (right top panel), respectively. The notations regarding to 'net_charge' denote the net charge transfer between atoms, and the notations regarding to 'diff_net_charge denote the difference of the net charge transfer between atoms on the SiGe/GeC-VH and on the corresponding pristine sheets.

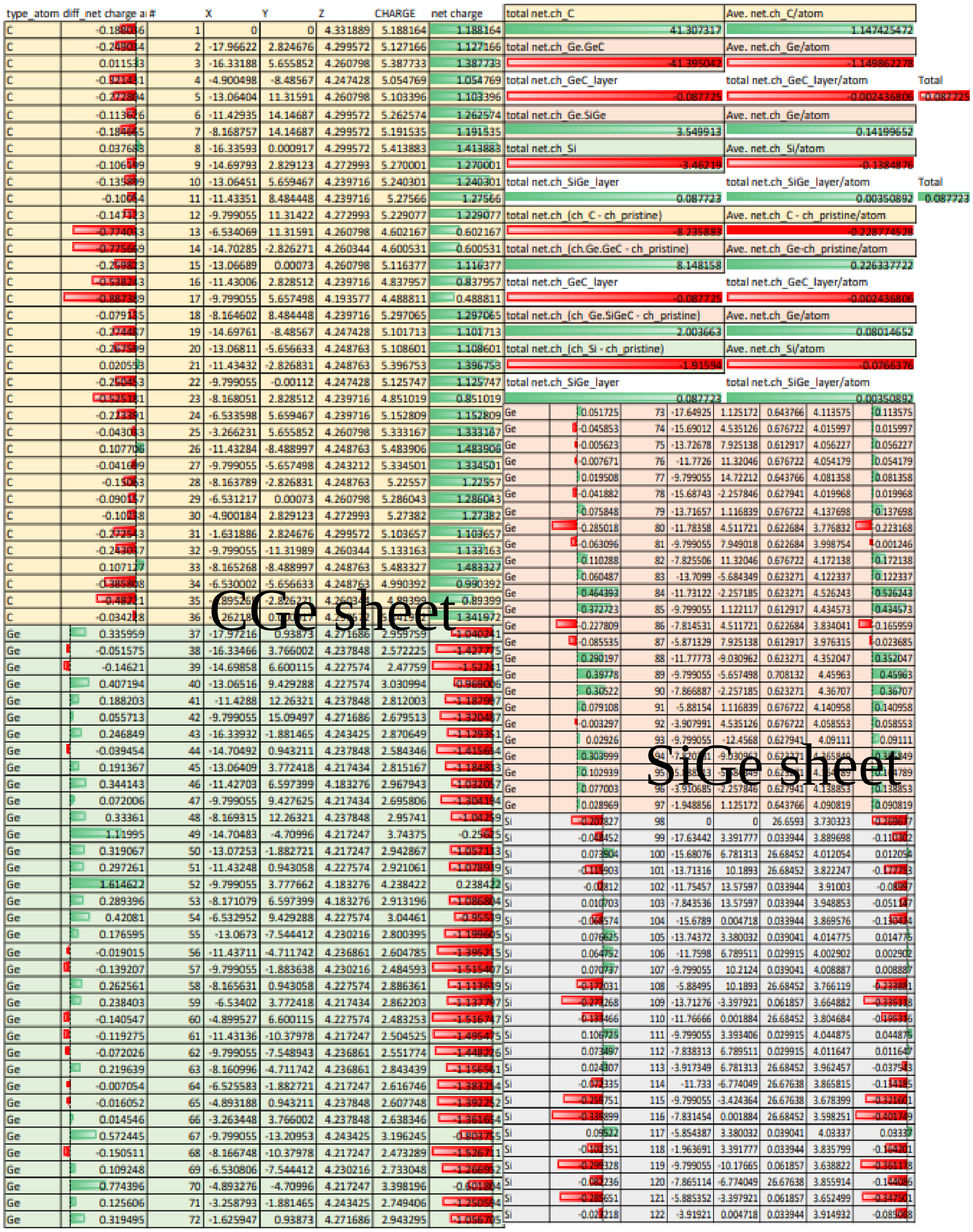

type_atom	diff_net charge ai	#	X	Y	Z	CHARGE	net charge
C	-0.188036	1	0	0	4.331889	5.188164	1.188164
C	-0.249034	2	-17.96622	2.824676	4.299572	5.127166	1.127166
C	0.011533	3	-16.33188	5.655852	4.260798	5.387733	1.387733
C	-0.321431	4	-4.900498	-8.48567	4.247428	5.054769	1.054769
C	-0.272804	5	-13.06404	11.31591	4.260798	5.103396	1.103396
C	-0.113626	6	-11.42935	14.14687	4.299572	5.262574	1.262574
C	-0.184465	7	-8.168757	14.14687	4.299572	5.191535	1.191535
C	0.037683	8	-16.33593	0.000917	4.299572	5.413883	1.413883
C	-0.106199	9	-14.69793	2.829123	4.272993	5.270001	1.270001
C	-0.135899	10	-13.06451	5.659467	4.239716	5.240301	1.240301
C	-0.10054	11	-11.43351	8.484448	4.239716	5.27566	1.27566
C	-0.147123	12	-9.799055	11.31422	4.272993	5.229077	1.229077
C	-0.774033	13	-6.534069	11.31591	4.260798	4.602167	0.602167
C	-0.775669	14	-14.70285	-2.826271	4.260344	4.600531	0.600531
C	-0.259823	15	-13.06689	0.00073	4.260798	5.116377	1.116377
C	-0.538243	16	-11.43006	2.828512	4.239716	4.837957	0.837957
C	-0.887389	17	-9.799055	5.657498	4.193577	4.488811	0.488811
C	-0.079135	18	-8.164602	8.484448	4.239716	5.297065	1.297065
C	-0.274487	19	-14.69761	-8.48567	4.247428	5.101713	1.101713
C	-0.267599	20	-13.06811	-5.656633	4.248763	5.108601	1.108601
C	0.020593	21	-11.43432	-2.826831	4.248763	5.396753	1.396753
C	-0.250453	22	-9.799055	-0.00112	4.247428	5.125747	1.125747
C	-0.525181	23	-8.168051	2.828512	4.239716	4.851019	0.851019
C	-0.223391	24	-6.533598	5.659467	4.239716	5.152809	1.152809
C	-0.043083	25	-3.266231	5.655852	4.260798	5.333167	1.333167
C	0.107706	26	-11.43284	-8.488997	4.248763	5.483906	1.483906
C	-0.041699	27	-9.799055	-5.657498	4.243212	5.334501	1.334501
C	-0.15063	28	-8.163789	-2.826831	4.248763	5.22557	1.22557
C	-0.090157	29	-6.531217	0.00073	4.260798	5.286043	1.286043
C	-0.10238	30	-4.900184	2.829123	4.272993	5.27382	1.27382
C	-0.272543	31	-1.631886	2.824676	4.299572	5.103657	1.103657
C	-0.243067	32	-9.799055	-11.31989	4.260344	5.133163	1.133163
C	0.107127	33	-8.165268	-8.488997	4.248763	5.483327	1.483327
C	-0.385898	34	-6.530002	-5.656633	4.248763	4.990392	0.990392
C	-0.48221	35	[illegible]	-2.826271	4.260344	4.89399	0.89399
C	-0.034228	36	[illegible]	[illegible]	[illegible]	[illegible]	1.341972
Ge	0.335959	37	-17.97216	0.93873	4.271686	2.959759	-1.040241
Ge	-0.051575	38	-16.33466	3.766002	4.237848	2.572225	-1.427775
Ge	-0.14621	39	-14.69858	6.600115	4.227574	2.47759	-1.52241
Ge	0.407194	40	-13.06516	9.429288	4.227574	3.030994	-0.969006
Ge	0.188203	41	-11.4288	12.26321	4.237848	2.812003	-1.187997
Ge	0.055713	42	-9.799055	15.09497	4.271686	2.679513	-1.320487
Ge	0.246849	43	-16.33932	-1.881465	4.243425	2.870649	-1.129351
Ge	-0.039454	44	-14.70492	0.943211	4.237848	2.584346	-1.415654
Ge	0.191367	45	-13.06409	3.772418	4.217434	2.815167	-1.184833
Ge	0.344143	46	-11.42703	6.597399	4.183276	2.967943	-1.032057
Ge	0.072006	47	-9.799055	9.427625	4.217434	2.695806	-1.304194
Ge	0.33361	48	-8.169315	12.26321	4.237848	2.95741	-1.04259
Ge	1.11995	49	-14.70483	-4.70996	4.217247	3.74375	-0.25625
Ge	0.319067	50	-13.07253	-1.882721	4.217247	2.942867	-1.057133
Ge	0.297261	51	-11.43248	0.943058	4.227574	2.921061	-1.078939
Ge	1.614622	52	-9.799055	3.777662	4.183276	4.238422	0.238422
Ge	0.289396	53	-8.171079	6.597399	4.183276	2.913196	-1.086804
Ge	0.42081	54	-6.532952	9.429288	4.227574	3.04461	-0.95539
Ge	0.176595	55	-13.0673	-7.544412	4.230216	2.800395	-1.199605
Ge	-0.019015	56	-11.43711	-4.711742	4.236861	2.604785	-1.395215
Ge	-0.139207	57	-9.799055	-1.883638	4.230216	2.484593	-1.515407
Ge	0.262561	58	-8.165631	0.943058	4.227574	2.886361	-1.113639
Ge	0.238403	59	-6.53402	3.772418	4.217434	2.862203	-1.137797
Ge	-0.140547	60	-4.899527	6.600115	4.227574	2.483253	-1.516747
Ge	-0.119275	61	-11.43136	-10.37978	4.217247	2.504525	-1.495475
Ge	-0.072026	62	-9.799055	-7.548943	4.236861	2.551774	-1.448226
Ge	0.219639	63	-8.160996	-4.711742	4.236861	2.843439	-1.156561
Ge	-0.007054	64	-6.525583	-1.882721	4.217247	2.616746	-1.383254
Ge	-0.016052	65	-4.893188	0.943211	4.237848	2.607748	-1.392252
Ge	0.014546	66	-3.263448	3.766002	4.237848	2.638346	-1.361654
Ge	0.572445	67	-9.799055	-13.20953	4.243425	3.196245	-0.803755
Ge	-0.150511	68	-8.166748	-10.37978	4.217247	2.473289	-1.526711
Ge	0.109248	69	-6.530806	-7.544412	4.230216	2.733048	-1.266952
Ge	0.774396	70	-4.893276	-4.70996	4.217247	3.398196	-0.601804
Ge	0.125606	71	-3.258793	-1.881465	4.243425	2.749406	-1.250594
Ge	0.319495	72	-1.625947	0.93873	4.271686	2.943295	-1.056705
Ge	0.051725	73	-17.64925	1.125172	0.643766	4.113575	0.113575
Ge	-0.045853	74	-15.69012	4.535126	0.676722	4.015997	0.015997
Ge	-0.005623	75	-13.72678	7.925138	0.612917	4.056227	0.056227
Ge	-0.007671	76	-11.7726	11.32046	0.676722	4.054179	0.054179
Ge	0.019508	77	-9.799055	14.72212	0.643766	4.081358	0.081358
Ge	-0.041882	78	-15.68743	-2.257846	0.627941	4.019968	0.019968
Ge	0.075848	79	-13.71657	1.116839	0.676722	4.137698	0.137698
Ge	-0.285018	80	-11.78358	4.511721	0.622684	3.776832	-0.223168
Ge	-0.063096	81	-9.799055	7.949018	0.622684	3.998754	-0.001246
Ge	0.110288	82	-7.825506	11.32046	0.676722	4.172138	0.172138
Ge	0.060487	83	-13.7099	-5.684349	0.623271	4.122337	0.122337
Ge	0.464393	84	-11.73122	-2.257185	0.623271	4.526243	0.526243
Ge	0.372723	85	-9.799055	1.122117	0.612917	4.434573	0.434573
Ge	-0.227809	86	-7.814531	4.511721	0.622684	3.834041	-0.165959
Ge	-0.085535	87	-5.871329	7.925138	0.612917	3.976315	-0.023685
Ge	0.290197	88	-11.77773	-9.030962	0.623271	4.352047	0.352047
Ge	0.39778	89	-9.799055	-5.657498	0.708132	4.45963	0.45963
Ge	0.30522	90	-7.866887	-2.257185	0.623271	4.36707	0.36707
Ge	0.079108	91	-5.88154	1.116839	0.676722	4.140958	0.140958
Ge	-0.003297	92	-3.907991	4.535126	0.676722	4.058553	0.058553
Ge	0.02926	93	-9.799055	-12.4568	0.627941	4.09111	0.09111
Ge	0.303999	94	[illegible]	-9.030962	0.623271	4.365849	0.365849
Ge	0.102939	95	[illegible]	[illegible]	[illegible]	[illegible]	[illegible]
Ge	0.077003	96	-3.910685	-2.257846	0.627941	4.138853	0.138853
Ge	0.028969	97	-1.948856	1.125172	0.643766	4.090819	0.090819
Si	-0.207827	98	0	0	26.6593	3.730323	-0.269677
Si	-0.048452	99	-17.63442	3.391777	0.033944	3.889698	-0.110302
Si	0.073904	100	-15.68076	6.781313	26.68452	4.012054	0.012054
Si	-0.115903	101	-13.71316	10.1893	26.68452	3.822247	-0.177753
Si	-0.028812	102	-11.75457	13.57597	0.033944	3.91003	-0.08997
Si	0.010703	103	-7.843536	13.57597	0.033944	3.948853	-0.051147
Si	-0.068574	104	-15.6789	0.004718	0.033944	3.869576	-0.130424
Si	0.076625	105	-13.74372	3.380032	0.039041	4.014775	0.014775
Si	0.064752	106	-11.7598	6.789511	0.029915	4.002902	0.002902
Si	0.070737	107	-9.799055	10.2124	0.039041	4.008887	0.008887
Si	-0.172031	108	-5.88495	10.1893	26.68452	3.766119	-0.233881
Si	-0.273268	109	-13.71276	-3.397921	0.061857	3.664882	-0.335118
Si	-0.133466	110	-11.76666	0.001884	26.68452	3.804684	-0.195316
Si	0.106725	111	-9.799055	3.393406	0.029915	4.044875	0.044875
Si	0.073497	112	-7.838313	6.789511	0.029915	4.011647	0.011647
Si	0.024307	113	-3.917349	6.781313	26.68452	3.962457	-0.037543
Si	-0.072335	114	-11.733	-6.774049	26.67638	3.865815	-0.134185
Si	-0.259751	115	-9.799055	-3.424364	26.67638	3.678399	-0.321601
Si	-0.339899	116	-7.831454	0.001884	26.68452	3.598251	-0.401749
Si	0.09522	117	-5.854387	3.380032	0.039041	4.03337	0.03337
Si	-0.102351	118	-1.963691	3.391777	0.033944	3.835799	-0.164201
Si	-0.299328	119	-9.799055	-10.17665	0.061857	3.638822	-0.361178
Si	-0.082236	120	-7.865114	-6.774049	26.67638	3.855914	-0.144086
Si	-0.285651	121	-5.885352	-3.397921	0.061857	3.652499	-0.347501
Si	-0.023218	122	-3.91921	0.004718	0.033944	3.914932	-0.085068

total net.ch_C	Ave. net.ch_C/atom	
41.307317	1.147425472	
total net.ch_Ge.GeC	Ave. net.ch_Ge/atom	
-41.395042	-1.149862278	
total net.ch_GeC_layer	total net.ch_GeC_layer/atom	Total
-0.087725	-0.002436806	-0.087725
total net.ch_Ge.SiGe	Ave. net.ch_Ge/atom	
3.549913	0.14199652	
total net.ch_Si	Ave. net.ch_Si/atom	
-3.46219	-0.1384876	
total net.ch_SiGe_layer	total net.ch_SiGe_layer/atom	Total
0.087723	0.00350892	0.087723
total net.ch_(ch_C - ch_pristine)	Ave. net.ch_C - ch_pristine/atom	
-8.235883	-0.228774528	
total net.ch_(ch.Ge.GeC - ch_pristine)	Ave. net.ch_Ge-ch_pristine/atom	
8.148158	0.226337722	
total net.ch_GeC_layer	total net.ch_GeC_layer/atom	
-0.087725	-0.002436806	
total net.ch_(ch_Ge.SiGeC - ch_pristine)	Ave. net.ch_Ge/atom	
2.003663	0.08014652	
total net.ch_(ch_Si - ch_pristine)	Ave. net.ch_Si/atom	
-1.91594	-0.0766376	
total net.ch_SiGe_layer	total net.ch_SiGe_layer/atom	
0.087723	0.00350892	

Table B-2 The charge distribution analyses of SiGe/GeC-VH (II-CGe_GeSi pattern) for the top GeC layer (left panel), the bottom SiGe layer (right bottom panel), and the summary of the charge analysis (right top panel), respectively. The notations regarding to 'net_charge' denote the net charge transfer between atoms, and the notations regarding to 'diff_net_charge denote the difference of the net charge transfer between atoms on the SiGe/GeC-VH and on the corresponding pristine sheets.

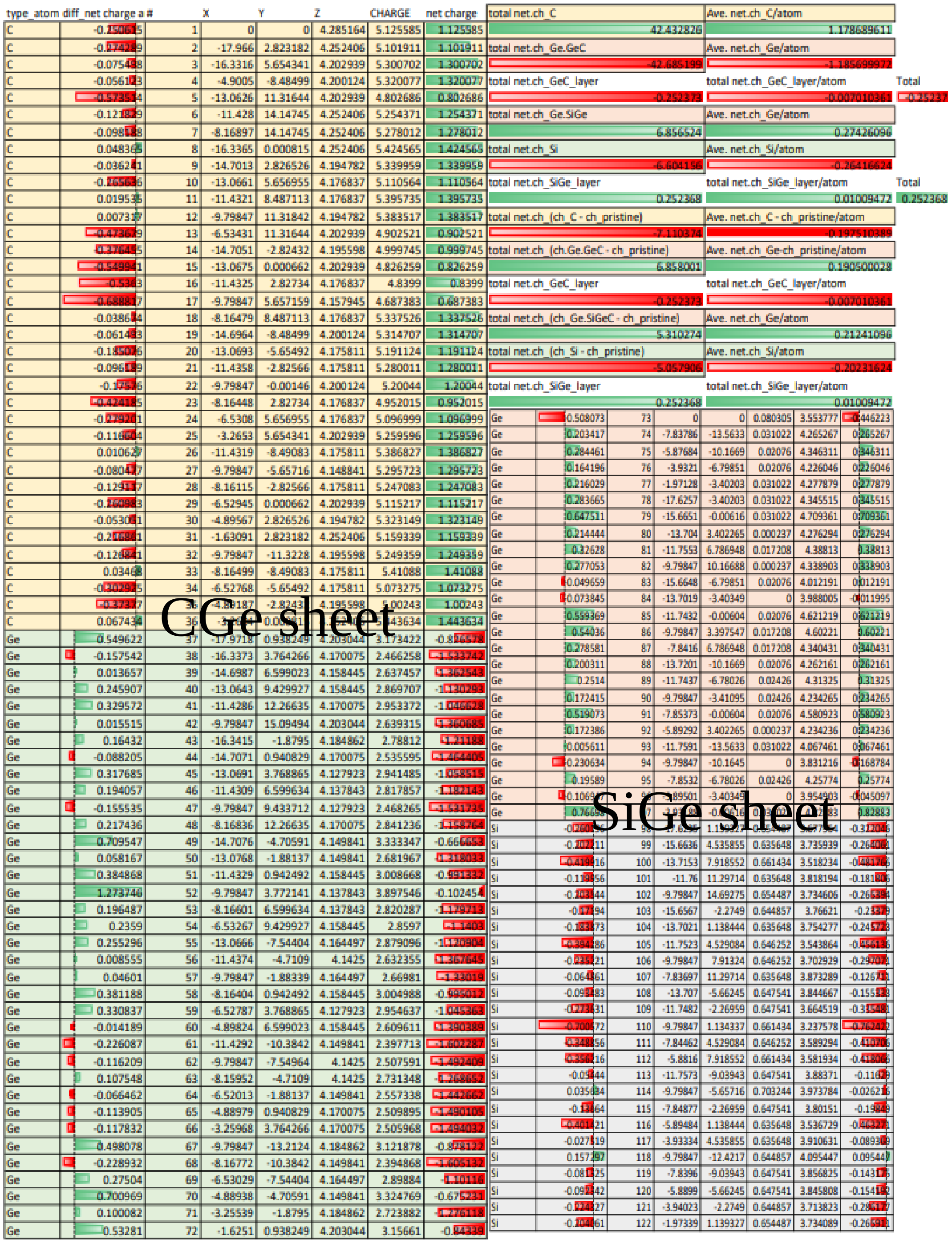

type_atom	diff_net charge	a #	X	Y	Z	CHARGE	net charge
C	-0.250615	1	0	0	4.285164	5.125585	1.125585
C	-0.274289	2	-17.966	2.823182	4.252406	5.101911	1.101911
C	-0.075498	3	-16.3316	5.654341	4.202939	5.300702	1.300702
C	-0.056123	4	-4.9005	-8.48499	4.200124	5.320077	1.320077
C	-0.573514	5	-13.0626	11.31644	4.202939	4.802686	0.802686
C	-0.121829	6	-11.428	14.14745	4.252406	5.254371	1.254371
C	-0.098188	7	-8.16897	14.14745	4.252406	5.278012	1.278012
C	0.048365	8	-16.3365	0.000815	4.252406	5.424565	1.424565
C	-0.036241	9	-14.7013	2.826526	4.194782	5.339959	1.339959
C	-0.265636	10	-13.0661	5.656955	4.176837	5.110564	1.110564
C	0.019535	11	-11.4321	8.487113	4.176837	5.395735	1.395735
C	0.007317	12	-9.79847	11.31842	4.194782	5.383517	1.383517
C	-0.473679	13	-6.53431	11.31644	4.202939	4.902521	0.902521
C	-0.376455	14	-14.7051	-2.82432	4.195598	4.999745	0.999745
C	-0.549941	15	-13.0675	0.000662	4.202939	4.826259	0.826259
C	-0.5343	16	-11.4325	2.82734	4.176837	4.8399	0.8399
C	-0.688817	17	-9.79847	5.657159	4.157945	4.687383	0.687383
C	-0.038674	18	-8.16479	8.487113	4.176837	5.337526	1.337526
C	-0.061493	19	-14.6964	-8.48499	4.200124	5.314707	1.314707
C	-0.185076	20	-13.0693	-5.65492	4.175811	5.191124	1.191124
C	-0.096189	21	-11.4358	-2.82566	4.175811	5.280011	1.280011
C	-0.17576	22	-9.79847	-0.00146	4.200124	5.20044	1.20044
C	-0.424185	23	-8.16448	2.82734	4.176837	4.952015	0.952015
C	-0.279201	24	-6.5308	5.656955	4.176837	5.096999	1.096999
C	-0.116604	25	-3.2653	5.654341	4.202939	5.259596	1.259596
C	0.010627	26	-11.4319	-8.49083	4.175811	5.386827	1.386827
C	-0.080477	27	-9.79847	-5.65716	4.148841	5.295723	1.295723
C	-0.129117	28	-8.16115	-2.82566	4.175811	5.247083	1.247083
C	-0.260983	29	-6.52945	0.000662	4.202939	5.115217	1.115217
C	-0.053081	30	-4.89567	2.826526	4.194782	5.323149	1.323149
C	-0.216881	31	-1.63091	2.823182	4.252406	5.159339	1.159339
C	-0.126841	32	-9.79847	-11.3228	4.195598	5.249359	1.249359
C	0.03468	33	-8.16499	-8.49083	4.175811	5.41088	1.41088
C	-0.202975	34	-6.52768	-5.65492	4.175811	5.073275	1.073275
C	-0.373727	35	-4.89187	-2.82432	4.195598	5.00243	1.00243
C	0.067434	36	[illegible]	[illegible]	[illegible]	5.443634	1.443634
Ge	0.549622	37	-17.9718	0.938249	4.203044	3.173422	-0.826578
Ge	-0.157542	38	-16.3373	3.764266	4.170075	2.466258	-1.533742
Ge	0.013657	39	-14.6987	6.599023	4.158445	2.637457	-1.362543
Ge	0.245907	40	-13.0643	9.429927	4.158445	2.869707	-1.130293
Ge	0.329572	41	-11.4286	12.26635	4.170075	2.953372	-1.046628
Ge	0.015515	42	-9.79847	15.09494	4.203044	2.639315	-1.360685
Ge	0.16432	43	-16.3415	-1.8795	4.184862	2.78812	-1.21188
Ge	-0.088205	44	-14.7071	0.940829	4.170075	2.535595	-1.464405
Ge	0.317685	45	-13.0691	3.768865	4.127923	2.941485	-1.058515
Ge	0.194057	46	-11.4309	6.599634	4.137843	2.817857	-1.182143
Ge	-0.155535	47	-9.79847	9.433712	4.127923	2.468265	-1.531735
Ge	0.217436	48	-8.16836	12.26635	4.170075	2.841236	-1.158764
Ge	0.709547	49	-14.7076	-4.70591	4.149841	3.333347	-0.666653
Ge	0.058167	50	-13.0768	-1.88137	4.149841	2.681967	-1.318033
Ge	0.384868	51	-11.4329	0.942492	4.158445	3.008668	-0.991332
Ge	1.273746	52	-9.79847	3.772141	4.137843	3.897546	-0.102454
Ge	0.196487	53	-8.16601	6.599634	4.137843	2.820287	-1.179713
Ge	0.2359	54	-6.53267	9.429927	4.158445	2.8597	-1.1403
Ge	0.255296	55	-13.0666	-7.54404	4.164497	2.879096	-1.120904
Ge	0.008555	56	-11.4374	-4.7109	4.1425	2.632355	-1.367645
Ge	0.04601	57	-9.79847	-1.88339	4.164497	2.66981	-1.33019
Ge	0.381188	58	-8.16404	0.942492	4.158445	3.004988	-0.995012
Ge	0.330837	59	-6.52787	3.768865	4.127923	2.954637	-1.045363
Ge	-0.014189	60	-4.89824	6.599023	4.158445	2.609611	-1.390389
Ge	-0.226087	61	-11.4292	-10.3842	4.149841	2.397713	-1.602287
Ge	-0.116209	62	-9.79847	-7.54964	4.1425	2.507591	-1.492409
Ge	0.107548	63	-8.15952	-4.7109	4.1425	2.731348	-1.268652
Ge	-0.066462	64	-6.52013	-1.88137	4.149841	2.557338	-1.442662
Ge	-0.113905	65	-4.88979	0.940829	4.170075	2.509895	-1.490105
Ge	-0.117832	66	-3.25968	3.764266	4.170075	2.505968	-1.494032
Ge	0.498078	67	-9.79847	-13.2124	4.184862	3.121878	-0.878122
Ge	-0.228932	68	-8.16772	-10.3842	4.149841	2.394868	-1.605132
Ge	0.27504	69	-6.53029	-7.54404	4.164497	2.89884	-1.10116
Ge	0.700969	70	-4.88938	-4.70591	4.149841	3.324769	-0.675231
Ge	0.100082	71	-3.25539	-1.8795	4.184862	2.723882	-1.276118
Ge	0.53281	72	-1.6251	0.938249	4.203044	3.15661	-0.84339

CGe sheet

total net.ch_C	Ave. net.ch_C/atom	
42.432826	1.178689611	
total net.ch_Ge.GeC	Ave. net.ch_Ge/atom	
-42.685199	-1.185699972	
total net.ch_GeC_layer	total net.ch_GeC_layer/atom	Total
-0.252373	-0.007010361	-0.25237
total net.ch_Ge.SiGe	Ave. net.ch_Ge/atom	
6.856524	0.27426096	
total net.ch_Si	Ave. net.ch_Si/atom	
-6.604156	-0.26416624	
total net.ch_SiGe_layer	total net.ch_SiGe_layer/atom	Total
0.252368	0.01009472	0.252368
total net.ch_(ch_C - ch_pristine)	Ave. net.ch_C - ch_pristine/atom	
-7.110374	-0.197510389	
total net.ch_(ch.Ge.GeC - ch_pristine)	Ave. net.ch_Ge-ch_pristine/atom	
6.858001	0.190500028	
total net.ch_GeC_layer	total net.ch_GeC_layer/atom	
-0.252373	-0.007010361	
total net.ch_(ch_Ge.SiGeC - ch_pristine)	Ave. net.ch_Ge/atom	
5.310274	0.21241096	
total net.ch_(ch_Si - ch_pristine)	Ave. net.ch_Si/atom	
-5.057906	-0.20231624	
total net.ch_SiGe_layer	total net.ch_SiGe_layer/atom	
0.252368	0.01009472	

Ge	-0.508073	73	0	0	0.080305	3.553777	-0.446223
Ge	0.203417	74	-7.83786	-13.5633	0.031022	4.265267	0.265267
Ge	0.284461	75	-5.87684	-10.1669	0.02076	4.346311	0.346311
Ge	0.164196	76	-3.9321	-6.79851	0.02076	4.226046	0.226046
Ge	0.216029	77	-1.97128	-3.40203	0.031022	4.277879	0.277879
Ge	0.283665	78	-17.6257	-3.40203	0.031022	4.345515	0.345515
Ge	0.647511	79	-15.6651	-0.00616	0.031022	4.709361	0.709361
Ge	0.214444	80	-13.704	3.402265	0.000237	4.276294	0.276294
Ge	0.32628	81	-11.7553	6.786948	0.017208	4.38813	0.38813
Ge	0.277053	82	-9.79847	10.16688	0.000237	4.338903	0.338903
Ge	-0.049659	83	-15.6648	-6.79851	0.02076	4.012191	0.012191
Ge	-0.073845	84	-13.7019	-3.40349	0	3.988005	-0.011995
Ge	0.559369	85	-11.7432	-0.00604	0.02076	4.621219	0.621219
Ge	0.54036	86	-9.79847	3.397547	0.017208	4.60221	0.60221
Ge	0.278581	87	-7.8416	6.786948	0.017208	4.340431	0.340431
Ge	0.200311	88	-13.7201	-10.1669	0.02076	4.262161	0.262161
Ge	0.2514	89	-11.7437	-6.78026	0.02426	4.31325	0.31325
Ge	0.172415	90	-9.79847	-3.41095	0.02426	4.234265	0.234265
Ge	0.519073	91	-7.85373	-0.00604	0.02076	4.580923	0.580923
Ge	0.172386	92	-5.89292	3.402265	0.000237	4.234236	0.234236
Ge	0.005611	93	-11.7591	-13.5633	0.031022	4.067461	0.067461
Ge	-0.230634	94	-9.79847	-10.1645	0	3.831216	-0.168784
Ge	0.19589	95	-7.8532	-6.78026	0.02426	4.25774	0.25774
Ge	-0.1069[illegible]	96	-5.89501	-3.40349	0	3.954903	-0.045097
Ge	0.76669[illegible]	97	[illegible]	-0.00616	0.031022	4.82883	0.82883
Si	[illegible]	98	[illegible]	[illegible]	0.654487	3.677954	-0.322046
Si	-0.202211	99	-15.6636	4.535855	0.635648	3.735939	-0.264061
Si	-0.419916	100	-13.7153	7.918552	0.661434	3.518234	-0.481766
Si	-0.119956	101	-11.76	11.29714	0.635648	3.818194	-0.181806
Si	-0.203344	102	-9.79847	14.69275	0.654487	3.734606	-0.265394
Si	-0.17194	103	-15.6567	-2.2749	0.644857	3.76621	-0.23379
Si	-0.183873	104	-13.7021	1.138444	0.635648	3.754277	-0.245723
Si	-0.394286	105	-11.7523	4.529084	0.646252	3.543864	-0.456136
Si	-0.235121	106	-9.79847	7.91324	0.646252	3.702929	-0.297071
Si	-0.064861	107	-7.83697	11.29714	0.635648	3.873289	-0.126711
Si	-0.093483	108	-13.707	-5.66245	0.647541	3.844667	-0.155333
Si	-0.273631	109	-11.7482	-2.26959	0.647541	3.664519	-0.335481
Si	-0.700572	110	-9.79847	1.134337	0.661434	3.237578	-0.762422
Si	-0.248856	111	-7.84462	4.529084	0.646252	3.589294	-0.410706
Si	-0.356216	112	-5.8816	7.918552	0.661434	3.581934	-0.418066
Si	-0.09444	113	-11.7573	-9.03943	0.647541	3.88371	-0.11629
Si	0.035024	114	-9.79847	-5.65716	0.703244	3.973784	-0.026216
Si	-0.13664	115	-7.84877	-2.26959	0.647541	3.80151	-0.19849
Si	-0.401421	116	-5.89484	1.138444	0.635648	3.536729	-0.463271
Si	-0.027519	117	-3.93334	4.535855	0.635648	3.910631	-0.089369
Si	0.157297	118	-9.79847	-12.4217	0.644857	4.095447	0.095447
Si	-0.081325	119	-7.8396	-9.03943	0.647541	3.856825	-0.143175
Si	-0.092142	120	-5.8899	-5.66245	0.647541	3.845808	-0.154192
Si	-0.224327	121	-3.94023	-2.2749	0.644857	3.713823	-0.286177
Si	-0.204061	122	-1.97339	1.139327	0.654487	3.734089	-0.265911

SiGe sheet

Table B-3: The charge distribution analyses of SiGe/GeC-VH (III-GeC_SiGe pattern) for the top GeC layer (left panel), the bottom SiGe layer (right bottom panel), and the summary of the charge analysis (right top panel), respectively. The notations regarding to 'net_charge' denote the net charge transfer between atoms, and the notations regarding to 'diff_net_charge denote the difference of the net charge transfer between atoms on the SiGe/GeC-VH and on the corresponding pristine sheets.

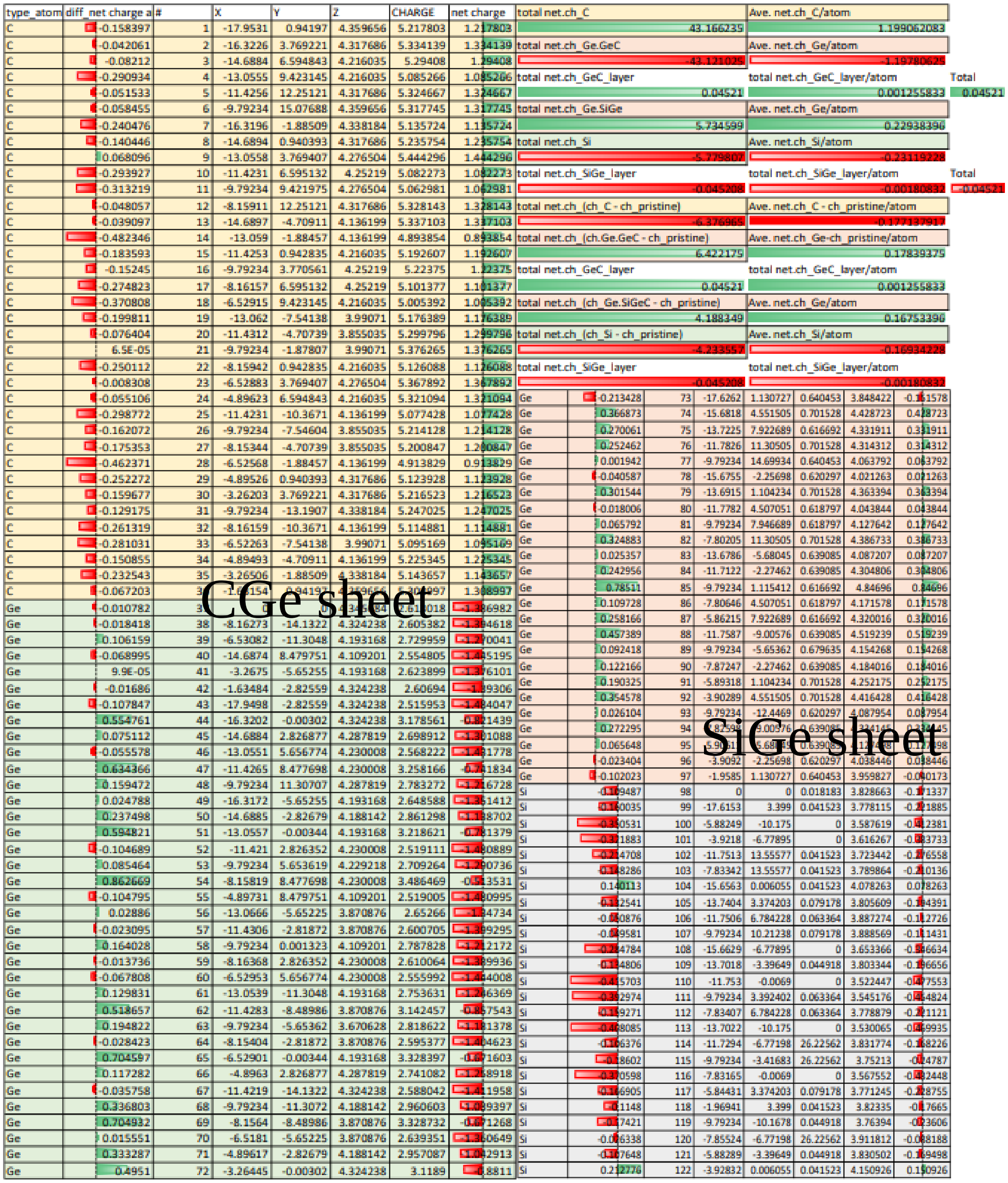

type_atom	diff_net charge a	#	X	Y	Z	CHARGE	net charge
C	-0.158397	1	-17.9531	0.94197	4.359656	5.217803	1.217803
C	-0.042061	2	-16.3226	3.769221	4.317686	5.334139	1.334139
C	-0.08212	3	-14.6884	6.594843	4.216035	5.29408	1.29408
C	-0.290934	4	-13.0555	9.423145	4.216035	5.085266	1.085266
C	-0.051533	5	-11.4256	12.25121	4.317686	5.324667	1.324667
C	-0.058455	6	-9.79234	15.07688	4.359656	5.317745	1.317745
C	-0.240476	7	-16.3196	-1.88509	4.338184	5.135724	1.135724
C	-0.140446	8	-14.6894	0.940393	4.317686	5.235754	1.235754
C	0.068096	9	-13.0558	3.769407	4.276504	5.444296	1.444296
C	-0.293927	10	-11.4231	6.595132	4.25219	5.082273	1.082273
C	-0.313219	11	-9.79234	9.421975	4.276504	5.062981	1.062981
C	-0.048057	12	-8.15911	12.25121	4.317686	5.328143	1.328143
C	-0.039097	13	-14.6897	-4.70911	4.136199	5.337103	1.337103
C	-0.482346	14	-13.059	-1.88457	4.136199	4.893854	0.893854
C	-0.183593	15	-11.4253	0.942835	4.216035	5.192607	1.192607
C	-0.15245	16	-9.79234	3.770561	4.25219	5.22375	1.22375
C	-0.274823	17	-8.16157	6.595132	4.25219	5.101377	1.101377
C	-0.370808	18	-6.52915	9.423145	4.216035	5.005392	1.005392
C	-0.199811	19	-13.062	-7.54138	3.99071	5.176389	1.176389
C	-0.076404	20	-11.4312	-4.70739	3.855035	5.299796	1.299796
C	6.5E-05	21	-9.79234	-1.87807	3.99071	5.376265	1.376265
C	-0.250112	22	-8.15942	0.942835	4.216035	5.126088	1.126088
C	-0.008308	23	-6.52883	3.769407	4.276504	5.367892	1.367892
C	-0.055106	24	-4.89623	6.594843	4.216035	5.321094	1.321094
C	-0.298772	25	-11.4231	-10.3671	4.136199	5.077428	1.077428
C	-0.162072	26	-9.79234	-7.54604	3.855035	5.214128	1.214128
C	-0.175353	27	-8.15344	-4.70739	3.855035	5.200847	1.200847
C	-0.462371	28	-6.52568	-1.88457	4.136199	4.913829	0.913829
C	-0.252272	29	-4.89526	0.940393	4.317686	5.123928	1.123928
C	-0.159677	30	-3.26203	3.769221	4.317686	5.216523	1.216523
C	-0.129175	31	-9.79234	-13.1907	4.338184	5.247025	1.247025
C	-0.261319	32	-8.16159	-10.3671	4.136199	5.114881	1.114881
C	-0.281031	33	-6.52263	-7.54138	3.99071	5.095169	1.095169
C	-0.150855	34	-4.89493	-4.70911	4.136199	5.225345	1.225345
C	-0.232543	35	-3.26506	-1.88509	4.338184	5.143657	1.143657
C	-0.067203	36	[illegible]	0.94197	4.359656	5.308997	1.308997
Ge	-0.010782	37	0	0	[illegible]	2.613018	-1.386982
Ge	-0.018418	38	-8.16273	-14.1322	4.324238	2.605382	-1.394618
Ge	0.106159	39	-6.53082	-11.3048	4.193168	2.729959	-1.270041
Ge	-0.068995	40	-14.6874	8.479751	4.109201	2.554805	-1.445195
Ge	9.9E-05	41	-3.2675	-5.65255	4.193168	2.623899	-1.376101
Ge	-0.01686	42	-1.63484	-2.82559	4.324238	2.60694	-1.39306
Ge	-0.107847	43	-17.9498	-2.82559	4.324238	2.515953	-1.484047
Ge	0.554761	44	-16.3202	-0.00302	4.324238	3.178561	-0.821439
Ge	0.075112	45	-14.6884	2.826877	4.287819	2.698912	-1.301088
Ge	-0.055578	46	-13.0551	5.656774	4.230008	2.568222	-1.431778
Ge	0.634366	47	-11.4265	8.477698	4.230008	3.258166	-0.741834
Ge	0.159472	48	-9.79234	11.30707	4.287819	2.783272	-1.216728
Ge	0.024788	49	-16.3172	-5.65255	4.193168	2.648588	-1.351412
Ge	0.237498	50	-14.6885	-2.82679	4.188142	2.861298	-1.138702
Ge	0.594821	51	-13.0557	-0.00344	4.193168	3.218621	-0.781379
Ge	-0.104689	52	-11.421	2.826352	4.230008	2.519111	-1.480889
Ge	0.085464	53	-9.79234	5.653619	4.229218	2.709264	-1.290736
Ge	0.862669	54	-8.15819	8.477698	4.230008	3.486469	-0.513531
Ge	-0.104795	55	-4.89731	8.479751	4.109201	2.519005	-1.480995
Ge	0.02886	56	-13.0666	-5.65225	3.870876	2.65266	-1.34734
Ge	-0.023095	57	-11.4306	-2.81872	3.870876	2.600705	-1.399295
Ge	0.164028	58	-9.79234	0.001323	4.109201	2.787828	-1.212172
Ge	-0.013736	59	-8.16368	2.826352	4.230008	2.610064	-1.389936
Ge	-0.067808	60	-6.52953	5.656774	4.230008	2.555992	-1.444008
Ge	0.129831	61	-13.0539	-11.3048	4.193168	2.753631	-1.246369
Ge	0.518657	62	-11.4283	-8.48986	3.870876	3.142457	-0.857543
Ge	0.194822	63	-9.79234	-5.65362	3.670628	2.818622	-1.181378
Ge	-0.028423	64	-8.15404	-2.81872	3.870876	2.595377	-1.404623
Ge	0.704597	65	-6.52901	-0.00344	4.193168	3.328397	-0.671603
Ge	0.117282	66	-4.8963	2.826877	4.287819	2.741082	-1.258918
Ge	-0.035758	67	-11.4219	-14.1322	4.324238	2.588042	-1.411958
Ge	0.336803	68	-9.79234	-11.3072	4.188142	2.960603	-1.039397
Ge	0.704932	69	-8.1564	-8.48986	3.870876	3.328732	-0.671268
Ge	0.015551	70	-6.5181	-5.65225	3.870876	2.639351	-1.360649
Ge	0.333287	71	-4.89617	-2.82679	4.188142	2.957087	-1.042913
Ge	0.4951	72	-3.26445	-0.00302	4.324238	3.1189	-0.8811

CGe sheet

total net.ch_C		Ave. net.ch_C/atom		
43.166235		1.199062083		
total net.ch_Ge.GeC		Ave. net.ch_Ge/atom		
-43.121025		-1.19780625		
total net.ch_GeC_layer		total net.ch_GeC_layer/atom		Total
0.04521		0.001255833		0.04521
total net.ch_Ge.SiGe		Ave. net.ch_Ge/atom		
5.734599		0.22938396		
total net.ch_Si		Ave. net.ch_Si/atom		
-5.779807		-0.23119228		
total net.ch_SiGe_layer		total net.ch_SiGe_layer/atom		Total
-0.045208		-0.00180832		-0.04521
total net.ch_(ch_C - ch_pristine)		Ave. net.ch_C - ch_pristine/atom		
-6.376965		-0.177137917		
total net.ch_(ch.Ge.GeC - ch_pristine)		Ave. net.ch_Ge-ch_pristine/atom		
6.422175		0.17839375		
total net.ch_GeC_layer		total net.ch_GeC_layer/atom		
0.04521		0.001255833		
total net.ch_(ch_Ge.SiGeC - ch_pristine)		Ave. net.ch_Ge/atom		
4.188349		0.16753396		
total net.ch_(ch_Si - ch_pristine)		Ave. net.ch_Si/atom		
-4.233557		-0.16934228		
total net.ch_SiGe_layer		total net.ch_SiGe_layer/atom		
-0.045208		-0.00180832		

Ge	-0.213428	73	-17.6262	1.130727	0.640453	3.848422	-0.151578
Ge	0.366873	74	-15.6818	4.551505	0.701528	4.428723	0.428723
Ge	0.270061	75	-13.7225	7.922689	0.616692	4.331911	0.331911
Ge	0.252462	76	-11.7826	11.30505	0.701528	4.314312	0.314312
Ge	0.001942	77	-9.79234	14.69934	0.640453	4.063792	0.063792
Ge	-0.040587	78	-15.6755	-2.25698	0.620297	4.021263	0.021263
Ge	0.301544	79	-13.6915	1.104234	0.701528	4.363394	0.363394
Ge	-0.018006	80	-11.7782	4.507051	0.618797	4.043844	0.043844
Ge	0.065792	81	-9.79234	7.946689	0.618797	4.127642	0.127642
Ge	0.324883	82	-7.80205	11.30505	0.701528	4.386733	0.386733
Ge	0.025357	83	-13.6786	-5.68045	0.639085	4.087207	0.087207
Ge	0.242956	84	-11.7122	-2.27462	0.639085	4.304806	0.304806
Ge	0.78511	85	-9.79234	1.115412	0.616692	4.84696	0.84696
Ge	0.109728	86	-7.80646	4.507051	0.618797	4.171578	0.171578
Ge	0.258166	87	-5.86215	7.922689	0.616692	4.320016	0.320016
Ge	0.457389	88	-11.7587	-9.00576	0.639085	4.519239	0.519239
Ge	0.092418	89	-9.79234	-5.65362	0.679635	4.154268	0.154268
Ge	0.122166	90	-7.87247	-2.27462	0.639085	4.184016	0.184016
Ge	0.190325	91	-5.89318	1.104234	0.701528	4.252175	0.252175
Ge	0.354578	92	-3.90289	4.551505	0.701528	4.416428	0.416428
Ge	0.026104	93	-9.79234	-12.4469	0.620297	4.087954	0.087954
Ge	0.272295	94	[illegible]	-9.00576	0.639085	4.334145	0.334145
Ge	0.065648	95	[illegible]	-5.68045	0.639085	4.127498	0.127498
Ge	-0.023404	96	-3.9092	-2.25698	0.620297	4.038446	0.038446
Ge	-0.102023	97	-1.9585	1.130727	0.640453	3.959827	-0.040173
Si	-0.109487	98	0	0	0.018183	3.828663	-0.171337
Si	-0.160035	99	-17.6153	3.399	0.041523	3.778115	-0.221885
Si	-0.350531	100	-5.88249	-10.175	0	3.587619	-0.412381
Si	-0.321883	101	-3.9218	-6.77895	0	3.616267	-0.383733
Si	-0.214708	102	-11.7513	13.55577	0.041523	3.723442	-0.276558
Si	-0.148286	103	-7.83342	13.55577	0.041523	3.789864	-0.210136
Si	0.140113	104	-15.6563	0.006055	0.041523	4.078263	0.078263
Si	-0.132541	105	-13.7404	3.374203	0.079178	3.805609	-0.194391
Si	-0.050876	106	-11.7506	6.784228	0.063364	3.887274	-0.112726
Si	-0.049581	107	-9.79234	10.21238	0.079178	3.888569	-0.111431
Si	-0.284784	108	-15.6629	-6.77895	0	3.653366	-0.346634
Si	-0.134806	109	-13.7018	-3.39649	0.044918	3.803344	-0.196656
Si	-0.415703	110	-11.753	-0.0069	0	3.522447	-0.477553
Si	-0.392974	111	-9.79234	3.392402	0.063364	3.545176	-0.454824
Si	-0.159271	112	-7.83407	6.784228	0.063364	3.778879	-0.221121
Si	-0.408085	113	-13.7022	-10.175	0	3.530065	-0.469935
Si	-0.106376	114	-11.7294	-6.77198	26.22562	3.831774	-0.168226
Si	-0.18602	115	-9.79234	-3.41683	26.22562	3.75213	-0.24787
Si	-0.370598	116	-7.83165	-0.0069	0	3.567552	-0.432448
Si	-0.166905	117	-5.84431	3.374203	0.079178	3.771245	-0.228755
Si	-0.1148	118	-1.96941	3.399	0.041523	3.82335	-0.17665
Si	-0.17421	119	-9.79234	-10.1678	0.044918	3.76394	-0.23606
Si	-0.026338	120	-7.85524	-6.77198	26.22562	3.911812	-0.088188
Si	-0.107648	121	-5.88289	-3.39649	0.044918	3.830502	-0.169498
Si	0.212776	122	-3.92832	0.006055	0.041523	4.150926	0.150926

SiGe sheet

Table B-4: The charge distribution analyses of SiGe/GeC-VH (IV-GeC_GeSi pattern) for the top GeC layer (left panel), the bottom SiGe layer (right bottom panel), and the summary of the charge analysis (right top panel), respectively. The notations regarding to 'net_charge' denote the net charge transfer between atoms, and the notations regarding to 'diff_net_charge denote the difference of the net charge transfer between atoms on the SiGe/GeC-VH and on the corresponding pristine sheets.

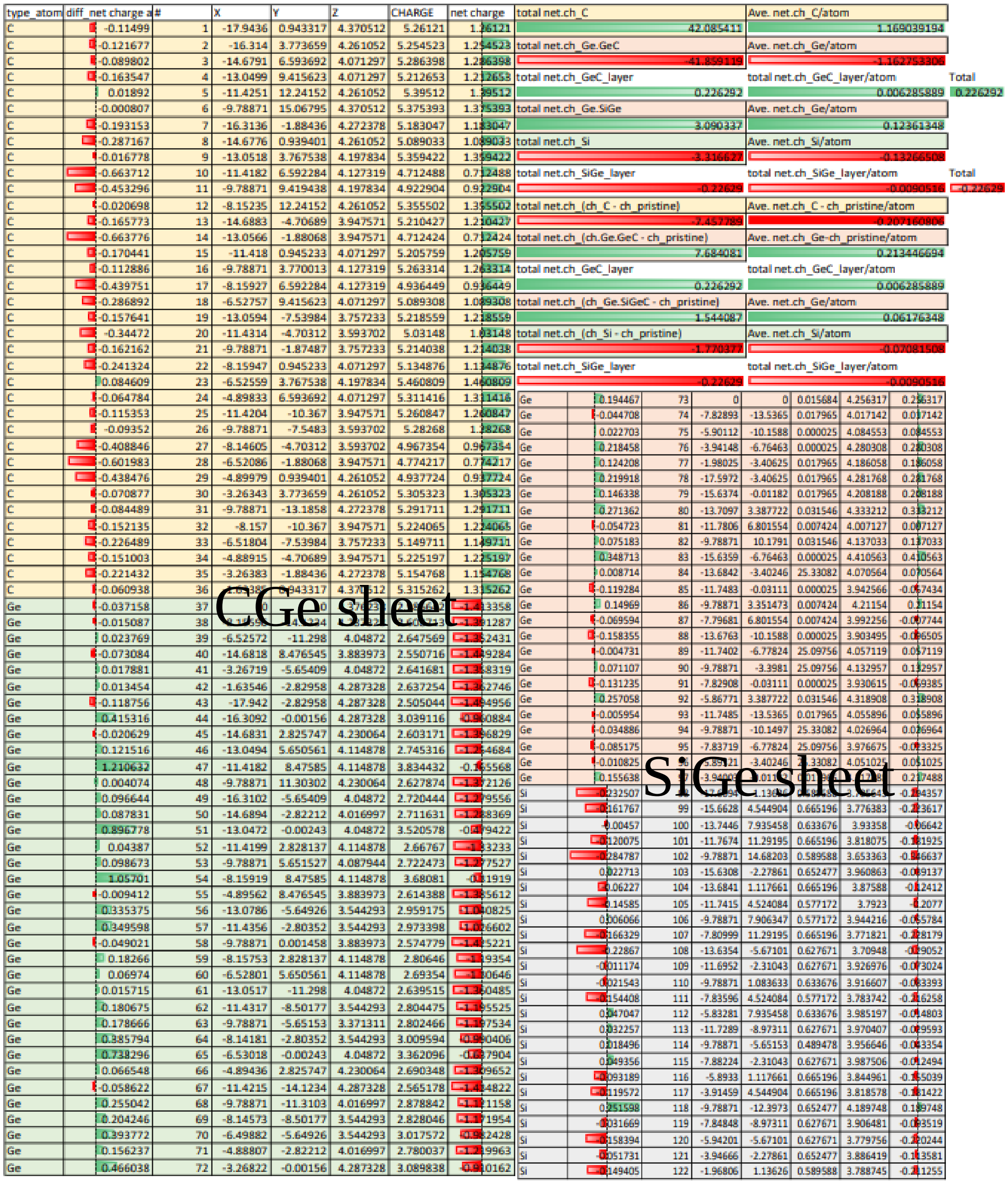

type_atom	diff_net charge a	#	X	Y	Z	CHARGE	net charge
C	-0.11499	1	-17.9436	0.943317	4.370512	5.26121	1.26121
C	-0.121677	2	-16.314	3.773659	4.261052	5.254523	1.254523
C	-0.089802	3	-14.6791	6.593692	4.071297	5.286398	1.286398
C	-0.163547	4	-13.0499	9.415623	4.071297	5.212653	1.212653
C	0.01892	5	-11.4251	12.24152	4.261052	5.39512	1.39512
C	-0.000807	6	-9.78871	15.06795	4.370512	5.375393	1.375393
C	-0.193153	7	-16.3136	-1.88436	4.272378	5.183047	1.183047
C	-0.287167	8	-14.6776	0.939401	4.261052	5.089033	1.089033
C	-0.016778	9	-13.0518	3.767538	4.197834	5.359422	1.359422
C	-0.663712	10	-11.4182	6.592284	4.127319	4.712488	0.712488
C	-0.453296	11	-9.78871	9.419438	4.197834	4.922904	0.922904
C	-0.020698	12	-8.15235	12.24152	4.261052	5.355502	1.355502
C	-0.165773	13	-14.6883	-4.70689	3.947571	5.210427	1.210427
C	-0.663776	14	-13.0566	-1.88068	3.947571	4.712424	0.712424
C	-0.170441	15	-11.418	0.945233	4.071297	5.205759	1.205759
C	-0.112886	16	-9.78871	3.770013	4.127319	5.263314	1.263314
C	-0.439751	17	-8.15927	6.592284	4.127319	4.936449	0.936449
C	-0.286892	18	-6.52757	9.415623	4.071297	5.089308	1.089308
C	-0.157641	19	-13.0594	-7.53984	3.757233	5.218559	1.218559
C	-0.34472	20	-11.4314	-4.70312	3.593702	5.03148	1.03148
C	-0.162162	21	-9.78871	-1.87487	3.757233	5.214038	1.214038
C	-0.241324	22	-8.15947	0.945233	4.071297	5.134876	1.134876
C	0.084609	23	-6.52559	3.767538	4.197834	5.460809	1.460809
C	-0.064784	24	-4.89833	6.593692	4.071297	5.311416	1.311416
C	-0.115353	25	-11.4204	-10.367	3.947571	5.260847	1.260847
C	-0.09352	26	-9.78871	-7.5483	3.593702	5.28268	1.28268
C	-0.408846	27	-8.14605	-4.70312	3.593702	4.967354	0.967354
C	-0.601983	28	-6.52086	-1.88068	3.947571	4.774217	0.774217
C	-0.438476	29	-4.89979	0.939401	4.261052	4.937724	0.937724
C	-0.070877	30	-3.26343	3.773659	4.261052	5.305323	1.305323
C	-0.084489	31	-9.78871	-13.1858	4.272378	5.291711	1.291711
C	-0.152135	32	-8.157	-10.367	3.947571	5.224065	1.224065
C	-0.226489	33	-6.51804	-7.53984	3.757233	5.149711	1.149711
C	-0.151003	34	-4.88915	-4.70689	3.947571	5.225197	1.225197
C	-0.221432	35	-3.26383	-1.88436	4.272378	5.154768	1.154768
C	-0.060938	36	[illegible]	0.943317	4.370512	5.315262	1.315262
Ge	-0.037158	37	[illegible]	[illegible]	[illegible]	[illegible]	-1.413358
Ge	-0.015087	38	[illegible]	[illegible]	[illegible]	[illegible]	-1.391287
Ge	0.023769	39	-6.52572	-11.298	4.04872	2.647569	-1.352431
Ge	-0.073084	40	-14.6818	8.476545	3.883973	2.550716	-1.449284
Ge	0.017881	41	-3.26719	-5.65409	4.04872	2.641681	-1.358319
Ge	0.013454	42	-1.63546	-2.82958	4.287328	2.637254	-1.362746
Ge	-0.118756	43	-17.942	-2.82958	4.287328	2.505044	-1.494956
Ge	0.415316	44	-16.3092	-0.00156	4.287328	3.039116	-0.960884
Ge	-0.020629	45	-14.6831	2.825747	4.230064	2.603171	-1.396829
Ge	0.121516	46	-13.0494	5.650561	4.114878	2.745316	-1.254684
Ge	1.210632	47	-11.4182	8.47585	4.114878	3.834432	-0.165568
Ge	0.004074	48	-9.78871	11.30302	4.230064	2.627874	-1.372126
Ge	0.096644	49	-16.3102	-5.65409	4.04872	2.720444	-1.279556
Ge	0.087831	50	-14.6894	-2.82212	4.016997	2.711631	-1.288369
Ge	0.896778	51	-13.0472	-0.00243	4.04872	3.520578	-0.479422
Ge	0.04387	52	-11.4199	2.828137	4.114878	2.66767	-1.33233
Ge	0.098673	53	-9.78871	5.651527	4.087944	2.722473	-1.277527
Ge	1.05701	54	-8.15919	8.47585	4.114878	3.68081	-0.31919
Ge	-0.009412	55	-4.89562	8.476545	3.883973	2.614388	-1.385612
Ge	0.335375	56	-13.0786	-5.64926	3.544293	2.959175	-1.040825
Ge	0.349598	57	-11.4356	-2.80352	3.544293	2.973398	-1.026602
Ge	-0.049021	58	-9.78871	0.001458	3.883973	2.574779	-1.425221
Ge	0.18266	59	-8.15753	2.828137	4.114878	2.80646	-1.19354
Ge	0.06974	60	-6.52801	5.650561	4.114878	2.69354	-1.30646
Ge	0.015715	61	-13.0517	-11.298	4.04872	2.639515	-1.360485
Ge	0.180675	62	-11.4317	-8.50177	3.544293	2.804475	-1.195525
Ge	0.178666	63	-9.78871	-5.65153	3.371311	2.802466	-1.197534
Ge	0.385794	64	-8.14181	-2.80352	3.544293	3.009594	-0.990406
Ge	0.738296	65	-6.53018	-0.00243	4.04872	3.362096	-0.637904
Ge	0.066548	66	-4.89436	2.825747	4.230064	2.690348	-1.309652
Ge	-0.058622	67	-11.4215	-14.1234	4.287328	2.565178	-1.434822
Ge	0.255042	68	-9.78871	-11.3103	4.016997	2.878842	-1.121158
Ge	0.204246	69	-8.14573	-8.50177	3.544293	2.828046	-1.171954
Ge	0.393772	70	-6.49882	-5.64926	3.544293	3.017572	-0.982428
Ge	0.156237	71	-4.88807	-2.82212	4.016997	2.780037	-1.219963
Ge	0.466038	72	-3.26822	-0.00156	4.287328	3.089838	-0.910162

total net.ch_C	Ave. net.ch_C/atom	
42.085411	1.169039194	
total net.ch_Ge.GeC	Ave. net.ch_Ge/atom	
-41.859119	-1.162753306	
total net.ch_GeC_layer	total net.ch_GeC_layer/atom	Total
0.226292	0.006285889	0.226292
total net.ch_Ge.SiGe	Ave. net.ch_Ge/atom	
3.090337	0.12361348	
total net.ch_Si	Ave. net.ch_Si/atom	
-3.316627	-0.13266508	
total net.ch_SiGe_layer	total net.ch_SiGe_layer/atom	Total
-0.22629	-0.0090516	-0.22629
total net.ch_(ch_C - ch_pristine)	Ave. net.ch_C - ch_pristine/atom	
-7.457789	-0.207160806	
total net.ch_(ch.Ge.GeC - ch_pristine)	Ave. net.ch_Ge-ch_pristine/atom	
7.684081	0.213446694	
total net.ch_GeC_layer	total net.ch_GeC_layer/atom	
0.226292	0.006285889	
total net.ch_(ch_Ge.SiGeC - ch_pristine)	Ave. net.ch_Ge/atom	
1.544087	0.06176348	
total net.ch_(ch_Si - ch_pristine)	Ave. net.ch_Si/atom	
-1.770377	-0.07081508	
total net.ch_SiGe_layer	total net.ch_SiGe_layer/atom	
-0.22629	-0.0090516	

Ge	0.194467	73	0	0	0.015684	4.256317	0.256317
Ge	-0.044708	74	-7.82893	-13.5365	0.017965	4.017142	0.017142
Ge	0.022703	75	-5.90112	-10.1588	0.000025	4.084553	0.084553
Ge	0.218458	76	-3.94148	-6.76463	0.000025	4.280308	0.280308
Ge	0.124208	77	-1.98025	-3.40625	0.017965	4.186058	0.186058
Ge	0.219918	78	-17.5972	-3.40625	0.017965	4.281768	0.281768
Ge	0.146338	79	-15.6374	-0.01182	0.017965	4.208188	0.208188
Ge	0.271362	80	-13.7097	3.387722	0.031546	4.333212	0.333212
Ge	-0.054723	81	-11.7806	6.801554	0.007424	4.007127	0.007127
Ge	0.075183	82	-9.78871	10.1791	0.031546	4.137033	0.137033
Ge	0.348713	83	-15.6359	-6.76463	0.000025	4.410563	0.410563
Ge	0.008714	84	-13.6842	-3.40246	25.33082	4.070564	0.070564
Ge	-0.119284	85	-11.7483	-0.03111	0.000025	3.942566	-0.057434
Ge	0.14969	86	-9.78871	3.351473	0.007424	4.21154	0.21154
Ge	-0.069594	87	-7.79681	6.801554	0.007424	3.992256	-0.007744
Ge	-0.158355	88	-13.6763	-10.1588	0.000025	3.903495	-0.096505
Ge	-0.004731	89	-11.7402	-6.77824	25.09756	4.057119	0.057119
Ge	0.071107	90	-9.78871	-3.3981	25.09756	4.132957	0.132957
Ge	-0.131235	91	-7.82908	-0.03111	0.000025	3.930615	-0.069385
Ge	0.257058	92	-5.86771	3.387722	0.031546	4.318908	0.318908
Ge	-0.005954	93	-11.7485	-13.5365	0.017965	4.055896	0.055896
Ge	-0.034886	94	-9.78871	-10.1497	25.33082	4.026964	0.026964
Ge	-0.085175	95	-7.83719	-6.77824	25.09756	3.976675	-0.023325
Ge	-0.010825	96	[illegible]	-3.40246	[illegible]	4.051025	0.051025
Ge	0.155638	97	[illegible]	[illegible]	[illegible]	[illegible]	0.217488
Si	-0.232507	98	[illegible]	[illegible]	[illegible]	[illegible]	-0.284357
Si	-0.161767	99	-15.6628	4.544904	0.665196	3.776383	-0.223617
Si	-0.00457	100	-13.7446	7.935458	0.633676	3.93358	-0.06642
Si	-0.120075	101	-11.7674	11.29195	0.665196	3.818075	-0.181925
Si	-0.284787	102	-9.78871	14.68203	0.589588	3.653363	-0.346637
Si	0.022713	103	-15.6308	-2.27861	0.652477	3.960863	-0.039137
Si	-0.06227	104	-13.6841	1.117661	0.665196	3.87588	-0.12412
Si	-0.14585	105	-11.7415	4.524084	0.577172	3.7923	-0.2077
Si	0.006066	106	-9.78871	7.906347	0.577172	3.944216	-0.055784
Si	-0.166329	107	-7.80999	11.29195	0.665196	3.771821	-0.228179
Si	-0.22867	108	-13.6354	-5.67101	0.627671	3.70948	-0.29052
Si	-0.011174	109	-11.6952	-2.31043	0.627671	3.926976	-0.073024
Si	-0.021543	110	-9.78871	1.083633	0.633676	3.916607	-0.083393
Si	-0.154408	111	-7.83596	4.524084	0.577172	3.783742	-0.216258
Si	0.047047	112	-5.83281	7.935458	0.633676	3.985197	-0.014803
Si	0.032257	113	-11.7289	-8.97311	0.627671	3.970407	-0.029593
Si	0.018496	114	-9.78871	-5.65153	0.489478	3.956646	-0.043354
Si	0.049356	115	-7.88224	-2.31043	0.627671	3.987506	-0.012494
Si	-0.093189	116	-5.8933	1.117661	0.665196	3.844961	-0.155039
Si	-0.119572	117	-3.91459	4.544904	0.665196	3.818578	-0.181422
Si	0.251598	118	-9.78871	-12.3973	0.652477	4.189748	0.189748
Si	-0.031669	119	-7.84848	-8.97311	0.627671	3.906481	-0.093519
Si	-0.158394	120	-5.94201	-5.67101	0.627671	3.779756	-0.220244
Si	-0.051731	121	-3.94666	-2.27861	0.652477	3.886419	-0.113581
Si	-0.149405	122	-1.96806	1.13626	0.589588	3.788745	-0.211255

CURRICULUM VITA

NAME: Safia Abdullah R Alharbi

ADDRESS: 4048 Crawford Ave. Louisville, KY,40218 USA

PHONE: +1 (832) 903 8940

EMIAL: Saalha02@louisville.edu

EDUCATION

- Spring 2018-present

Ph.D. of science in Physics, University of Louisville, Louisville, KY, USA

- ➢ Under supervision of Prof. Dr. Ming Yu, Department of Physics and Astronomy, University of Louisville, Louisville, KY, USA

- Spring 2016 – Fall 2017

Master of science in Physics, University of Louisville, Louisville, KY, USA

- ➢ With First honor and 4 out of 4 in GPA
- ➢ Earned Distinguished Student Award

- Fall 2009 – Spring 2012

Master of Business Administration in Public Administration, king Saud University, Riyadh, Saudi Arabia

- ➢ With First honor
- ➢ Honor of learning under supervision of H.E. Prof. Dr. Ahmad Al-Ameri, Rector of Imam Mohammad Ibn Saud Islamic University (currently)

- Fall 1997 – Spring 2001

Bachelor of Science and Education in Physics, Princess Nora Bint Abdul Rahman University, Riyadh, Saudi Arabia

- ➢ Grade average: Excellent with honor
- ➢ Earned 2nd place among 68 students.

EXPERIENCE

- Aug 2019– current

Lecturer • Department of Physics • College of Science • Imam Mohammad Ibn Saud Islamic University (IMSIU), Riyadh, Saudi Arabia

- Developing and conducting high-quality original research in condensed matter
- Publishing research papers in top-level academic journals

- Oct 2014– Aug 2019

Teaching Assistant • Department of Physics • College of Science • Imam Mohammad Ibn Saud Islamic University (IMSIU), Riyadh, Saudi Arabia

- Taught physics labs: optics, thermodynamic and electrodynamic.
- Coordinator of student’s activity: The International day of light and Metastatic Breast Cancer Awareness Day

- Jun 2001– Oct 2014

Administrator • Ministry of Health • Riyadh, Saudi Arabia

- Vice Director of Scholarship administration
- High job performance – developed management information systems

PROFESSIONAL MEMBERSHIPS

American Physical Society 2018– current

TECHNICAL SKILLS

Python and FORTRAN

VASP and Quantum espresso (QE)

PHONOPY and Bader

Origin, Xmgrace, VESTA, and Molden

MATLAB, Mathematica, and Maple

SPSS, SAS, Microsoft Word, Access, Excel, and PowerPoint

PUBLICATIONS

"The first-principles study of structural and electronic properties of two-dimensional SiC/GeC lateral polar heterostructures," Safia Abdullah R Alharbi, Kazi Jannatul Tasnim, and Ming Yu, Journal of Applied Physics, 132, 184301 (2022)

"Insight into the stacking and species-ordering dependence of interlayer interactions on stabilizing two-dimensional polar heterostructures and their electronic properties," Kazi Jannatul Tasnim, Safia Abdullah R Alharbi, Md Rajib Khan Musa, Simon Hosch Lovell, Zachary Alexander Akridge, and Ming Yu, Nanotechnology, 33, 155706 (2022)

"Anisotropic and Nonlinear Mechanical Properties in Two-dimensional Nanomaterials," Ming Yu, Congyan Zhang, Safia Abdullah R Alharbi, Anna Zeng, Kevin Zeng, Emily Liu, Advanced Materials Letters 10, 880-886 (2019)

PRESENTATIONS

Invited Presenter, "The stability and electronic properties of SiGe/GeC vertical heterostructure," Safia Abdullah R Alharbi, Ahmad Nagab R Alharbi, and Ming Yu, 5th International Conference on Polymer Science & Composite Materials, Dubai, UAE, June 21-22, 2023.

Presenter, "Vertical Heterostructure of 2D Polar Binary Compounds (GeC/SiGe): First- Principles study", Safia Abdullah R Alharbi, Ahmad Nagab Alharbi , and Ming Yu, March Meeting of APS, Las Vegas, NV, March 20–22, 2023

Presenter, “Strain and interface effects on the stability and electronic properties of SiGe/GeC lateral heterostructure,” Safia Abdullah R Alharbi, Kazi Jannatul Tasnim, and Ming Yu, March Meeting of APS, Chicago, IL, March 14–18, 2022

Presenter, “First principles study of the structural and electronic properties of the in-plane SiC/GeC heterostructures,” Safia Abdullah R Alharbi, Kazi Jannatul Tasnim, and Ming Yu, Virtual APS March Meeting 2021, March 15-19, 2021

Co-Author, “The role of the electrostatic interlayer interaction in SiC/GeC heterostructures,” Kazi Jannatul Tasnim, Safia Abdullah R Alharbi, Md Rajib khan Musa, Simon Hosch Lovell, Zachary Alexander Akridge, and Ming Yu, Virtual APS March Meeting 2021, March 15-19, 2021

Poster, “The effect of van der Waals force on two-dimensional SiC/GeC heterostructures,” Safia Abdullah R Alharbi, and Ming Yu, Virtual Annual Graduate Student Regional Research Conference, March 11-12, 2021

Poster, “The effect of van der Waals force on two-dimensional SiC/GeC heterostructures,” Safia Abdullah R Alharbi and Ming Yu, March Meeting of APS, Denver, CO, March 2-6, 2020

Presenter, “Strain induced bandgap engineering on two-dimensional SiC/GeC in-plane heterostructures,” Safia Abdullah R Alharbi, Sultan Alzahrani, and Ming Yu, the 2nd UofL GRADtalks Brown Bag Series, Louisville, KY, November 12-14, 2018.

Presenter, “Strain induced bandgap engineering on two-dimensional SiC/GeC in-plane heterostructures,” Safia Abdullah R Alharbi, Sultan Alzahrani, and Ming Yu, March Meeting of APS, Los Angeles, CA, March 5-9, 2018.

AWARDS

Graduate Student Council Research Award, Graduate School, University of Louisville, Louisville, KY, USA (2023)

Graduate Student Council Travel Award, Graduate School, University of Louisville, Louisville, KY, USA (2023)

Young Woman Researcher in Physics Award, 8th Venus International Women Awards (VIWA), Venus International Foundation, Chennai, India (2023)

Iris M. Ovshinsky Student Travel Award, APS Division of Materials Physics (DMP), 2022 APS March Meeting, Chicago, IL, USA (2022)

Arts and Sciences Research & Creative Activities Award, College of Arts and Sciences, University of Louisville, Louisville, KY, USA (2022)

Graduate Student Council Travel Award, Graduate School, University of Louisville, Louisville, KY, USA (2018)

Distinguished Student Award, The Cultural Mission of the Royal Embassy of Saudi Arabia (SACM), Washington DC., VA, USA (2018)